DEVELOPMENT OF PHOTOSENSITIVE BIOPOLYMERS FOR OCULAR TISSUE ENGINEERING

by

INÊS PIRES MOEDAS DE ALMEIDA BARROSO

A thesis submitted to the
University of Birmingham
for the degree of
DOCTOR OF PHILOSOPHY

Biochemical Engineering
School of Chemical Engineering
College of Engineering and Physical Sciences
University of Birmingham
May 2022

UNIVERSITY OF
BIRMINGHAM

University of Birmingham Research Archive

e-theses repository

This unpublished thesis/dissertation is copyright of the author and/or third parties. The intellectual property rights of the author or third parties in respect of this work are as defined by The Copyright Designs and Patents Act 1988 or as modified by any successor legislation.

Any use made of information contained in this thesis/dissertation must be in accordance with that legislation and must be properly acknowledged. Further distribution or reproduction in any format is prohibited without the permission of the copyright holder.

ABSTRACT

A healthy cornea is essential for vision since this transparent and avascular tissue plays a pivotal role in light transmission and focusing. Corneal diseases and injuries can lead to corneal thinning and opacification, eventually leading to blindness. This thesis aims to engineer novel polymers for corneal tissue repair, reducing the demand for corneal transplants and the usage of sutures and toxic tissue adhesives, such as cyanoacrylates. Here, two cytocompatible and biodegradable biopolymers, silk fibroin and gelatine, were chemically modified with vinyl groups to enable hydrogel photocrosslinking. Using light-mediated crosslinking, hydrogels could be rapidly polymerised *in situ* under wet physiological conditions at body temperature, which are essential requirements for the success of an ocular tissue adhesive. While *in situ* curing allows the hydrogel to fully adapt to the irregular wound shape, a rapid crosslinking reaction prevents adhesive dilution and reduces the intervention time. The overall properties of the hydrogels could be controlled by changing the polymer concentration, photoinitiating system, light characteristics and irradiation time.

Methacrylated silk fibroin (SilkMA) hydrogels prepared using a low UV intensity (3 mW/cm^2) for 5 minutes showed a light transmittance profile and water content (83-90%) similar to the human cornea. Further, gentamicin-loaded SilkMA hydrogels were able to inhibit *in vitro* bacterial growth of two of the most comment causes of ocular infections, *Staphylococcus aureus* and *Pseudomonas aeruginosa*, for 72 h. However, SilkMA hydrogels were not successful sealing *ex vivo* full-thickness corneal perforations due to the presence of residual uncured solution between the hydrogel and the corneal tissue after curing.

Conversely, gelatine methacryoloyl (GelMA) hydrogels crosslinked using visible or UV light for 2 minutes, exhibited *ex vivo* burst pressures comparable to cyanoacrylate adhesives (49 ± 9 kPa) and 25 times higher than the human physiological intraocular pressure (2 ± 0.2 kPa). In addition to superior adhesion onto wet and dry substrates, optical coherence tomography images also demonstrated that the injectable GelMA adhesives were able to fill the wound bed and restore the ocular curvature by forming a transparent smooth contour on the ocular surface. In contrast, cyanoacrylate-based adhesives showed no adhesion on the semi-dry cornea and formed a rough and opaque patch. GelMA bioadhesives have high translational potential due to its adhesive properties, transparency,

cytocompatibility, viscoelasticity and safety in comparison to commercially available options (e.g. fibrin sealants and cyanoacrylates).

Together, the research presented herein highlighted the development of silk and gelatine-based photosensitive polymers that, due to their intrinsic biocompatibility together with the fast kinetics and spatial and temporal control of photocrosslinking reactions, have potential to be applied for several tissue engineering applications, such as drug delivery, cell therapy or light-based bioprinting.

ACKNOWLEDGMENTS

First and foremost, I would like to thank my supervisors, Dr Anita K. Ghag and Dr Sophie C. Cox for all their time, support, thoughtful suggestions and encouragement throughout my PhD research. Thank you for providing me with the chance to pursue my interest in ocular tissue engineering. The knowledge and skills that I have developed under your supervision will follow me for the rest of my life and I will forever be grateful. I would also like to extend my immense appreciation to Dr Kenny Man for his kindness, valuable advice and contributions to this project.

I would like to express my appreciation to the staff members of the School of Chemical Engineering during these years, in particular Emma Lardner and Lynn Draper for their help with the administrative side of things, and Elaine Mitchel, Ronnie Baglin and David French for all their support in the lab and help to find the most amazing pieces of equipment in Biochemical Engineering.

I would also like to express my gratitude to my friends on campus with whom I have had the pleasure to share this journey, thank you for all the memories, laughs and unforgettable debates in the atrium, you are great. To my longtime friends, thank you for being there for me, for all your advice and perspective.

Lastly, I would like to thank my family who stimulated my interest in science from a very young age and always encouraged and supported me unconditionally. Most importantly, I would like to express a heartfelt thanks to my partner Carlos for his support, patience and love, I couldn't have done this without you.

TABLE OF CONTENTS

1 INTRODUCTION 1

2 LITERATURE REVIEW 6

2.1 CLINICAL RELEVANCE 6

2.2 CORNEAL STRUCTURE AND PHYSIOLOGY 6

2.2.1 Epithelium 8

2.2.2 Bowman's layer 8

2.2.3 Stroma 9

2.2.4 Descemet's membrane 10

2.2.5 Endothelium 11

2.3 CORNEAL WOUND HEALING 11

2.4 CORNEAL PROPERTIES AND DESIGN CONSIDERATIONS 13

2.5 TISSUE ADHESIVES 14

2.5.1 Ideal tissue adhesive properties 16

2.5.2 Commercially available tissue adhesives 17

2.5.2.1 Cyanoacrylates 17

2.5.2.2 PEG-based tissue adhesives 22

2.5.2.3 Fibrin-based tissue adhesives 24

2.6 CORNEAL PERFORATIONS 28

2.6.1 Definition and causes 28

2.6.2 Surgical management 29

2.7 THE NEED FOR NOVEL TISSUE ADHESIVES 34

2.8 FDA-APPROVED CORNEAL COLLAGEN CROSSLINKING TREATMENT 36

2.9 PHOTOPOLYMERISATION 39

2.9.1 (Meth)acrylate-based photosensitive polymers 40

2.9.1.1 GelMA 41

2.9.1.2 SilkMA *45*
2.9.2 Photoinitiation systems 49
2.9.2.1 Type I photoinitiators *50*
2.9.2.2 Type II photoinitiators *51*
3 GENERAL METHODS 54
3.1 MATERIAL PREPARATION 54
3.1.1 Preparation of methacrylated silk fibroin hydrogels 54
3.1.1.1 Silk Fibroin extraction *54*
3.1.1.2 SilkMA synthesis *55*
3.1.1.3 Degree of functionalisation *55*
3.1.1.4 Hydrogel fabrication *56*
3.1.2 Preparation of gelatine methacryloyl hydrogels 56
3.1.2.1 GelMA synthesis *56*
3.1.2.2 Degree of functionalisation *57*
3.1.2.3 Hydrogel preparation *57*
3.2 PHYSICOCHEMICAL PROPERTIES 58
3.2.1 Transparency 58
3.2.2 Swelling properties 58
3.2.3 Enzymatic degradation 59
3.2.4 Scanning electron microscopy 59
3.2.5 Micro computed tomography 59
3.3 MECHANICAL AND ADHESIVE PROPERTIES 60
3.3.1 Rheology 60
3.3.2 Compressive modulus 60
3.3.3 Tensile modulus 61
3.3.4 *Ex vivo* burst pressure 61
3.3.5 Lap shear strength 62
3.4 *IN VITRO* CELL STUDIES 63
3.4.1 Cell viability 63
3.4.2 Metabolic activity 64
3.4.3 Cell proliferation 64
3.5 STATISTICAL ANALYSIS 65

4 METHACRYLATED SILK FIBROIN HYDROGELS: PH AS A TOOL TO CONTROL FUNCTIONALITY 66

4.1 INTRODUCTION 67

4.2 METHODS 71

4.2.1 Fourier transform infrared spectroscopy 71

4.2.2 Thioflavin T binding assay 71

4.2.3 *In vitro* cytocompatibility of uncured SilkMA solutions 71

4.2.4 *In vitro* cytocompatibility of SilkMA hydrogels 72

4.3 RESULTS 73

4.3.1 Physicochemical characterisation of SilkMA gels 73

4.3.2 Natural conformational changes in SilkMA hydrogels over time 77

4.3.3 *In vitro* assessment of cytocompatibility 81

4.4 DISCUSSION 84

4.5 CONCLUSIONS 89

5 PHOTOCURABLE ANTIMICROBIAL SILK-BASED HYDROGELS FOR CORNEAL REPAIR 90

5.1 INTRODUCTION 91

5.2 METHODS 95

5.2.1 Preparation of gentamicin-loaded SilkMA gels 95

5.2.2 Cell viability 96

5.2.3 2D cell seeding on SilkMA gels 96

5.2.4 *In vitro* release of gentamicin from SilkMA gels 97

5.2.5 *In vitro* antimicrobial efficacy testing 98

5.2.5.1 Preparation of bacterial inocula 98

5.2.5.2 Zones of inhibition 98

5.3 RESULTS 99

5.3.1 Physicochemical characterisation of SilkMA gels 99

5.3.2 *In vitro a*ssessment of cytocompatibility 104

5.3.3 *In vitro* drug release studies 106

5.3.4 Antimicrobial efficacy testing 106

5.4 DISCUSSION 107

5.5 CONCLUSION 115

6 PRODUCT DEVELOPMENT: PHOTOSENSITIVE OCULAR ADHESIVES 116

6.1 INTRODUCTION 116

6.2 MATERIALS AND METHODS 120

6.2.1 Molar extinction coefficient 120

6.2.2 Optical coherence tomography imaging and relative stiffness estimation 121

6.2.3 Residual mass 122

6.3 RESULTS 122

6.3.1 Synthesis of SilkMA and GelMA 122

6.3.2 Molar extinction coefficient of different photoinitiators 124

6.3.3 Fabrication of SilkMA hydrogels 125

6.3.4 Fabrication of GelMA hydrogels 128

6.4 DISCUSSION 133

6.5 CONCLUSION 138

7 PHOTOCURABLE GELMA ADHESIVES FOR CORNEAL PERFORATIONS 140

7.1 INTRODUCTION 141

7.2 METHODS 145

7.2.1 *Ex vivo* retention time 145

7.2.2 2D cell seeding on GelMA gels 146

7.3 RESULTS 146

7.3.1 Adhesive properties of GelMA bioadhesives 146

7.3.2 Physicochemical characterisation of GelMA bioadhesives 149

7.3.3 *Ex vivo* retention of GelMA bioadhesives 155

7.3.4 *In vitro* assessment of cytocompatibility 156

7.4 DISCUSSION 158

7.5 CONCLUSION 166

8 CONCLUSIONS AND FUTURE WORK 167

8.1 GENERAL OVERVIEW 167

8.2 OVERARCHING FUTURE WORK 169

8.2.1 *Ex vivo* and *in vivo* studies 169

8.2.2 Drug delivery 170

8.2.3 3D printing....171
8.3 SILKMA HYDROGEL DEVELOPMENT....171
8.3.1 Main limitations....171
8.3.1.1 Limited biological activity....172
8.3.1.2 Low content of lysine residues....172
8.3.1.3 Free-radical polymerisation reaction inhibition by oxygen....173
8.3.1.4 Transparency decrease overtime....173
8.3.2 Future applications....174
8.3.2.1 Cartilage tissue engineering....174
8.3.2.2 Hydrogel adhesives....174
8.4 GELMA ADHESIVE DEVELOPMENT....175
8.4.1 Curing time optimisation....175
8.4.2 Burst pressure for different wound sizes and locations in the cornea and sclera....176
8.4.3 Potential application of GelMA-RF/SPS hydrogels for vascular and lung sealing....176
REFERENCES 178
APPENDIX A: CHAPTER 7 SUPPLEMENTARY MATERIAL....207
APPENDIX B: PUBLISHED PAPERS....209

LIST OF FIGURES

Figure 2.1 – a) Main anatomical components of the human eye with detailed view of the corneal organisation. b) Histologic section of the human cornea labelling the five main sections and its thicknesses: epithelium, Bowman's layer, stroma, Descemet's membrane and endothelium. Adapted from [31].....8

Figure 2.2 – The hierarchical structure of the cornea showing its four main composite-like regions: the Bowman's membrane, anterior stroma, posterior stroma and Descemet's membrane. These structures characterise the overall stiffness, strength and toughness of the corneal. The macroscopic, microscopic and nanoscopic features of the corneal tissue are illustrated (from left to right). Adapted from [31]. 10

Figure 2.3 - Schematic representation of the corneal wound healing mechanism. When the stroma is injured, the keratocytes beneath the corneal epithelium within the zone of injury suffer apoptosis (1) and pro-inflammatory cytokines are released into the anterior stroma (2). Quiescent keratocytes proliferate, migrate, and acquire the phenotype of activated keratocytes (fibroblasts) (3). The fibroblasts transform into myofibroblasts (repair phenotype) and secrete provisional matrix scaffold (4). The normal stromal function is slowly restored by resorption of abnormal ECM and apoptosis of the myofibroblasts (5). However, in pathological conditions myofibroblast secrete irregular matrix (6) causing corneal haze (7) [43,44].....12

Figure 2.4 – Clinical applications of tissue adhesives. Adapted from [53]. 15

Figure 2.5 – a) Polymerisation of cyanoacrylate monomers. b) Degradation of cyanoacrylate adhesives via hydrolysis and production of cyanoacetate and formaldehyde. Adapted from [65]. 18

Figure 2.6 – OcuSeal preparation: a) After breaking the membrane between the transparent and green container the surgeon should shake the applicator for 5 seconds to mix the powder PEG with the liquid polyethylene amine and apply through a brush it within 10 seconds [25]. b) Slitlamp photograph of a non- treated corneal incision one day postoperatively (control). c) Slitlamp photograph of a corneal incision sealed with OcuSeal one day postoperatively [25]. ReSure preparation: d) the diluent is added to the trilysine acetate deposit (blue) and then the applicator is used to mix the solutions for five seconds. The uncured solution should be applied to the eye within 12 seconds after mixing is initiated. e) Sutureless excision of pterygium with amniotic membrane and ReSure: nasal pterygium before surgery; same eye after application of ReSure to secure the amniotic membrane graft to the defective conjunctiva; same eye at 6-weeks post-surgery [97]. 23

Figure 2.7 – a) Fibrin adhesive composition: protein solution and setting solution. b) Schematic representation of the functioning mechanism of fibrin glue: conversion of fibrinogen to fibrin (monomer) and clot formation (insoluble) c) Tisseel Tissue adhesive (Baxter Healthcare Corporation, USA) kit: components (fibrinogen, aprotinin, calcium chloride and thrombin solutions in vials) and standard glue applicator. To seal a defect, both fibrin components are loaded in a dual syringe system with the tips forming a joint port. When the common plunger is pressed, the two components are applied to the delivery site in equal volumes [104]. Alternatively, each component can be applied to opposite sides of the tissue, postponing the polymerisation until two sides are together and allowing better control of the glue amount and distribution [33]. d) Limbal dermoid removal and replacement by a lamellar corneoscleral patch attached with fibrin: 7-mm opaque dermoid; lamellar keratectomy to remove the dermoid; graft attachment with fibrin glue and slit-lamp examination of the graft 10 weeks after surgery [106]. 27

Figure 2.8 – Slit-lamp photograph showing a) a corneal perforation; b) corneal melting; c) corneal perforation sealed with cyanoacrylate glue and d) postoperative photograph after corneal transplant. Adapted from [29,108]. 29

Figure 2.9 – Slit-lamp photograph showing a) large peripheral corneal perforation; b) sutured scleral patch graft incorporated in the corneal stroma after removal of the cyanoacrylate glue at 5 weeks; c) healed corneal perforation 3 months after the intervention. Adapted from [125]. 32

Figure 2.10 – Slit-lamp photograph showing a) corneal perforation; b) tenon patch and cyanoacrylate glue in situ at 3 months post-surgery and c) healed perforation with corneal scar 18 months after surgery. Adapted from [115]. 33

Figure 2.11 – Corneal collagen crosslinking: a) a silicone ring was placed in direct contact with the cornea and filled with RF solution for 30 min before UV-irradiation [140]; b) corneal irradiation with UV-A for 30 minutes, with addition of more RF each 5 minutes [137]....38

Figure 2.12 – Free-radical chain polymerisation: a) general reaction mechanisms: initiation, propagation and termination; b) Schematic of meth(acrylated) polymer chains crosslinked through free-radical polymerisation upon light exposure in the presence of an initiator system. Adapted from [157]. 40

Figure 2.13 – Methacrylation of gelatine with MA and preparation of photocrosslinked GelMA hydrogels in the presence of a photoinitiator and UV/visible light. 44

Figure 2.14 – Methacrylation of silk fibroin with GMA and preparation of photocrosslinked SilkMA hydrogels in the presence of a photoinitiator and UV/visible light. 48

Figure 2.15 – Cleavage of type I radicals into free-radicals following proton absorption: a) I2959 and b) LAP. Adapted from [201]. 50

Figure 3.1 - Workflow for SF extraction and SilkMA synthesis: degumming, dissolution in lithium bromide, methacrylation, dialysis and freeze-drying. 54

Figure 3.2 – Ex vivo burst pressure measurements after creating a full-thickness incision with a 2 mm biopsy punch followed by the adhesive application and in situ curing: a) measurement in wet conditions, a 27-gauge needle was inserted into the anterior chamber; b) measurement in dry conditions, a porcine cornea is mounted in an AAC. Both a) and b) are connected to a syringe pump and a pressure sensor. 62

Figure 3.3 – Schematic of the modified ASTM F2255-05 test for lap shear strength calculation. 63

Figure 4.1 – ^{1}H-NMR spectra of SilkMA (top) and raw SF (bottom). The presence of the methacrylate vinyl group signal (δ = 6.2 ppm) and methyl group signal (δ = 1.8 ppm) after the removal of unreacted GMA by dialysis confirmed the covalent functionalisation of SF with methacrylate groups.....73

Figure 4.2 – SilkMA hydrogel transmittance in the visible range: a) transmittance profiles, b) average optical transmittance and c) optical clarity and rigidity of SilkMA hydrogels. (%). Swelling properties of SilkMA hydrogels in PBS at 37°C: d) swelling (%) and e) hydrogel expansion (%). Hydrogel diameter = 12 mm. Data presented as mean value ± SD (*p<0.05, **p<0.01, ***p<0.001, ****p<0.0001). 75

Figure 4.3 – Rheological properties of SilkMA hydrogels: a) representative frequency sweep, b) storage modulus (G'), c) loss modulus (G'') and d) damping factor (tan δ). Cyclic compressive mechanical testing of SilkMA hydrogels: e) representative compressive strain-stress curves and f) compressive moduli. Data presented as mean value ± SD (*p<0.05, **p<0.01, ***p< 0.001, ****p<0.0001). 76

Figure 4.4 – Study of conformational transitions on SilkMA hydrogels over time: a) FTIR spectra of SilkMA hydrogels after crosslinking (day 0) and 28 days after incubation under physiological conditions, b) β-sheet crystallinity content over time (days 0, 7, 14 and 28), c)

random coil content over time (days 0, 7, 14 and 28) and d) comparison of the β-sheet content between groups at different time points (days 0, 7, 14 and 28). e) ThT staining of SilkMA hydrogels at 1, 7, and 14 days. Emission spectrum in the 440-700 nm range under 360 nm excitation. Data presented as mean value ± SD (*p<0.05, **p<0.01, ***p<0.001, ****p<0.0001).....78

Figure 4.5 – Study of the natural conformational changes in SilkMA hydrogels incubated in PBS at 37°C. a) Average optical transmittance in the visible range of SilkMA hydrogels at 0, 7, 14, and 28 days. b) Appearance of SilkMA hydrogels after incubation for 0, 7, 14, 21 and 28 days (hydrogel diameter = 1 cm). c) Mechanical toughening impact of the increasing β-sheet content on SilkMA hydrogels. d) Compression moduli of SilkMA hydrogels after incubating for 7 days. e) Compression moduli of SilkMA hydrogels after incubating for 14 days. Data presented as mean value ± standard deviation (*p<0.05, **p<0.01, ***p<0.001, ****p<0.0001).....81

Figure 4.6 – Cytotoxicity of uncrosslinked SilkMA prepolymer solutions. a) Live/dead images of HDFs seeded on tissue culture well-plates with media (control) and media supplemented with SF5 and SF7 prepolymer solutions. Scale bar = 200 μm. b) Quantification of the metabolic activity by the alamarBlue assay 24 and 48 h after cell seeding. c) Quantification of cell proliferation by the Picogreen DNA assay 24 and 48 h after cell seeding. Data presented as mean value ± SD (*p<0.05, **p<0.01, ***p< 0.001, ****p<0.0001).....82

Figure 4.7 – Cytotoxicity of SilkMA prepolymer hydrogels: a) live/dead images of HDFs seeded on GelMA, SF5 and SF7 hydrogels. b) Quantification of the metabolic activity by the alamarBlue assay 2, 7 and 14 days after cell seeding. Data presented as mean value ± SD (*p<0.05, **p<0.01, ***p<0.001, ****p<0.0001). 84

Figure 5.1 – Experimental outline investigating the properties of gentamicin-loaded SilkMA hydrogels. 1) Photocrosslinking of 15, 20 and 25% gentamicin-loaded SilkMA hydrogels. The transparency in the visible range, swelling, in vitro degradation, porosity/pore size, compressive young's modulus, and rheological properties of the SilkMA hydrogels were studied. 2) In vitro cytocompatibility of gentamicin-loaded SilkMA hydrogels. Firstly, the cytocompatibility of SF and SilkMA prepolymer solutions and SilkMA hydrogels was assessed. Then, the ability of HDF cells to attach and proliferate on SilkMA hydrogels was studied and compared with GelMA hydrogels. 3) In vitro gentamicin drug release from SilkMA hydrogels. The cumulative drug release of gentamicin from SilkMA hydrogels and gentamicin concentration in the media were calculated. 4) Antimicrobial testing of gentamicin-SilkMA hydrogels. The antimicrobial activity of SilkMA hydrogels against two of the most common causes of ocular infections, Staphylococcus aureus and Pseudomonas aeruginosa was assessed in vitro. 95

Figure 5.2 – SilkMA hydrogels transparency (n=3): a) transmittance profiles, b) average optical transmittance in the visible range and c) optical clarity. Hydrogel diameter = 10 mm. Swelling characteristics of SilkMA hydrogels in PBS at 32°C (n=3): d) swelling ratio (q), e) water content (%) and f) expansion (%). Data presented as mean value ± SD (*p<0.05, **p<0.01, ***p<0.001, ****p<0.0001). 100

Figure 5.3 – Rheological properties of SilkMA hydrogels (n=3): a) representative frequency sweep, b) storage modulus (G'), c) loss modulus (G'') and d) damping factor (tan δ). Data presented as mean value ± SD (*p<0.05, **p<0.01, ***p<0.001, ****p<0.0001). 101

Figure 5.4 – a) In vitro degradation of SilkMA hydrogels incubated in 1 U/mL collagenase II at 32°C for 2, 5 and 7 days (n=5). b) Measurement of the macromers not crosslinked in the hydrogel network after photocrosslinking (mass loss, %) (n=3). Cyclic compressive mechanical testing of SilkMA hydrogels (n=3): c) representative compressive strain-stress curves and d)

Young's moduli. Data presented as mean value ± SD (*p<0.05, **p<0.01, ***p< 0.001, ****p<0.0001).....102

Figure 5.5 – Morphology and microstructure analysis of SilkMA hydrogels after freeze drying (n=3): a) 3D micro-CT reconstruction and 2D images (slices) of SilkMA scaffolds. Diameter = 7 mm. Quantitative analysis of porosity by micro-CT: b) total porosity, c) mean pore thickness, d-e) pore size distribution in the hydrogels and f) mean pore size. Representative SEM images of freeze-dried SilkMA scaffolds: g) 15% SilkMA and h) 20% SilkMA. Scale bar: 150 μm. Data presented as mean value ± SD (*p<0.05, **p<0.01, ***p<0.001, ****p<0.0001).....104

Figure 5.6 – Cytocompatibility study: a) Live/Dead images of HDFs seeded on tissue culture well-plates with media (control) and SF/SilkMA solutions and SilkMA gels in inserts (n=3). Scale bar = 200 μm. b) Quantification of the metabolic activity of HDFs seeded on SilkMA and GelMA hydrogels by AlamarBlue assay 1, 2, 7 and 14 days after cell seeding (n=5). Data presented as mean value ± SD (*****p<0.0001). 105

Figure 5.7 – In vitro properties of gentamicin-loaded SilkMA hydrogels (n=5): a) Cumulative gentamicin drug release from SilkMA scaffolds after 1, 2, 3, 4 and 5 h. b) Gentamicin concentration in the media after 24 and 48 h. Zone of inhibition study (n=3): c) Average zone of inhibition of SilkMA hydrogels after 24, 48 and 72 h. d) Staphylococcus aureus and e) Pseudomonas aeruginosa. Scale bar = 1.5 cm. 107

Figure 6.1 – Schematic outline investigating: 1) The absorption spectra and molar extinction coefficient of different photoinitiators; 2) The development of SilkMA and GelMA-based photosensitive hydrogels for corneal injuries by changing the polymer concentration, photoinitiating system, light source and intensity and time. The ex vivo performance of the hydrogels was assessed by measuring the hydrogel ability to fill the wound, restore the

curvature and remain in situ after incubation using OCT, while mechanical adhesion to porcine corneal tissue was studied by measuring the ex vivo burst pressure.....119

Figure 6.2 – ^{1}H-NMR spectra of GelMA (top) and unfunctionalised gelatine (bottom).....123

Figure 6.3 – Absorption spectra and molar extinction coefficients of commonly used type I (LAP and Irgacure 2959) and type II (RF, ruthenium and eosin-Y) photoinitiators.....124

Figure 6.4 – Appearance of 15% SilkMA hydrogels prepared using different light conditions (wavelength and intensity), curing times and photoinitiators: a) LAP and b) RF and SPS. ..126

Figure 6.5 – SilkMA-LAP hydrogel performance: a) Ex vivo optical coherence tomography images of the native porcine cornea: intensity and mechanical contrast of porcine corneas before and after in situ curing of 15 and 20% SilkMA hydrogels. The stiffness map ranges from dark blue (soft) to yellow (stiff). The arrows indicate areas of uncured gel. b) Relative stiffness of 15 and 20% SilkMA hydrogels calculated from OCT scans. b) Storage modulus of 15 and 20% SilkMA hydrogels. d) Residual mass after photocrosslinking of 15 and 20% SilkMA and GelMA hydrogels. e) Residual mass after photocrosslinking of 20% hydrogels with different formulations: SilkMA, GelMA and different ratios of both polymers. Data presented as mean value ± SD (*p<0.05, **p<0.01, ***p< 0.001, ****p<0.0001).....127

Figure 6.6 – GelMA-LAP and GelMA/SilkMA-LAP hydrogel performance: a) Ex vivo optical coherence tomography images of the native porcine cornea with 15% GelMA and 15% GelMA:SilkMA (1:1) immediately after photocrosslinking (t_0) and after 1 and 5 days. The darker areas below the hydrogel indicate the presence of voids (yellow arrows). b) Representative pressure curves of the studied groups. c) Ex vivo burst pressure of GelMA and GelMA:SilkMA adhesives on the artificial anterior chamber (n=8). Data presented as mean value ± SD (*p<0.05). 129

Figure 6.7 – GelMA-LAP and GelMA-RF/SPS hydrogel performance: a) Appearance of GelMA hydrogels prepared using a RF/SPS photoinitiating system and different curing times,

immediately after curing and after incubation in PBS for 1, 24 and 72 h. b) Mean burst pressure of GelMA adhesives photocrosslinked using LAP and UV light or RF/SPS and visible light in the AAC (n=8). c) Representative pressure curves of the studied groups. Data presented as mean value ± SD (****p<0.0001). 130

Figure 6.8 – GelMA-RF/SPS adhesives mean ocular burst pressure optimisation: a) polymer concentration and curing time and b) light energy and intensity. c) Wavelength maps generated by a self-developed algorithm for optical coherence elastography analysis [314]. The stiffness of the tissue increases from dark blue (soft) to yellow (stiff). d) Relative stiffness of the studied groups overtime (day 0, 1 and 7). Data presented as mean value ± SD (*p<0.05, **p<0.01, ***p< 0.001, ****p<0.0001). 132

Figure 7.1 – Schematic outline investigating the properties of GelMA bioadhesives. 145

Figure 7.2 – Ex vivo burst pressure of GelMA bioadhesives: a) representative pressure curves of the studied groups when the cornea was mounted in the artificial anterior chamber; b) mean burst pressure of GelMA adhesives in the artificial anterior chamber (n = 8); c) representative pressure curves of the studied groups and Histoacryl glue in the porcine eyeball; d) mean burst pressure of GelMA adhesives and Histoacryl glue in the porcine eyeball (n = 8); e) porcine eyeball before, during and after the burst pressure experiment; f) appearance of full-thickness corneal injuries sealed with Histoacryl and GelMA. Data presented as mean value ± SD (* p < 0.05). 147

Figure 7.3 – In vitro shear strength of GelMA adhesives: a) mean shear strength of GelMA bioadhesives and Histoacryl in wet and dry conditions; c,d) Representative stress–strain curves of GelMA hydrogels and Histoacryl in dry and wet substrates, respectively. Data presented as mean value ± SD (* p < 0.05, ** p < 0.01, *** p < 0.001, **** p < 0.0001). 148

Figure 7.4 – In vitro characterisation of GelMA bioadhesives. GelMA hydrogels transmittance in the visible range: a) average optical transmittance and b) optical transparency of the

hydrogels overtime. Hydrogel diameter = 1 cm. Swelling properties of GelMA hydrogels in PBS at 32 °C: c) equilibrium water content (%), d) mass loss (%), e) expansion (%) in PBS and f) lateral image of the hydrogels after photocrosslinking (t_0) and after 24 h incubation in PBS (swollen). g) In vitro degradation of GelMA hydrogels incubated in 1 U/mL collagenase II at 32 °C for 1, 3 and 7 days. Data are presented as mean value ± SD (* $p < 0.05$, ** $p < 0.01$, *** $p < 0.001$, **** $p < 0.0001$). 150

Figure 7.5 – GelMA bioadhesives morphology and microstructure analysis after freeze drying. a) Representative SEM images of GelMA scaffolds at different magnifications. Quantitative analysis of porosity by micro-CT: b-d) pore size distribution in the hydrogels, e) total porosity, f) mean pore wall thickness and g) mean pore size. Data are presented as mean value ± SD (* $p < 0.05$, ** $p < 0.01$, *** $p < 0.001$ and **** $p < 0.0001$). 153

Figure 7.6 – Rheological properties of GelMA bioadhesives: a) frequency sweep, b) storage modulus (G'), c) loss modulus (G'') and d) damping factor (tan δ). Cyclic compressive mechanical testing of GelMA hydrogels: e) representative compressive stress–strain curves and f) compressive moduli. Tensile mechanical testing of GelMA hydrogels: g) representative tensile stress–strain curves, h) tensile moduli and i) maximum tensile strength. Data are presented as mean value ± SD (* $p < 0.05$, ** $p < 0.01$, *** $p < 0.001$, **** $p < 0.0001$). ..155

Figure 7.7 – Ex vivo optical coherence tomography images of the native porcine cornea, partial-thickness corneal injury (≃ 50% deep) and GelMA bioadhesives immediately after photocrosslinking (t_0) and after 1, 3 and 7 days. Scale bar = 500 μm. 156

Figure 7.8 – Cytotoxicity of GelMA hydrogels. a) Live/Dead images of HDFs seeded on GelMA adhesives. Scale bar = 45 μm. b) Normalised metabolic activity 2 and 7 days after cell seeding. Data are presented as mean value ± SD (* $p < 0.05$). 157

Figure 8.1 - In vitro shear strength of 15 and 20% SilkMA hydrogels (3 mW/cm^2 UV-light, 5 min) and Histoacryl in wet and dry conditions (n=7). Data presented as mean value ± SD (* $p < 0.05$, *** $p < 0.001$). 175

LIST OF TABLES

Table 2.1 – List of corneal properties relevant for the development of corneal substitutes and adhesives..... 14

Table 2.2 – Differences between surgical hemostats, sealants and adhesives [7,50,51]..... 15

Table 2.3 – Ideal tissue adhesive characteristics [1,4,5,7,54]. 17

Table 2.4 – Structure, chemical names, uses and trademarks of commercially available cyanoacrylate adhesives [7,61]. 19

Table 2.5 – Commercially available cyanoacrylate tissue adhesives, composition, FDA/CE approval (Yes/No) and indications for use [67–75]. 20

Table 2.6 – Commercially available PEG-based tissue adhesives, composition, FDA/CE approval (Yes/No) and indications for use [69,70,83,84,86–89]. 22

Table 2.7 – Commercially available fibrin tissue adhesives, composition, FDA/CE approval (Yes/No) and indications for use [69,70,95–99]. 25

Table 2.8 – Advantages and drawbacks of fibrin-based, cyanoacrylates and PEG-based tissue adhesives [1,5,50,81,100,109,122]..... 35

Table 2.9 – Parameters used to optimise the properties of photosensitive polymers. 39

Table 4.1 – Relative Content of Secondary Structures in SilkMA Hydrogels Incubated at 37ºC for 0, 7, 14 and 28 Days. Data obtained from deconvolution of the infrared spectra covering the amide I region. Data presented as mean value ± SD (n=4). 79

Table 6.1 – Comparison between different biocompatible photoinitiators: toxicity, water solutibility and molar extinction coefficient at different wavelenghts (365, 405, 450, 500 and 550 nm)..... 125

LIST OF ABBREVIATIONS

AAC	Barron artificial anterior chamber
ACXL	Accelerated corneal crosslinking
ASTM	American Society for Testing and Materials
ATCC	American Type Culture Collection
BSA	Bovine serum albumin
CA	Cyanoacrylate
Micro-CT	Micro computed tomography
CXL	Corneal crosslinking
DF%	Degree of functionalisation
DLP	Digital light processing
DMEM	Dulbecco's modified eagle medium
ECM	Extracellular matrix
FDA	Food and Drug Administration
FSD	Fourier self-deconvolution
FTIR	Fourier transform infrared
G'	Storage modulus
G''	Loss modulus
GAG	Glycosaminoglycan
GELGYM	Glycidyl methacrylate-modified gelatine
GelMA	Gelatine methacryloyl
GMA	Glycidyl methacrylate

GRFG	Gelatine-resorcinol-formaldehyde/glutaraldehyde
HCEC	Human corneal endothelial cell
HDF	Human dermal fibroblasts
^{1}H-NMR	Proton nuclear magnetic resonance
HRP	Horseradish peroxidase
IOP	Intraocular pressure
KPro	Keratoprosthese
LAP	Lithium phenyl-2,4,6-trimethylbenzoylphosphinate
LASIK	Laser *in situ* keratomileusis
MA	Methacrylic anhydride
MIC	Minimum inhibitory concentration
mTG	Gelatine-microbial transglutaminase
NBCA	N-Butyl-2-cyanoacrylates
OCA	2-octyl-cyanoacrylate
OCE	Optical coherence elastography
OCT	Optical coherence tomography
OPA	O-phthaldialdhehyde reagent
PBS	Phosphate-buffered saline
PEG	Polyethylene glycol
RF	Riboflavin
RGD	Arginine-glycine-aspartic acid
SD	Standard deviation
SEM	Scanning electron microscopy
SF	Silk fibroin

SilkMA	Methacrylated silk fibroin
SPS	Sodium persulfate
SR	Swelling
TEA	Triethanolamine
ThT	Thioflavin T
UV	Ultraviolet
VC	N-vinyl-caprolactam
ZOI	Zone of inhibition

PEER-REVIEWED JOURNAL PUBLICATIONS

Thomas J. Hall, Ioannis Azoidis, **Inês A. Barroso**, Erik A.B. Hughes, Liam M. Grover, Sophie C. Cox, "*Formulation of an antimicrobial superabsorbent powder that gels in situ to produce reactive oxygen*", Materials Science and Engineering: C, Volume 118, 111479, DOI: 10.1016/j.msec.2020.111479 (2021)

Inês A. Barroso, Kenny Man, Victor M. Villapun, Sophie C. Cox, and Anita K. Ghag, "*Methacrylated Silk Fibroin Hydrogels: pH as a Tool to Control Functionality*", ACS Biomaterials Science & Engineering *7* (10), 4779-4791, DOI: 10.1021/acsbiomaterials.1c00791 (2021)

Kenny Man, **Inês A. Barroso**, Mathieu Y. Brunet, Ben Peacock, Angelica S. Federici, David A. Hoey, and Sophie C. Cox. "*Controlled Release of Epigenetically-Enhanced Extracellular Vesicles from a GelMA/Nanoclay Composite Hydrogel to Promote Bone Repair*", International Journal of Molecular Sciences, 23, no. 2: 832. DOI: 10.3390/ijms23020832 (2022)

Inês A. Barroso, Kenny Man, Thomas E. Robinson, Sophie C. Cox, and Anita K. Ghag. "*Photocurable GelMA Adhesives for Corneal Perforations*", Bioengineering 9, no. 2: 53. DOI: 10.3390/bioengineering9020053 (2022)

Inês A. Barroso, Kenny Man, Thomas J. Hall, Thomas E. Robinson, Sophie E.T. Louth, Sophie C. Cox, and Anita K. Ghag. "*Photocurable antimicrobial silk-based hydrogels for corneal repair*", Journal of Biomedical Materials Research Part A, 1-15. DOI:10.1002/jbm. a.37381 (2022)

CHAPTER ONE

1 Introduction

The need for efficient wound closure techniques is as old as mankind. Failure to successfully close soft tissue brings both short and long-term risks as leaking fluids can cause haemorrhage and infection, thereby increasing mortality rates. In ancient times, prehistoric man used grass and leaves as wound dressings, while evidence relating to the use of sutures dates back to 1100 BC when leather ligatures were used to close abdominal incisions on mummies [1, 2]. Nowadays, sutures remain the gold standard for many surgical procedures due to their high tensile strength and lower dehiscence [1]. However, when using these traditional surgical closure techniques, fluids (e.g. blood, cerebrospinal fluid) or air (e.g. lungs) can escape through suture/staple lines, needle holes or staple punctures [3]. This can have considerable negative implications since a small oozing blood vessel can cause considerable blood loss, while leakage of intestinal contents can lead to local infection or sepsis [4]. In addition, the consistency of some organs (e.g. kidney, lungs or liver) is not compatible with the use of strong fastening staples and sutures [5]. Therefore, despite recent improvements in suturing and stapling techniques, the development of effective and secure techniques for wound closure and tissue reattachment is still a priority in clinical medicine [4].

Tissue adhesives exhibit lower infection rates than sutures and form a continuous seal, adapting to the wound morphology, distributing the load and decreasing scarring [6,7]. The development of an effective and safe tissue adhesive for external and internal application could reduce surgical time and hospital length of stay, lower the incidence of complications and reduce bleeding and leakage from wounds [4]. Tissue adhesives play a critical role in the management and control of

rapid bleeding and wound closure, but could also be useful in drug delivery (e.g. antibiotics, growth factors) and tissue regeneration applications (e.g. cell encapsulation).

In the eye, full-thickness corneal wounds can arise from surgical procedures, trauma or infections [8]. Sutures have been traditionally employed to seal corneal wounds, however this approach is not ideal since the placement of sutures inflicts additional trauma on the tissue, thereby inducing astigmatism and inciting inflammation and vascularisation [4,9,10]. Therefore, the use of adhesives in ocular surgery has several benefits such as improving comfort and inflammation, and reducing surgery time, postoperative complications and the need for human donor tissue. The most widely used ocular adhesives and sealants are cyanoacrylates (CAs), fibrin/blood-based and polyethylene glycol (PEG)-based derivatives [11].

CAs were first used in ophthalmology in 1968 for the management of corneal perforations [12]. Since then, these adhesives have also been used in cataract surgery [13–15], scleral reinforcement [16] or stromal thinning repair [17]. Despite effectively sealing wounds within seconds, CAs lack transparency, form a rough surface that cause patient discomfort and are associated with many postoperative complications, such as infection [18,19], unintentional entry into the anterior chamber [20,21] and corneal neovascularisation [11].

Fibrin glues have many advantages over CA-based glues: biodegradability, minimal toxic reactions, easy application and improved comfort. The main drawbacks of these bioinspired glues are the potential risk of disease transmission, and short retention time (generally less than 2 weeks), which limits its use and/or requires re-application. Currently, fibrin-based sealants are mainly used ‘off-label’ for amniotic membrane fixation [11,22,23].

PEG-based adhesives work independently of the clotting cascade, do not carry risks of disease transmission and some formulations remain *in situ* longer than fibrin sealants [24]. Despite having regulatory approval for sealing corneal incisions (e.g. ReSure and OcuSeal), PEG-based adhesives are not appropriate to function as tissue adhesives due to poor adhesion, high swelling rates and short lifetime [8,25].

Consequently, there is a clinical need to develop strong and leak-free tissue adhesives as none of the commercially available options have been designed for long-term integration in the cornea. Despite being associated with a wide range of complications, CA glues are currently used 'off label' in the treatment of ocular injuries due to their quick preparation, easy application and secure adhesion [11].

This thesis aims to develop non-toxic and optically clear bioadhesives that could replace the use of CA glues.

To achieve this, it was firstly important to:

- Understand the ocular structure and physiology,
- Define the requirements for a successful corneal tissue adhesive,
- Study the current formulations available on the market,
- Investigate which crosslinking strategies and materials would be better suited to achieve fast, *in situ* curing and outstanding mechanical properties without toxic effects.

These topics are addressed in the literature review (Chapter 2). Chapters 4 – 7, the results chapters, are focused on the development and testing of methacrylated silk fibroin (SilkMA) and gelatine methacryloyl (GelMA) for corneal tissue engineering applications. These chapters

contain a brief introduction and the methods specific to the work conducted in the results section. The general methods are compiled in Chapter 3.

Chapter 4, the first published chapter, results from batch-to-batch variability observations made during the development phase of SilkMA hydrogels. It discusses the effect of the prepolymer solution pH on properties of SilkMA hydrogels by influencing the protein conformational structure development and, therefore, its physicochemical properties. It highlights the need to rigorously control the pH of SilkMA prepolymer solutions to enhance reproducible manufacturing processes, thereby increasing the potential clinical adoption of silk-based materials.

Chapter 5, the second published chapter, builds on the fundamental work presented in chapter 4 to investigate the potential of gentamicin-loaded SilkMA hydrogels as stromal fillers. It compares the hydrogel properties, such as light transmittance, water content and rheology with the human cornea while also assessing the impact of chemical modification on material biodegradability and cytocompatibility. Lastly, the antibacterial efficiency of gentamicin-loaded SilkMA hydrogels against *S.aureus* and *P.aeruginosa*, two of the most common causes of ocular infections, was studied.

Chapter 6 focuses on the development and optimisation of a photosensitive corneal adhesive. It looks at different SilkMA and GelMA formulations, photoinitiators, light conditions and curing times to enhance a material that simultaneously shows transparency, cohesive strength, strong adhesion to corneal collagen and fast *in situ* curing. The adhesive's ability to fill corneal wounds, restore the corneal curvature and resist high intraocular pressures were measured *ex vivo* using porcine eyes.

In Chapter 7, the third published chapter, the physicochemical, mechanical and biological properties of the formulations optimised in Chapter 6 are thoroughly characterised. The hydrogel's adhesive properties are compared with a commercially available CA glue (Histoacryl) by measuring the *ex vivo* burst pressure and shear strength on dry, semi-dry and wet substrates.

This thesis then concludes by summarising the key findings within each chapter and presenting the recommended future work (Chapter 8).

CHAPTER TWO

2 Literature Review

2.1 Clinical relevance

Globally it is estimated that 4.9 million individuals have bilateral corneal blindness and 23 million are unilaterally corneal blind [26]. Currently, the cornea is the most transplanted tissue worldwide and, due to the increased average life expectancy, the demand for transplantable tissue is increasing, with recent reports estimating that 53% of the global population do not have access to corneal transplantation [26–28].

Several corneal dystrophies, trauma and infectious and inflammatory corneal disorders can cause irreversible loss of corneal transparency, leading to blindness [28]. In some cases, these conditions can also lead to corneal melting [29]. In the event of a corneal perforation, urgent intervention is needed to seal the perforation and restore globe integrity, preventing further complications, such as endophthalmitis. Currently, CAs are often employed to seal corneal perforations, despite leading to scarring and vascularisation [30].

Consequently, there is a clinical need to develop novel bioadhesives and stromal fillers that could effectively seal corneal wounds while preventing inflammation, scarring and vascularisation and reduce the need for donor corneas, respectively.

2.2 Corneal structure and physiology

The cornea is the dome-shaped outermost layer of the eye that covers 1/6th of the total surface area of the globe, while the opaque sclera covers the remaining part (Figure 2.1) [31]. A healthy

cornea is essential for vision since it is the window of the eye. In fact, the cornea, lens and vitreous are the only optically clear structures in the human body. In addition to its transparency, the cornea is also a mechanically strong and avascular tissue, comprising three main functions [27,28,31,32]:

- Protection of the inner ocular structures against trauma, infections and ultraviolet (UV) light;
- Structural integrity and transparency maintenance under the action of the intraocular pressure (IOP);
- Light refraction through the lens on the retina, providing approximately 80% of eye refractive power.

The hierarchical structure of the cornea was described by Kaufman et al. as a fibril-reinforced laminate biocomposite, consisting of five layers: the epithelium, Bowman's layer, stroma, Descemet's membrane and the endothelium [33]. All layers play a critical role in maintaining corneal homeostasis [28,32].

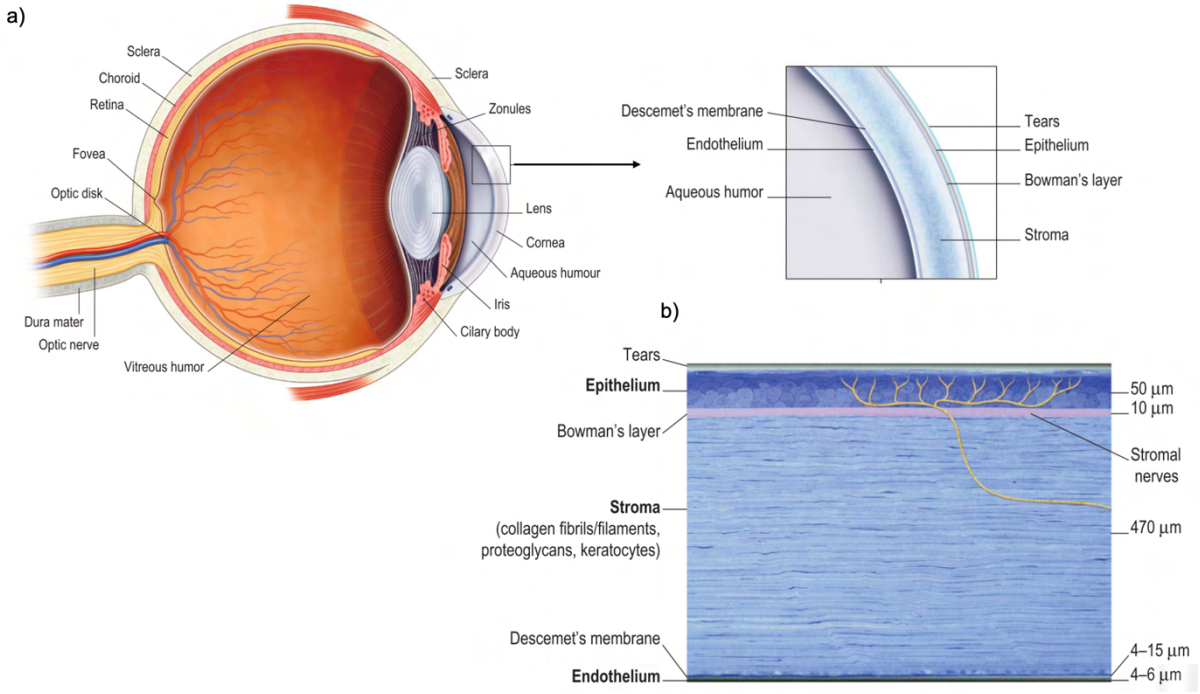


Figure 2.1 *– a) Main anatomical components of the human eye with detailed view of the corneal organisation. b) Histologic section of the human cornea labelling the five main sections and its thicknesses: epithelium, Bowman's layer, stroma, Descemet's membrane and endothelium. Adapted from* [31].

2.2.1 Epithelium

The epithelium consists of five to seven layers (40-50 μm) of stratified and nonkeratinized epithelial cells and constitutes around 10% of the corneal thickness [27,32,34]. The most superficial epithelial cells form tight junctions that block the passage of foreign materials (e.g. bacteria, dust, toxins) from entering the eye, despite allowing the diffusion of oxygen and nutrients from the tear film [32,35,36]. The corneal epithelium is in a state of constant renewal, with an estimated turnover between 7 and 10 days [31].

2.2.2 Bowman's layer

The Bowman's layer, lying between the epithelium and the stroma, helps the cornea to preserve its mechanical strength [31,34]. This acellular layer is approximately 10-15 μm thick and is

composed of a network of small collagen fibrils (20-25 nm), which interconnect to generate an 8-12 μm sheet. This stiff and collagenous layer thins with aging, and it does not regenerate upon trauma or removal [36,37].

2.2.3 Stroma

Comprising approximately 90% of the corneal thickness (~ 470 μm), the architecture of the corneal stroma is responsible for maintaining the corneal strength, curvature (i.e. visual acuity) and transparency (**Figure 2.2**) [36–38]. The function of the stroma depends on the uniform alignment and spacing of highly organised collagen fibrils (type I, V and VI) having an average interfibrillary distance of approximately 42 nm and fibril diameters between 25 to 35 nm, depending on the collagen type. As shown in **Figure 2.2**, the collagen fibrils align to form lamellar sheets, with adjacent lamellae oriented randomly in the anterior stroma and nearly orthogonally in the posterior two-thirds [31,37,38]. The central corneal stroma is composed of 200-300 collagen lamellae, which are enveloped by hydrophilic proteoglycans, keratin sulfate and chondroitin sulfate that contribute to the preservation of corneal hydration and transparency [36]. Keratocytes occupy about 2-3% of the stroma's volume and can be found in the intervals between lamellae. These cells are responsible for the stability of the lamellar organisation due to the synthesis of collagen and proteoglycans and enzyme secretion to renew the matrix [33,36]. Any changes to the hierarchal structure of the stroma may contribute to ocular pathologies [37].

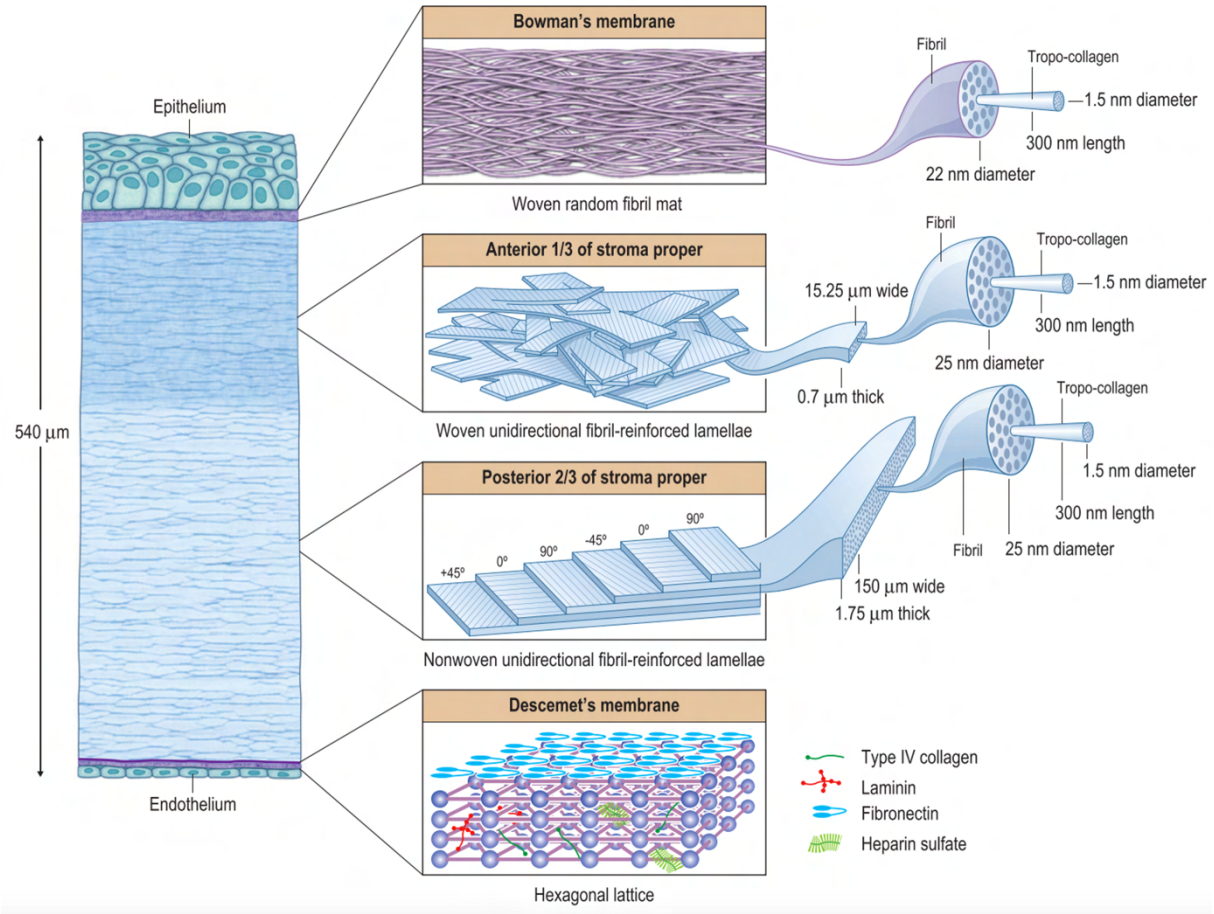


Figure 2.2 *– The hierarchical structure of the cornea showing its four main composite-like regions: the Bowman's membrane, anterior stroma, posterior stroma and Descemet's membrane. These structures characterise the overall stiffness, strength and toughness of the corneal. The macroscopic, microscopic and nanoscopic features of the corneal tissue are illustrated (from left to right). Adapted from* [31].

Notably, corneal transparency depends on the nanoscopic organisation of the collagen fibrils. As suggested by Dr. Maurice in 1957, collagen fibrils scatter the incoming electromagnetic waves in such a way that only light transmitted in the forward direction is not cancelled [27,39].

2.2.4 Descemet's membrane

The Descemet's membrane (4-15 μm) is an acellular layer that contains high amounts of collagen type VIII [31,34]. This membrane is formed in fetal life and gets progressively thicker

with age [37]. Its main function is to support the endothelium by anchoring it to the posterior stroma [27]. The Bowman's layer and Descemet's membrane contribute less than 4% to the total corneal thickness [27].

2.2.5 Endothelium

The innermost layer of the human cornea is the endothelium, being composed by a single layer of hexagonal-shaped cells (4-6 μm), it separates the cornea from the anterior chamber [31,32]. The main function of the endothelium is to maintain corneal transparency and nutrition. The endothelial cells regulate corneal hydration and maintain corneal deturgescence by a Na/K ATPase pump that moves ions and water from the hypotonic stroma to the hypertonic aqueous humor [32,36]. Variations in corneal hydration change the corneal fibril spacing, causing loss of transparency due to light scattering [40]. Finally, since the cornea is avascular and does not contain lymph vessels for fluid flow, most small nutrients, water and other metabolites are delivered to the cornea through intercellular spaces in the endothelial barrier [31,33].

2.3 Corneal wound healing

Wound healing refers to a series of cellular events and interaction of different cell lines that results in the replacement of the injured tissue and elimination of debris and microbes [41]. In general, this complex cascade is divided into four stages (hemostasis, inflammation, cell proliferation and remodelling) involving cytokine mediated interactions between the epithelial cells, keratocytes, corneal nerves, tear film and the immune system cells [28,41,42]. Despite some similarities related to growth factor dependence, cell migration and ECM remodelling, there are significant differences in healing scenarios of different corneal cells. Corneal epithelium healing depends on the migration and differentiation of limbal stem cells, however these do not

undergo transformation to different cell types. On the other hand, during stromal wound healing, keratocytes get transformed to contractile myofibroblast due to the activation of the transforming growth factor-β system. Lastly, the corneal endothelium mostly heals by cell migration and spreading, with cell proliferation playing a secondary role [42]. A schematic representation of the corneal wound healing mechanism is shown in **Figure 2.3**.

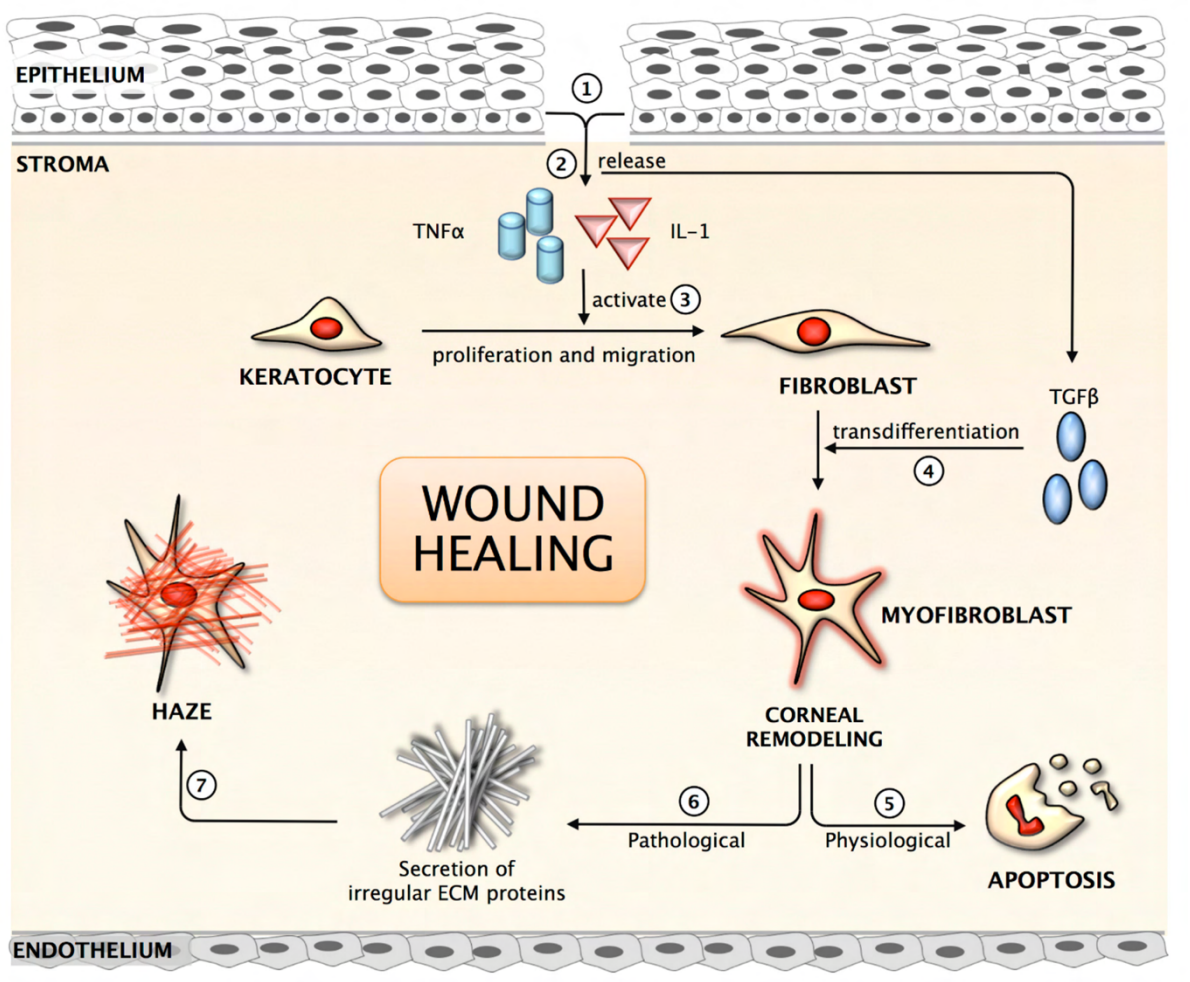


Figure 2.3 *- Schematic representation of the corneal wound healing mechanism. When the stroma is injured, the keratocytes beneath the corneal epithelium within the zone of injury suffer apoptosis (1) and pro-inflammatory cytokines are released into the anterior stroma (2). Quiescent keratocytes proliferate, migrate, and acquire the phenotype of activated keratocytes (fibroblasts) (3). The fibroblasts transform into myofibroblasts (repair phenotype) and secrete provisional matrix scaffold (4). The normal stromal function is slowly restored by resorption of abnormal ECM and apoptosis of the myofibroblasts (5). However, in pathological conditions myofibroblast secrete irregular matrix (6) causing corneal haze (7)* [43,44].

As previously mentioned, the avascularity and transparency of the cornea are essential for corneal clarity. Therefore, when wound healing is taking place the immune response needs to be regulated and limited to prevent the excessive influx of inflammatory cells from destroying the limbus and cause long-term deleterious effects due to the hyperactivity of cytokines, growth factors and chemokines (excessive wound healing) [28,43]. In the last decades, therapeutic strategies have shifted from corneal replacement to the development of corneal wound healing and regeneration strategies by focusing on the immune response, avoiding vascularisation and modulating cell signalling by studying ways to block immune signalling pathways, the role of exosomes in corneal repair or the use of biocompatible materials that promote wound healing (e.g. hyaluronic acid, silk fibroin, etc).

2.4 Corneal properties and design considerations

Before commencing the design of novel engineered biomaterials, it is important to fully characterise the physical and mechanical properties of the cornea. A summary of the most relevant human corneal characteristics to consider during the development of stromal fillers and bioadhesives is presented in **Table 2.1**. In addition, the temperature and pH of the ocular surface correspond to 32 ºC and 7.1 ± 1.5, respectively [45,46].

***Table 2.1** – List of corneal properties relevant for the development of corneal substitutes and adhesives.*

Corneal properties		Ref.
Transparency	78%	[31,47]
Water content	75 - 85% (mean = 78%)	[28,36,48]
Thickness	Central = 0.5 mm Peripheral = 0.7 mm Mean = 0.58 mm	[33,48]
Dimensions	Horizontal diameter = 11 - 12 mm Vertical diameter = 9 - 11 mm Anterior radius of curvature = 7.8 mm	[31,34,36]
Rheology	Storage modulus = 2 - 8 kPa	[49]
	Loss modulus = 0.3 - 1.2 kPa	
Young's modulus	0.13 – 0.43 MPa	[50]
Refractive index	1.376	[35]
Intraocular pressure	2 ± 0.4 kPa	[51]
Rupture pressure (intact eye)	0.46-0.89 MPa	[26]

2.5 Tissue adhesives

The general purpose of surgical adhesives is to quickly close tissue, reducing fluid leakage and operative time, as well as improving patient comfort and the quality of surgical repair [52,53]. Surgical adhesives are currently used in a wide variety of surgical applications since all wounds require immediate closure to prevent blood loss, infection and promote healing (**Figure 2.4**)[53]. However, often confusion exists regarding the differences between the different surgical sealants: hemostats, sealants and adhesives. The overall characteristics of each surgical material are summarised in Table 2.2.

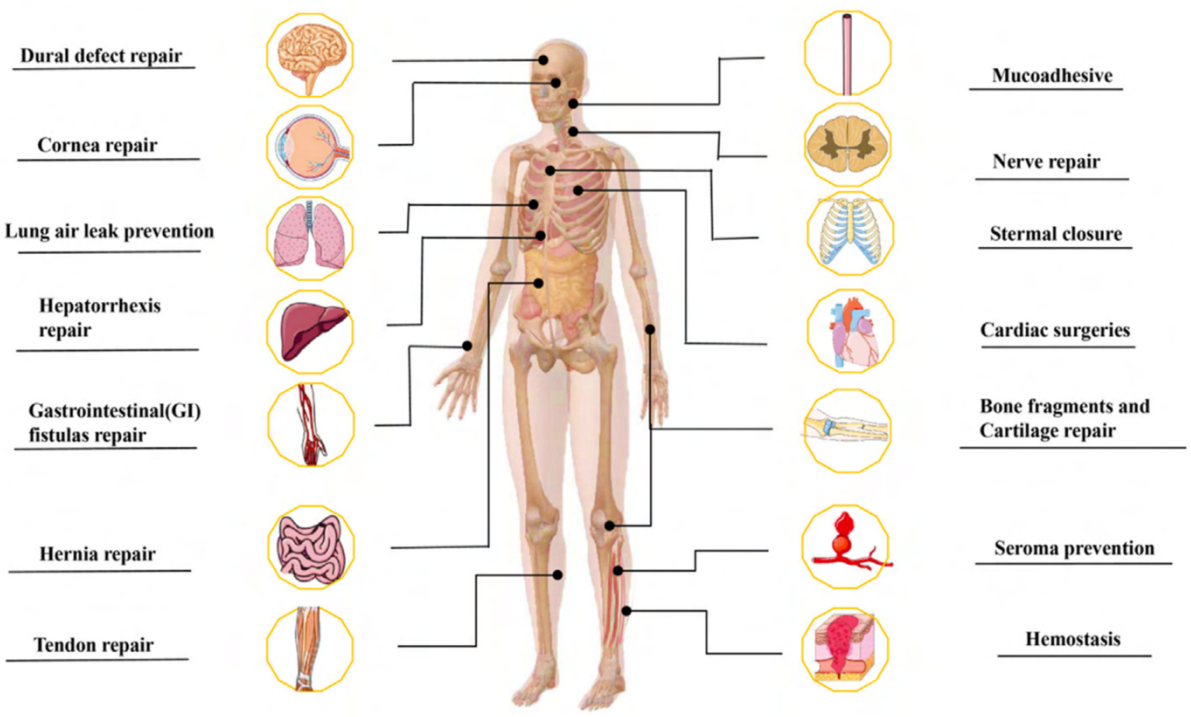


Figure 2.4 *– Clinical applications of tissue adhesives. Adapted from* [53].

Table 2.2 *– Differences between surgical hemostats, sealants and adhesives* [7,54,55].

Hemostat	Sealant	Adhesive
• Causes the blood to clot	• Form a sealing barrier that prevents leakage of liquids or gases	• Glue structures together (tissue fixation or attachment)
• Ineffective unless blood is present	• Low adhesive strength	• High adhesive strength
• Indicated for all surgical procedures	• Most effective in dry surfaces	• Most effective in dry surfaces
	• Usually degrade fast (few days to weeks)	• Long-term durability
	• May have hemostatic effect: intended for light bleeding wounds	• May have hemostatic effect: intended for heavy bleeding
	• Often applied to incisions as hemostatic agents	• Alternative to sutures and staples

In all cases, the surgical materials are liquid or semi-liquid compounds that form an insoluble adhesive matrix via *in-situ* crosslinking when applied to a wound or incision [1,7]. Although sealants are considered to have lower adhesive strength, the functional boundaries between sealants and adhesives are not strict. Clinically, hemostats, sealants and adhesives may be used

as hemostats to limit blood loss, as primary closing agents of lacerations and incisions or adjuncts to staples or sutures [4].

2.5.1 Ideal tissue adhesive properties

Over the last decades, there has been an increased demand for effective tissue management with recent reports indicating that the global market for surgical sealants is expected to grow from $5.7 billion in 2016 to 9.3 billion in 2022 [56]. Although significant progress has been made, further research is still required in order to develop the ideal hemostat, sealant or adhesive [52]. The ideal tissue adhesive characteristics are summarised in **Table 2.3**. Briefly, an ideal adhesive for *in vivo* use must be able to crosslink within a few seconds to minutes, have high adhesion to the body tissue and be biocompatible, without having any negative influence on healing. Further, requirements related to safety, manufacturing costs and usability should also be considered.

Albeit a variety of synthetic and biological tissue adhesives are commercially available, issues concerning their toxicity, biological safety and performance are limiting their wide use due to a complex regulatory route. A few of these adhesives are currently being used off-label in ophthalmic surgery: CAs, polyethylene glycols and fibrin-based adhesives [57].

Table 2.3 *– Ideal tissue adhesive characteristics* [1,4,5,7,58].

Physicochemical and mechanical properties	• Strong adhesiveness to target tissue • Sufficient cohesive strength • Elasticity (tough but pliable) • Adequate swelling characteristics
Biocompatibility	• Both adhesive and its degradation products must be non-cytotoxic, non-inflammatory, non-hemolytic and non-carcinogenic • Permeability to gases, metabolites and fluids to prevent necrosis • Negligible heat production
Biodegradation and wound healing	• Biodegradable via hydrolysis or enzymatic degradation within an appropriate time • Must not induce foreign body response or fibrosis • Should provide a microbial barrier to infection
Usability	• Sterilisable • Ready-to-use device • The mixture should have the desired flow characteristics to be easily delivered (e.g., through thin applicators) • Patient-specific: should crosslink or polymerise *in situ* adapting to host geometry • Rapid curing under wet physiological conditions at body temperature • Should provide sufficient adhesion for early fixation with opportunity for repositioning
Marketability	• Manufacture should be scalable to industrial level and reproducible • Safe, accessible and cost-effective • Approvability (e.g., FDA and CE mark) • Long shelf-life at room temperature • Sustainable

2.5.2 Commercially available tissue adhesives

2.5.2.1 Cyanoacrylates

The first patent concerning the synthesis of CA monomers was issued to Goodrich Corporation in 1949 [4,7]. However, the adhesive properties of CAs were only realised incidentally years later. During the Vietnam War, CAs were used for the first time as tissue adhesives, providing emergency treatment in the battlefield [7]. Since then, these adhesives have been employed by surgeons in ophthalmic, vascular and cosmetic surgery [59–61].

CA tissue adhesives are liquid monomers that quickly polymerise in contact with alkaline substances, creating a strong film that holds apposed wound edges [7,62]. More specifically, when the adhesive monomer makes contact with water or blood, the hydroxide ions (OH-) present on the substrate neutralise the acidic stabiliser in the CA formulation, thereby triggering an exothermic hydroxylation reaction that polymerises the adhesive (**Figure 2.5**a) [3,7,63]. Due to the presence of trace amounts of adsorbed water and amino acids in human tissues, CA adhesives can securely close wounds and reattach tissue within seconds. Furthermore, if the polymerisation is initiated by amino acid functional groups (e.g. NH_2) on the tissue surface, CAs will strongly adhere to the tissue through covalent bonding [4,64].

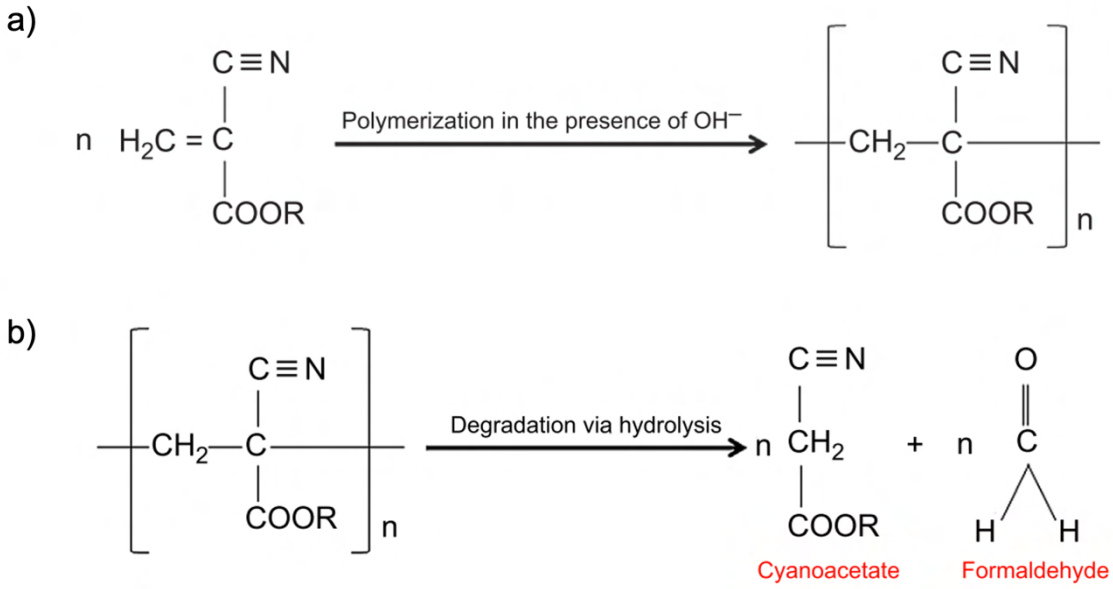
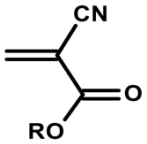


Figure 2.5 *– a) Polymerisation of cyanoacrylate monomers. b) Degradation of cyanoacrylate adhesives via hydrolysis and production of cyanoacetate and formaldehyde. Adapted from* [65].

Currently, cyanoacrylate-based adhesives are the most widely used surgical adhesive in the market due to their instantaneous adhesive properties and high bonding strength [66]. The shorter the alkyl side chain (-COOR), the faster the rate of polymerisation and more heat is released

during the process. Short-chain CAs (e.g. methyl-2-cyanoacrylate, Eastman 910; ethyl-2-cyanoacrylate, Krazy glue) are called 'super glues', and are the most commonly used household instant adhesives (**Table 2.4**) [67]. The shorter the side chains, the faster the breakdown and, therefore the formation of toxic degradation products (formaldehyde and cyanoacetate) (**Figure 2.5**b). In large concentrations, these substances have cytotoxic and inflammatory effects, threatening the wound healing process [3,68]. Therefore, these popular 'do-it-yourself' and industrial adhesives are not suitable for clinical use [7].

Table 2.4 *– Structure, chemical names, uses and trademarks of commercially available cyanoacrylate adhesives* [7,65].

Structure	Alkyl variable chain (R)	Chemical name	Uses and trademarks
	CH_3	methyl-2-cyanoacrylate	Super glue: Eastman 910, Loctite 496
	C_2H_5	ethyl-2-cyanoacrylate	Super glue: Krazy Glue, Loctite 401
	C_4H_9	butyl-2-cyanoacrylate	Surgical adhesive: Histoacryl, Glubran2, Indermil, Trufill
	C_8H_{17}	octyl-2-cyanoacrylate	Surgical adhesive: Dermabond, SurgiSeal

However, the fact that CA formulations are single component and rely only on trace amounts of fluids to strongly bond tissues within seconds, have attracted the attention of the medical community, leading to the development of less toxic long-chain formulations (Table 2.4) [7].

CAs degrade by hydrolysis and the hydrophobicity of the polymer is proportional to the size of the alkyl chain. Thus, long-chain CAs, such as Histoacryl and Dermabond, have slower degradation rates. Since their degradation can take between months to years, the concentration of toxic degradation products at the wound site is negligible [7,69,70]. Consequently, many long-

chain CA formulations have received Food and Drug Administration (FDA) approval, predominantly for superficial skin closure (**Table 2.5**) [7].

***Table 2.5** – Commercially available cyanoacrylate tissue adhesives, composition, FDA/CE approval (Yes/No) and indications for use* [71–79].

Brand name	Composition	FDA-approval	CE marked	Application
Dermabond	2-octyl-cyanoacrylate	Y	Y	Topical, skin adhesive
SurgiSeal		Y	Y	
LiquiBand	Blend: 2-octyl-cyanoacrylate and N-Butyl-2-cyanoacrylate	Y	Y	Topical, skin adhesive
Histoacryl	N-Butyl-2-cyanoacrylate	Y	Y	Topical, skin adhesive
Glubran2		Y	Y	Internal and external use
Indermil		Y	Y	Topical, skin adhesive
Trufill		Y	Y	Internal and external use (e.g. embolisation of cerebral arteriovenous malformations)

Commercially available formulations mainly differ in monomer type, presence of additives (e.g. dyes, thickeners, plasticisers, accelerators, stabilisers or polymerisation inhibitors) and applicators [7,66]. Dyes are added to help visualisation during surgery, while stabilisers and inhibitors prevent polymerisation during storage. The rate of polymerisation can be controlled by changing the type and concentration of accelerators and/or inhibitors. However, most formulations are customised for specific surgical procedures [7]. For example, rapid polymerisation might be beneficial for skin closure, however a slower polymerisation rate is desired for ophthalmic applications where precise application is required [66].

The two main monomer families of cyanoacrylates used as tissue adhesives are:

- N-Butyl-2-cyanoacrylate (Histoacryl, Glubran2, Indermil and Trufill)
- 2-octyl-cyanoacrylate (Dermabond and SurgiSeal)

N-Butyl-2-cyanoacrylates

N-Butyl-2-cyanoacrylates (NBCA) were the first CAs to be broadly used in the management of cutaneous wounds [63]. Histoacryl has been extensively used in the closure of lacerations, sclerotherapy of large varices and fixation of hernia meshes since its approval in the early 1980s [80–82]. More recently, Trufill, a combination of NBCA and a polymerising retardant has been approved by the FDA for neurological embolisation and wound closure, while Glubran2, a combination of NBCA and metacryloxysulpholane, was approved for endoscopic use in Europe [7,62,83]. Both Trufill and Glubran2 react slower than Histoacryl, which makes its application technically easier for surgeons. Finally, Glubran2 produces a milder exothermic reaction (≃ 45 °C) due to the presence of metacryloxysulpholane which ultimately leads to reduced local inflammation and toxicity in comparison to Histoacryl or Trufill [84].

2-octyl-cyanoacrylate

Having a longer chain than its butyl counterpart, 2-octyl-cyanoacrylate (OCA) adhesives have a lower polymerisation rate than NBCAs (60 vs 30s, respectively) and higher flexibility [7]. Since its FDA-approval in 1998, Dermabond has been used worldwide for superficial wound closure (0.1 cm to 50 cm) and in cosmetic surgery [7]. More recently, an accelerator has been incorporated at the tip of the Dermabond applicator to improve the polymerisation rate and usability [7,52]. Finally, SurgiSeal is a more recent OCA adhesive formulation that obtained FDA approval for topical use in 2014. This novel formulation has a higher moisture permeability than Dermabond, which could lead to better wound healing [72].

2.5.2.2 PEG-based tissue adhesives

Another class of synthetic tissue adhesives are based on the FDA-approved polymer PEG. PEG is a very versatile polymer that has found many applications in tissue engineering due to its distinctive properties, such as nontoxicity, water-solubility, low immunogenicity and stealth-like behaviour *in vivo*. Linear or branched PEG-based hydrogels can be functionalised to improve bioactivity, degradation profile and mechanical behaviour [1,85,86]. The most relevant commercially available PEG-based adhesives are summarised in **Table 2.6**. Importantly, OcuSeal and ReSure, are the only sealants that have received regulatory approval for ocular use [87–89].

Table 2.6 *– Commercially available PEG-based tissue adhesives, composition, FDA/CE approval (Yes/No) and indications for use* [73,74,87,88,90–93].

Brand name	Composition	FDA-approval	CE marked	Application
CoSeal	2 PEG powders: four-armed PEG capped with either a glutaryl-succinimidyl ester or a thiol	Y	Y	Vascular sealant, enforcement/sealing of suture and staple lines
DuraSeal	Four-armed PEG encapped with N-hydroxysuccinimide esters and trilysine amine solution	Y	Y	Adjunct to sutured dural repair during cranial/spinal surgery
FocalSeal	Triblock copolymer of poly(lactide) and PEG with acrylated end groups, PEG-co-trimethylene carbonate-co-lactide with acrylated-end groups and and eosin Y	Withdrawn		Adjunct to standard closure of pleural air leaks
Progel	PEG di-succinimidyl succinate and human serum albumin	Y	Y	Adjunct to standard closure of pleural air leaks
OcuSeal	PEG and polyethylene amine	N	Y	Ocular bandage
ReSure	PEG and trilysine acetate	Y	N	Ocular bandage

OcuSeal

OcuSeal is currently used in Europe to stabilise ocular wounds after receiving CE marking in 2007 [87]. After mixing its components in a small applicator for 5 seconds, the prepolymer mixture can be directly applied to the eye using a brush (**Figure 2.6** a-c). It polymerises on the ocular surface within 15 seconds creating a transparent, smooth adhesive that is naturally resorbed within 3 to 4 days [25,87,94]. OcuSeal's main disadvantage is concerned with its rapid and uncontrollable polymerisation and quick *in vivo* degradation. Since the product polymerises within 10-15 seconds after mixing, delayed application can result in polymer hardening within the applicator. Conversely, if the adhesive is applied prematurely, the wound will not be properly sealed due to the low viscosity of the material [25,95]. OcuSeal was proven an effective, rapid and safe option for sealing of ocular wounds in experimental *in vitro* studies as well as in clinical trials [25,94,96]. In a randomised clinical trial (n= 90), this sealant effectively reduced astigmatism and improved patient comfort when compared with sutured incision closure [25].

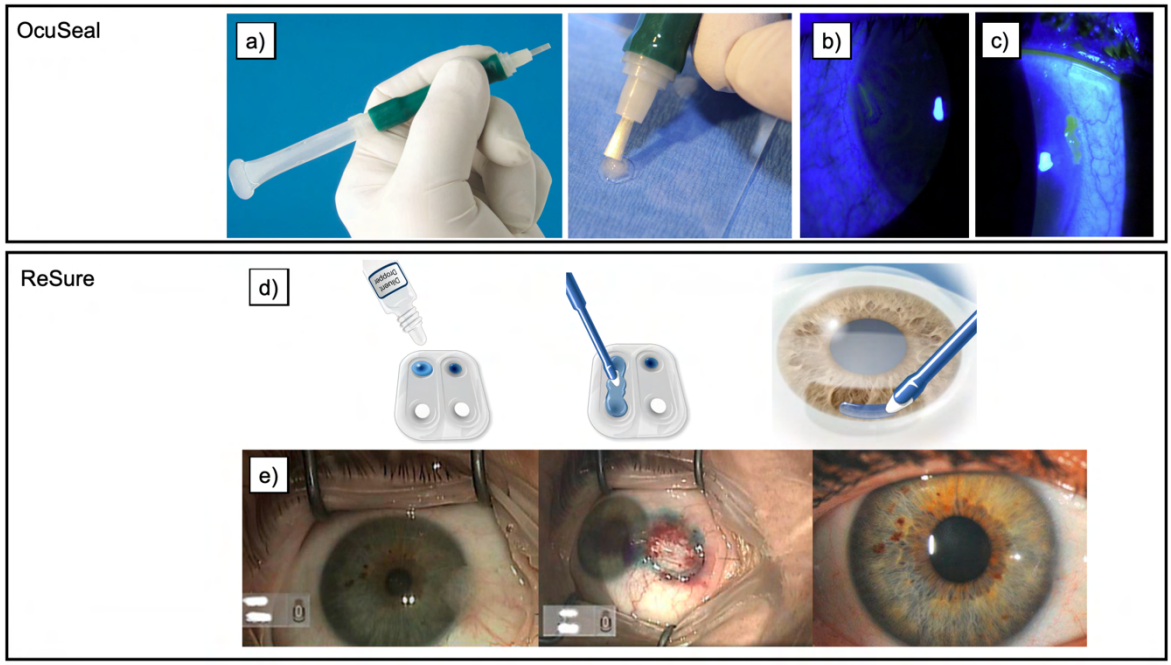


Figure 2.6 *– OcuSeal preparation: a) After breaking the membrane between the transparent and green container the surgeon should shake the applicator for 5 seconds to mix the powder PEG with the liquid polyethylene amine and apply through a brush it within 10 seconds [25]. b) Slitlamp photograph of a non-*

treated corneal incision one day postoperatively (control). c) Slitlamp photograph of a corneal incision sealed with OcuSeal one day postoperatively [25]*. ReSure preparation: d) the diluent is added to the trilysine acetate deposit (blue) and then the applicator is used to mix the solutions for five seconds. The uncured solution should be applied to the eye within 12 seconds after mixing is initiated. e) Sutureless excision of pterygium with amniotic membrane and ReSure: nasal pterygium before surgery; same eye after application of ReSure to secure the amniotic membrane graft to the defective conjunctiva; same eye at 6-weeks post-surgery* [97]*.*

ReSure

Currently, ReSure is the only FDA approved sealant for intraoperative management of corneal incisions. This sealant exhibits lower swelling than other PEG-based adhesives (only 35% weight increase), successfully withstands high pressures (> 9 kPa) and forms a smooth and lubricious surface, avoiding the use of a bandage contact lens for improved comfort [89,95]. The main disadvantages of ReSure are related to its usability and degradation profile. Although showing a similar onset of gelation (14-18 s) and retention time (1-3 days) to OcuSeal, ReSure's preparation is more complex since it involves a two-step procedure (**Figure 2.6**d) [88,89,98]. Lastly, recent studies have shown that ReSure was effective in reducing the incidence of transplant dislocations and corneal incision leakages in clinical studies (**Figure 2.6**e) [8,97].

2.5.2.3 Fibrin-based tissue adhesives

The use of fibrin as a biological glue dates back to 1910s where fibrin patches were used to control bleeding during the First World War [1]. In ophthalmology, fibrin-based adhesives were used for the first time in the early 1940s in penetrating keratoplasty surgery [22]. Since then, it has been used in humans to seal corneal perforations or lens capsule lacerations and to repair leaking blebs [11,22]. As shown in **Table 2.7**, commercially available fibrin glues include Evicel, Cryoseal and Tisseel.

***Table 2.7** – Commercially available fibrin tissue adhesives, composition, FDA/CE approval (Yes/No) and indications for use* [73,74,99–103].

Brand name	Composition	FDA-approval	CE marked	Application
Evicel	Human pooled plasma thrombin (800-1200 IU/mL) and fibrinogen (55-85 mg/mL)	Y	Y	Surgical hemostat
VistaSeal	Human fibrinogen (80 mg) and human thrombin (500 IU/mL)	Y	Y	Surgical hemostat
Artiss	Human pooled plasma thrombin (5 IU/mL) and fibrinogen (85 mg/mL), synthetic aprotinin (3000 KIU/mL)	Y	Y	Surgical hemostat, skin grafts, face-lift surgery
Tisseel	Human pooled plasma thrombin (400-635 IU/mL) and fibrinogen (67-106 mg/mL), synthetic aprotinin (2250-3750 KIU/mL)	Y	Y	Surgical hemostat
Tachosil	Equine collagen patch coated with dry human thrombin (2 IU/cm^2) and fibrinogen (5.5 mg/cm^2)	Y	Y	Surgical hemostat, neurological surgery
Raplixa	Human fibrinogen (79mg) and human thrombin (699 IU/mL), gelatine sponge	Y	Withdrawn	Surgical hemostat
Evarrest	Oxidised cellulose patch with dry human thrombin (37.5 IU/cm^2) and fibrinogen (55.5 mg/cm^2)	Y	Discontinued	Surgical hemostat
Cryoseal	Autologous plasma thrombin and fibrinogen	Y	N	Surgical hemostat
Vitagel	Autologous fibrinogen, bovine thrombin (300 IU/mL) and collagen (20 mg/mL)	Y	N	Surgical hemostat

Fibrin adhesives are complex blood-derived formulations constituted by two major components: the protein solution (component 1) and the setting solution (component 2) (**Figure 2.7**a). The mechanism of action of these glues mimics the final stages of the coagulation cascade (**Figure 2.7**b). When a tissue is injured, the coagulation cascade is active through the

hydrolysation of prothrombin to thrombin by factor XIII. Once in the presence of thrombin, fibrinogen is converted into an elastic and filamentous protein called fibrin [22]. In the presence of calcium chloride, thrombin also activates factor XIII into factor XIIIa, which stabilises the clot by crosslinking of fibrin chains into long and highly branched fibres. To prevent the breakdown of the fibrin cloth by human plasmin and trypsin, some formulations include an antifibrinolytic agent (e.g. aprotinin) [1,86,104]. The polymerisation time can be controlled by changing the concentration of thrombin. Panda et al. determined that a highly concentrated thrombin solution (500 IU/mL) produces a cloth in approximately 10 seconds while a lower concentration of 4 IU/mL, takes around 60 seconds [22]. Further, the adhesion strength of fibrin glues is mainly a function of fibrinogen content [1,3]. Despite having the same essential components (fibrinogen, thrombin, factor XIII and $CaCl_2$), different commercial formulations have different ratios/concentration of individual components (**Table 2.7**, **Figure 2.7**c) [105]. Consequently, the polymerisation speed and adhesive strength of different commercial fibrin glues vary.

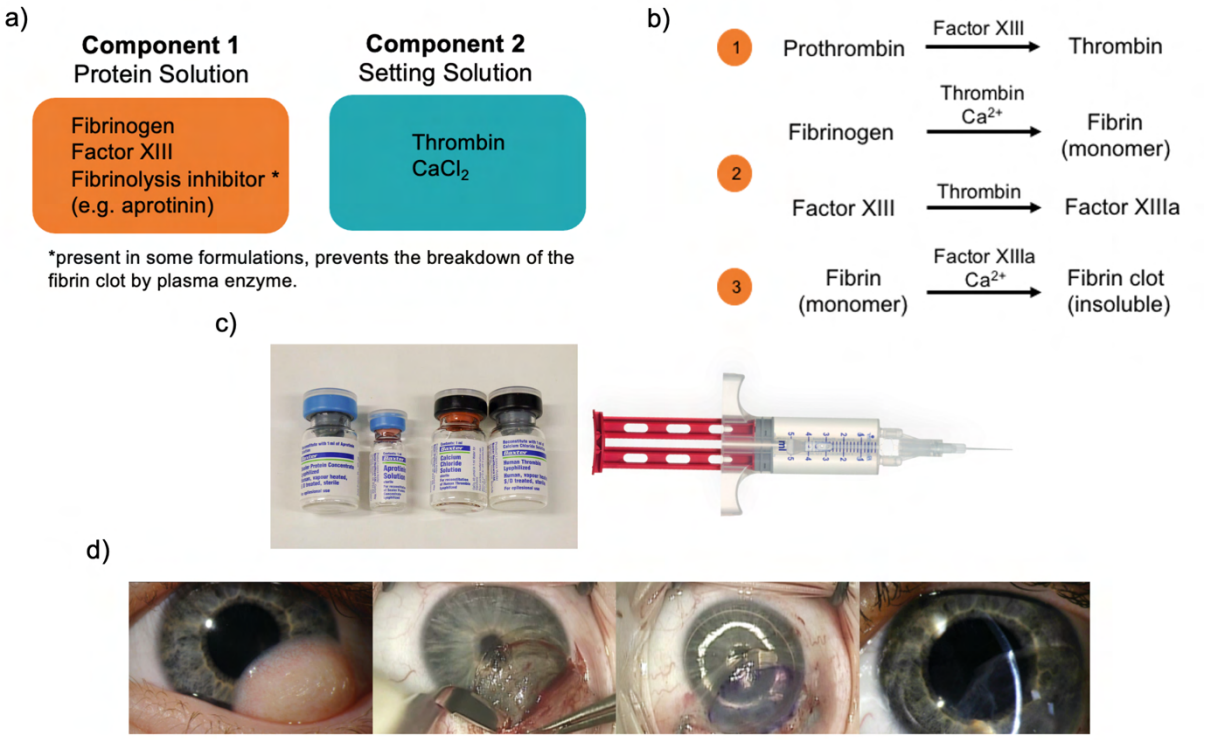


Figure 2.7 *– a) Fibrin adhesive composition: protein solution and setting solution. b) Schematic representation of the functioning mechanism of fibrin glue: conversion of fibrinogen to fibrin (monomer) and clot formation (insoluble) c) Tisseel Tissue adhesive (Baxter Healthcare Corporation, USA) kit: components (fibrinogen, aprotinin, calcium chloride and thrombin solutions in vials) and standard glue applicator. To seal a defect, both fibrin components are loaded in a dual syringe system with the tips forming a joint port. When the common plunger is pressed, the two components are applied to the delivery site in equal volumes* [104]*. Alternatively, each component can be applied to opposite sides of the tissue, postponing the polymerisation until two sides are together and allowing better control of the glue amount and distribution* [33]*. d) Limbal dermoid removal and replacement by a lamellar corneoscleral patch attached with fibrin: 7-mm opaque dermoid; lamellar keratectomy to remove the dermoid; graft attachment with fibrin glue and slit-lamp examination of the graft 10 weeks after surgery* [106]*.*

Fibrin glues are used in many surgical procedures due to their biocompatibility, biodegradability, fast curing (from 30 s to several minutes) and low immunogenicity [107]. However, despite these benefits, fibrin sealants still have some disadvantages including batch-to-batch variability and fast degradation *in vivo* (within days to weeks). In ocular surgery, a

bandage contact lens or an overlying tissue may be applied, decreasing the harmful effect of shear caused by blinking and thereby increasing retention time.

Nonetheless, the major issues associated with these sealants are related to the potential risk of disease transmission. Early commercial formulations of fibrin glue used fibrinogen, factor VIII and aprotinin from bovine origin. When bovine sources were used, there was a risk of potential disease transmission (e.g. bovine spongiform encephalopathy), immune reactions and haemorrhages due to cross-reactions with human clotting factors. In an attempt to minimise safety concerns, components are now extracted from human pooled plasma (e.g. Evicel, Tisseel) or autologous plasma (Vitagel, Cryoseal) [1,54]. The use of fibrinogen extracted from patients' blood plasma avoids the risk of human disease transmission (e.g. hepatitis A, B and C or HIV). However, bovine aprotinin is still used nowadays and may be a source of disease transmission and antigenic responses [107].

2.6 Corneal perforations

2.6.1 Definition and causes

Many ocular disorders, such as infection, xerosis, trauma (e.g. abrasion, laceration) or chemical injuries can lead to loss of corneal epithelial integrity, predisposing the cornea to thinning and perforation (**Figure 2.8**a) [33]. Stromal melting is promoted by altered epithelial cells and polymorphonuclear neutrophils with proteolytic and collagenolytic activity (**Figure 2.8**b) [29,108]. Symptoms usually include pain, vision loss and aqueous leakage usually mistaken as tears [29]. The persistent loss of integrity of the anterior chamber and constant leaking of aqueous humor promotes corneal damage, cataract formation, secondary glaucoma, endophthalmitis or even

loss of the eye [33,109,110]. Therefore, prompt diagnosis and intervention to seal the perforation, is key to preserve visual function and retain structural integrity [33].

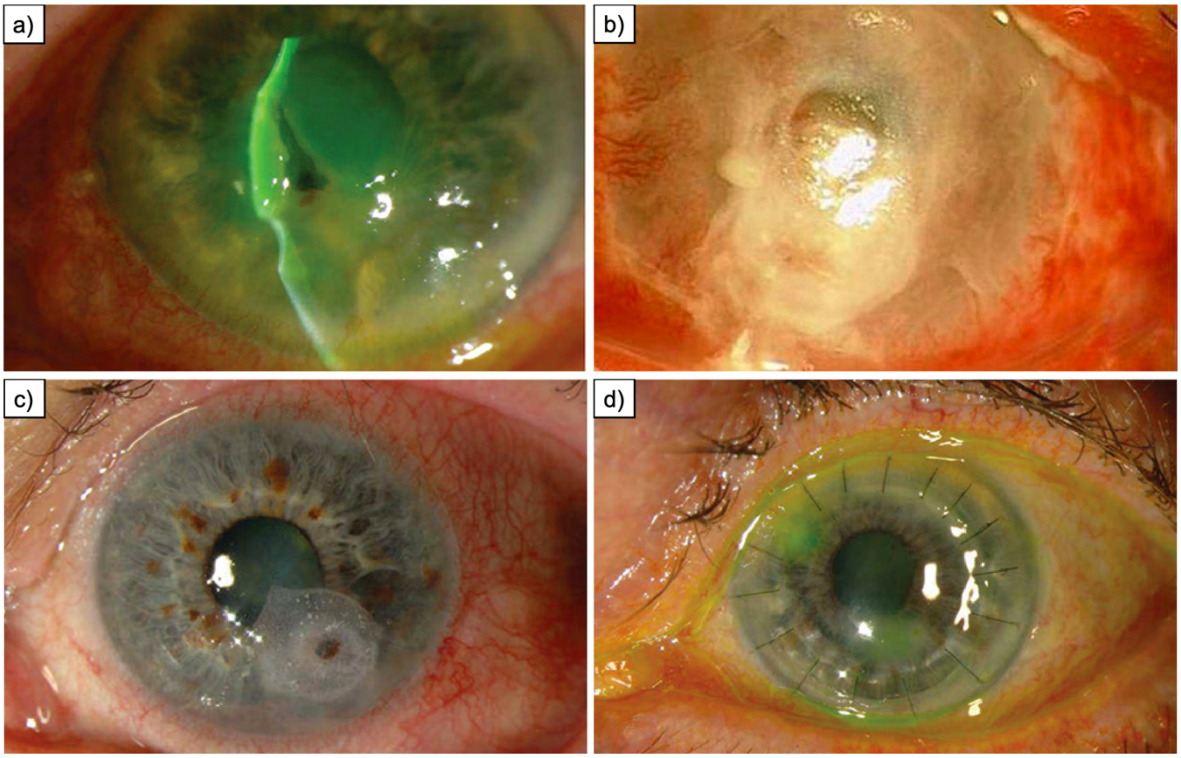


Figure 2.8 *– Slit-lamp photograph showing a) a corneal perforation; b) corneal melting; c) corneal perforation sealed with cyanoacrylate glue and d) postoperative photograph after corneal transplant. Adapted from* [29,108].

2.6.2 Surgical management

The surgical management of corneal perforations ranges from temporary measures, such as application of a bandage lens or gluing, to definitive treatments, such as corneal transplantation (**Figure 2.8**c, d). The treatment selection depends mostly on the size and location of the injury, extent of stromal involvement, presence of infection and association with autoimmune disease [29,33].

Self-sealing micro-perforations might be treated with a bandage contact lens, while small perforations (<3 mm) can be treated with tissue adhesives, amniotic membrane patches, or Tenon's membrane auto-grafts. Perforations that are larger than 3 mm, require firm closure with definitive lamellar of full-thickness corneal transplantation, which may not be possible in all emergency settings [109–115]. Tissue adhesives and sealants might be used as a temporary measure until the corneal transplant, or to reinforce sutures and secure donor transplant materials, depending on the size of the wound bed [113,115].

The first use of a tissue adhesive in the eye was reported more than 50 years ago by Refojo and co-workers [116]. Since then, several studies concerning the use of CAs and fibrin sealants in ophthalmic surgery and the development of novel adhesives and sealants have followed. Although CAs and fibrin are not FDA approved for ophthalmic use, these adhesives have been used off-label in the eye for several decades [66,86].

CAs have been successfully used in cataract surgery [13–15], leaking blebs [16,117–119], scleral reinforcement [16], stromal thinning repair [17] and management of corneal perforations [17,120,121]. Studies have shown that early glueing with CAs may prevent or delay corneal thinning since the adhesive acts as a barrier to tear film and collagenase-secreting cells, preventing enzymes from reaching the stroma [11,107,122]. These glues are also reported to have significant bacteriostatic activity against Gram-positive bacteria [3].

However, CAs form a rough and opaque seal, causing patient discomfort, occluding vision and impeding wound healing assessment and visualisation of infectious infiltrates under the glue [11,66]. Thus, they have been associated with many postoperative complications, such as infection,

keratitis [18,19], unintentional entry into the anterior chamber [20,21] and corneal neovascularisation [11].

Recently, a retrospective review of the clinical outcomes of corneal perforations glued with CA glues between 2001 and 2018 was published (n= 140). The authors analysed the success rate of CAs in sealing and maintaining the globe integrity over time and reported the factors associated with glue failure. CAs were successful in restoring globe integrity in 72% of the cases 10 days after surgery. However, the success rate decreased to 30% after 90 days, with nearly 66% of the eyes requiring reapplication of the glue within the first month. Interestingly, age, sex, wound location, use of topical steroids and autoimmune conditions were not correlated with glueing failure. The results have shown that CA is moderately successful in the short term. However, patients should be closely monitored since multiple applications are often required and the need for future surgical interventions remains high [110].

Similarly to CAs, fibrin sealants have been successfully used in the treatment of corneal perforations [123,124]. Fibrin glues are biodegradable, provide faster healing and induce less vascularisation and discomfort than CAs [104,108]. However, these sealants are more complex to prepare and apply than CAs and require longer times for plug formation [33,104,107]. Sharma et al. compared the efficacy of fibrin glue and N-butyl-2-cyanoacrylate in the treatment of corneal perforations (n = 41). The authors concluded that both adhesives were effective at closing corneal perforations up to 3 mm ($p > 0.05$). Notably, fibrin provided faster healing, with 63% of the fibrin-treated eyes healing in less than 6 weeks, against 31% for CA-treated eyes. CAs also induced vascularisation in 46% of the cases, against 11% in eyes treated with fibrin ($p < 0.05$). Finally, fibrin adhesives remained in the eye for a maximum of 14 days, while residual cyanoacrylate could be found in four eyes after 90 days [123].

As previously mentioned, the management of larger corneal perforations is more surgically challenging. Due to the lack of tectonic support, the adhesive plug may not remain *in situ* and enter in the anterior chamber, which can lead to cataract formation and glaucoma. In these cases, readily available but not optically clear scleral grafts can be used to provide underlying scaffolding. As shown in **Figure 2.9**, Sharma et al., studied the ability of scleral patch grafts and CA glues to seal larger perforations (3.5-4.5 mm, n=16). After the scleral patch was placed at the perforation site and the area dried, the CA glue was applied to the interface between the cornea and the scleral patch. This approach promoted a stable reconstruction of the ocular surface, with 88% of the eyes healing in 5-9 weeks despite the formation of a corneal scar (**Figure 2.9**c). However, reapplication was required in 19% of the cases [125].

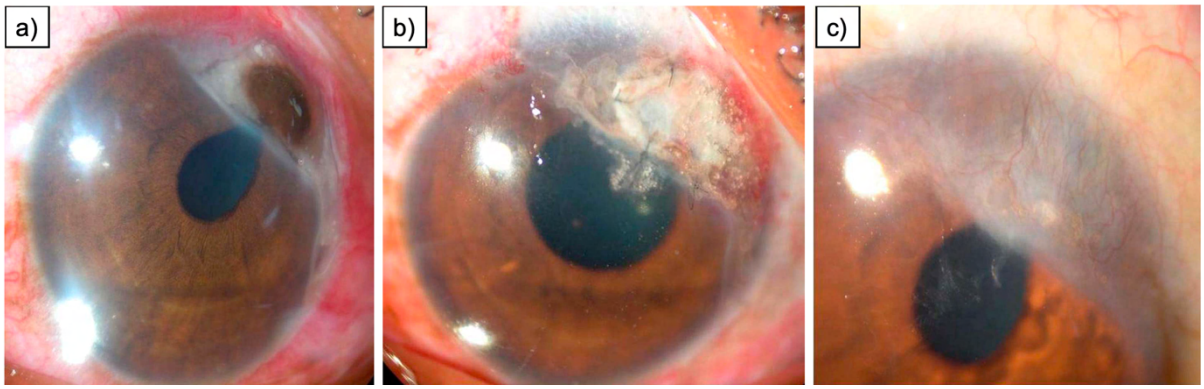


Figure 2.9 *– Slit-lamp photograph showing a) large peripheral corneal perforation; b) sutured scleral patch graft incorporated in the corneal stroma after removal of the cyanoacrylate glue at 5 weeks; c) healed corneal perforation 3 months after the intervention. Adapted from* [125].

Recently, the application of the patient's tenon capsule, an elastic connective tissue layer that envelops the eye, together with CA for the management of large corneal perforations was studied (3-5 mm, n= 31). Since the tenon capsule is a tough structure, the authors hypothesised that this material would provide good tectonic support with minimal risk of graft rejection and

vascularisation. This method was successful in restoring the ocular integrity in 87.1% of cases. As shown in **Figure 2.10** the cornea healed with the formation of a scar. In addition to the autologous nature of the graft, this approach is also readily available and cost-effective. However, since the tenon patch is opaque, the patient visual acuity might not improve despite adequate healing (**Figure 2.10**c) [115].

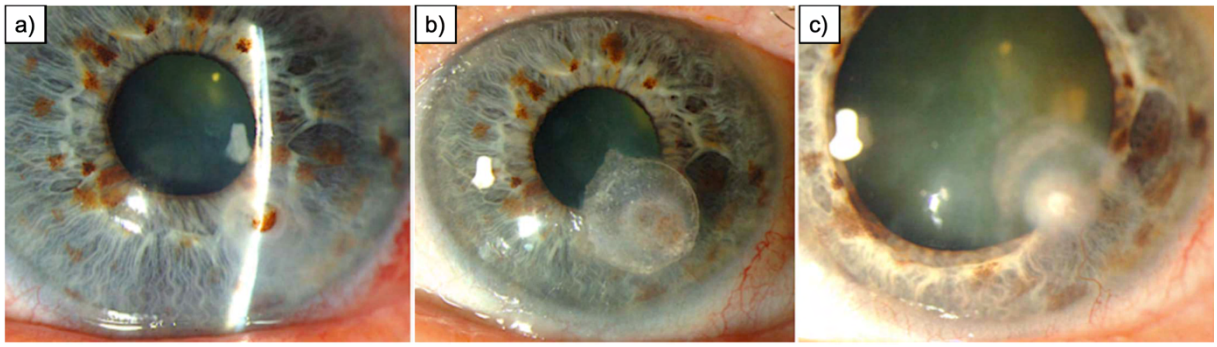


Figure 2.10 *– Slit-lamp photograph showing a) corneal perforation; b) tenon patch and cyanoacrylate glue in situ at 3 months post-surgery and c) healed perforation with corneal scar 18 months after surgery. Adapted from* [115].

In summary, cyanoacrylate-based adhesives are the most commonly used ocular adhesive in modern day ophthalmic practice due to their quick preparation, easy application and high bonding strength [57]. However, in most cases, patients would require a corneal transplant in the future as these adhesives often cause long-term vision impairment due to corneal scarring and vascularisation. Consequently, the development of a novel biocompatible adhesive that is readily available in any setting and does not incite scarring and vascularisation is of utmost importance.

2.7 The need for novel tissue adhesives

Although several tissue adhesives have been developed over the past 30 years, it is difficult to develop a single material that fulfils all the medical requirements, including biocompatibility, biodegradability, cost-effectiveness, easy application, fast gelation *in vivo*, strong adhesion to wet tissues, long *in situ* retention and adequate mechanical properties to be applied to different human tissues [73].

To date, none of the commercially available adhesives have been developed for long-term integration in the cornea. The pros and cons of the most used tissue adhesives in ophthalmic surgery are summarised in **Table 2.8**. While cyanoacrylate and fibrin-based adhesives are being used off-label, OcuSeal and ReSure (PEG-based adhesives) were recently approved for ocular use. However, despite being effective in sealing corneal incisions, reducing recovery time and improving comfort, both ReSure and OcuSeal show rapid and uncontrollable polymerisation, poor adhesion to corneal tissue and short lifetime, which halt their application as stromal fillers [99]. Hence, considering the existing demand and requirements in ophthalmic surgery, the performance of all currently available materials is inadequate.

***Table 2.8** – Advantages and drawbacks of fibrin-based, cyanoacrylates and PEG-based tissue adhesives* [1,5,54,85,104,113,126].

Adhesives	Advantages	Drawbacks
Fibrin-based	• Biocompatibility • Biodegradability • Fast curing • Low immunogenicity • Polymerisation time can be controlled by diluting the thrombin solution	• Poor mechanical properties • Low adhesion strength • Fast degradation *in vivo* (typically < 2 weeks) • Risk of disease transmission and/or allergic reaction • Long preparation time (around 20 min) • Not bacteriostatic • Expensive production
Cyanoacrylates	• High adhesion strength • Fast polymerisation (30-60s) • Ready-to-use device • Bacteriostatic properties • Inexpensive • Waterproof • No risk of disease transmission	• Toxic • Inadequate for moist surfaces due to risk of premature curing • Exothermic polymerisation • Low biodegradability • Production of toxic degradation products • Foreign body response (neovascularisation, necrosis) • High stiffness - inadequate for organs with physiological movement (e.g. heart, lungs) • Proinflammatory - can only be used externally (e.g. skin, cornea) • Impermeable to fluids and metabolites
PEG-based	• No risk of disease transmission • Safe and well-tolerated • Transparent • Good elasticity • Biodegradable	• Require reconstitution by mixing the powder with the liquid components • Rapid polymerisation might clog the applicator and prevents sufficient time for thorough application • Require a relatively dry surface for better results • Poor adhesion • High swelling (35-400%) • Short retention

Finally, since transparency is one of the specific requirements for corneal glues, the adhesive and its degradation products must be non-cytotoxic and non-inflammatory, preventing scarring and vascularisation from precluding vision at a later stage. Chemically modified proteins, such as gelatine or silk, show great potential for the development of novel adhesives since [32,73]:

1) Natural polymers offer a more biocompatible alternative than synthetic polymers;

2) Collagen and proteoglycans form the scaffolding of most tissues, including the cornea.

2.8 FDA-approved corneal collagen crosslinking treatment

Photopolymerisation can be used to improve the mechanical properties of biopolymers through network crosslinking. The biomechanical behaviour of the corneal stroma depends on the structure and arrangement of collagen molecules [127,128]. Cross-linkages across the collagen fibres provide structural stability and prevent the fibrils from sliding apart. Physiologically, collagen molecules are crosslinked by the enzyme lysyl oxidase, which transforms the amino groups of determined amino acids into aldehyde groups. These aldehyde groups can react with a neighbour aldehyde or react with ε-amino group of amino acids to create aldimine cross-linkages [128]. However, in some pathologies, such as keratoconus, the activity of this enzyme might be compromised due to gene defects, thereby compromising the mechanical stability of the cornea [128,129].

Keratoconus is a noninflammatory dystrophy characterised by progressive corneal thinning and steepening, which prevents the light from being correctly focused on the retina [130,131]. Despite the normal corneal collagen content, the corneal stiffness is decreased by a factor of ≈ 0.7 [128]. Although keratoconus progression slows with ageing, it is a common cause of corneal transplantation in young adults [129]. An analogous reduction in the corneal stiffness can also occur due to complications with laser *in situ* keratomileusis (LASIK). During LASIK surgery, a laser is used to precisely reshape the corneal curvature as needed to address refractive errors [132]. In cases of pre-existing keratoconus or excessive tissue ablation, the remaining stroma might not be able to compensate the force per cross-sectional area, causing the cornea to bulge with deterioration of visual acuity [128].

There are several strategies to crosslink corneal collagen, increasing the mechanical stability of the tissue, such as chemical agents (eg. genipin, formaldehyde or glutaraldehyde) or photo-crosslinking [128].

Corneal collagen cross-linking (CXL) is an FDA approved clinical procedure that uses long-wavelength ultraviolet light (UV-A) and a chromophore (riboflavin) to increase the stromal tensile strength, halting the progression of keratoconus and other corneal thinning processes [133–135]. Briefly, in the presence of UV-A (365 nm), riboflavin (RF) is excited into its triplet state crosslinking corneal collagen through radical reactions with electron-donating substrates (eg. histidine, hydroxyproline, hydroxylysine, tyrosine and threonine) [128,130,134,136]. After CXL treatment, several changes related with the improved stromal crosslink density have been reported: increased stiffness (by a factor of 1.7), increased resistance to enzymatic degradation and decreased swelling [128,137]. This treatment is widely used since it is relatively fast (3-30 minutes), localised and does not reduce corneal transparency [128].

The CXL safety parameters concern the protection of the limbal stem cells, corneal endothelium, lens and retina [134]. The standard CXL procedure, known as Dresden protocol, uses an irradiance of 3 mW/cm^2 for 30 minutes (total dose of 5.4 J/m^2) after 30 minutes of RF instillation to ensure stromal saturation (**Figure 2.11**)[138]. Due to the short distance between the light source and the eye (1 cm), the UV radiation is not focused on the retina [128]. However, CXL is not recommended in patients with a corneal thickness inferior to 400 μm due to the risk of endothelium damage. Therefore, if RF is diffused throughout the stroma (acts as a photosensitizer and UV-blocker), the irradiation is homogenous (preventing hot-spots) and the

cornea is at least 400 μm thick, the inner ocular structures are protected from cytotoxic damage [128,130,134,138,139]. Finally, the thermal effect of CXL is negligible with a maximum increase of 2-3 °C [128].

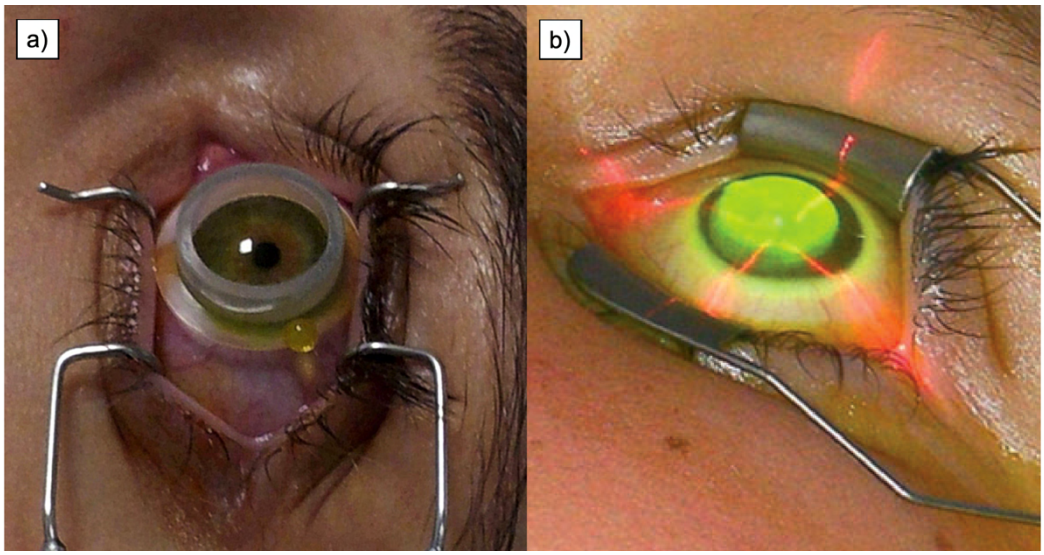


Figure 2.11 *– Corneal collagen crosslinking: a) a silicone ring was placed in direct contact with the cornea and filled with RF solution for 30 min before UV-irradiation [140]; b) corneal irradiation with UV-A for 30 minutes, with addition of more RF each 5 minutes [137].*

With the objective of reducing the treatment time, accelerated corneal crosslinking protocols (ACXL) using were developed by keeping the total energy delivered (5.4 J/m^2) constant while using higher UV-intensities for shorter time periods: 9 mW/cm^2 for 10 minutes, 18 mW/cm^2 for 5 minutes and 30 mW/cm^2 for 3 minutes [138]. Although the Dresden protocol remains the gold standard, recent randomised-controlled trials demonstrated the efficacy of ACXL (9 mW/cm^2 and 18 mW/cm^2) in the short-term [141–143]. Given the success of CXL therapy in crosslinking corneal collagen, we hypothesise that photopolymerisation could be a safe and effective way to trigger *in situ* crosslinking of biopolymers.

2.9 Photopolymerisation

Photopolymerisation is used in a large variety of industrial applications due to its speed and spatial resolution, low energy consumption, solvent-free formulations and cost [144]. In the last decade, light-induced polymerisation has become a common approach in the design of hydrogels for biomedical applications. Using visible or UV light, it is possible to polymerise liquid monomers *in situ,* thereby having spatial and temporal control over the initiation process and generating patient-specific scaffolds, which are essential features in the development of adhesives [145,146]. Further, this approach is minimally invasive, can be performed using biocompatible precursors, does not generate heat and is compatible with cell encapsulation and drug delivery [58,147].

Table 2.9 *– Parameters used to optimise the properties of photosensitive polymers.*

Polymer	• Molecular weight • Concentration • Amino acid composition • Degree of functionalisation
Light	• Wavelength • Intensity • Exposition time
Photoinitiation system	• Concentration • Molar extinction coefficient (ε) • Quantum yield (number of radicals generated per photon) • Water solubility • Toxicity

The hydrogel properties are highly dependent on several experimental parameters (**Table 2.9**), which can be optimised depending on the application and desired material performance. For tissue engineering applications, ensuring the cytocompatibility of the components (e.g, initiators, monomers and degradation products) and light energy and intensity used is essential to protect the viability of the nearby tissue [99,148].

2.9.1 (Meth)acrylate-based photosensitive polymers

Recently, significant efforts to develop novel meth(acrylated) polymers have been made since light-mediated gelation can be used in a wide range of applications, such as lithography, extrusion printing, adhesives, dental composites or drug delivery systems [149–155]. Monomers containing olefinic double bons (C=C), such as acrylate and methacrylate groups, are photopolymerised via chain growth free-radical polymerisation [148,156]. This photocrosslinking reaction includes three main stages: initiation, propagation and termination (**Figure 2.12**a).

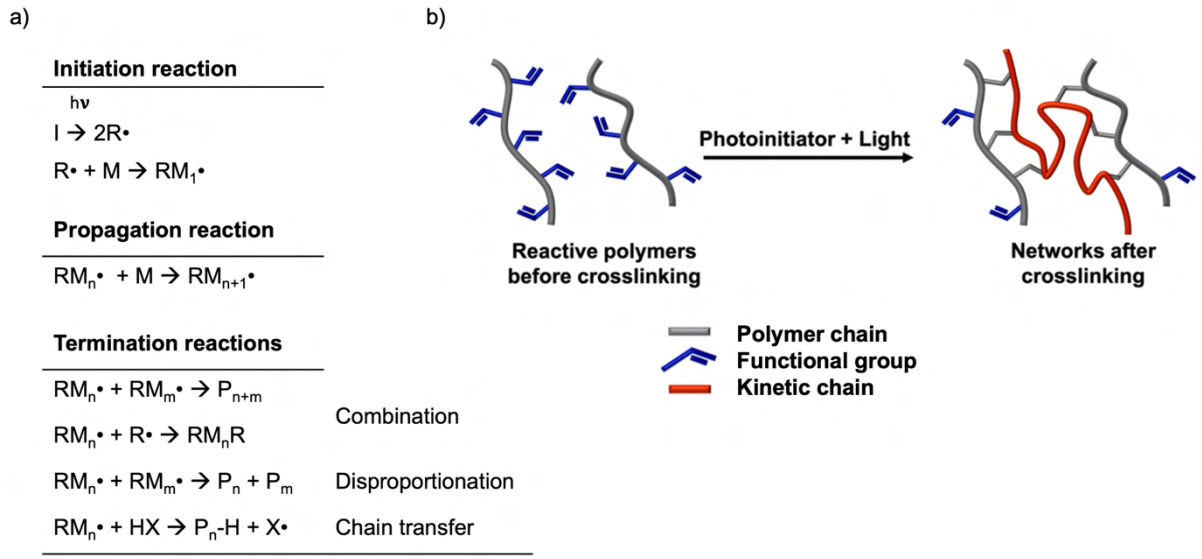


Figure 2.12 *– Free-radical chain polymerisation: a) general reaction mechanisms: initiation, propagation and termination; b) Schematic of meth(acrylated) polymer chains crosslinked through free-radical polymerisation upon light exposure in the presence of an initiator system. Adapted from* [157].

Since most monomers do not produce initiating species upon light exposure, it is necessary to use an initiator to start polymerisation by generating primary radicals upon light exposure [148]. The rate of initiation is directly proportional to the light intensity, initiator concentration, efficiency, molar extinction coefficient (ε) and the quantum yield (number of radicals per photon absorbed) [144,148]. The propagation starts when the free radicals react with the carbon-

carbon double bonds on the specific functional groups (e.g. methacrylates, acrylates, acrylamides) forming new radicals at the end of the growing chain. These reactive terminals then react with subsequent reactive functional groups, forming a kinetic chain that crosslinks the polymer together (**Figure 2.12**b) [148,157]. The propagation process concludes when reaction termination occurs via one of these mechanisms: combination (radical coupling), disproportionation (hydrogen transfer, one chain with a saturated terminal group and one chain with an unsaturated terminal group) and chain transfer event [157].

The number of polymerisable groups per molecule (degree of functionalisation) is of major importance since it leads to a faster onset of gelation with higher crosslinking densities due to an increased concentration of functional groups [156]. However, for tissue engineering applications, the extent of functionalisation needs to be optimised to ensure the biocompatibility and biodegradability of the semi-synthetic polymer. Also, in highly crosslinked systems, termination reactions might be hindered by entrapped radicals within the polymer network [148].

The main limitations associated with radical photopolymerisation concern oxygen inhibition due to radical scavenging, presence of entrapped residual/unreacted components and shrinkage during polymerisation [158]. The effect of oxygen inhibition can be reduced by increasing the initiator concentration and light intensity, or eliminated by photocuring the materials under argon or nitrogen atmosphere or by using a closed mould [148,159].

2.9.1.1 GelMA

Gelatine is a protein that can be obtained by denaturation of the triple helical structure of collagen that can be derived from several sources, such as fish, porcine or bovine [160,161]. Type A

gelatine (isoelectric point at pH 8-9) is produced by acid extraction whereas type B gelatine (isoelectric point at pH 4-5) is produced from alkaline treatment [162]. The amino acid composition of gelatine depends on the animal species, tissue (e.g. bone, tail) and manufacturing process, leading to an heterogenous mixture of peptides [163]. The gel strength (bloom) depends on the amount of intact collagen chains and on the molecular weight distribution [164,165]. This protein has several characteristics that makes it potentially attractive for tissue engineering applications, such as biocompatibility, presence of natural cell binding motifs like arginine-glycine-aspartic acid sequences (RGD) and protease cleavage sites, low immunogenicity, affordability, ease of chemical modification and water solubility [152,166,167]. In comparison to collagen, an endogenous corneal component, gelatine shows reduced risk of antigenic response, and improved water solubility and bio-absorption due reduced content of tertiary structures [38,162,168,169].

However, due to thermal instability at physiological temperature, weak mechanical properties and fast degradation, gelatine requires chemical crosslinking or blending with another polymer [166,170]. Several crosslinking strategies have been reported to date to improve the performance of gelatine hydrogels in corneal tissue engineering, including aldehydes (e.g. glutaraldehyde [171], formaldehyde) and enzymatic crosslinking (e.g. transglutaminase [172], tyrosinase [173]). Gelatine-resorcinol-formaldehyde/glutaraldehyde (GRFG) is an adhesive firstly described by Albes et al. [174]. Briefly, formaldehyde and glutaraldehyde create a strong bond with the tissue by reacting with resorcinol and with the amines present on the gelatine backbone and on the tissue surface [175]. GRFG crosslinks within a few minutes and is reported to show good adhesive properties in both wet and dry tissue, with an adhesive strength similar to CA and significantly higher than fibrin glue [74]. In one of the only studies concerning the use of GRFG in ophthalmology, Tonelli et al. compared the performance of fibrin, CAs and GRFG in strabismus surgery. All groups

showed firm adhesion three weeks post-surgery. However, while fibrin and CAs induced minimal and acceptable inflammatory reactions, respectively, GRFG produced an excessive inflammatory reaction with fibrosis and calcification [176]. Transglutaminase enzyme can also be used to crosslink gelatine. Gelatine-microbial transglutaminase (mTG) is formed within 3-30 minutes when the polymer is mixed with the enzyme, which catalyses the formation of an amide bond between the carboxylic groups of glutamic acid and the amines present in both the polymer (lysine residues) and the tissue [162,172,177,178]. Chen et al. injected mTG into the rat vitreous cavity to study its potential for retinal reattachment procedures. The adhesive did not elicit any cellular or structural damage 2-weeks post-surgery. Further, *in vitro* studies showed that mTG bonded to the wet bovine retinal tissue with lap-shear strengths comparable to fibrin sealants [177]. Yamamoto et al. conducted additional *in vivo* studies by using mTG to treat experimental induced retinal tears and retinal detachments in rabbit eyes. The results show that mTG adhered and sealed retinal tears for more than 7 days following vitrectomy without noticeable inflammatory reaction. However, the adhesive concentration and composition, strength and long-term inflammatory reaction need to be further studied [172]. In conclusion, these crosslinking strategies are associated with several issues. While aldehydes are cytotoxic and associated inflammatory responses *in vivo*, enzymatic crosslinking agents are more cytocompatible but do not allow fine control over the crosslinking reaction [163].

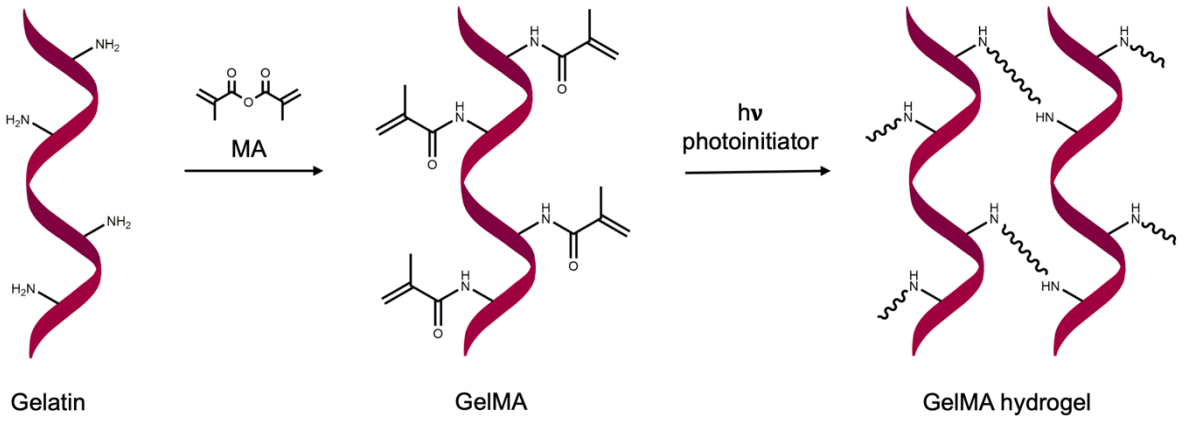


***Figure 2.13** – Methacrylation of gelatine with MA and preparation of photocrosslinked GelMA hydrogels in the presence of a photoinitiator and UV/visible light.*

To preserve the biocompatibility of the polymer and reduce process complexity, both the chemical modification extension and the amount of chemical additives used should be minimised [179]. In 2000, Van Den Bulcke et al. reported the modification of gelatine with methacrylic anhydride (MA) to form GelMA, a polymer that can be photocrosslinked in the presence of a photoinitiation system and light via free radical crosslinking (**Figure 2.13**) [180]. This approach uses short reaction times with mild processing conditions that allow the entrapment of cells, yielding mechanically strong, highly transparent and cytocompatible hydrogels with tailorable physical properties [166,170]. Since RGD sequences do not contain free-amino groups, the cell-binding capability of gelatine is not decreased by the methacrylation [160]. Due to these advantages, recently GelMA has been studied for several different applications in ocular tissue engineering, including development of a hybrid cornea together with decellularised extracellular matrix (ECM) [181], stromal scaffolds [152,170,182], endothelial sheets [179] and corneal adhesives [126]. Rizwan et al. developed a GelMA-based micro- and nano-patterned human corneal endothelial cell (HCEC) monolayer to treat corneal blindness due to endothelial dysfunction. The authors compared the physical and mechanical properties of GelMA films

photocrosslinked without previous incubation with membranes physically crosslinked at 4 ºC for 1h before irradiation (GelMA+). The presence of triple helixes and physical network formation in GelMA+ increased the homogeneity and decreased pore size, which resulted in a 5-fold greater compressive modulus in comparison with GelMA. Further, the optically transparent and pliable GelMA+ films could withstand the implantation procedure without any visible damage or HCEC monolayer detachment [179]. Recently, several GelMA-based adhesives have been developed for distinct applications, such as corneal repair [126], nerve repair [183] and lung leakages [184]. The engineered GelMA hydrogels outperformed clinical standard glues (e.g. fibrin, PEG sealants) and were shown to be biodegradable and biocompatible, supporting cellular adhesion, proliferation and migration [126,183,184]. Sani et al. studied the suitability of GelMA crosslinked with eosin Y and visible light (GelCORE) to seal corneal defects. 20% GelCORE adhesives (30.1 ± 4.3 kPa) could withstand burst pressures higher than ReSure (15.4 ± 6.3 kPa) and *in vivo* experiments using a rabbit stromal defect model demonstrated its ability to seal corneal defects and induce re-epithelisation and stromal regeneration [126].

2.9.1.2 SilkMA

In nature, silk-like proteins with distinct amino acid sequences and hierarchical structures are spun by different organisms, such as spiders, silkworms, bees and ants. Currently, silk fibroin (SF) extracted from the domestic silkworm *Bombyx Mori* is the most studied silk for medical applications due to its stablished supply chain, abundance and cost [185,186]. The main advantages of using silk when compared to the main component of the corneal ECM, collagen, are related to its ease of production, chemical modification and affordability [36].

Native *B.mori* silk is composed of silk fibroin, a filament core protein, and sericin, a protein that glues silk filaments together facilitating cocoon construction. In addition to inspire scientists to develop novel synthetic fibres due to their remarkable tensile strength, ductility and toughness, silk fibroin has gained attention as a biomaterial due to its biocompatibility, biodegradability and aqueous processing under mild conditions [187,188]. Kaplan et al. developed a method to reverse engineer silk cocoons into an aqueous silk fibroin solution that can be readily processed into different forms, such as films, sponges, scaffolds, hydrogels or microspheres [188]. The first step involves the unspinning of the *B.mori* cocoons and degumming to remove sericin since this protein has been linked to *in vivo* inflammatory responses [187]. Sericin is usually removed by boiling the cocoons in an alkaline solution (e.g. sodium carbonate) for 5 to 60 minutes. To ensure reproducibility, the boiling time must be controlled since it affects the overall molecular weight of the protein [187]. Then, the degummed silk fibroin fibres can be dissolved in chaotropic agents (e.g. urea or lithium bromide) to disassemble its highly ordered structure. After extensive dialysis to remove residual salts and impurities, the aqueous silk solution is stable for weeks to several months, depending on the storage conditions [188]. However, due to the above mentioned processes, the structural arrangement, molecular weight and rheological properties of the reversed engineered silk protein is significantly different from the silk fibroin found in the silkworm's glands [189]. Importantly, when designing novel SF-based materials, the *in vivo* assembly of silk proteins must be considered. As liquid SF flows through the secretory pathway, changes in protein concentration, water content, pH and metal ion concentrations drive the transition from noncrystalline liquid silk to its fibre structure [190]. Therefore, changes in these parameters during silk processing might influence protein aggregation.

Over recent years, silk fibroin membranes have been investigated as a replacement for amniotic membrane in corneal regeneration. In addition to provide a useful substrate to incorporate topographical cues that affect cell migration and phenotype, silk films are more transparent than the amniotic membrane [166,191]. Although these materials can be easily prepared by solvent evaporation after casting the aqueous silk fibroin solutions, the preparation of silk-based hydrogels is more challenging. Most of the works concerning the development of silk hydrogels are based on the protein assembly to form insoluble β-sheet-rich networks, referred as physical crosslinking. Several processes have been demonstrated to induce β-sheet formation including organic solvents, vortexing, sonication, pH and temperature [192]. However, the preparation and overall properties of physically crosslinked hydrogels show several disadvantages that prevent them to be used for corneal tissue engineering. Beyond the incompatibility of the above mentioned processes with *in situ* curing or cell encapsulation due to the harsh environmental conditions used, the overall properties of the hydrogels are inadequate for stromal replacement due to their opacity and brittleness caused by the formation nanocrytallites that block long range displacements [185].

Alternatively to physical crosslinking, silk fibroin hydrogels can also be prepared through chemical crosslinking using enzymes (e.g. horseradish peroxidase, tyrosinase). Despite allowing the preparation of elastic hydrogels, this method is unsuitable for fast *in situ* crosslinking due to slow gelation (5 min to hours) [193,194]. Therefore, recent efforts have been made to develop techniques that allow rapid covalent crosslinking of silk hydrogels.

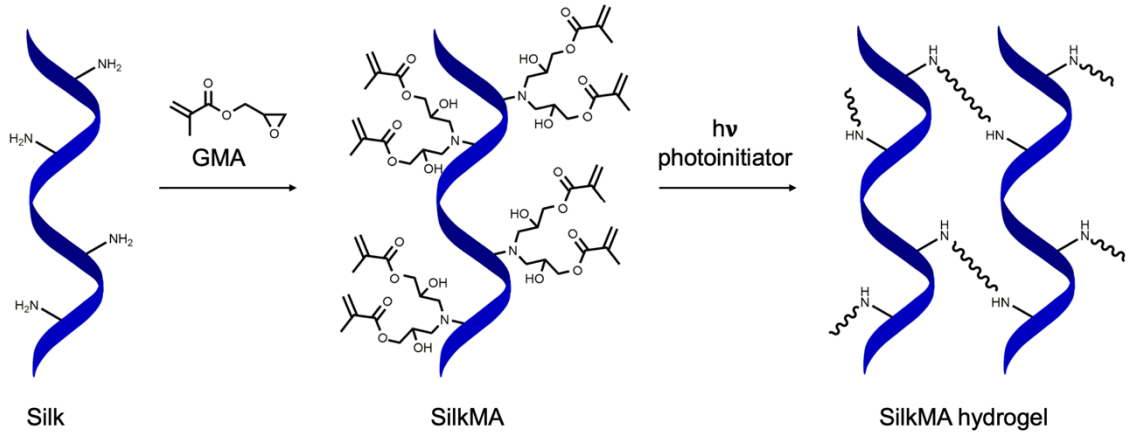


Figure 2.14 *– Methacrylation of silk fibroin with GMA and preparation of photocrosslinked SilkMA hydrogels in the presence of a photoinitiator and UV/visible light.*

The methacrylation of silk fibroin (SilkMA) was firstly reported in 2018 by Soon Hee Kim et and co-workers [151]. After dissolving the silk fibres with lithium bromide, the authors added (GMA) to the solution, which reacted with the free amino groups on the lysine residues though an epoxide-ring opening reaction, thereby introducing photocrosslinkable methacrylate groups on the polymer chain (**Figure 2.14**). The authors tried to use MA, the reagent used in GelMA manufacturing, however premature silk crystallisation was observed due to the presence of an acidic by-product (methacrylic-acid). In addition to yield a stable reaction, GMA can also maximise the number of methacrylate groups grafted onto the protein backbone as two GMA molecules are reported to react with one free amino group (NH_2), while MA reacts with a single residue. Since silk contains small quantities of lysine residues (0.2 mol%), maximising the number of vinyl groups is essential to increase the crosslinking density and obtain robust hydrogels. Lastly, GMA is also proposed to react with other groups, such as hydroxyl (-OH) and carboxyl (-COOH), via both transesterification and epoxide ring-opening mechanisms [151,193,195,196]. Recently, several highly complex organ structures were prepared using SilkMA bioinks via digital light processing (DLP) 3D printing [151,197,198]. The 3D-printed SilkMA

constructs exhibited outstanding mechanical and rheological properties and excellent biocompatibility [151]. Heesun Hong et al. investigated the suitability of SilkMA hydrogels for cartilage tissue engineering. After confirming the capability of SilkMA constructs to provide *in vitro* proliferation and differentiation of chondrocytes up to four weeks, the authors studied the *in vivo* application of cultured SilkMA hydrogels in a trachea defect rabbit model. Cellular analysis showed histological characteristics of cartilage tissue with new blood vessels and collagen matrix found in the epithelial layer under the transplanted chondrocyte-laden SilkMA gel [197]. In conclusion, the water-based processing, cytocompatibility and physical properties of SilkMA-based materials make them promising candidates for tissue engineering applications.

2.9.2 Photoinitiation systems

The initiating system plays a key role in light-initiated polymerisation reactions since it influences the reaction efficiency, polymerisation speed and the final mechanical properties of the polymer [199]. These systems can be one or two-component, however, regardless of its composition and initiation mechanism, the initiating system should exhibit several characteristics [148,199]:

- High rate of initiation at the light source emission wavelength;
- Good solubility in both water and the prepolymer solution – essential for tissue engineering applications since it prevents the usage of solvents;
- Cytocompatibility;
- Thermal and temporal stability;
- High quantum efficiency;
- High reactivity towards the monomers when compared with reactivity with solvents, oxygen and impurities;

- Should not cause hydrogel colouring;
- Affordability.

Free-radical photoinitiation systems are divided into two classes, type I or type II initiators (PI), depending on their radical generation mechanism.

2.9.2.1 Type I photoinitiators

Type I photoinitiators are single component since they undergo hemolytic cleavage following proton absorption, creating free radicals ($R_x^{\bullet}$) that can subsequently initiate the polymerisation process:

$$PI \xrightarrow{h\nu} R_1^{\bullet} + R_2^{\bullet} \quad (1)$$

The most used Type I initiators in tissue engineering are shown in **Figure 2.15** [157,200].

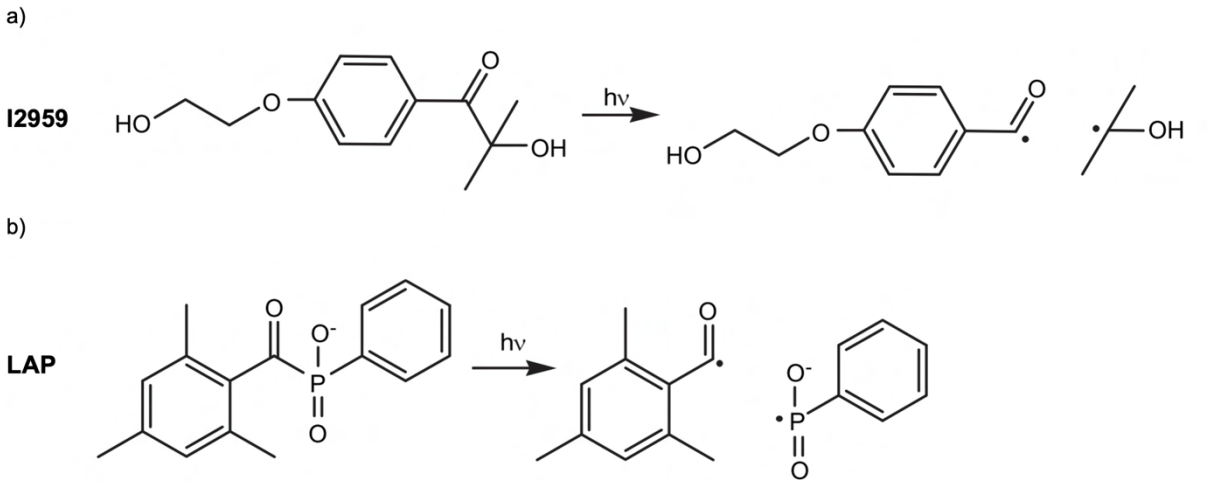


***Figure 2.15** – Cleavage of type I radicals into free-radicals following proton absorption: a) I2959 and b) LAP. Adapted from* [201].

In the last two decades, 1-[4-(2-hydroxyethoxy)-phenyl]-2hydroxy-2-methyl-1-propanone (Irgacure-2959 or I2959) has been the most researched photoinitiator for tissue engineering

applications (**Figure 2.15**a). Although being reasonably cheap and well tolerated by many cells, its low water solubility (< 2 wt%), difficult re-constitution even at concentrations around 0.5 wt% (agitation/heating required for dissolution) and a narrow absorption UV-A range absorption ($\lambda_{max} = 276$ nm) present significant drawbacks [201]. Since the use of light below 300 nm has cytotoxic and genotoxic effects, most research groups have used I2959 together with 365 nm light source despite its low reactivity ($\varepsilon_{365\,nm} = 3$ M^{-1} cm^{-1}) and crosslinking efficiency, which ultimately leads to the use of higher photoinitiator concentrations, UV irradiation dosages and longer curing times [157].

Another commonly used type I photoinitiator for biomedical applications is lithium phenyl-2,4,6-trimethylbenzoylphosphinate (LAP). Initially described by Majima et al., this photoinitiator exhibits many advantages over I2959 since it exhibits higher water solubility (up to 8.5 w/v%) and higher absorption at 365 nm ($\varepsilon_{365\,nm} = 216$ M^{-1} cm^{-1}) together with some absorption in the visible range ($\varepsilon_{405\,nm} = 19$ M^{-1} cm^{-1}) [157,202]. Fairbanks et al., reported that LAP improved the polymerisation kinetics and enabled cell encapsulation at lower photoinitiator concentration and longer wavelength light relative to I2959 [201].

2.9.2.2 Type II photoinitiators

On the other hand, type II photoinitiators, such as eosin-Y, ruthenium and RF, have a more complex initiating mechanism since these uncleavable photoinitiators require a co-initiator, which does not absorb light but is involved in the production of free radicals. Upon irradiation, the co-initiator (AH) donates an hydrogen atom to the excited photoinitiator, forming radicals that initiate the crosslinking reaction [158,203]:

$$PI + AH \xrightarrow{h\nu} PIH^{\bullet} + A^{\bullet} \quad (2)$$

Depending on the nature of the photoinitiator, an electron-transfer might occur upon electronic excitation with subsequent proton transfer [204].

Eosin-Y, a pink organic dye, has been recently used as a photoinitiator for tissue engineering applications due to its high water solubility and superior absorption in the green range when compared to other type II photoinitiators ($\varepsilon_{500\,nm} \approx 50\,000\ M^{-1}\,cm^{-1}$) [126,157,205–207]. Upon light absorption, the photoexcited eosin-Y extracts hydrogen atoms from the coinitator, such as triethanolamine (TEA), which will facilitate the crosslinking reaction. The main drawback concerning the use of eosin-Y is the need to use a co-monomer (e.g. N-vinyl-caprolactam (VC), N-vinylpyrrolidone) to accelerate the gelation process, which makes the prepolymer preparation and concentration optimisation more complex [157,207].

Recently, photo initiating systems composed of tris(2,2-bipyridyl) dichlororuthenium (II) hexahydrate (ruthenium) and sodium persulfate (SPS) have been studied by several research groups since they allow 3D-printing of cell-laden constructs with high shape fidelity, cell viability and lower oxygen inhibition than type I photoinitiators [193,208–210]. Ruthenium supports the use of both UV ($\varepsilon_{365\,nm} \approx 6000\ M^{-1}\,cm^{-1}$) and visible light ($\varepsilon_{450\,nm} \approx 19\,000\ M^{-1}\,cm^{-1}$). When irradiated, the photoexcited Ru^{2+} oxidises to Ru^{3+} via electron donation to the co-initiator. After accepting the electrons, SPS dissociates into sulfate anions and sulfate radicals, triggering the photocrosslinking reaction [209].

As previously mentioned, RF (vitamin B2) is a naturally occurring yellow pigment which is widely used for biomedical applications, including CXL, due to its biocompatibility and water

solubility. The main limitation of the use of RF is its slow reaction kinetics, which might be incompatible with several applications such as cell-encapsulation, bioprinting or bioadhesive development [199]. Similarly to ruthenium, RF exhibits high molar extinction coefficients in the UV ($\varepsilon_{365\,nm} \approx 10\,000\ M^{-1}\,cm^{-1}$) and visible range ($\varepsilon_{450\,nm} \approx 12\,000\ M^{-1}\,cm^{-1}$) and has been recently used together with SPS to photo-crosslink silk and keratin hydrogels, improving its gelation kinetics [211,212]. To conclude, despite requiring a co-initiator and often an accelerator to achieve reasonable polymerisation kinetics, type II photoinitiators are often preferred over type I photoinitiators due to their higher absorption in both UV and visible range, solubility and biocompatibility [213].

CHAPTER THREE

3 General Methods

3.1 Material preparation

3.1.1 Preparation of methacrylated silk fibroin hydrogels

3.1.1.1 Silk Fibroin extraction

Bombyx Mori cocoons were supplied by The Yarn Tree (Roanoke, USA). Each cocoon was sliced into four pieces and the silkworms were discarded. To remove the sericin, 10 g of sliced cocoons were boiled in 4 L of 0.02 M Na_2CO_3 (Acros Organics, Belgium) for 30 minutes. Subsequently, the degummed silk fibroin (SF) was washed three times in 2 L of distilled water for 20 minutes and left in a fume hood overnight to dry at room temperature (Figure 3.1).

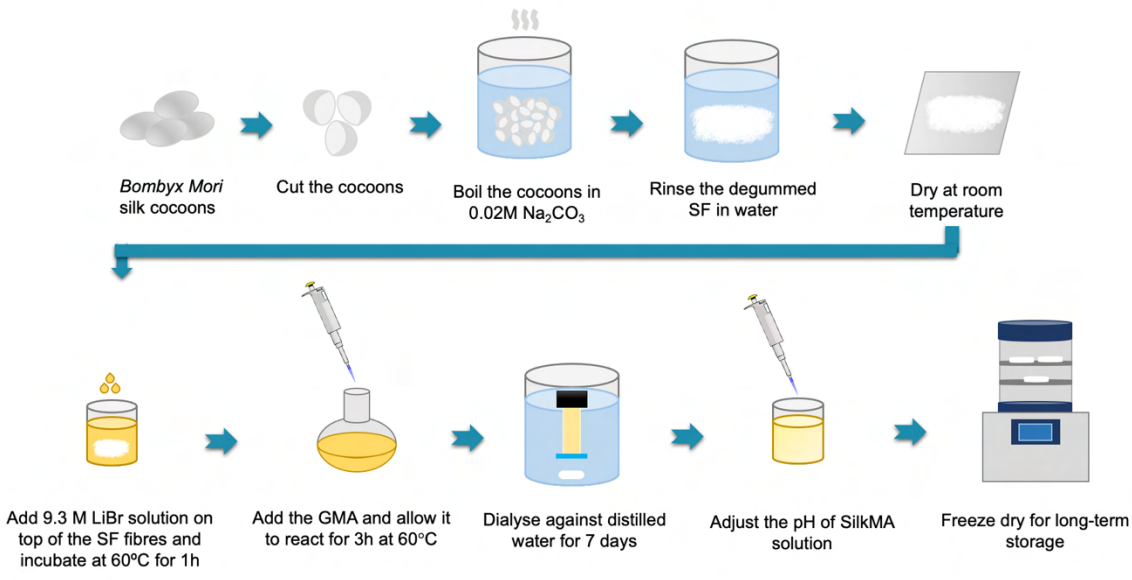


Figure 3.1 - Workflow for SF extraction and SilkMA synthesis: degumming, dissolution in lithium bromide, methacrylation, dialysis and freeze-drying.

3.1.1.2 SilkMA synthesis

As shown in Figure 3.1, 25% (w/v) of degummed SF solution was prepared by pouring a 9.3 M lithium bromide solution (Acros Organics, Belgium) on the tightly packed degummed silk fibroin fibres. After incubation at 60°C for 1 h, the fibres were completely dissolved and GMA (Sigma-Aldrich, USA) was added to the solution (10% v/v) and allowed to react for 3 h at 60°C with a stirring speed of 300 rpm. The solution was then dialysed against distilled water for 7 days at 4°C using 12-14 kDa cut-off dialysis tubes (Thermo Scientific, USA). After dialysis, the SilkMA solution was diluted to 2% (w/v) and the pH adjusted to 5, 7, 7.4 or 8 using 1 mM sodium hydroxide solution (Sigma-Aldrich, USA). Lastly, SilkMA solutions were lyophilised for 2 days to generate a white porous foam, which was stored at -80°C until further use.

3.1.1.3 Degree of functionalisation

The degree of functionalisation (DF%) was quantified by proton nuclear magnetic resonance (^{1}H-NMR). Briefly, 5 mg of SilkMA was dissolved in 600 µL of deuterium oxide (Sigma-Aldrich, USA). The ^{1}H-NMR spectra of raw SF and SilkMA were recorded using a Bruker NEO NMR spectrometer fitted with a 'smart'-BBFO probe (Bruker, Austria) operating at 400 MHz for 1 hour. Spectra were recorded at 25°C using 250 scans and a delay of 12 seconds between scans. Baseline and phase correction were applied before integrating the peaks of interest with Topspin software (Bruker, Austria). The signal from the aromatic amino acids (6.9 - 7.5 ppm) was used as the internal reference to normalise the amine signals (2.83 - 3.14 ppm) [151]. As GMA is reported to react with SF through the primary amines on lysine residues, the extent of substitution was calculated by normalisation to the number of free amino groups of the original SF [151]. The DF% was calculated using the following equation:

$$\text{DF}\ (\%) = \frac{\text{lysine integration signal of SilkMA}}{\text{lysine integration signal of SF}} \times\ 100 \qquad (3)$$

3.1.1.4 Hydrogel fabrication

SilkMA prepolymer solutions were prepared by dissolving an appropriate amount of SilkMA in distilled water at room temperature overnight. The resulting viscous solutions were filtrated using Miracloth (Merck Millipore, USA) and the final concentration was calculated. A fresh stock solution of 2% (w/v) lithium phenyl-2,4,6-trimethylbenzoylphospinate (LAP) (Sigma-Aldrich, UK) in phosphate-buffered saline (PBS) with pH 7.4, (Sigma-Aldrich, UK) was prepared. The photoinitiator was added to the SilkMA solution to a final concentration of 0.5% (w/v) and the resulting solution was mixed at room temperature. The hydrogel precursor solutions were photocured through UV-light using an OmniCure S1500 (Lumen Dynamics, Ontario, Canada) with a 365 nm filter. Briefly, 200 μL of SilkMA prepolymer solution was pipetted onto a 12 mm cylindrical mould and then exposed to 3 mW/cm^2 UV-A for 5 minutes.

3.1.2 Preparation of gelatine methacryloyl hydrogels

3.1.2.1 GelMA synthesis

Briefly, a 10% (w/v) gelatine type A solution (porcine skin, 300 bloom strength, Sigma-Aldrich, UK) was dissolved in PBS (Sigma-Aldrich, UK) at 60 °C for 30 min. MA (Sigma-Aldrich, UK) was added to the gelatine solution to a final concentration of 6% (v/v) and left to react for 2 h at 50 °C under vigorous stirring. After the reaction period, the solution was transferred to 50 mL tubes and the unreacted MA was partially removed by centrifugation at 3500 rpm for 5 min at room temperature. The solution was then dialysed against distilled water for 7 days at 37 °C using 12–14 kDa cut-off dialysis tubes (Thermo Scientific, UK). After dialysis, the GelMA solution was diluted to 2% (w/v) and the pH adjusted to 7.4 using 1 mM sodium hydroxide

solution (Sigma-Aldrich, UK). Lastly, GelMA solutions were lyophilised for 2 days to generate a white porous foam, which was stored at −80 °C until further use.

3.1.2.2 Degree of functionalisation

The DF% was quantified by ^{1}H-NMR. Briefly, 5 mg of GelMA was dissolved in 600 µL deuterium oxide (Sigma-Aldrich, UK). The ^{1}H-NMR spectra of raw gelatine and GelMA were recorded using a 400 MHz spectrometer (Brucker, USA). Baseline and phase correction were applied before integrating the peaks of interest with Topspin software (Brucker, USA). The phenylalanine signal (7.2–7.5 ppm) was used as the internal reference to normalise the amine signals (3.13–3.22 ppm) of lysine [214]. As MA reacts with gelatine through the primary amines on lysine residues, the extent of substitution was calculated by normalisation to the number of free amino groups of raw gelatine. The DF% was calculated using the following equation:

$$\mathrm{DF}(\%) = \frac{\text{lysine integration signal of GelMA}}{\text{lysine integration signal of Gelatine}} \times 100 \qquad (4)$$

3.1.2.3 Hydrogel preparation

GelMA prepolymer solutions were prepared by dissolving an appropriate amount of polymer in PBS at 60 °C for 30 min. Fresh stock solutions of 40 mM phosphated RF (Sigma-Aldrich, UK) and 456 mM SPS (Sigma-Aldrich, UK) in PBS were prepared. The photoinitiator system RF/SPS was added to the GelMA solution to a final concentration of 2/20 mM and the resulting solution was vigorously mixed at 60 °C. The hydrogel precursor solutions were photocured using 30 mW/cm^2 UV light with an OmniCure S1500 (Excelitas Technologies, Canada) with a 365 nm filter or using 100 mW/cm^2 visible light (Knightsbridge FLF Floodlight, RS, UK). Briefly, 200 µL of GelMA prepolymer solution was pipetted onto a 12 mm cylindrical mould and then exposed to light for 2 min.

3.2 Physicochemical properties

3.2.1 Transparency

Light absorbance of hydrogels in the visible range was measured using a microplate reader (Spark Multimode, Tecan, Switzerland). The measurements were carried out in triplicate using hydrogels soaked in PBS (diameter = 12 mm, thickness = 1.2 mm), with pure PBS serving as a blank control. Subsequently, the transmittance was calculated using the following equation:

$$\text{Transmittance (\%)} = 10^{2-\text{Absorbance}} \quad (5)$$

3.2.2 Swelling properties

Immediately after calculating the initial hydrogel weight (m_{t0}), three samples (diameter = 12 mm, thickness = 1.2 mm) from each condition were freeze dried ($\text{m}_{\text{t0,dry}}$) and three samples were hydrated in PBS and placed in an incubator at 32 °C. After 24 h, the samples were blotted dry using a filter paper and the swollen weight ($\text{m}_{swollen}$) was measured. Finally, the swollen hydrogels were lyophilised and weighed to determine the dry sample weight ($m_{swollen,\text{dry}}$). The sol fraction is a measurement of the macromers not crosslinked in the hydrogel network and was defined as the mass loss after 24 h [215,210]. The swelling (SR), mass swelling ratio (q), water content, and mass loss were calculated according to the following equations:

$$\text{SR (\%)} = \frac{m_{swollen} - m_{\text{t0}}}{m_{\text{t0}}} \times 100 \quad (6)$$

$$\text{Mass swelling ratio (q)} = \frac{\text{m}_{swollen}}{\text{m}_{\text{t0,dry}}} \quad (7)$$

$$\text{Water content (\%)} = \frac{m_{\text{swollen}} - m_{\text{t0,dry}}}{m_{swollen}} \times 100 \quad (8)$$

$$\text{Mass loss (\%)} = \frac{m_{\text{t0,dry}} - m_{swollen,\text{dry}}}{m_{t0,dry}} \times 100 \quad (9)$$

The thickness of the fresh and swollen hydrogels was estimated using ImageJ software (version 2.0) and the expansion (%) in PBS after 24 h calculated. Tests were performed in triplicate.

3.2.3 Enzymatic degradation

Disc-shaped hydrogels (radius = 3 mm, thickness = 2 mm) were prepared as previously described. After photocrosslinking, five samples of each group were immediately freeze-dried to calculate the initial weight. To determine the *in vitro* degradation, five samples of each group were placed in 1.5 mL tubes with 1 mL of 1 U/mL collagenase II in PBS (Fisher Scientific, UK) or in 1 mL PBS (control group) and incubated at 32°C. At the end of the incubation period the hydrogels were lyophilised. The degradation was calculated using the following equation:

$$\text{Degradation (\%)} = \frac{m_{\text{t0,dry}} - m_{\text{dry}}}{m_{dry}} \times 100 \quad (10)$$

Where $m_{\text{t0,dry}}$ is the initial dry weight of the hydrogels and m_{dry} is the final dry weight of the sample after degradation (n= 5).

3.2.4 Scanning electron microscopy

Scanning electron microscopy (SEM) was used to assess the morphology and pore size of freeze-dried hydrogels. All samples (diameter = 6 mm, thickness = 2 mm) were mounted onto aluminium stubs using carbon tape and gold sputter coated. Images were captured using a TM3030Plus benchtop SEM (Hitachi High Technologies, USA) at an electron acceleration voltage of 15 kV.

3.2.5 Micro computed tomography

Freeze-dried hydrogels were scanned using a Skyscan 1172 (Bruker, USA) with 80 kV beam voltage and 100 μA current, 140 ms exposure per projection, 12.99 μm pixel size, rotation step

0.6° and 4 frame averaging. The same parameters were used for all scans. The XY projections were reconstructed into a 3D model using NRecon (Bruker, USA). A cylindrical volume of interest was taken in the centre of each sample, excluding any outside space. A binary threshold was then applied to this volume of interest to separate polymer material and air in the pores of the sample. The pore size distribution was then calculated using the 3D analysis software in CTAn (Bruker). Sample reconstructions were visualised in 3D using CTVox (Bruker, USA). The experiments were conducted in triplicate.

3.3 Mechanical and adhesive properties

3.3.1 Rheology

The viscoelastic properties of the hydrogels were investigated via rheometry. The storage modulus and loss modulus of freshly prepared hydrogels were measured in oscillatory mode at 32 °C using a plate–plate geometry and a 1.2 mm gap between plates (Kinexus Pro+, Malvern Instruments, UK). After running an amplitude sweep to determine the linear viscoelastic range, a frequency sweep was conducted between 0.01–10 Hz at 0.5% shear strain. The experiments were conducted in triplicate. The damping factor (tan δ) was calculated using the following equation:

$$\tan \delta = \frac{G''}{G'} \tag{11}$$

3.3.2 Compressive modulus

Cyclic testing was performed using an Instron 5542 mechanical tester (Instron, MA, USA) with a 2 kN load cell. Cylindrical hydrogels were prepared as previously described and incubated in PBS for 4 h prior to testing. The dimensions of the samples were determined using a digital calliper. Compressive tests were performed at a rate of 1 mm/min up to a maximum strain of

60% of the original height by performing 8 cycles of loading and unloading. The compressive strain (mm) and load (N) was recorded using Bluehill 3 software (Instron, MA, USA). The compressive moduli were calculated from the slope of the linear region on the stress (kPa) versus strain (mm/mm) curves. Samples were tested in triplicate for each condition.

3.3.3 Tensile modulus

Uniaxial tensile testing was performed using an Instron 5542 mechanical tester (Instron, Norwood, MA, USA) with a 100 N load cell. Hydrogels were prepared as previously described in dog-bone shaped moulds (width = 4 mm, gauge length = 10 mm) and incubated in PBS for 4 h prior to testing. After measuring the swollen sample dimensions using a digital calliper, hydrogels were placed between two pieces of double-sided tape, fastened to the instrument's tension grips and extended at a rate of 2 mm/min until failure. The load (N) and tensile strain (mm) were measured using Bluehill 3 software and the tensile modulus was calculated from the slope of the stress–strain curves. The tensile strength and maximum elongation were obtained at point of failure. At least five samples were tested for each condition.

3.3.4 *Ex vivo* burst pressure

The ability of engineered adhesives to seal corneal perforations was assessed on wet and dry conditions. Porcine eyes were chosen as an *ex vivo* model due to their availability, which allowed freshly enucleated eyes to be obtained from a local butcher on a daily basis. To study adhesion on wet conditions, a full-thickness incision was created on the porcine eyeball using a 2 mm biopsy punch and 20 μL of SilkMA, GelMA or Histoacryl (control group, B. Braun Surgical S.A., Spain) was added to the perforation and cured *in situ*. Then, the sealed eyes were connected to a pressure testing system (**Figure 3.2**a) through the insertion of a 27-gauge needle

into the anterior chamber of a porcine eyeball. Finally, a syringe pump (SINO SN-50F66, SINO MDT, China) injected PBS mixed with fluorescein (Sigma-Aldrich, Gillingham, UK) into the anterior chamber at a rate of 20 mL/h, while a wireless pressure sensor (PASCO, USA) recorded the intraocular pressure. The test was stopped at adhesive failure or when the pressure reached 50 kPa (n = 8). The burst pressure on dry conditions was studied by mounting a porcine cornea with a 2 mm full-thickness perforation on a Barron artificial anterior chamber (AAC, Katena, New Jersey, USA) (**Figure 3.2**b). The burst pressure was measured as previously described (n = 8).

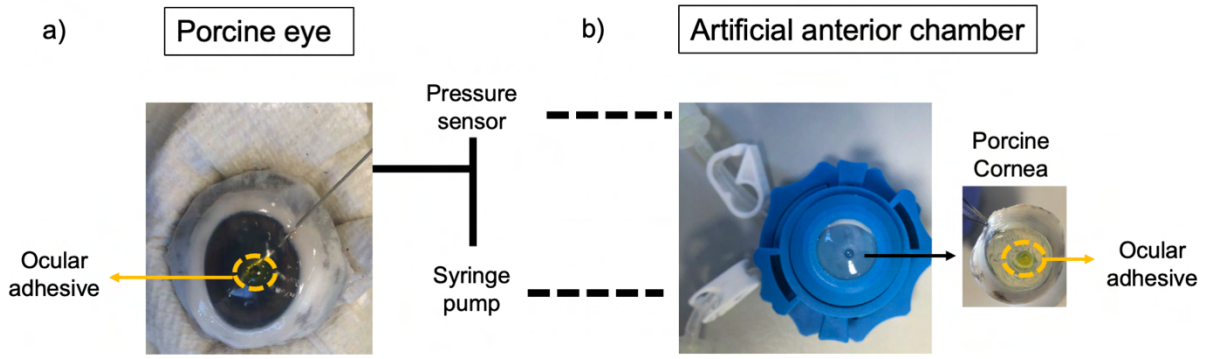


Figure 3.2 *– Ex vivo burst pressure measurements after creating a full-thickness incision with a 2 mm biopsy punch followed by the adhesive application and in situ curing: a) measurement in wet conditions, a 27-gauge needle was inserted into the anterior chamber; b) measurement in dry conditions, a porcine cornea is mounted in an AAC. Both a) and b) are connected to a syringe pump and a pressure sensor.*

3.3.5 Lap shear strength

The shear strength of SilkMA, GelMA and Histoacryl (control group, B. Braun Surgical S.A., Spain) was tested according to the modified American Society for Testing and Materials (ASTM) F2255-05 standard for tissue adhesives using an Instron 5542 mechanical tester (Instron, Norwood, MA, USA) with a 2 kN load cell. As substrate, two pieces of glass slides (50 × 10 mm) were coated with 20% (*w*/*v*) gelatine solution (porcine, 300 bloom, Sigma-Aldrich, UK) at 60 °C and left to dry at room temperature overnight. Then, 20 µL of prepolymer

solution was crosslinked between two gelatine-coated glass slides (total area = 100 mm^2). The two glass slides were placed between two pieces of double-sided tape, fastened to the instrument's tension grips and extended with a strain rate of 2 mm/min (**Figure 3.3**). The shear strength of the adhesives was calculated at the detachment point on dry and wet substrates (n = 7).

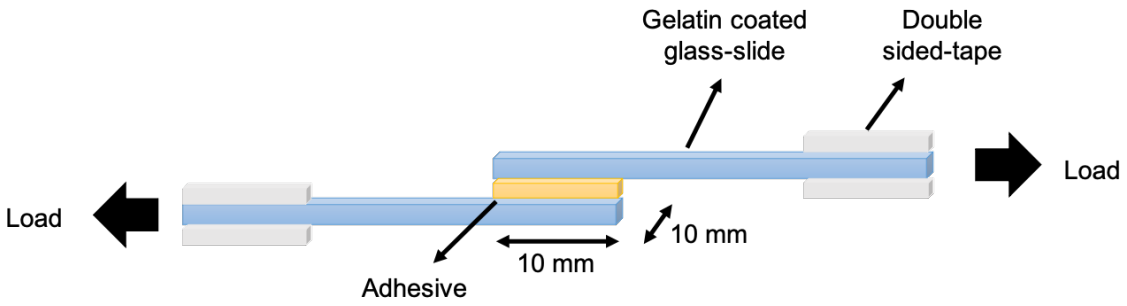


Figure 3.3 *– Schematic of the modified ASTM F2255-05 test for lap shear strength calculation.*

3.4 *In vitro* cell studies

Human dermal fibroblasts (HDFs, American Type Culture Collection (ATCC), USA Passage number 9) were cultured in Dulbecco's modified eagle medium (DMEM, Sigma-Aldrich, UK) and supplemented with 10% foetal bovine serum (Sigma-Aldrich, UK), 1% penicillin/streptomycin (Sigma-Aldrich, UK) and 2 mM L-glutamine (Sigma-Aldrich, UK). All cultures were maintained in tissue culture treated polystyrene flasks at 37 °C with 5% CO_2 in a humidified incubator and passaged at 80% confluency.

3.4.1 Cell viability

Cell viability was evaluated using a live/dead assay (Thermo Fisher Scientific, MA, USA) following the manufacturer's protocol. Briefly, SYTO 10 green fluorescent nucleic acid stain (2 µL/mL) and ethidium homodimer-2 nucleic acid stain (2 µL/mL) were diluted in PBS to

form the staining solution. At each time point, the samples were incubated with the staining solution for 15 min in the dark at 37 °C. The staining solution was removed, and the samples were washed twice with PBS. The monolayer cultures and cell-seeded hydrogels were imaged with a fluorescence microscope (EVOS M5000, Thermo Fisher, UK) and a confocal scanning microscope (Zeiss LSM710, Carl Zeiss, Germany), respectively.

3.4.2 Metabolic activity

AlamarBlue™ assay (Thermo Fisher, UK) was used to determinate the relative metabolic activity according to the manufacturer's protocol. Briefly, the samples were incubated with 0.5 mL of 10% alamarBlue™ reagent in culture medium for 4 h at 37°C with 5% CO_2. Thereafter, 50 μL of cell culture medium were transferred to a 96-well plate (Corning, UK) and the fluorescence intensity was measured with a microplate reader (Spark Multimode, Tecan, Switzerland) using an excitation wavelength of 540 nm and an emission wavelength of 590 nm. Acellular hydrogels were used as a negative control and their fluorescence was subtracted from the same group seeded hydrogels to account for the background ($n \geq 4$).

3.4.3 Cell proliferation

DNA content was quantified using the Quant-iT PicoGreen DNA assay (Life Technologies, UK). Briefly, cell-laden hydrogels were lysed in 0.1% TritonTM X-100 in PBS (Sigma-Aldrich, UK) via performing freeze–thaw cycles between 37 °C and –80 °C. After spinning down the samples at 300 g for 5 min to remove non-genomic material, 10 μL of cell lysate was added to 90 μL of TE (10 mM Tris-HCl, 1 mM EDTA) buffer in a 96-well plate (Corning, USA). A total of 100 μL of PicoGreen was added to all samples and then incubated for 5 min.

The fluorescence intensity was then measured with a microplate reader (Spark Multimode, Tecan, Switzerland) at an excitation and emission wavelength of 480 and 520 nm, respectively.

3.5 Statistical analysis

For each experiment, at least three samples were tested. One or two-way analysis of variance (ANOVA) and Tukey's test were used to determine statistically significant differences with GraphPad Prism 8.0 software (GraphPad Software, USA). The level of significance was set at $p < 0.05$. Data are presented as mean value ± standard deviation (SD).

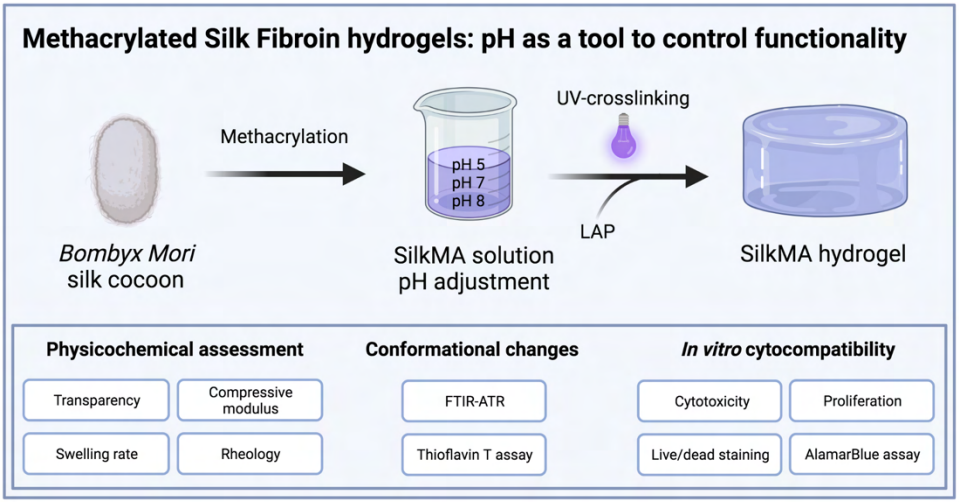
CHAPTER FOUR

4 Methacrylated Silk Fibroin Hydrogels: pH as a Tool to Control Functionality

Data in this chapter is also presented in the published article found in Appendix B:

Inês A. Barroso, Kenny Man, Victor M. Villapun, Sophie C. Cox, and Anita K. Ghag, "*Methacrylated Silk Fibroin Hydrogels: pH as a Tool to Control Functionality*", ACS Biomaterials Science & Engineering *7* (10), 4779-4791, DOI: 10.1021/acsbiomaterials.1c00791 (2021)

The last decade has witnessed significant progress in the development of photosensitive polymers for *in situ* polymerisation and 3D printing applications. Light-mediated sol-gel transitions have immense potential for tissue engineering applications as cell-laden materials can be crosslinked within minutes under mild environmental conditions. Silk fibroin (SF) is extensively explored in regenerative medicine applications due to its ease of modification and exceptional mechanical properties along with cytocompatibility. To efficiently design SF materials, the *in vivo* assembly of SF proteins must be considered. During SF biosynthesis, changes in pH, water content and metal ion concentrations throughout the silkworm gland divisions drive the transition from liquid silk to its fibre form. Herein, we study the effect of glycidyl-methacrylate-modified SF (SilkMA) solution pH on the properties and secondary structure of SilkMA hydrogels by testing formulations prepared at pH 5, 7 and 8. Our results demonstrate an influence of the prepolymer solution pH on the hydrogel rheological properties, compressive modulus, optical transmittance and network swellability. The hydrogel pH did not affect the *in vitro* viability and morphology of human dermal fibroblasts. This work demonstrates the utility of the solution pH to tailor SilkMA conformational structure development towards utility and function and shows the need to strictly control pH to reduce batch-to-batch variability and ensure reproducibility.



4.1 Introduction

Hydrogels have been extensively studied in the tissue engineering field due to their three-dimensional hydrophilic networks, biodegradability and elasticity [216,217]. In particular, polypeptides (e.g. collagen, gelatine, silk) are particularly attractive due to their resemblance with the native extracellular matrix environment [218]. Recently, there has been increasing interest in the development of photosensitive hydrogels for 3D printing and *in situ* polymerisation applications. These materials can be combined with cells, growth factors and bioactive factors and crosslinked within seconds using light. Despite these advantages, limited reproducibility and batch-to-batch variability remain the main preventive factors to the wide application of natural polymers in tissue engineering.

In the last decade, SF has proved itself to be one of the most versatile materials available for regenerative medicine applications. Its water-based processing and ease of modification along with exceptional mechanical properties, biocompatibility and slow *in vivo* degradation, makes it an attractive material for regenerative medicine [219,220]. Silks are naturally-derived fibrous proteins produced by spiders, silkworms, bees, moths and scorpions [221,222]. The composition, structure and properties of silk extracted from different species are variable. Silk obtained from

the *Bombyx mori* (domesticated silkworm) has been most extensively studied and used in textile production for more than 4000 years [223]. *B. mor*i silk is composed of two main proteins: sericin (20-30%) and SF (70-80%) with trace amounts of carbohydrates and waxes [224]. Since sericin generally yields an inflammatory response, this protein is typically removed through a process called degumming [225].

To efficiently optimise SF materials and design synthetic polymers that mimic natural silk, the *in vivo* assembly of silk proteins must be understood [190]. *In vivo*, silk exhibits a water-soluble structure composed of random coil, α-helix, and hydrated β-strands. However, after spinning, SF assumes a remarkably stable and insoluble β-sheet crystalline structure stabilised by hydrogen bonds [190]. In the mulberry silkworm, *B. mori*, the silk glands consist of a posterior, middle and anterior division followed by the spinning duct [190]. As liquid SF flows through the secretory pathway, changes in pH, water content and metal ion concentrations are thought to drive the transition from noncrystalline liquid silk to its fibre structure [190]. Foo et al. studied how variations in pH and salt concentrations throughout the silk glands affect the assembly of silk proteins during natural processing [190]. From the posterior to the anterior part of the secretory pathway, the pH decreases from 6.9 to 4.8. At near neutral pH, strong repulsive forces prevent protein-protein interactions due to the prevalence of negative charges [226]. As the acidity increases the hydrophilic spacers (pI = 4.03), L-chain (pI = 5.06) and the N-termini (pI = 4.59) and C-termini (pI = 10.53) of the H-chain become less negatively charged. The charge suppression by acidification allows hydrophobic and hydrophilic interactions to occur and initiates changes in the protein secondary structure [190,226]. Simultaneously, the water content falls from 88 to 70% and the cation concentration increases to neutralise the repulsion forces between the chains. This close packing is fundamental for proper folding and formation of

micellar structures, which will then aggregate and form globular structures before being converted into fibres due to the strain-induced β-sheet formation in the spinneret [190].

The majority of studies published to date concerning the development of SF materials are based on protein self-assembly into β-sheet-rich networks, referred to as physical crosslinking. Many processes have been identified to induce β-sheet transition; decreased pH [222,227,228], high temperatures [229,230], addition of Ca^{2+} ions [222], methanol/ethanol treatments [231–235] and direct electric currents [219,236,237]. Strong shear forces mimicking the natural silkworm spinning process also induce gelation (e.g. sonication [238] and vortexing [239]). However, despite providing strength to the hydrogels through physical cross-linking, these β-sheet structures also result in brittle behaviour as the crystals block long-range molecular displacements [194]. Therefore, despite their high stiffness, these hydrogels lack the adequate elastic properties needed for the repair of many tissues (e.g. skin and cartilage) [218]. Furthermore, the protocols used to prepare physically crosslinked SF materials are incompatible with cell encapsulation due to long gelation times (from 30 minutes to several hours) and unsuitable environmental conditions, limiting the clinical application of these materials [218].

Over the last decade, efforts to develop chemically crosslinked SF hydrogels have been made [194,218]. These materials have completely distinct properties when compared with the physically crosslinked hydrogels previously mentioned. Partlow et al. developed a highly elastic SF hydrogel using horseradish peroxidase (HRP) mediated crosslinking approach [194]. The gelation kinetics of these enzymatically crosslinked hydrogels can be tailored by changing the HRP and oxygen peroxidase content. Yan et al., prepared 16 wt% SF hydrogels with a storage modulus

between several hundred Pa and 5 kPa within 5 - 21 minutes, by changing the oxygen peroxidase concentration between 0.8 and 1.45‰ [218].

Recently, due to the increasing interest in 3D printing technologies, several polymers have been successfully chemically modified to allow photocrosslinking, such as collagen [240], gelatine [209,210,241], hyaluronan [242,243], SF [151], alginate [242], dextran [244], polyvinyl alcohol [210] or PEG [245]. Herein, we developed SilkMA hydrogels that can be prepared within minutes via free radical polymerisation (chemical crosslinking). Notably, cells can be encapsulated within the hydrogels and the physical properties of the hydrogels can be easily tailored by changing the DF%, polymer concentration and the photoinitiator system [151].

Due to the novelty of SilkMA hydrogels, little is known about the role of the prepolymer solution pH in the initial and long-term properties of the gels. Given the importance of pH changes during *in viv*o processing, we hypothesise that it will influence the overall properties of SilkMA gels and could be used to control the secondary structure towards functionality. The pH influence on the initial properties of SilkMA gels was studied in terms of physicochemical properties and cell behaviour. Finally, the spontaneous conformation transitions under physiological conditions and the mechanically toughening impact of β-sheet crystallinity were also addressed. This work highlights the need to rigorously control the pH of silk prepolymer solutions to enhance the reproducible manufacturing process, thereby increasing the potential clinical adoption of silk-based materials for numerous therapeutic applications.

4.2 Methods

4.2.1 Fourier transform infrared spectroscopy

Fourier Transform infrared (FTIR) was used to assess conformational structural changes in SilkMA hydrogels prepared at pH 5, 7 or 8 after different incubation times (0, 7, 14, 21 and 28 days). Freeze-dried samples were analysed using a Nicolet iS5 spectrometer equipped with an iD5 ATR accessory (Thermo Scientific, USA). For each spectrum, 64 scans were acquired in the spectral range of 4000-550 cm^{-1} with a resolution of 4 cm^{-1}. Fourier self-deconvolution (FSD) of the infrared spectra covering the amide I region (1595-1705 cm^{-1}) was conducted using OMNIC software (Thermo Scientific, USA). Deconvolution was automatically performed using the Gaussian/Lorentzian line shape with a noise reduction factor of 0.3. The deconvoluted amide I spectra were area normalised and single band areas were used to calculate the percentage of secondary structures. The peak band assignment was based on the work of Hu et al. [246].

4.2.2 Thioflavin T binding assay

Thioflavin T (ThT) (Sigma Aldrich, USA) was used to qualitatively study the β–sheet content overtime on hydrogels prepared at pH 5, 7 and 8. Briefly, the hydrogels were stained for 10 minutes in a freshly prepared 1% (w/v) ThT solution in PBS. Subsequently, the samples were rinsed with 70% (v/v) ethanol and washed three times with distilled water. A fluorescence intensity scan was performed using a microplate reader (Spark Multimode, Tecan, Switzerland) at 360 nm excitation, measuring the emission spectrum in the 400-700 nm range.

4.2.3 In vitro cytocompatibility of uncured SilkMA solutions

SilkMA prepolymer solutions were UV-sterilised for 20 minutes prior to use. Tissue culture treated 24-well plates (Corning, UK) were initially seeded with HDFs (1 x 10^4 cells/well). After

24 h, DMEM was replaced with fresh supplemented DMEM containing 20% (v/v) prepolymer solution or 20% (v/v) PBS (control group). The monolayer cultures were incubated at 37°C with 5% CO_2 in a humidified incubator and cell viability, metabolic activity and cell proliferation were assessed after 24 and 48 h.

4.2.4 In vitro cytocompatibility of SilkMA hydrogels

SilkMA prepolymer solutions were prepared as previously described and gelatine methacryloyl (GelMA - type A, bloom 300), a well-studied photosensitive polymer was used for comparison purposes. Briefly, 15% (w/v) GelMA prepolymer solution was prepared by dissolving an appropriate amount of polymer in PBS at 37°C for 30 minutes. SilkMA and GelMA prepolymer solutions were sterilised by exposure to germicidal UV light for 20 minutes. Then, filter-sterile LAP was added to the SilkMA and GelMA prepolymer solutions to a final concentration of 0.5% (w/v) and the resulting solutions were mixed. The SilkMA and GelMA hydrogels were photocrosslinked using 3 mW/cm^2 UV-A for 5 minutes in 48-well suspension cell culture plates (Sarstedt, UK). After curing, the hydrogels were washed with sterile PBS (Sigma Aldrich, UK) for 15 minutes and soaked in supplemented DMEM overnight. One hour before cell seeding, the hydrogel matrices were partially dried to potentiate cell penetration. Then, 60 μL of cell suspension was added dropwise onto each hydrogel (9 x 10^3 cells per scaffold) and samples were incubated for 1 h at 37°C with 5% CO_2 to bolster cell adhesion. After 1 h, DMEM was carefully added to the wells without disturbing the cell-laden hydrogels [247]. The culture medium was changed every 2 days. Cell viability and metabolic activity were assessed after 2, 7 and 14 days.

4.3 Results

4.3.1 Physicochemical characterisation of SilkMA gels

^{1}H-NMR spectroscopy was used to confirm the methacrylate-functionalisation of SF (**Figure 4.1**). The appearance of the characteristic resonances of the methacrylate vinyl group (olefinic hydrogen, δ = 6.2 ppm) and methyl group (methyl hydrogen, δ = 1.8 ppm) of GMA confirmed the covalent functionalisation of SF with methacrylate groups, while the absence of the epoxide ring group (aliphatic protons, δ = 2.82 and 2.67 ppm) indicates the complete removal of unreacted GMA through dialysis [151,206]. The decrease in the lysine methylene signal (δ = 3 ppm) indicated that the DF% was 35-40% after a 3 h reaction with 10% (v/v) GMA. In this work, three different 15% (w/v) SilkMA hydrogel formulations were prepared: SF5 (pH 5), SF7 (pH 7) and SF8 (pH 8).

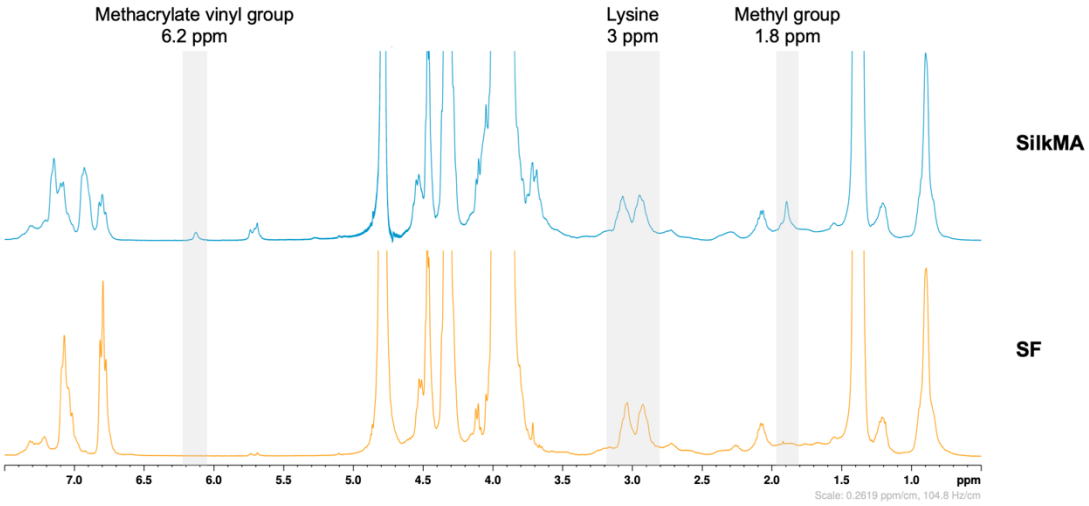


Figure 4.1 *– ^{1}H-NMR spectra of SilkMA (top) and raw SF (bottom). The presence of the methacrylate vinyl group signal (δ = 6.2 ppm) and methyl group signal (δ = 1.8 ppm) after the removal of unreacted GMA by dialysis confirmed the covalent functionalisation of SF with methacrylate groups.*

Transmittance profiles of 15% (w/v) SilkMA hydrogels in the visible light range are shown in **Figure 4.2**a. In general, all SilkMA hydrogels displayed high optical clarity, with transmittance values ranging from 82.1 ± 3.0 to 91.6 ± 0.9% (**Figure 4.2**b,c). The SilkMA hydrogels exhibited enhanced transparency in the visible range with increasing pH, with the SF8 hydrogel eliciting a statistically significant increase in transparency compared to the SF5 hydrogels (10.4 ± 2.3%, $p<0.01$) (Figure 4.2b).

To determine the swelling (SR), water uptake (q) and expansion, SF5, SF7 and SF8 hydrogels were incubated in PBS buffer at 37°C for 24 h. The swelling characteristics were directly proportional to the hydrogel pH; the SR values of SF5, SF7 and SF8 were 39.3 ± 3.7, 80.9 ± 11.9 and 86.2 ± 7.9%, respectively, with SF 7 ($p<0.001$) and SF8 ($p<0.0001$) exhibiting a 2-fold significant increased compared to SF5 (**Figure 4.2**d). As shown in **Figure 4.2**e, the expansion of SilkMA hydrogels in PBS is not statistically significant between groups, despite ranging from 13.0 ± 7.0 to 34.4 ± 13.9% for SF5 and SF8, respectively.

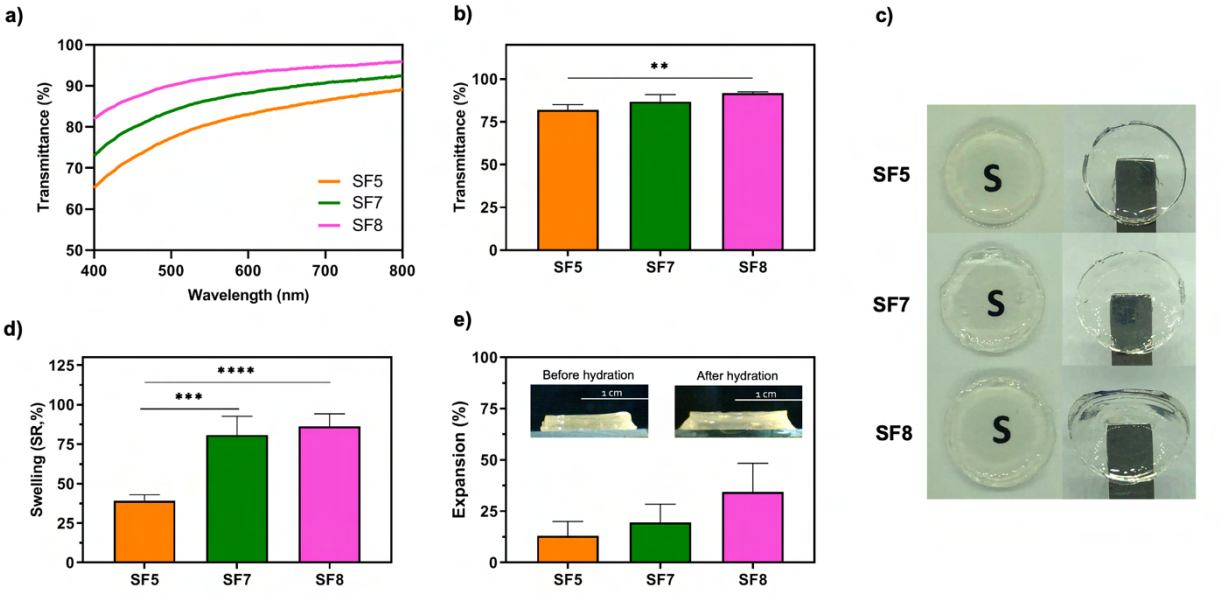


Figure 4.2 *– SilkMA hydrogel transmittance in the visible range: a) transmittance profiles, b) average optical transmittance and c) optical clarity and rigidity of SilkMA hydrogels. (%). Swelling properties of SilkMA hydrogels in PBS at 37°C: d) swelling (%) and e) hydrogel expansion (%). Hydrogel diameter = 12 mm. Data presented as mean value ± SD (*p<0.05, **p<0.01, ***p<0.001, ****p<0.0001).*

The viscoelastic properties of the SilkMA hydrogels were investigated via rheometry. The storage modulus (G') represents the instantaneous, elastic and reversible response of a material to stretching and deformation of chemical bonds, while the loss modulus (G'') represents the time-dependent, viscous response and irreversible rearrangement of the internal polymeric structure of the material [248]. Firstly, the linear viscoelastic range was determined by varying the strain at a constant frequency. Up to 1% strain, all groups were structurally stable with constant values for G' and G'' (data not shown). Then, G' and G'' values of the hydrogels were recorded as a function of frequency (0.01-10 Hz, 0.5% strain) at 37°C. As shown in **Figure 4.3**a, limited changes were observed in the storage modulus G' in the frequency range studied, confirming the high stability of the hydrogels. Moreover, G'' is an order of magnitude lower than G', which is a typical behaviour of viscoelastic materials (**Figure 4.3**c). Importantly, our results indicate that decreasing the pH of the prepolymer solution resulted in significantly stiffer hydrogels;

SF5 hydrogels had a storage modulus significantly greater than SF7 ($p<0.0001$) and SF8 ($p<0.0001$) hydrogels by 3 and 6-fold, respectively (**Figure 4.3**b). The differences in stiffness were noticeable when handling the hydrogels, with SF8 hydrogels being substantially more difficult to handle (**Figure 4.2**c). Finally, the damping factor (tan δ = G''/G') was greater for SF 7 and SF8 but lower than 0.08 for all groups, suggesting that all SilkMA hydrogels behaved as elastomeric materials (**Figure 4.3**d) [151,249].

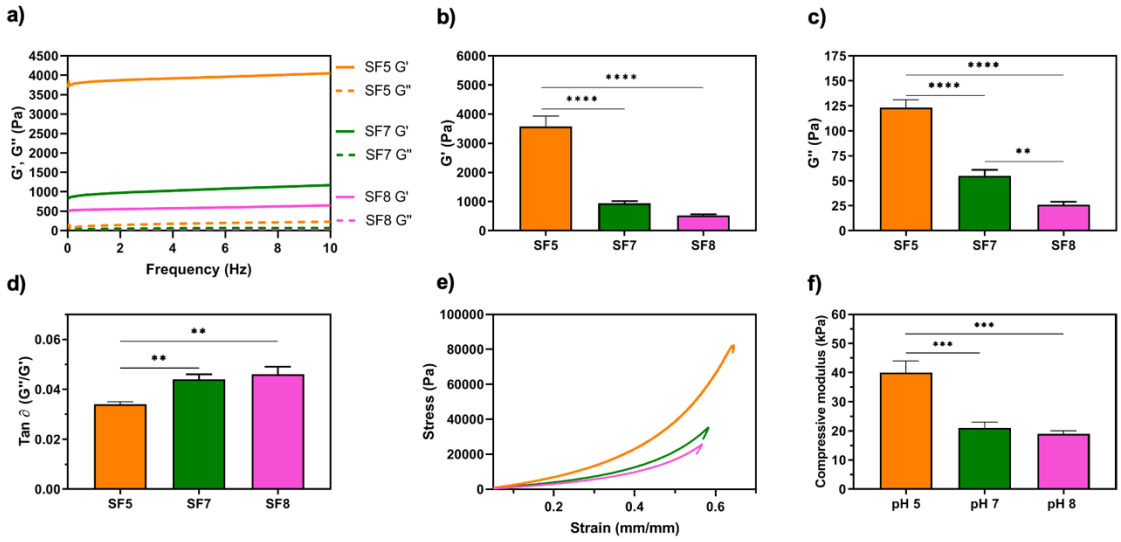


Figure 4.3 *– Rheological properties of SilkMA hydrogels: a) representative frequency sweep, b) storage modulus (G'), c) loss modulus (G'') and d) damping factor (tan δ). Cyclic compressive mechanical testing of SilkMA hydrogels: e) representative compressive strain-stress curves and f) compressive moduli. Data presented as mean value ± SD (*p<0.05, **p<0.01, ***p< 0.001, ****p<0.0001).*

The mechanical properties of SilkMA hydrogels were determined through compression testing. Our results revealed that all groups were mechanically stable for cyclic compressive mechanical testing (**Figure 4.3**e). In agreement with the rheology data, statistical analysis illustrated a significant pH effect on the compressive modulus of SilkMA hydrogels with SF5 hydrogels showcasing a significantly higher compressive modulus than SF7 and SF8 ($p<0.001$).

Specifically, the compressive modulus is 21 ± 2 kPa for SF7 and 40 ± 4 kPa for SF5, a 2-fold increase (**Figure 4.3**f).

4.3.2 Natural conformational changes in SilkMA hydrogels over time

SF materials are reported to suffer spontaneous conformational changes under physiological conditions [218,220,250,251]. To further understand the observed differences in the properties of SilkMA gels, the secondary structure of the hydrogels was studied using FTIR and a ThT binding assay (**Figure 4.4**). As shown in **Figure 4.4**a, the major bands of the protein infrared spectrum can be observed in SilkMA hydrogels: the amide I (1700-1600 cm^{-1}), amide II (1600-1500 cm^{-1}) and amide III (1350-1200 cm^{-1}) [252]. At day 0, the main absorption bands were observed at 1643 cm^{-1} (amide I) and 1525 cm^{-1} (amide II), which are characteristic of the random coil conformation. However, after incubating the hydrogels for 28 days under physiological conditions, these absorption bands shifted to 1629 cm^{-1} (amide I) and 1512 cm^{-1} (amide II), suggesting an increase in the β-sheet content [252]. Importantly, the amide I (1700-1600 cm^{-1}) region is very sensitive to the secondary structure and can be deconvoluted into discreet component bands indicative of tyrosine side chains, random coil, turns, α-helixes and β-sheet structures [253,252]. Deconvoluted amide I spectra were area normalised and the areas of the single bands were used to calculate the relative content of secondary structures, as shown in **Table 4.1**.

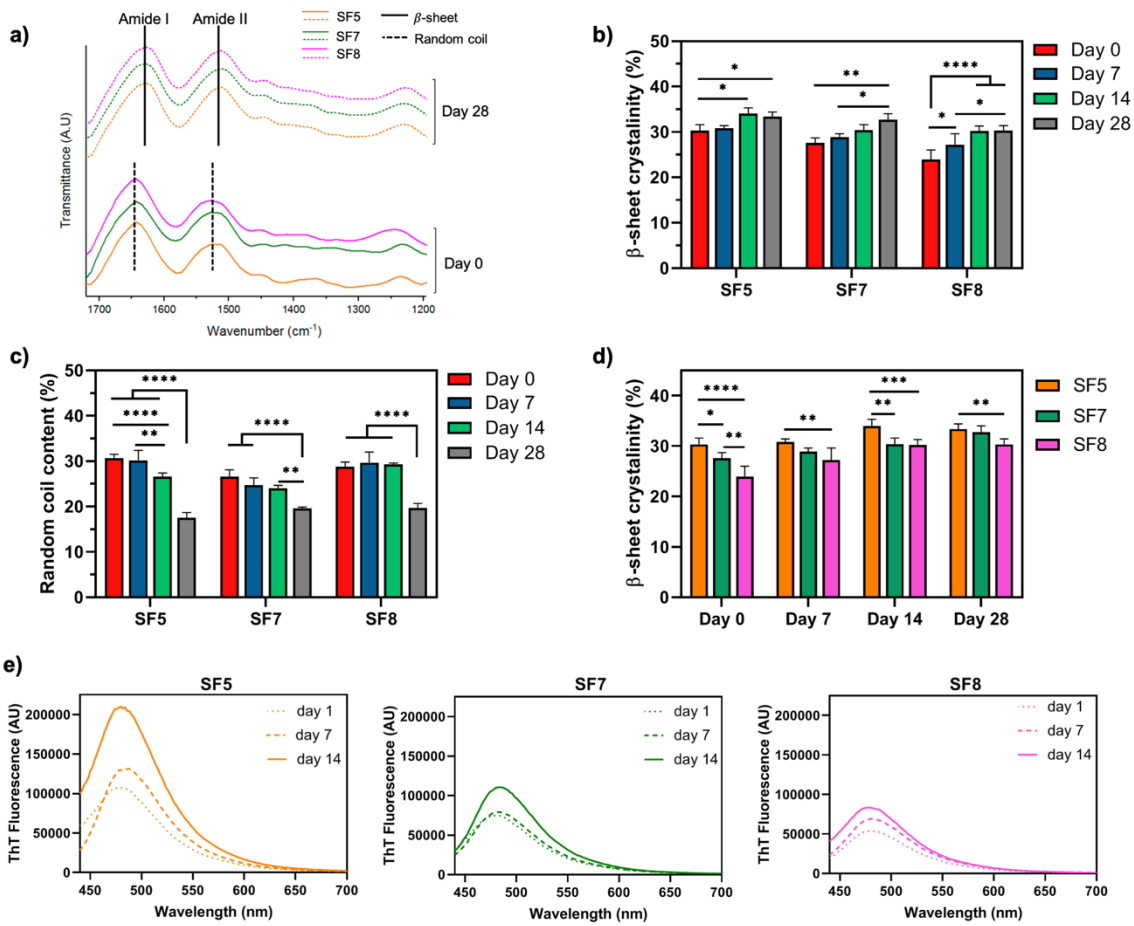


Figure 4.4 *– Study of conformational transitions on SilkMA hydrogels over time: a) FTIR spectra of SilkMA hydrogels after crosslinking (day 0) and 28 days after incubation under physiological conditions, b) β-sheet crystallinity content over time (days 0, 7, 14 and 28), c) random coil content over time (days 0, 7, 14 and 28) and d) comparison of the β-sheet content between groups at different time points (days 0, 7, 14 and 28). e) ThT staining of SilkMA hydrogels at 1, 7, and 14 days. Emission spectrum in the 440-700 nm range under 360 nm excitation. Data presented as mean value ± SD (*p<0.05, **p<0.01, ***p<0.001, ****p<0.0001).*

An increase in the β-sheet content was accompanied by a decrease in the random coil content upon ageing for all groups studied (**Figure 4.4**b,c). Moreover, the β-sheet crystallinity was shown to be inversely proportional to the SilkMA hydrogel pH (**Figure 4.4**d). The β-sheet content was significantly different between the groups at day 0, corresponding to 30.3 ± 1.3%, 27.6 ± 1.1% and 23.9 ± 2.1% for SF5, SF 7 and SF 8, respectively. In contrast, after 28 days of

incubation and although the β-sheet crystallinity in SF5 is greater than those in SF7 and SF8, the difference is only statistically significant for the latter ($p<0.01$).

Table 4.1 *– Relative Content of Secondary Structures in SilkMA Hydrogels Incubated at 37ºC for 0, 7, 14 and 28 Days. Data obtained from deconvolution of the infrared spectra covering the amide I region. Data presented as mean value ± SD (n=4).*

SilkMA sample	Time (days)	Side Chains (%)	Turns (%)	Random coil (%)	α-helices (%)	β-sheet (%)
SF5	0	5 ± 0.4	23.6 ± 0.8	30.7 ± 0.8	10.5 ± 0.3	30.3 ± 1.3
	7	12.3 ± 3.3	16.2 ± 0.5	30.2 ± 2.2	10.5 ± 4.0	30.8 ± 0.6
	14	12.6 ± 0.8	18.8 ± 0.4	26.6 ± 0.8	8.0 ± 1.5	34.0 ± 1.3
	28	19.9 ± 2.1	22.5 ± 1.4	17.5 ± 1.2	6.8 ± 0.3	33.4 ± 1.0
SF7	0	14.6 ± 1.2	21.1 ± 0.4	26.6 ± 1.5	10.2 ± 0.4	27.6 ± 1.1
	7	16.0 ± 1.8	21.1 ± 0.9	24.7 ± 1.6	9.3 ± 0.4	28.9 ± 0.7
	14	15.6 ± 0.5	20.4 ± 1.9	24.0 ± 0.7	9.5 ± 0.5	30.4 ± 1.2
	28	24.5 ± 1.2	16.1 ± 0.6	19.6 ± 0.3	7.1 ± 0.6	32.7 ± 1.3
SF8	0	14.7 ± 1.4	22.5 ± 1.4	28.8 ± 1.0	10.1 ± 0.3	23.9 ± 2.1
	7	12.5 ± 4.2	19.1 ± 3.5	29.7 ± 2.3	11.5 ± 1.0	27.2 ± 2.4
	14	14.1 ± 0.4	15.6 ± 1.7	29.3 ± 0.3	10.8 ± 0.7	30.2 ± 1.1
	28	27.7 ± 1.7	15.4 ± 2.5	19.7 ± 1.0	7.0 ± 0.1	30.3 ± 1.1

ThT is a powerful fluorescent marker to identify β-aggregates, such as β-amyloid and β-sheet [254,255]. Herein, this staining approach was used to qualitatively confirm time-dependent conformational changes assessed by FTIR. Since the intensity is proportional to the sample mass, the hydrogels were prepared with the same volume of prepolymer solution. However, different degradation profiles might have interfered with the intensities obtained at days 7 and 14. The emission spectra of SilkMA hydrogels at days 1, 7 and 14 can be observed in **Figure 4.4**e. Our results show that the fluorescence intensity increased with time for all groups studied. Moreover, the fluorescence intensity is inversely proportional to the hydrogel pH, in agreement

with the FTIR deconvolution data. When comparing the results at day 1, the maximum ThT fluorescence for SF5 (107000 AU) was higher than those for SF7 (75000 AU) and SF8 (54000 AU) hydrogels. Similarly, after 14 days, the SF5 maximum intensity (210000 AU) was 2 and 2.2-fold higher than SF7 (110000 AU) and SF8 (94000 AU).

To further analyse the effect of the spontaneous conformational transitions on the physical and mechanical properties of SilkMA hydrogels, the optical transmittance and compressive modulus were determined at different incubation time points (**Figure 4.5**). The obtained results show that the optical transparency of SilkMA hydrogels is directly proportional to the prepolymer solution pH and decreases over time, as the hydrogel crystallinity increases. As previously mentioned, the transmittance of SilkMA hydrogels at day 0 was between 82.1 ± 3.0 and 91.6 ± 0.9%, for SF5 and SF8 hydrogels ($p<0.01$), respectively (**Figure 4.5**a). Despite this 9.5% difference, all samples were initially transparent to the naked eye (**Figure 4.5**b). After 7 days, SF5 hydrogels had the highest decrease in transparency (12.1%) to 71.8 ± 2.3%, while SF8 hydrogels exhibited a reduction of 0.9% to 89.9 ± 1.4%, with the SF5 group displaying a significant reduction in transparency when compared to the SF7 ($p<0.001$) and SF8 ($p<0.0001$) gels. At day 14, the optical properties of SF5 and SF7 hydrogels were not statistically different, however, SF8 hydrogels had a transmittance of 85.1 ± 4.9%, which is higher than the transmittance of SF5 hydrogels at day 0 (83.9 ± 3.7%). After 28 days of incubation, the optical transmittance of all SilkMA groups decreased to values of approximately 50% (Figure 4.5a and b). Finally, the mechanical toughening impact of the increasing β-sheet content on the hydrogels was studied by cyclic compressive testing. The hydrogel stiffness consistently increased over time driven by the higher β-sheet crystallinity. The compressive modulus rose by 2 orders of magnitude for SF5 (from 40 kPa to 1.1 MPa) and 1 order of magnitude for SF7 (from 21 to 870 kPa) and SF8 (from 19 to 631 kPa) within 14 days (Figure 4.5c). The difference

between day 0 and day 7 was not statistically significant for SF7 and SF8 samples, however, at day 7, SF5 showed a compressive modulus 25 and 81-fold superior to SF7 ($p<0.001$) and SF8 ($p<0.0001$), respectively (Figure 4.5d). After 14 days, the compressive modulus ranged from 631 kPa to 1.1 MPa, being statistically different between all groups (Figure 4.5e).

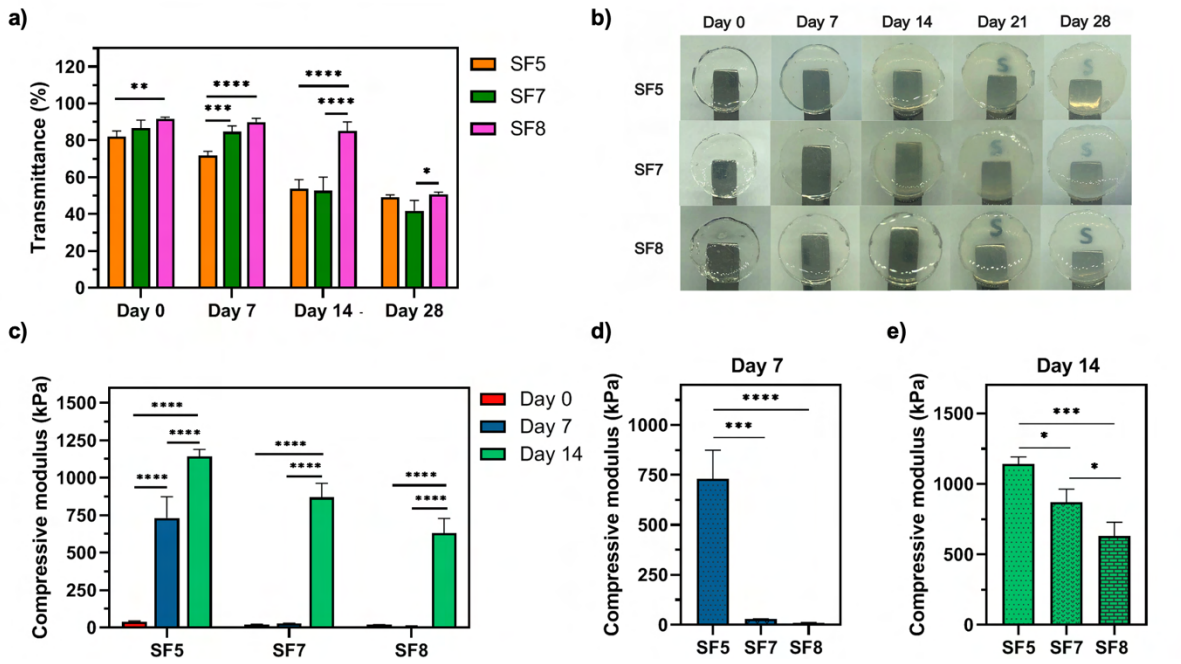


Figure 4.5 *– Study of the natural conformational changes in SilkMA hydrogels incubated in PBS at 37°C. a) Average optical transmittance in the visible range of SilkMA hydrogels at 0, 7, 14, and 28 days. b) Appearance of SilkMA hydrogels after incubation for 0, 7, 14, 21 and 28 days (hydrogel diameter = 1 cm). c) Mechanical toughening impact of the increasing β-sheet content on SilkMA hydrogels. d) Compression moduli of SilkMA hydrogels after incubating for 7 days. e) Compression moduli of SilkMA hydrogels after incubating for 14 days. Data presented as mean value ± standard deviation (*p<0.05, **p<0.01, ***p<0.001, ****p<0.0001).*

4.3.3 In vitro assessment of cytocompatibility

The cytotoxicity of uncrosslinked SilkMA prepolymer solutions was studied by using HDF cells seeded on tissue culture well-plates and compared with cells cultured in complete media. Fluorescence staining (**Figure 4.6**a) indicates high cell viability (>90%) for all tested

conditions, suggesting that SilkMA prepolymer solutions did not induce cytotoxicity. Variations in the cell metabolism and proliferation were not statistically different between SilkMA samples throughout the experiment, with a time-dependant increase observed in both groups. However, the controls showed a higher metabolic activity than SF5 ($p<0.0001$) and SF7 ($p<0.0001$) (**Figure 4.6**b). DNA content results were in agreement with the metabolic activity, with controls showing higher DNA concentration compared to SF5 ($p<0.01$) and SF7 ($p<0.001$) 48 h post seeding (**Figure 4.6**c).

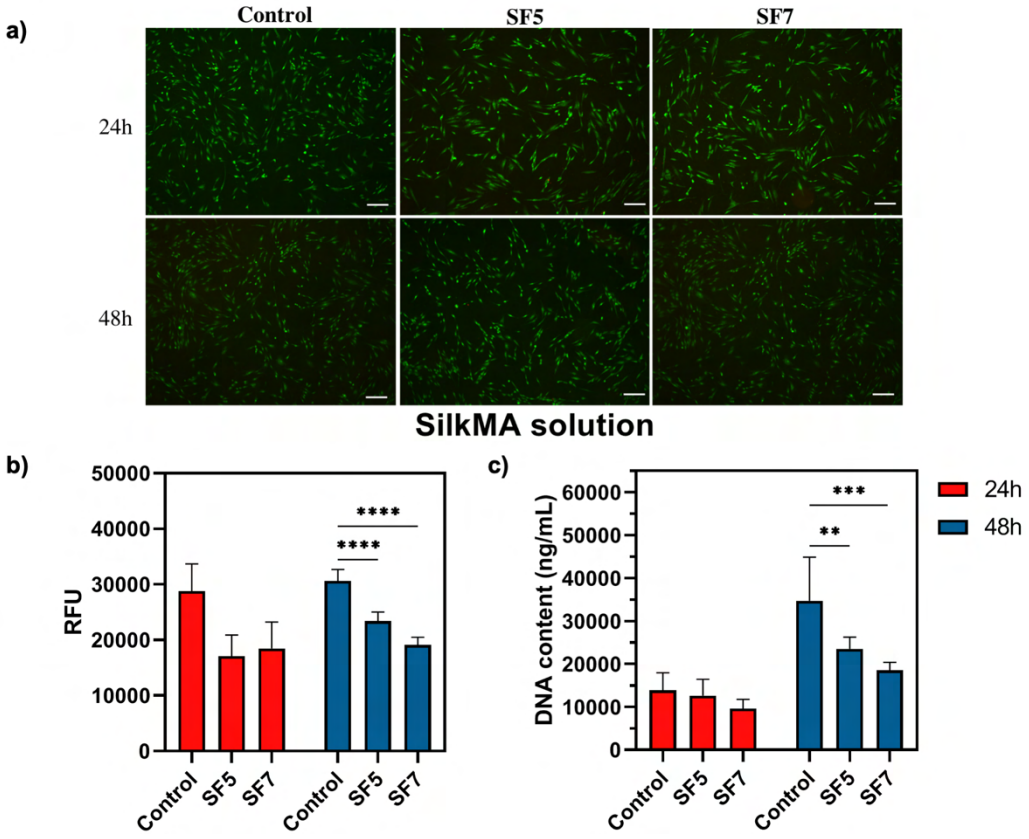


Figure 4.6 *– Cytotoxicity of uncrosslinked SilkMA prepolymer solutions. a) Live/dead images of HDFs seeded on tissue culture well-plates with media (control) and media supplemented with SF5 and SF7 prepolymer solutions. Scale bar = 200 μm. b) Quantification of the metabolic activity by the alamarBlue assay 24 and 48 h after cell seeding. c) Quantification of cell proliferation by the Picogreen DNA assay 24 and 48 h after cell seeding. Data presented as mean value ± SD (*p<0.05, **p<0.01, ***p< 0.001, ****p<0.0001).*

The ability of SilkMA hydrogels to support cell attachment and proliferation was evaluated by the direct seeding of HDF cells on SF5 and SF7 hydrogels and compared with GelMA, an extensively studied hydrogel for 3D cells culture applications [256]. Cell viability, metabolic activity and proliferation were assessed 2, 7 and 14 days post seeding. As shown in **Figure 4.7**a, live/dead staining showed that SilkMA hydrogels can support cell attachment and proliferation for up to 14 days. Two days after seeding, most cells deposited on SilkMA hydrogels exhibited a rounded morphology with limited spreading, whereas cells on GelMA hydrogels actively spread, showing a spindle-shaped morphology characteristic of HDFs. This effect is in line with the available literature as previous reports indicate that SF from *B. mori* has limited initial cellular response as a result of limited adhesive amino acid sequences (e.g. RGD) on its composition [249,257]. However, 7 days post-seeding the cells exhibited a typical fibroblastic morphology and proliferated to reach confluence on the SilkMA gels, similar to that observed on GelMA hydrogels. After 14 days, some dead cells can be observed in all groups due to over confluency. This limited initial interaction for the SilkMA hydrogels is further observed in the metabolic activity measurements which is likely to be influenced by cell adhesion. Cell metabolism was significantly ($p<0.0001$) higher on GelMA hydrogels at each time point (**Figure 4.7**b). However, despite both SilkMA groups showing a significantly lower metabolic activity than GelMA at day 7, specifically 46% (SF5, $p<0.0001$) and 39% (SF7, $p<0.0001$), this difference decreases to approximately 19% for both groups ($p<0.0001$) after 14 days (**Figure 4.7**b). The metabolic activity of cells seeded on SF5 and SF7 was not statistically different at each time point assessed, with a time-dependant increase in the metabolic activity observed in both groups.

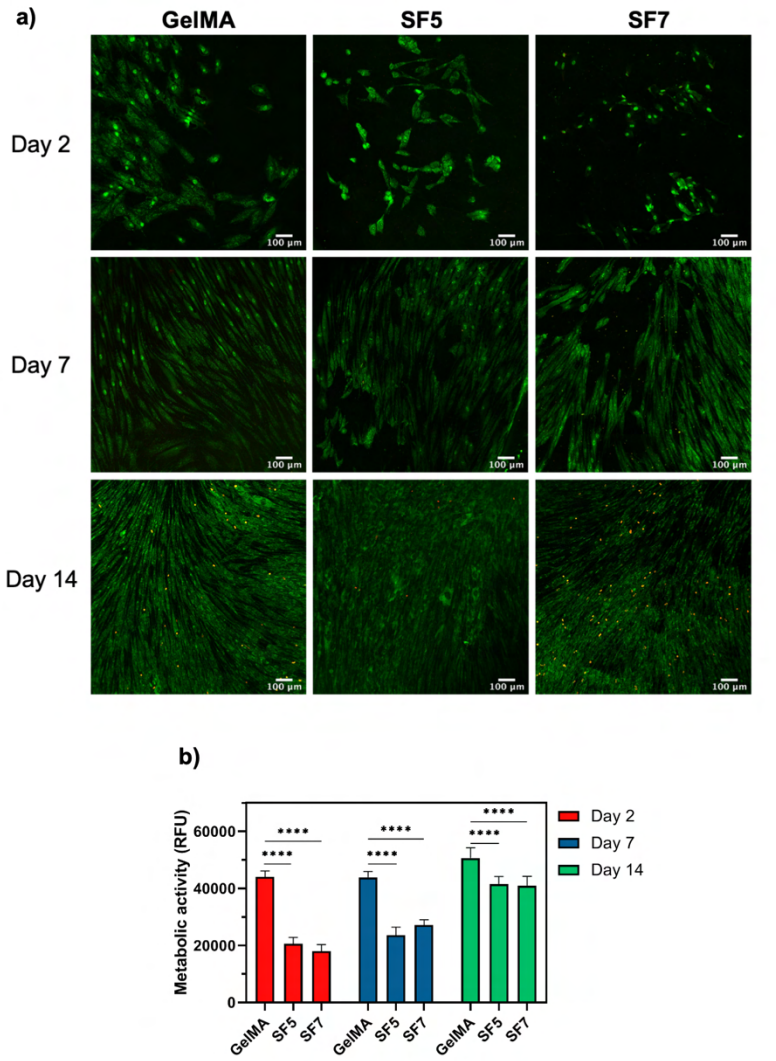


Figure 4.7 *– Cytotoxicity of SilkMA prepolymer hydrogels: a) live/dead images of HDFs seeded on GelMA, SF5 and SF7 hydrogels. b) Quantification of the metabolic activity by the alamarBlue assay 2, 7 and 14 days after cell seeding. Data presented as mean value ± SD (*p<0.05, **p<0.01, ***p<0.001, ****p<0.0001).*

4.4 Discussion

Over the last decade efforts to develop chemically crosslinked SF hydrogels have been made [194,218]. Herein, we developed a glycidyl-methacrylate-modified SF solution that can be chemically crosslinked within a few minutes using light. Cells can be encapsulated within the hydrogels by gentle mixing with the prepolymer solution before crosslinking. Several natural and synthetic polymers such as gelatine, collagen or hyaluronic acid have been previously

methacrylated [258–260]. Vinyl-containing monomers, such as GMA and MA are commonly used to methacrylate proteins. After dialysis, the purified methacrylated-protein solution has a pH between 4.5 and 5.5, in contrast with the neutral pH of pure silk solutions. Considering the role of pH in the molecular aggregation of SF proteins *in vivo,* we hypothesise that the pH of the prepolymer solution will play a determinant role in the short and long-term properties of SilkMA hydrogels, being essential to control the function and ensure reproducible manufacturing.

To study the impact of the prepolymer solution pH on the properties of SilkMA gels, three different formulations were prepared: SF5, SF7 and SF8. In general, all SilkMA hydrogels presented high transparency and elasticity and were easy to handle (**Figure 4.2**c). Despite perceptible differences in rigidity, all SilkMA gels behaved as viscoelastic solids, as demonstrated by the higher G' for all groups studied (**Figure 4.3**a). When freshly prepared hydrogels were studied, we found that SF5 hydrogels exhibited a significantly greater storage and compressive modulus than SF7 and SF8 hydrogels (**Figure 4.3**b and f).

To further understand the observed differences in the properties of SilkMA gels, the secondary structure of the gels was investigated using FTIR. Since the amide I region of the spectra is very sensitive to the secondary structure, it can be deconvoluted using a FSD algorithm to determine the relative contribution of each structure fraction [252,253]. As shown in **Table 4.1**, our results show a time-dependent reduction in the random coil content, accompanied by a β-sheet content rise for all groups. The conformational changes assessed by FTIR were qualitatively confirmed using ThT staining, a fluorescent marker that binds β-sheet structures (**Figure 4.4**e). Time-

dependent conformational transitions are expected in silk-based materials and have been previously reported by other authors [218,220,251,261,262].

As described by Burke et al., the hydrogen bonding between adjacent β-sheets (physical crosslinking) is responsible for the aqueous insolubility and remarkable mechanical properties of SF [263]. In this work, the mechanical toughening impact of the β-sheet crystallinity was studied by compressive mechanical testing. As shown in **Figure 4.5**c, the hydrogel stiffness consistently increased over time for all studied groups, in agreement with the FTIR data. Remarkably, the compressive modulus of SF5 hydrogels, increased by 2 orders of magnitude in 14 days, while SF7 and SF8 gels increased by an order of magnitude. Typically, one of the strategies used to enhance the mechanical strength of gels is by increasing the polymer concentration, however, it may negatively impact cell viability and proliferation within the scaffold as reported in the literature [264], [265]. Herein, we demonstrated that by adjusting the pH of the prepolymer solution, SilkMA hydrogel stiffness can be tailored without changing the polymer concentration or the molecular weight. Despite improving the compressive modulus, which might be advantageous for certain applications, the increase in crystallinity has a negative impact on elasticity. As shown in **Figure 4.2**b and c, both the optical transparency and the swelling characteristics were shown to be significantly lower for SF5 gels.

Swelling properties are critical for tissue engineering applications since a material's water content influences the transport of oxygen, nutrients and metabolites, as well as the viability and proliferation of cells [58]. As shown in **Figure 4.2**d, SF5 has enhanced structural stability against swelling, with a significantly lower SR than SF 7 and SF8 ($p<0.001$ and $p<0.0001$, respectively). A decrease in the network swellability is expected with an increase in the

hydrophobic β-sheet content [266]. On day 0, the β-sheet content was shown to be significantly different between samples, with SF5 having on average 2.7% and 6.4% higher crystallinity than SF7 and SF8, respectively (**Table 4.1**, **Figure 4.4**d). Moreover, swelling can have an impact on the overall shape of a material, which must be retained *in vivo* [151]. These materials should have a minimal volume change thereby reducing the risk of implant mismatch and imparting additional stress on the surrounding tissues [184]. Thus, the dimensional stability of *in situ* crosslinked hydrogels is of critical importance. All experimental groups retained their shape and were easily handled in the swollen state. Although hydrogel expansion was not statistically significant between experimental groups, the volume increase seems to be proportional to the hydrogel pH, in agreement with the swelling characteristics (**Figure 4.2**f).

One of the outstanding properties of SF hydrogels is the high optical transparency in the visible range. This property is of utmost importance for many applications in tissue engineering, such as long-term corneal substitutes and ocular adhesives [247,267,268]. In this work, we have quantified hydrogel transparency over time for the different studied groups. As shown in Figure 4.5a**,** the transparency of SF hydrogels progressively decreased after curing. Remarkably, SF8 remained optically clear after 14 days of incubation (transmittance > 85%) while SF5 and SF7 gels became opaque, transmittance ≈ 53% (Figure 4.5b). It has been previously reported that SF-based hydrogels become increasingly opaque over time, as the main protein conformation changes from random coil to the β-sheet crystalline form [218,251,255]. It is important to note that crystallinity is not the only factor determining the transparency of hydrogels since amorphous materials can still be opaque [255]. Since all SilkMA hydrogels were prepared at the same concentration, the ratio of polymeric network/water phase is the same. However, as shown in **Figure 4.2**d, the swelling characteristics are statistically different between the samples. The

higher water content in SF7 and SF8 hydrogels might also play a role in the increased optical clarity.

Due to the short photocrosslinking times and mild environmental conditions, SilkMA hydrogels can be used to deliver cells. However, SF is reported to lack cell binding sequences necessary for cellular adhesion and proliferation [249,257]. In this study, the cytocompatibility of uncrosslinked SilkMA prepolymer solutions and SilkMA hydrogels was assessed *in vitro*. As shown in **Figure 4.6**, SilkMA prepolymer solutions did not induce cytotoxicity despite the significantly lower metabolic activity and proliferation in comparison with the control. HDF adhesion to SF5 and SF7 hydrogels was compared with GelMA, a material which provides cells with an optimal biological environment such as adhesion sequences [256]. As shown in Figure 4.7a, SilkMA hydrogels exhibited low toxicity although the hydrogels showed a delayed attachment and lower metabolic activity relative to the control. Despite the previously mentioned differences in stiffness and hydrophilicity, the metabolic activity of HDFs on SF5 and SF7 gels was not statistically significant. In summary, the pH of the gels did not affect cytocompatibility. Importantly, our findings showed that the seeded HDFs were able to spread and proliferate on the SilkMA hydrogels, similar to the observations on the GelMA control. The cytocompatibility of SilkMA hydrogels confirmed that SF is a promising material for tissue engineering. In the future, it would be interesting to evaluate the impact of pH-induced scaffold properties on the behaviour of cells more sensitive to environmental stimuli (e.g. stem cells). This would provide a greater understanding of the effects of pH control on the mechanotransductive properties of the SilkMA hydrogels.

4.5 Conclusions

The present work studies the effect of the prepolymer solution pH on the initial and long-term properties of SilkMA hydrogels. We have demonstrated that, 1) the pH of the prepolymer solution can be effectively used to control the SilkMA conformational structure development towards utility and function, and 2) strict pH control is necessary to ensure reproducibility as physical crosslinking influences the hydrogel properties independently of the parameters controlling the chemical crosslinking reaction (e.g. DF%, polymer/photoinitiator concentration, and so forth). Furthermore, we developed injectable, highly elastic and transparent SilkMA hydrogels that can be photocrosslinked within minutes. These gels are suitable for cell encapsulation and displayed adequate physicochemical properties for tissue engineering applications. In the future, we believe SilkMA has the potential to be applied in the design of bioinks and bioresins. The next chapter reports the development a gentamicin-loaded SilkMA hydrogel for corneal regeneration.

CHAPTER FIVE

5 Photocurable antimicrobial silk-based hydrogels for corneal repair

Data in this chapter is also presented in the published article found in Appendix B:

Inês A. Barroso, Kenny Man, Thomas J. Hall, Thomas E. Robinson, Sophie E.T. Louth, Sophie C. Cox, and Anita K. Ghag. "*Photocurable antimicrobial silk-based hydrogels for corneal repair*", Journal of Biomedical Materials Research Part A, 1-15. DOI:10.1002/jbm. a.37381 (2022)

Corneal transplantation is the current gold standard treatment to restore visual acuity to patients with severe corneal diseases and injuries. Due to severe donor tissue shortage, efforts to develop a corneal equivalent have been made but the challenge remains unmet. Another issue of concern in ocular surgery is the difficult instillation and fast drainage of antibiotic ocular eye drops as bacterial infections can jeopardize implant success by delaying or impairing tissue healing. In this study, we developed antimicrobial silk-based hydrogels that have the potential to be photoactivated *in situ*, fully adapting to the corneal injury shape. Gentamicin-loaded SilkMA hydrogels were prepared within minutes using low UV intensity (3 mW/cm^2). SilkMA gels provided a young's modulus between 21 - 79 kPa together with a light transmittance spectrum and water content (83 - 90%) similar to the human cornea. Polymer concentration (15-25%) was found to offer a tool for tailoring the physical properties of the hydrogels. We confirmed that the methacrylation did not affect the material's *in vitro* degradation and biocompatibility by observing fibroblast adhesion and proliferation. Importantly, agar diffusion tests showed that the synthesized hydrogels were able to inhibit *Staphylococcus aureus* and *Pseudomonas aeruginosa* growth for 72 h. These characteristics along with their injectability and viscoelasticity demonstrate the potential of SilkMA hydrogels to be applied in several soft tissue engineering fields. As such, for the first time we demonstrate the potential of photocurable antimicrobial SilkMA hydrogels as a novel biomaterial to facilitate corneal regeneration.

5.1 Introduction

The cornea is a transparent avascular tissue located in the outermost surface of the eye. It is responsible for the protection of the inner ocular structures against trauma and infections, whilst playing a pivotal role in light transmission and focusing (80% of the eye refractive power) [58,152,269]. Corneal diseases and injuries can lead to corneal thinning and opacification, eventually leading to blindness. Currently, corneal blindness is estimated to affect 23 million people worldwide, with less than 1.5% of patients benefiting from a corneal transplant due to severe tissue shortage [269,270]. Although imposing risks of donor driven infection and rejection, corneal transplantation is still the gold standard treatment to restore visual acuity to patients [153,267,269]. Fully synthetic prostheses KPro (keratoprosthese) are currently the only non-allogenic treatment approved for human use [34]. Although innovations in prosthesis design and postoperative management has improved treatment outcomes [271], this procedure is associated with serious complications, such as glaucoma, retinal detachment and infections, whilst also requiring a high level of skill from the practitioner [272]. Due to the limitations of current clinical strategies, there has been extensive research focused on the use of polymeric biomaterials to replace damaged corneal tissue [269,270]. The use of injectable polymeric biomaterials such as hydrogels are favourable as they can either be administered directly to the corneal injury and crosslinked *in situ* using different methods [206,269,270,273–275] or 3D printed into complex and anatomically relevant geometries [153,267,268,276]. Upon implantation the long-term corneal substitute should act as a functional cornea nurturing tissue ingrowth and regeneration with low inflammatory host response. The engineered material should also be fully biodegradable, eliminating the need for further surgeries [277]. Challenges associated with bioengineered corneal substitutes include high optical transparency, sufficient cohesive strength to withstand the intraocular pressure (IOP) and eye movements, permeability to metabolites and ability to prevent infections while sustaining epithelial and stromal cell-ingrowth.

Recently, efforts to develop stromal fillers and corneal substitutes have been made [206,269,270,278]. Fernandes-Cunha et al. developed collagen hydrogels crosslinked via multi-arm-PEG-N-hydroxysuccinimide. The gels were crosslinked within 5-10 min without the use of catalysts and its physical properties were modulated as function of the PEG concentration and number of arms. *In vivo* studies demonstrated that the hydrogels could be formed *in situ* without the use of sutures and were proven to support multi-layered re-epithelisation [270]. Chen et al. used strain-promoted azide-alkyne cycloaddition to crosslink hyaluronate-collagen hydrogels under ambient conditions without the need for external initiators. The material showed a transmittance over 95% in the visible range. Hydrogels were crosslinked *in situ* without the need of sutures and remained clear on the rabbit corneal defect for 7 days supporting re-epithelisation [269]. However, although these strategies do not require any external triggers or catalysts, they might not be suitable for applications that require fast crosslinking (30-120 s) or cell-encapsulation given the chemistry used.

Light-mediated hydrogel gelation has immense potential for regenerative medicine as cell-laden hydrogels can be crosslinked within minutes in mild environmental conditions. Importantly, photo-curable hydrogels provide the clinician with increased flexibility in controlling *in situ* gelation when compared to other methods [269,270]. These photosensitive polymers have the potential to be applied as stromal fillers (*in situ* crosslinking) [58,126,152,206,274] or used to develop a patient-specific artificial cornea using 3D printing technologies such as lithography and extrusion-based bioprinting [151,153,268,279,280]. Sani et al. developed a highly biocompatible and transparent GelMA-based filler for corneal reconstruction. The hydrogels were photocured within minutes using visible light (100 mW/cm^2) and a photoinitiator solution composed of Eosin Y (photoinitiator), TEA (co-initiator) and VC (co-monomer). *In vivo* studies

performed using a rabbit stromal defect model demonstrated the sealing efficacy of the material while allowing re-epithelisation and stromal regeneration [126].

SF-based biomaterials have been extensively studied for numerous tissue engineering applications due to its amenability to modification, outstanding transparency, mechanical strength and biodegradability, making it an attractive material for corneal regenerative applications [219,220]. In particular, SF membranes have been widely explored for corneal and retinal reconstruction due to their permeability and high transparency (90.6%) [281–283]. However, most studies concerning SF hydrogels are based on the protein self-assembly into β-sheet-rich networks [284]. Despite providing strength to the hydrogels through physical crosslinking, these β-sheet structures decrease the optical clarity and elasticity of the gels since the crystals block long-range molecular displacements. Furthermore, the clinical application of these materials is limited due to the long gelation times and harsh environmental conditions used to induce β-sheet formation (e.g. low pH, vortexing or methanol treatments) [284]. Thus, chemically modifying SF via the addition of methacrylate side groups allows for the covalent crosslinking of SF hydrogels via photocrosslinking. This provides increased mechanical strength but also allows for greater control of the *in-situ* crosslinking kinetics. Finally, SilkMA prepolymer solutions are injectable and liquid at room temperature which makes solution handling easier than gelatine or GelMA. Thus, there is tremendous potential of harnessing photocurable SF-based hydrogels for corneal regeneration.

Bacterial infections can cause corneal scarring and prolong or impair the wound healing process [285,286]. Therefore, the application of antibiotic eye drops and ointments is standard procedure post-surgery. However, its efficacy is limited due to fast ocular drainage and difficulties in

instillation [154]. The hydrophilic nature of SF provides a solubilising environment for antibiotics, anti-inflammatory agents and growth factors, ultimately increasing the functionality of the medical device [287].

In this study, we investigated the development of a photocurable antimicrobial SF hydrogel for corneal regeneration. SF was modified by methacrylation to yield a photosensitive solution that can be chemically crosslinked using UV light. This Chapter aims to:

- Test the ability of SilkMA hydrogels to be photocured within minutes using low UV-intensity;
- Study the physical and mechanical properties of SilkMA hydrogels and compare them with the native human cornea;
- Assess the biocompatibility and biodegradability of the material;
- Test the antimicrobial activity of SilkMA hydrogels loaded with gentamicin against *Staphylococcus aureus* and *Pseudomonas aeruginosa*.

As shown in **Figure 5.1**, the physical, mechanical and biological properties of SilkMA hydrogels, including water content, rheology, porosity, compressive modulus, degradation and *in vitro* biocompatibility were studied. Finally, the drug release profile and antimicrobial properties of gentamicin-loaded SilkMA were assessed. The development of a semi-synthetic silk-based hydrogel has potential to be applied in ocular surface reconstruction due to its viscoelasticity, cytocompatibility and antimicrobial properties.

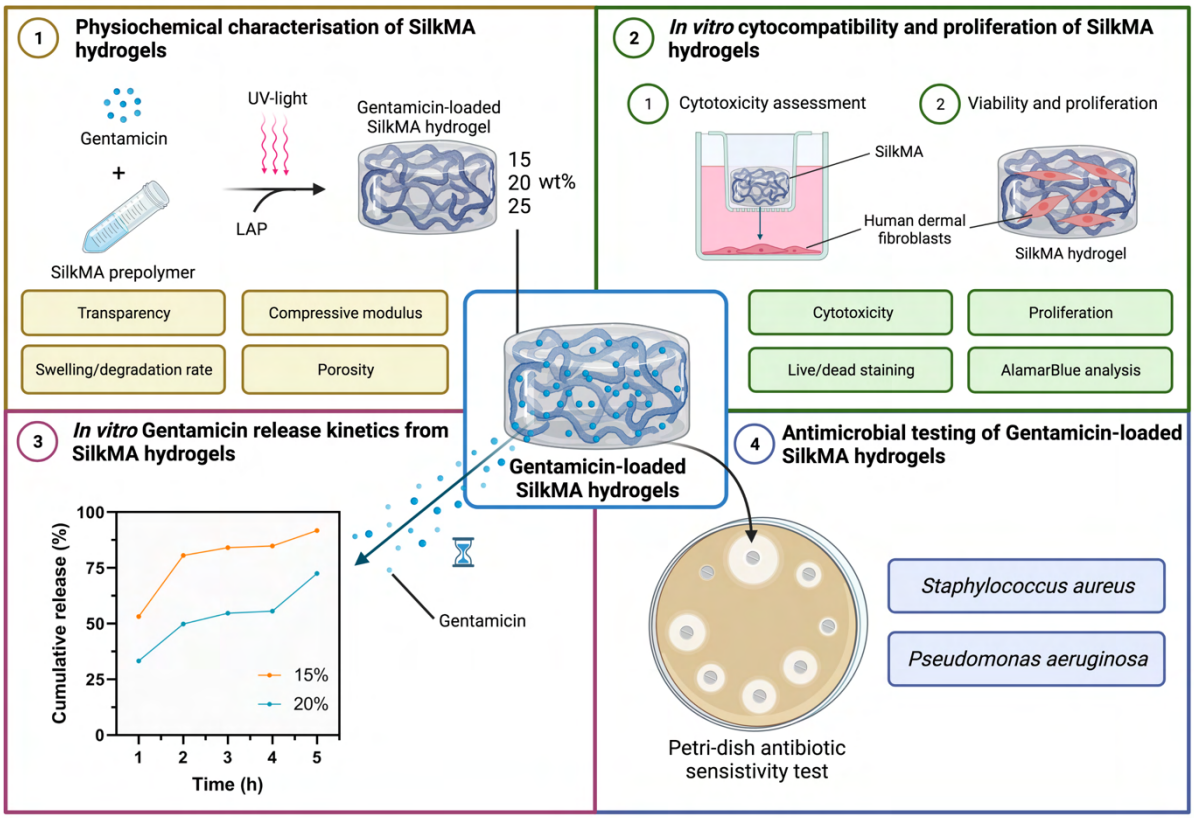


Figure 5.1 *– Experimental outline investigating the properties of gentamicin-loaded SilkMA hydrogels. 1) Photocrosslinking of 15, 20 and 25% gentamicin-loaded SilkMA hydrogels. The transparency in the visible range, swelling, in vitro degradation, porosity/pore size, compressive young's modulus, and rheological properties of the SilkMA hydrogels were studied. 2) In vitro cytocompatibility of gentamicin-loaded SilkMA hydrogels. Firstly, the cytocompatibility of SF and SilkMA prepolymer solutions and SilkMA hydrogels was assessed. Then, the ability of HDF cells to attach and proliferate on SilkMA hydrogels was studied and compared with GelMA hydrogels. 3) In vitro gentamicin drug release from SilkMA hydrogels. The cumulative drug release of gentamicin from SilkMA hydrogels and gentamicin concentration in the media were calculated. 4) Antimicrobial testing of gentamicin-SilkMA hydrogels. The antimicrobial activity of SilkMA hydrogels against two of the most common causes of ocular infections, Staphylococcus aureus and Pseudomonas aeruginosa was assessed in vitro.*

5.2 Methods

5.2.1 Preparation of gentamicin-loaded SilkMA gels

In this work, three different formulations were tested: 15, 20 and 25% (w/v) SilkMA gels loaded with 0.2% (w/v) gentamicin sulphate (G-Biosciences, USA). Briefly, 15, 20 and 25% SilkMA

solutions were prepared by dissolving an appropriate amount of SilkMA in PBS (pH 7.4, Sigma-Aldrich, UK) at room temperature overnight. The resulting viscous solutions were filtrated using Miracloth (Merck Millipore, USA). A fresh stock solution of 2% (w/v) LAP (Sigma-Aldrich, UK) in PBS was prepared. The photoinitiator was added to the SilkMA solution to a final concentration of 0.5% (w/v) and the resulting solution was mixed at room temperature. The hydrogel precursor solutions were photocured through UV-light using an OmniCure S1500 (Lumen Dynamics, Ontario, Canada) with a 365 nm filter. Briefly, 200 μL of SilkMA prepolymer solution was pipetted onto a 12 mm cylindrical mould and then exposed to 3 mW/cm^2 of UV-A for 5 minutes.

5.2.2 Cell viability

15% SF and SilkMA pre-polymer solutions and SilkMA hydrogels were UV-sterilised for 20 minutes prior to use. Tissue culture treated 24-well plates (Corning, UK) were initially seeded with HDFs (1 x 10^4 cells/well). After 24 h, 100 μL of each sample was added to 24 well ThinCert cell culture inserts (Greiner Bio-One, UK) with 0.4 μm pore size. The monolayer cultures were incubated at 37°C with 5% CO_2 in a humidified incubator. Cell viability was evaluated as described in Section 3.4.1.

5.2.3 2D cell seeding on SilkMA gels

15% SilkMA pre-polymer solutions were prepared as previously described and GelMA was used as the control. Briefly, 15% (w/v) GelMA pre-polymer solution was prepared by dissolving an appropriate amount of polymer in PBS at 37°C for 30 minutes. Then, LAP was added to the GelMA solution to a final concentration of 0.5% (w/v) and the resulting solution was mixed at 37°C. SilkMA and GelMA pre-polymer solutions were UV-sterilised and

photocrosslinked as described above in 48-well suspension cell culture plates (Sarstedt, UK). After curing, the hydrogels were washed with sterile PBS (Sigma-Aldrich, UK) for 15 minutes and soaked in supplemented DMEM overnight. One hour before cell seeding, the hydrogel matrices were partially dried to potentiate cell penetration. Then, 60 μL of cell suspension was added drop-wise onto each hydrogel (9 x 10^3 cells per scaffold) and samples were incubated for 1 h at 37°C with 5% CO_2 to bolster cell adhesion. After 1 h, DMEM was carefully added to the wells without disturbing the cell-laden hydrogels [247]. Culture medium was changed every two days.

5.2.4 *In vitro* release of gentamicin from SilkMA gels

To study the *in vitro* drug release profile of gentamicin from SilkMA hydrogels, samples were incubated in 0.5 mL PBS in 48-well tissue-culture plates at 32°C. As prepared SilkMA hydrogels were used as blank. At each time point, 33 μL of media was withdrawn from the well and immediately mixed with 33 μL of o-phthaldialdhehyde reagent (OPA, Sigma-Aldrich, UK) and 33 μL isopropanol (Sigma-Aldrich, UK) in a 96-well UV-transparent microplate (Greiner Bio-One, UK). The withdrawn samples were replaced with equal volumes of fresh PBS. Gentamicin release was measured with a microplate reader (Spark Multimode, Tecan, Switzerland) in fluorescence using an excitation wavelength of 340 nm and an emission wavelength of 430 nm. The concentration of gentamicin was extrapolated from a previously validated calibration curve and divided by the total amount of gentamicin encapsulated in the hydrogel to obtain the percentage released (n= 5).

5.2.5 *In vitro* antimicrobial efficacy testing

5.2.5.1 Preparation of bacterial inocula

Luria Bertani broth (Sigma-Aldrich, UK) and Luria Bertani broth with agar (Sigma-Aldrich, UK) were prepared using distilled water and at concentrations of 20 g/L and 35 g/L, respectively. Both broth and broth with agar were then sterilised via autoclaving for 20 minutes at 121°C under 100 KPa of pressure (Astell, UK). Overnight cultures of *Staphylococcus aureus* (ATCC 29213) and *Pseudomonas aeruginosa* (NCTC 13437) were prepared whereby one bacterial colony was inoculated in 5 mL of Luria Bertani broth. Using a Jenway 6300 UV-VIS spectrophotometer (Cole Parmer, UK) optical density measurements were taken at 600 nm for each overnight culture. Cultures were then diluted to an optical density of 0.06. Luria Bertani broth with agar was poured to form agar plates. These were then inoculated with the bacterial cultures using a hockey stick spreader.

5.2.5.2 Zones of inhibition

15 and 20% SilkMA gels loaded with gentamicin were prepared as previously described, and then placed onto the inoculated plates and incubated at 37°C for 24 h. The zones of inhibition (ZOI) formed from inhibited bacterial growth were then measured and recorded. SilkMA gels were then transferred from the 24 h plates onto freshly inoculated agar plates, incubated for a further 24 h and with measurements taken at 48 h. This process was repeated to obtain inhibitory results after 72 h. Each SilkMA formulation and bacterial strain were run in triplicate.

5.3 Results

5.3.1 Physicochemical characterisation of SilkMA gels

H^1-NMR spectroscopy showed that 35 - 40% of SF lysine groups were functionalised with methacrylate groups (**Figure 4.1**). Three different SilkMA hydrogel concentrations (w/v%) were prepared: 15, 20 and 25%. The optical transmittance measurements of SilkMA hydrogels in the visible range (400 – 800 nm) are shown in **Figure 5.2**a,b. The transparency of 15 and 20% SilkMA hydrogels was 83 ± 3% and 80 ± 1%, respectively, with both hydrogels showing high optical clarity (**Figure 5.2**c) [47]. However, a negative correlation between hydrogel concentration and transmittance was observed, with 25% hydrogels having a statistically significant lower transparency (63 ± 2%) compared to 15 and 20% ($p<0.001$). To determine the mass swelling ratio (q), water content and the expansion, hydrogels were incubated in PBS at the ocular temperature (32°C) for 24 h. The swelling characteristics were inversely proportional to the polymer concentration; the q of the 15, 20 and 25% gel was 9.8 ± 0.2, 8.6 ± 0.2 and 5.8 ± 0.1 respectively, with 15 and 20% ($p<0.0001$) showing a significantly higher q values compared to 25% (**Figure 5.2**d). The water content results followed a similar trend, with 15% (89.8 ± 0.3%) and 20% (88.3 ± 0.4%) exhibiting significantly higher values ($p<0.0001$) compared to 25% (82.7 ± 0.3%) (Figure 2e). As shown in **Figure 5.2**f, 15% SilkMA hydrogels (28.5 ± 7.1%) exhibited a two-fold significant higher expansion in PBS compared to 20% (14.4 ± 4.7%) and 25% (14.3 ± 4.1%) gels ($p<0.05$).

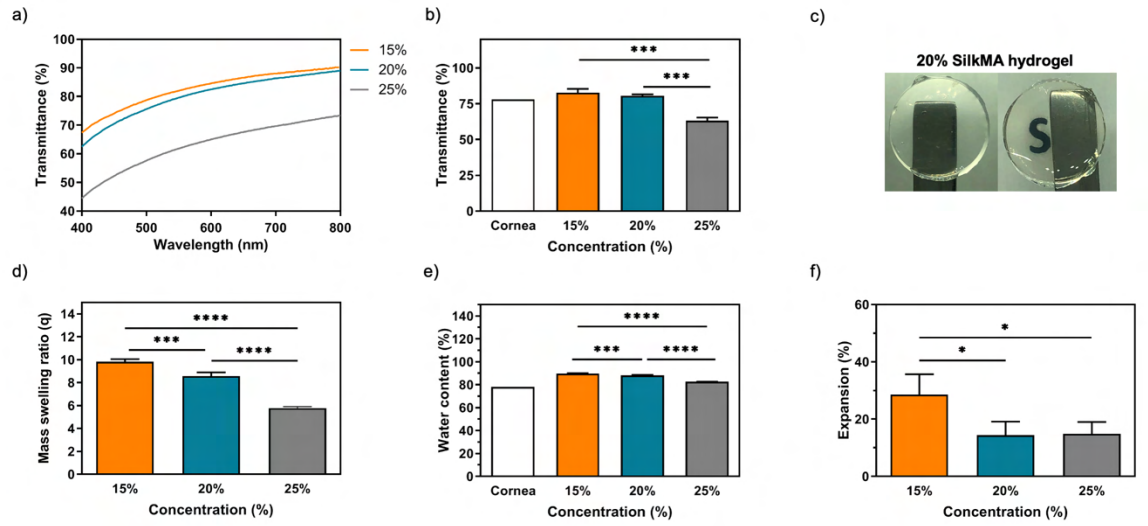


Figure 5.2 *– SilkMA hydrogels transparency (n=3): a) transmittance profiles, b) average optical transmittance in the visible range and c) optical clarity. Hydrogel diameter = 10 mm. Swelling characteristics of SilkMA hydrogels in PBS at 32°C (n=3): d) swelling ratio (q), e) water content (%) and f) expansion (%). Data presented as mean value ± SD (*p<0.05, **p<0.01, ***p<0.001, ****p<0.0001).*

G' and G'' represent the elastic and reversible response of the materials and the viscous and irreversible rearrangement of the polymeric structure of the hydrogel, respectively [248]. As shown in **Figure 5.3**a, G' is one order of magnitude higher than G'' regardless of the SilkMA concentration, which is a typical behaviour of elastomeric materials [151]. Moreover, a positive correlation between the rheological properties and polymer concentration was observed (**Figure 5.3**b and c). 25% (10.4 ± 0.2 kPa) hydrogels had a significantly higher G' than 20% (3.0 ± 0.4 kPa, $p<0.0001$) and 15% (1.1 ± 0.3 kPa, $p<0.0001$) hydrogels by 3 and 9-fold, respectively, while 20% hydrogels shown a 3-fold higher G' than 15% gels ($p<0.001$). Despite observing a non-significant difference in G'' between 15% and 20% SilkMA gels, G'' was proportional to the polymer concentration, ranging from 45 to 568 Pa for 15 and 25% hydrogels, respectively. 25% SilkMA hydrogels presented greater G'' than 15% ($p<0.001$) and 20% (164 Pa, $p<0.001$) gels by a 4 and 12-fold factor. Finally, the damping factor was lower than 0.06 for all the groups studied, suggesting a solid-like behaviour (**Figure 5.3**d) [249].

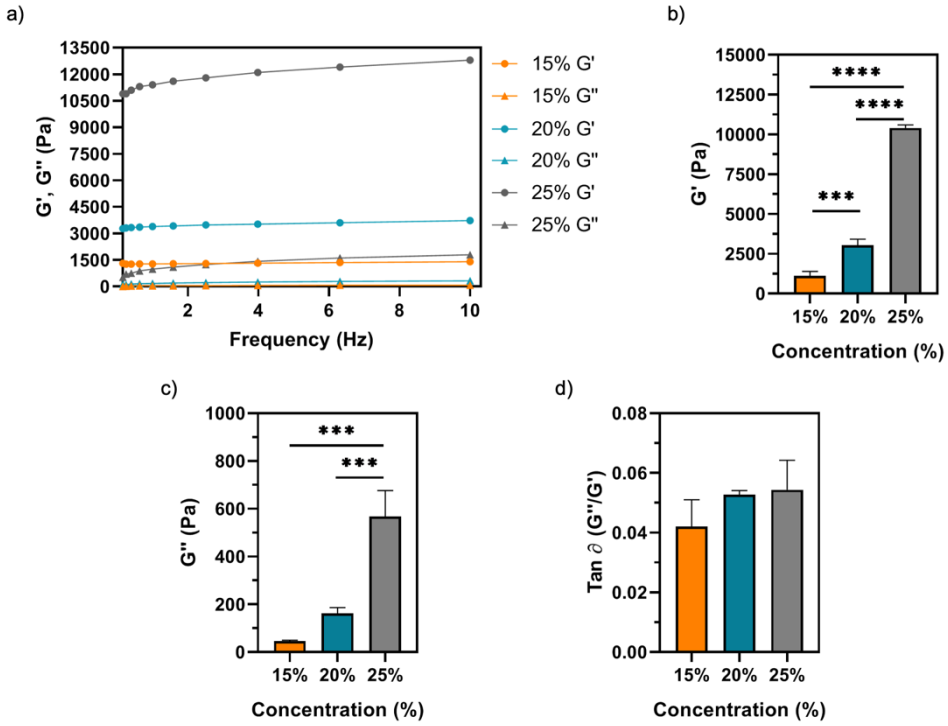


Figure 5.3 *– Rheological properties of SilkMA hydrogels (n=3): a) representative frequency sweep, b) storage modulus (G'), c) loss modulus (G'') and d) damping factor (tan δ). Data presented as mean value ± SD (*p<0.05, **p<0.01, ***p<0.001, ****p<0.0001).*

The *in vitro* susceptibility of SilkMA gels to enzymatic degradation was studied by incubating the hydrogels in 1 U/mL collagenase II for up to 7 days. Our results show that there was a time-dependent increase in degradation, with higher polymer concentrations exhibiting lower mass loss over time. As shown in **Figure 5.4**a, no significant differences were observed between the groups after 2 and 5 days of incubation. However, at day 7, 15% SilkMA gels were completely degraded, while 20% and 25% SilkMA showed a degradation of 88 ± 2% and 69 ± 12% ($p<0.01$), respectively. Due to the importance of the optical and swelling properties in the design of materials for corneal engineering, only SilkMA 15 and 20%, formulations with similar characteristics to the human cornea, were chosen for further characterisation [166]. The crosslinking efficiency was measured by mass loss, which is defined by the amount of uncrosslinked polymer after photocuring [155]. Regardless of the polymer concentration, there

was no significant difference in mass loss (≃5%, **Figure 5.4**b), suggesting that the increase in concentration and viscosity did not impact the mixing between the polymer and the photoinitiator/gentamicin solution or the free radical diffusion within the material during crosslinking. Finally, the mechanical performance of the SilkMA hydrogels was assessed by compressive mechanical testing (**Figure 5.4**c). In agreement with the rheology data, 20% hydrogels showed a significantly higher Young's modulus than 15% gels ($p<0.0001$). Specifically, the Young's modulus was 21 ± 2 kPa for 15% and 79 ± 2 kPa for 20%, a 4-fold increase (**Figure 5.4**d).

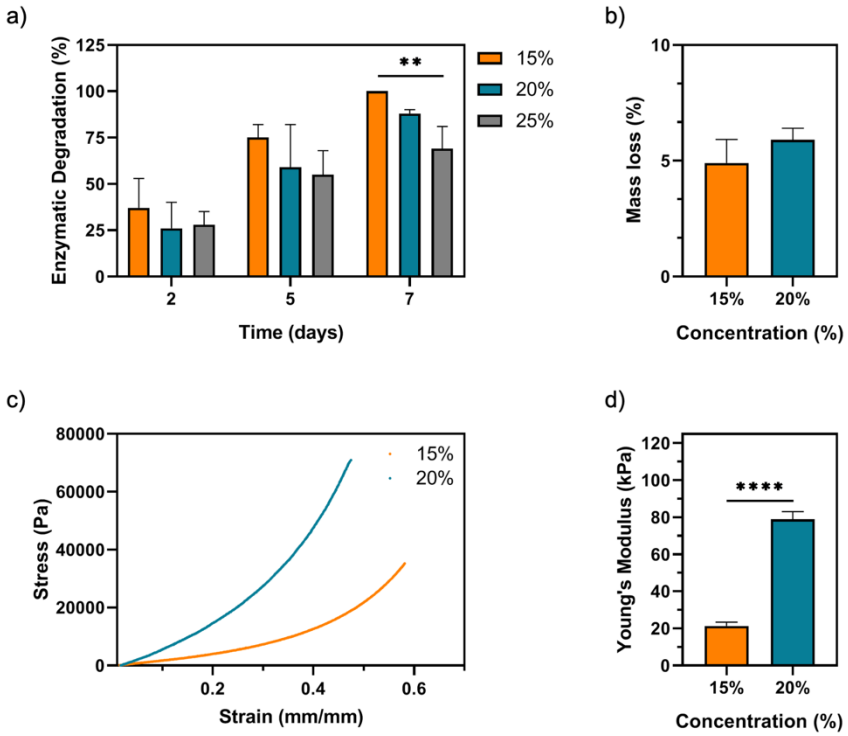


Figure 5.4 *– a) In vitro degradation of SilkMA hydrogels incubated in 1 U/mL collagenase II at 32°C for 2, 5 and 7 days (n=5). b) Measurement of the macromers not crosslinked in the hydrogel network after photocrosslinking (mass loss, %) (n=3). Cyclic compressive mechanical testing of SilkMA hydrogels (n=3): c) representative compressive strain-stress curves and d) Young's moduli. Data presented as mean value ± SD (*p<0.05, **p<0.01, ***p< 0.001, ****p<0.0001).*

The microstructure and morphology of SilkMA hydrogels were investigated using micro computed tomography (micro-CT) and SEM analysis. Micro-CT scanning was used to determine the porosity, pore size and pore wall thickness within the 15 and 20% SilkMA hydrogels (**Figure 5.5**a). As shown in Figure 5.5b, the total porosity was 79 ± 2% and 72 ± 2% for 15 and 20% SilkMA ($p<0.05$), respectively. However, despite the differences in porosity, the scaffolds exhibited similar pore thickness (≃26 μm, Figure 5.5c) and pore size distributions (**Figure 5.5**d-e), with a mean pore size of 56 ± 4 μm and 56 ± 3 μm for 15 and 20% SilkMA scaffolds, respectively (**Figure 5.5**f). SEM images revealed a uniform and interconnected pore structure for both groups (**Figure 5.5**g,h).

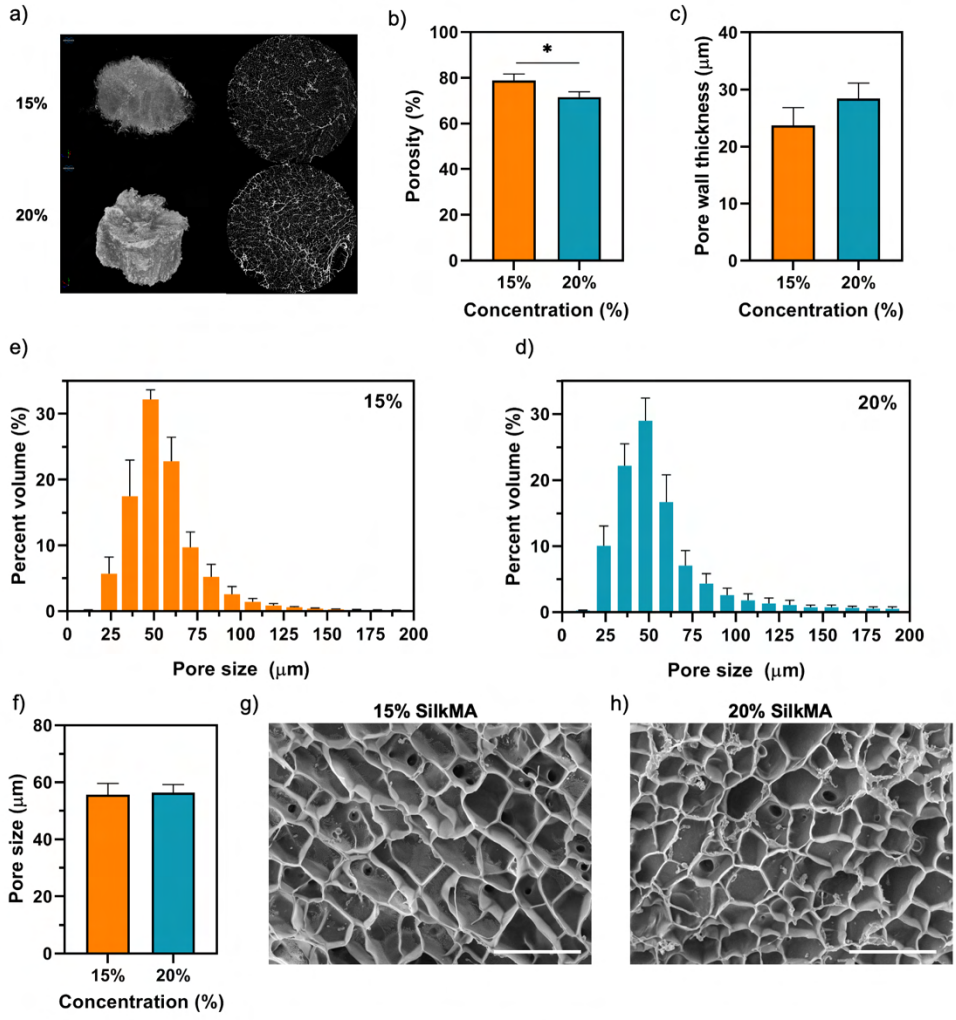


Figure 5.5 *– Morphology and microstructure analysis of SilkMA hydrogels after freeze drying (n=3): a) 3D micro-CT reconstruction and 2D images (slices) of SilkMA scaffolds. Diameter = 7 mm. Quantitative analysis of porosity by micro-CT: b) total porosity, c) mean pore thickness, d-e) pore size distribution in the hydrogels and f) mean pore size. Representative SEM images of freeze-dried SilkMA scaffolds: g) 15% SilkMA and h) 20% SilkMA. Scale bar: 150 µm. Data presented as mean value ± SD (*p<0.05, **p<0.01, ***p<0.001, ****p<0.0001).*

5.3.2 *In vitro* assessment of cytocompatibility

The cytocompatibility of SF and SilkMA prepolymer solutions and SilkMA hydrogels was studied using HDF cells seeded on tissue culture well-plates. Fluorescence staining (**Figure 5.6**a) indicates high cell viability (> 90%) for all tested conditions, suggesting that SF and

SilkMA materials did not induce toxicity. After 72 h, cells reached confluency for all groups studied. Furthermore, the ability of SilkMA gels to support cell attachment and proliferation was studied by direct seeding of HDF cells on SilkMA hydrogels and compared with GelMA, another semisynthetic-polymer and broadly used material for 3D cell culture applications [256]. As shown in **Figure 5.6**b, the metabolic activity progressively increased over the course of 14 days for both groups studied. The difference between the metabolic activity of HDF cells seeded on GelMA and SilkMA is only statistically significant at day 1 ($p < 0.0001$), with cells seeded on SilkMA hydrogels exhibiting a 47% lower metabolic activity. At days 2, 7 and 14, there was a 10% difference in cell metabolic activity between GelMA and SilkMA samples, however, it is not statistically significant (**Figure 5.6**b).

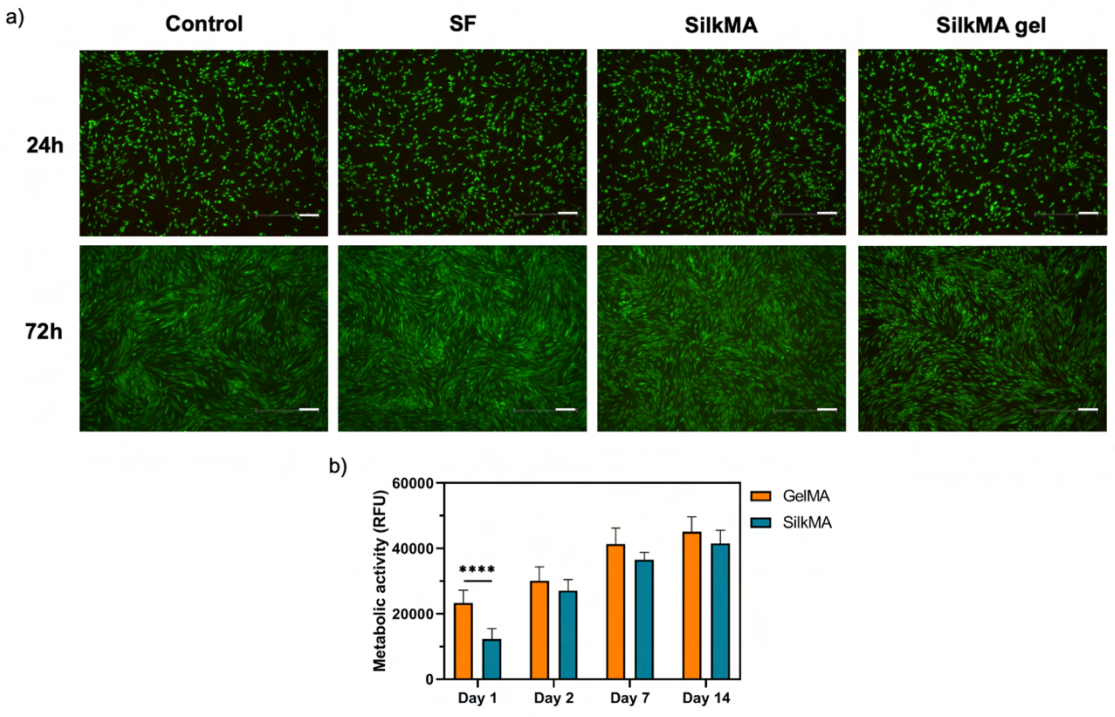


Figure 5.6 *– Cytocompatibility study: a) Live/Dead images of HDFs seeded on tissue culture well-plates with media (control) and SF/SilkMA solutions and SilkMA gels in inserts (n=3). Scale bar = 200 μm. b) Quantification of the metabolic activity of HDFs seeded on SilkMA and GelMA hydrogels by AlamarBlue assay 1, 2, 7 and 14 days after cell seeding (n=5). Data presented as mean value ± SD (*****p<0.0001).*

5.3.3 *In vitro* drug release studies

The release kinetics of gentamicin from 15 and 20% SilkMA hydrogels was studied. As shown in **Figure 5.7**a, 15 and 20% hydrogels released 53 ± 4% and 33 ± 8% ($p < 0.02$) of the total content of gentamicin within 1 h. After 2 h and 5 h, 15% SilkMA gels released 84 ± 4% and 92 ± 4% ($p > 0.05$), respectively, of the total gentamicin encapsulated, while 20% SilkMA hydrogels delivered 55 ± 4% and 72 ± 13% ($p < 0.02$), respectively. The concentration of gentamicin in the media after 24 and 48 h was determined and compared with the minimum inhibitory concentration (MIC) of gentamicin for *s.aureus* and *p.aeruginosa*. 15 and 20% SilkMA hydrogel delivered concentrations above the MIC for *s.aureus* (8 μg/mL) and *p.aeuruginosa* (2 μg/mL) after 24 and 48 h incubation [288]. As shown in **Figure 5.7**b, the concentration of gentamicin in the media was approximately 85 ± 6 μg/mL and 15 ± 2 μg/mL after 24 and 48 h, respectively, for both groups.

5.3.4 Antimicrobial efficacy testing

Agar diffusion tests were performed to study the antimicrobial efficacy of gentamicin-loaded SilkMA gels against *S.aureus* and *P.aeruginosa*. Briefly, 15% and 20% SilkMA gels were prepared and placed on culture dishes uniformly covered with *S.aureus* or *P.aeruginosa*. After incubation at 37°C for 24 h, the zones of inhibition (ZOI) were recorded, and the same hydrogel was transferred to a freshly inoculated plate. This process was repeated until a ZOI was present. As shown in **Figure 5.7**d,e, both 15 and 20% SilkMA hydrogels inhibited the growth of *S.aureus* and *P.aeruginosa* for 72 h. However, no statistical difference was observed between the ZOI of 15 and 20% SilkMA hydrogels throughout the experiment (**Figure 5.7**c). ZOI varied from 2.6 ± 0.2 cm and 3.0 ± 0.3 cm after 24 h to 1.4 ± 0.1 cm and 1.5 ± 0.1 cm after 72 h for

S.aureus and *P.aeruginosa*, respectively (**Figure 5.7**c). Finally, gentamicin-free SilkMA gels did not inhibit bacterial growth (data not shown).

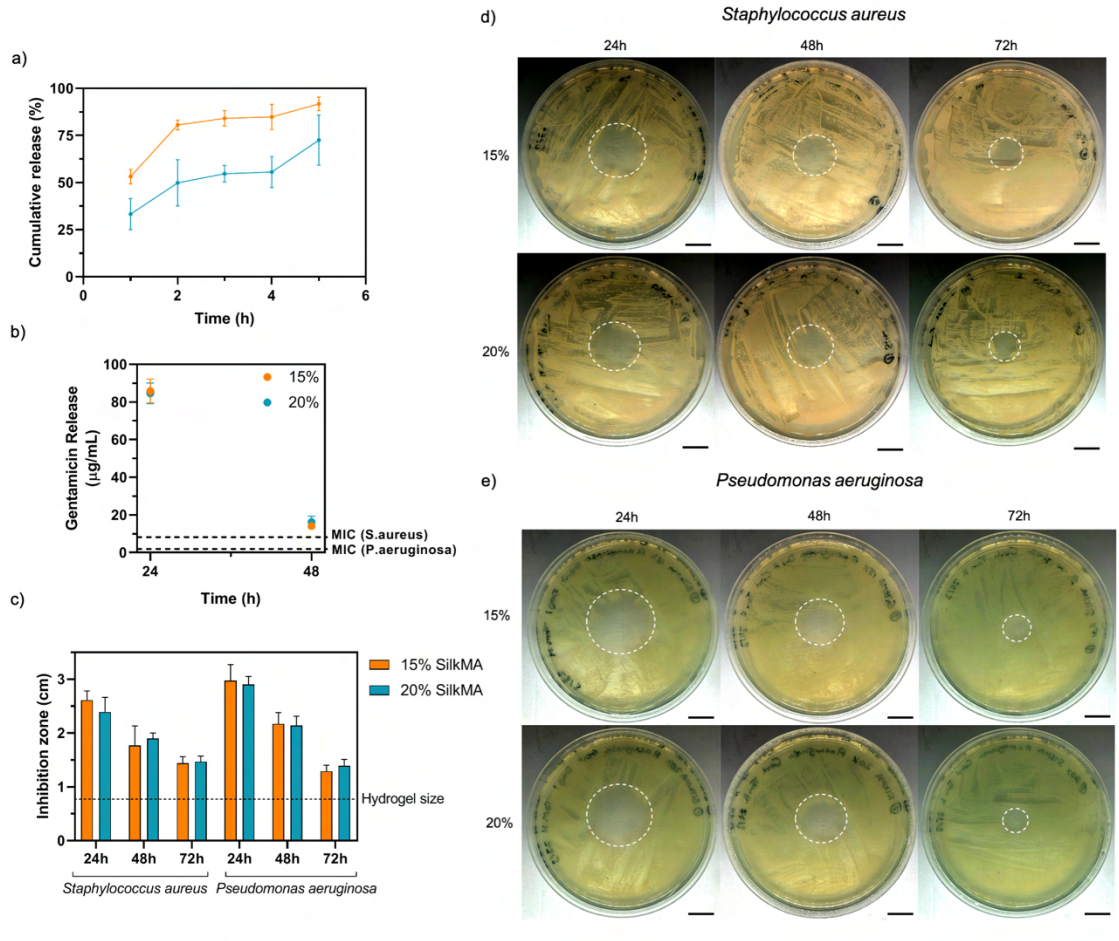


***Figure 5.7** – In vitro properties of gentamicin-loaded SilkMA hydrogels (n=5): a) Cumulative gentamicin drug release from SilkMA scaffolds after 1, 2, 3, 4 and 5 h. b) Gentamicin concentration in the media after 24 and 48 h. Zone of inhibition study (n=3): c) Average zone of inhibition of SilkMA hydrogels after 24, 48 and 72 h. d) Staphylococcus aureus and e) Pseudomonas aeruginosa. Scale bar = 1.5 cm.*

5.4 Discussion

In most cases, vision lost due to corneal-related injuries can be reversed with a corneal transplant. However, currently there is a severe mismatch between supply and demand of cadaveric donor corneal tissue (less than 1:70) [268,277]. Despite recent efforts to develop corneal stroma equivalents, the clinical need remains unmet with no products available for routine use

[153,268,276]. In this study, we developed an injectable and light-polymerisable SilkMA solution by modifying silk's lysine amino acids with methacrylate groups.

The photosensitive SilkMA solutions have potential to be crosslinked *in situ* using low UV-A intensities. In 2016, the US Food and Drug Administration (FDA) approved a therapy called corneal crosslinking (CXL) to treat patients with post LASIK/PRK ectasia and progressive corneal thinning (keratoconus). CXL uses UV-A light and RF to stiffen the cornea by inducing covalent bonds between corneal collagen molecules [133,134]. During the treatment, RF is added to the cornea and photoactivated with UV-A light at 365 nm with irradiance of 3 mW/cm^2 for 30 minutes [289]. In this study, the wavelength and intensity were chosen in agreement with CXL procedure, however instead of irradiating the eye for 30 minutes, the gels set within 5 min with minimal heat production. The impact of polymer concentration on the physical and mechanical properties of the hydrogels was studied. Our results indicate that SilkMA concentration influenced the transparency, swelling characteristics, rheology and mechanical properties of the hydrogels.

The optical functions of the cornea include 80% of the total ocular refractive power, UV light filtering (< 400 nm) and visible light transmission [28,166]. Thus, a successful stromal filler needs to have similar light transmittance to the native human cornea to replicate its visual acuity. The transmittance results obtained for 15 and 20% SilkMA hydrogels in the visible range match the values reported in the literature for a healthy human cornea (78 - 80%) [47,290]. Also, the light transmittance spectrum of the human cornea published by Freegard is very similar to the spectra obtained for 15 and 20% SilkMA, with 62% and 90% light transmittance at 400 and 780 nm, respectively [290].

Another important factor influencing the overall transparency of a hydrogel is the water content. The high hydrophilic character of hydrogels makes them attractive materials for tissue engineering applications since the swelling characteristics affect the diffusion and distribution of nutrients, oxygen and the functionality of encapsulated cells [58]. *In vivo* variations in water content cause a decrease in corneal transparency due to the changes in the collagen fibrillar spacing and are correlated with several pathologies and diseases (e.g. corneal graft rejection, keratoconus and Fuchs' dystrophy) [40,291]. In this study, all groups showed water content values similar to the human cornea (75 - 85%) [28,291]. However, as previously reported in the literature, the mass swelling of SilkMA hydrogels decreased with higher polymer concentrations [273,292–294]. An increase in the concentration of photocrosslinkable groups results in a higher crosslinking density, which ultimately creates a tighter hydrogel network and a lower mass swelling ratio. The storage and compressive Young's modulus were directly proportional to the polymer concentration, also indicating a greater crosslinking density. Bryant et al. studied the critical effect of the mass swelling ratio in the formation of a functional ECM [295]. The primary components of cartilage, glycosaminoglycan (GAG) and collagen, were evaluated histologically when varying q from 4.2 to 9.3. Results showed that q has a great effect on cell function. Despite having a similar GAG content in all hydrogels, its distribution depends on the gel properties. In systems with a q of 9.3 (low crosslinking density), GAG molecules were homogenously distributed throughout the gel. On the other hand, in highly crosslinked gels with q values lower than 5.2, GAGs were retained in pericellular regions [295]. In this work, all groups studied presented a $q > 5.2$, with values ranging between 9.8 ± 0.2 and 5.8 ± 0.1 for 15% and 25% SilkMA gels, respectively. [184] Moreover, swelling properties can also affect the overall shape of the material. A successful stromal filler should have minimal volume change thereby reducing the risk of implant mismatch and imparting stress on the surrounding tissues [184]. All

experimental groups handled well and retained their shape in the swollen state. However, 15% SilkMA hydrogels showed a 2-fold higher expansion percent than 20 and 25% SilkMA ($p<0.05$).

The success of a stromal filler is dependent on its ability to sustain epithelial and stromal regeneration. Controlling the degradation rate is paramount since the hydrogel's *in vivo* degradation should match that of corneal regeneration. Herein, we demonstrate that SilkMA hydrogels can be enzymatically degraded *in vitro*. A negative correlation between the polymer concentration and the polymer reactivity to enzymatic degradation was observed. At higher crosslinking densities, the enzyme accessibility to the cleavage sites of SF is restricted, decreasing the reactivity of hydrogels to enzymatic degradation [273]. However, the *in vitro* degradation rate reported in this study is not representative of the ocular *in vivo* microenvironment. The corneal environment is not as dilute as the conditions used in the swelling and degradation study. *In vivo*, the surface of the cornea is wetted by the tear film while the overall corneal hydration is controlled by a pumping mechanism in the endothelium [275]. Also, the concentration of collagenase II used in this experiment is not likely to be comparable to the concentrations found in the eye. Nevertheless, our results demonstrate that the chemical modifications on the SF structure did not affect the biodegradability of the polymer. In the future, the actual swelling characteristics, expansion % and the rate of *in vitro* degradation should be studied in an environment more representative of the ocular conditions (e.g. porcine eye model).

Indeed, 25% SilkMA gels exhibited a significantly lower transparency ($p<0.001$) and swelling ratio ($p< 0.0001$) than 15 and 20% SilkMA gels. Given the importance of transparency and

nutrient transport in the success of a stromal filler, we chose to move forward with 15 and 20% SilkMA formulations due to their superior transparency and swelling characteristics.

Comprising approximately 90% of the corneal thickness, the stroma provides the cornea with its mechanical and optical properties due the lamellar interweaving of collagen fibrils embedded in a hydrated matrix [26,33]. The cornea shows an increase in stiffness associated with age that could be related with a decrease in interfibrillar spacing and an increase in crosslinking between collagen molecules [50]. Despite being essential for the diagnosis of corneal diseases and corneal function maintenance, the rheological and mechanical properties of the cornea are not completely understood and the values reported in the literature span over a large range [296,297]. Hatami-Marbini et al. studied the dynamic shear properties of the corneal stroma using oscillatory experiments. The average G' and G'' varied from 2 to 8 kPa and 0.3 to 1.2 kPa, respectively. However, hydrogels derived from biopolymers or corneal ECM are reported to have poor mechanical properties compared to the native tissue [298]. In this work, only 20% SilkMA hydrogels exhibited a storage modulus within the above-mentioned range (3.0 ± 0.4 kPa). Despite the lower G'' of SilkMA hydrogels (0.04 - 0.6 kPa), the overall rheological properties of SilkMA hydrogels are higher than previously investigated light-free collagen-based hydrogels [269,270]. Ferraci et al. synthesised 10, 15 and 20% photocurable bovine serum albumin (BSA-MA) with different degrees of functionalisation (DF= 73-100%) using UV light (150 mW/cm^2, 6 min). The compressive modulus of 15 and 20% BSA-MA hydrogels with 92 DF% was approximately 18 and 30 kPa, respectively [273]. In this work, despite using a considerably lower DF% (40%) and intensity (3 mW/cm^2), the compressive modulus of 15 and 20% SilkMA hydrogels was 21 and 79 kPa, respectively. This demonstrates the potential of SilkMA-LAP system for tissue engineering applications, using a relatively low light intensity,

hydrogels with excellent mechanical properties can be prepared due to the outstanding mechanical properties of silk proteins.

Moreover, substrate stiffness is reported to influence stem cell differentiation and proliferation [299,300]. Similarly, the hydrogel microstructure also plays an important role in cytocompatibility since porosity and pore size have previously been reported to influence cellular attachment, migration and tissue ingrowth [301,302]. Although having low porosity (< 80%), which is required for structural properties, both 15 and 20% SilkMA hydrogels showed interconnected and uniform sized pores with an average pore size higher than 50 μm. Murphy et al. investigated the relationship between scaffold pore size and cell activity in bone tissue engineering. Scaffolds with small pores and increased surface area may show higher levels of initial cell attachment, however, the improved cell infiltration provided by scaffolds with larger pore sizes ultimately outweighs this effect [301,302]. In this study, we firstly verified the cytocompatibility of the SF/SilkMA pre-polymer solutions and SilkMA hydrogels. Live/dead results showed that the modified and unmodified polymers, photoinitiator and degradation products did not induce cytotoxicity after 72 h. Then, the hydrogel's ability to support cell attachment was studied. It has been previously reported that silk does not possess cell-adhesion sequences (e.g. RGD) present in other proteins, such as collagen, gelatine or laminin [249,257]. However, SilkMA hydrogels were shown to support adhesion and proliferation of HDFs for the entire duration of the experiment and the differences between the metabolic activity in SilkMA and GelMA cell-laden hydrogels was only statistically significant at day 1 ($p<0.0001$). The attachment of HDF cells to the SilkMA hydrogels possibly resulted from the hydrophilic nature of the hydrogels and their ability to immobilise adhesive proteins from the serum (e.g. vitronectin and fibrinogen) [273,303]. In the future, the viability of cells encapsulated within SilkMA gels should be studied to confirm the suitability of SilkMA as biomaterial and study the impact of

photocrosslinking. Importantly, the pore size obtained in this study should not compromise cell viability. Wang et al. encapsulated NIH/3T3 fibroblasts in GelMA hydrogels with similar pore sizes to the SilkMA hydrogels studied here (> 50 μm). The cell viability of 15 and 20% -GelMA hydrogels 24 h post cell-seeding was 85.9 and 91.5% ($p < 0.01$), respectively. The improved biocompatibility of 20% -GelMA gels was attributed to its higher stiffness [300]. In one of the first studies published using SilkMA, Kim et al. demonstrated the suitability of SilkMA bioinks for cell encapsulation. NIH/3T3 fibroblasts were suspended in 10 - 30% SilkMA or 10% GelMA (control) and printed using DLP. The authors concluded that cells remained viable regardless of the concentration, with 30% SilkMA gels having a cell proliferation as high as 10% GelMA despite the smaller pore size ($\simeq$ 40 μm) [151].

The antibacterial efficiency of gentamicin-loaded SilkMA hydrogels was assessed against *S.aureus* and *P.aeruginosa*, two of the most common causes of ocular infections [154]. Agar diffusion experiments were performed to test the antibacterial properties of 15 and 20% SilkMA hydrogels. Both groups inhibited bacterial growth for 72 h and the ZOIs were not statistically significant between groups throughout the experiment. The fact that the ZOIs for *P.aeruginosa* are higher than *S.aureus* is expected since the MIC for the latter is 4 times higher [288]. Following the confirmation that the gentamicin-loaded SilkMA hydrogels successfully inhibited bacterial growth, the drug release kinetics and gentamicin concentration in the media were studied. We observed a rapid drug release for both groups with 15 and 20% SilkMA hydrogels releasing 92 ± 4% and 72 ± 13% within 5 h, respectively. In this study, the gentamicin was solely entrapped in the polymer network. Consequently, a quick initial release and a negative correlation between the polymer concentration and the gentamicin drug release rate were expected since loose polymer networks are less able to retain the drug, yielding a quicker release. Importantly, both

groups delivered antibiotic concentrations higher than the MIC in the first 48 h which is critical for the successful eradication of a bacterial strain. We believe this discrepancy between the results regarding the antimicrobial testing (agar diffusion test) and the *in vitro* drug release experiment are due to the different nature of the experiments. When solid agar was used, the drug release profile was slower since only one surface of the gel was in contact with the agar and less liquid volume was available for elution, delaying the drug diffusion. Then, the drug loaded in the hydrogels was enough to inhibit bacterial growth for 72 h. However, for drug release studies, the hydrogels were soaked in PBS. Since the contact area between the gel the media was higher, gentamicin was released within a few hours (burst release). However, neither of these conditions is representative of the ocular *in vivo* microenvironment. In the future, the hydrogels should be tested in an ocular model that considers the presence of the tear film, blinking and ocular movements. Together, we have demonstrated the photocurable SilkMA hydrogels are able to successfully deliver antimicrobial agents and control their release kinetics to effectively inhibit bacterial growth, ultimately enhancing the potential clinical efficacy of this stromal filler.

In the present study, we have demonstrated the development of SilkMA hydrogels that replicate the corneal physical properties, in addition to being biodegradable and cytocompatible. The hydrogel biodegradability was tested with collagenase II, an enzyme that can be naturally found in tears [304]. Ideally the material degradation should match de novo tissue formation as cells would secrete enzymes as they migrate. Therefore, we expect the degradation properties of the hydrogels to be linked to cellular integration and tissue formation. Also, gentamicin-loaded SilkMA hydrogels were proven effective against *S.aureus* and *P.aeruginosa*, two of the most common causes of ocular infections, which could improve the overall graft acceptance of this

material when compared to the conventional therapies [154]. To our knowledge, this is the first study to assess the utility of SilkMA hydrogels for corneal applications.

The focus of the biological studies carried out in this study was the assessment of SilkMA's cytocompatibility given that the semi-synthetic polymer and the photoinitiator could be a source of cytotoxicity. In the future, the *in vitro* adhesion, differentiation, and tissue formation of corneal cells within these constructs needs to be investigated. Moreover, due to the difficulty in replicating the complex corneal physiological environment *in vitro*, such as the ocular movement, blinking or tear film, *in vivo* experiments will be required to further understand the therapeutic potential of this material in the repair of corneal injuries. More specifically, the ability of SilkMA hydrogels to fill the corneal defects, support corneal re-epithelisation, deliver the optimum release kinetics following surgery and degrade *in situ* will be addressed.

5.5 Conclusion

In conclusion, these findings demonstrate the development of an injectable and photocurable SilkMA hydrogel system for corneal regeneration. The material can be either crosslinked *in situ* within minutes at neutral pH and without heat production using a low-intensity UV light or printed using lithography-based biofabrication techniques. We demonstrated that gentamicin-loaded SilkMA hydrogels are biodegradable, biocompatible and antimicrobial along with exhibiting optical and mechanical properties similar to the native human cornea. Taken together, these findings demonstrate the considerable potential that SilkMA hydrogels possess as a stromal filler. To our knowledge, this is the first study to report the utility of photocurable SilkMA hydrogels to promote cornea regeneration. The suitability of SilkMA-based bioadhesives as stromal fillers will be investigated in the next chapter.

CHAPTER SIX

6 Product development: photosensitive ocular adhesives

Recently, several protein-based hydrogels have been studied for corneal tissue engineering applications due to their similarity with the native corneal tissue. To develop a successful corneal bioadhesive, the *in situ* crosslinking reaction needs to happen quickly under physiological conditions, whilst the final physical and mechanical characteristics of the hydrogel must match the corneal properties while exhibiting strong adhesion to corneal collagen. In this study, we have studied different combinations of photosensitive proteins (e.g. GelMA, SilkMA), photo initiating systems (e.g. RF/SPS and LAP), light sources (e.g. UV and visible), light intensities and exposure times (from 15s to 5min). The bioadhesive ex vivo performance was studied by measuring the burst pressure of porcine corneas treated with the bioadhesives after a full-thickness injury. Despite exhibiting excellent mechanical properties, SilkMA hydrogels could not seal the corneal injuries due to the presence of residual prepolymer solution between the bioadhesive and the corneal tissue. On the other hand, 15 and 20% GelMA-RF/SPS hydrogels photocured for 1-2min exhibited excellent corneal adhesion (burst pressure = 33-44 kPa) without signs of detachment or polymer degradation after 7 days of incubation in PBS.

6.1 Introduction

Hydrogels are 3D polymer networks that can mimic the native extracellular matrix, providing cells with an ideal microenvironment due to their hydrophilic nature, viscoelasticity and high permeability for nutrients and oxygen [211,305]. To engineer corneal adhesives, it is advantageous to consider protein-based hydrogels since the corneal stroma is mainly composed of collagen, glycoproteins and proteoglycans [37]. In recent years, several proteins have been studied for corneal tissue engineering applications, such as collagen [153,276], gelatine [58,126,152,306] and silk

[211,247,307,308]. Gelatine is a polydisperse protein produced from hydrolysed collagen. Despite having a similar amino acid composition, preserving the RGD sequences and protease cleavage sites, gelatine shows lower antigenicity and better solubility than collagen [162,206,309]. Gelatine is one of the most studied biopolymers due to its availability and affordability [152,309]. In the last decades, silk fibroin has been intensively studied for corneal tissue engineering applications due to its optical transparency and remarkable mechanical properties along with the ability to be processed in a wide variety of forms including films, hydrogels and fibres [188,247]. Importantly, both gelatine and silk fibroin are biocompatible, biodegradable, water soluble and can be easily chemically modified [166,188,309].

The success of gelatine and silk hydrogels as corneal bioadhesives depends on three requirements related with the chosen crosslinking mechanism. Firstly, a fast-crosslinking reaction is required for usability and performance purposes since in the case of full-thickness corneal perforations, the wound is leaking, which will cause glue dilution if the adhesive plug is not formed in a timely manner. Moreover, the reaction needs to happen under mild conditions as *in situ* crosslinking is required for full adaptation to the wound geometry. Lastly, the physical and mechanical properties of the hydrogels need to resemble the corneal properties with a strong adhesion to corneal collagen.

Recently, photo-activated crosslinking has attracted much attention for regenerative medicine applications since it allows temporal and spatial modulation of the hydrogel properties under mild conditions [157,310,311]. This crosslinking strategy typically requires the chemical modification of reactive groups in proteins (e.g. amine, carboxyl) with acrylate or methacrylate groups, which in the presence of a photoinitiating system and light will form covalent bonds, inducing gelation [312]. In this work, SilkMA and GelMA have been rendered photosensitive due to a

chemical modification with GMA and MA, respectively, thereby introducing vinyl groups on the polymer backbone.

Photoinitiators can be divided into two groups according to the radical generation mechanism: single component (type I) and bimolecular photoinitiation system (type II) [305]. Upon light absorption, type I photoinitiators undergo hemolytic cleavage from the excited triplet state, generating two free radicals that can initiate the polymerisation process (Equation 1, section 2.9.2.1). Conversely, the initiating mechanism of type II photoinitiators is more complex as it requires a co-initiator (e.g. SPS, TEA) and sometimes also an accelerator (e.g. VC) [157,310]. After absorbing a photon, the excited initiator abstracts an hydrogen atom from a donor molecule (e.g. SPS), forming H-donor radicals that will initiate the crosslinking reaction (Equation 2, section 2.9.2.2) [157].

The selection of the photoinitiator and light source are critical steps to achieve highly efficient photocrosslinking reactions [157,199]. Since the kinetics of gelation depends on the compatibility between the photoinitiator and the light energy used, the absorption profile of the photoinitiator should match the light source emission characteristics and it should be highly efficient generating free-radicals at that specific wavelength [157,305]. The photoinitiator's capacity to absorb specific wavelengths is measured by the molar extinction coefficient (ε).

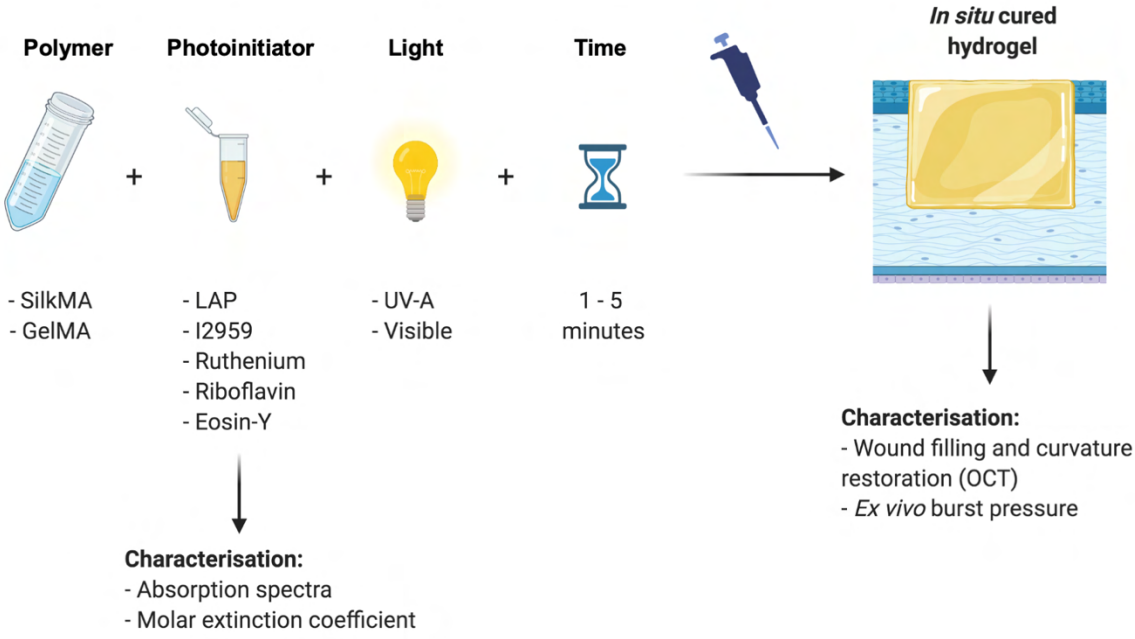


Figure 6.1 *– Schematic outline investigating: 1) The absorption spectra and molar extinction coefficient of different photoinitiators; 2) The development of SilkMA and GelMA-based photosensitive hydrogels for corneal injuries by changing the polymer concentration, photoinitiating system, light source and intensity and time. The ex vivo performance of the hydrogels was assessed by measuring the hydrogel ability to fill the wound, restore the curvature and remain in situ after incubation using OCT, while mechanical adhesion to porcine corneal tissue was studied by measuring the ex vivo burst pressure.*

In Chapter 6, we hypothesise that a highly efficient photocrosslinking reaction, and therefore, a mechanical robust bioadhesive, can be obtained within minutes by:

1) Optimising the SilkMA and/or GelMA polymer concentration and degree of functionalisation;
2) Testing different photoinitiating systems (e.g. photoinitiators Type I or Type II initiators together with co-initiators) and light energies to efficiently generate radicals at a given wavelength;
3) Studying different photocrosslinking reaction times.

Therefore, the absorbance spectra and extinction coefficients of several type I (I2959, LAP) and type II photoinitiators (RF, Eosin Y, Ruthenium) in the UV and visible range have been determined. Then, with the aim to develop a strong corneal adhesive that could be cured within minutes, we have studied the gelation of SilkMA and GelMA hydrogels by varying the polymer concentration, photoinitiating system, light source, and irradiation time. Finally, the bioadhesive's ability to fill corneal injuries and restore the ocular curvature has been assessed using optical coherence tomography (OCT) and their adhesion to corneal collagen was tested by measuring the adhesive's burst pressure on porcine eyes (**Figure 6.1**).

6.2 Materials and Methods

6.2.1 Molar extinction coefficient

The molar extinction coefficient (ε) is a measure of how strongly a substance absorbs light at a particular wavelength. The ε of various type I photoinitiators (LAP and I2959) and type II photoinitiators (RF, eosin Y and ruthenium) was measured in the 365- 550 nm range, using the Beer-Lambert Law:

$$\varepsilon\ (M^{-1}cm^{-1}) = \frac{\mathrm{A}}{\mathrm{lc}} \qquad (12)$$

Where A is the absorbance (AU) at a given wavelength, l is the path length (cm) and c is the concentration (M). Several concentrations of the same photoinitiator were prepared and the absorbance measured using UV fused quartz cuvettes (Thorlabs, USA) in a microplate reader (Spark Multimode, Tecan, Switzerland). The ε at a given wavelength was obtained through the division of the absorbance versus concentration curve slope by the cuvette path length (1 cm).

Each concentration was measured in triplicate. The ε at 365, 405, 450, 500 and 550 nm was calculated.

6.2.2 Optical coherence tomography imaging and relative stiffness estimation

Freshly enucleated porcine eyes were obtained from a local butcher. After the creation of a 5 mm corneal defect with a biopsy punch (50% deep), 10µL of prepolymer solution were applied to the injury and photocrosslinked. Samples were imaged with a Telesto II SD-OCT System (Thorlabs, Germany) at t_0 and after 1 and 7 days of incubation in 20 mL of PBS with 5% penicillin/streptomycin (Sigma Aldrich, UK) at 4°C. The relative stiffness of the engineered adhesives was estimated by means of shear wave based optical coherence elastography (OCE), assuming all samples are homogeneous and isotropic elastic materials and using the following equation:

$$E = 2(1 + \nu)\rho f^2 \lambda^2 \quad (13)$$

Where E is the Young's modulus, ν is the Poisson's ratio of the material, ρ is the density of the material, f is the temporal frequency of the shear wave and λ is the wavelength of the shear wave [313]. Assuming all hydrogel groups have a ν of 0.5 and ρ of 1000 kg/m^3 and f is a fixed constant, then E is directly proportional to the wavelength of the shear wave, λ (mm), which was then assessed by a self-developed algorithm for OCE analysis [314]. A wavelength map was also generated using the same algorithm for each hydrogel sample.

6.2.3 Residual mass

The mass of uncured polymer after photocrosslinking was calculated by comparing the weight corresponding to the same volume of prepolymer solution and blot-dried hydrogel using the following equation:

$$\text{Residual mass (\%)} = \frac{m_{\text{solution}} - m_{\text{gel}}}{m_{gel}} \times 100 \quad (14)$$

Where m_{solution} is the weight of the prepolymer solution and m_{gel} corresponds to the weight of the cured hydrogel (n= 4).

6.3 Results

6.3.1 Synthesis of SilkMA and GelMA

To engineer a functional ocular adhesive, silk fibroin and gelatine were modified with GMA and MA to form the photocrosslinkable biopolymers SilkMA and GelMA, respectively. ^{1}H-NMR spectra of dissolved Silk/SilkMA (**Figure 4.1**) and gelatine/GelMA (**Figure 6.2**) in D_2O were measured to quantify the degree of functionalisation.

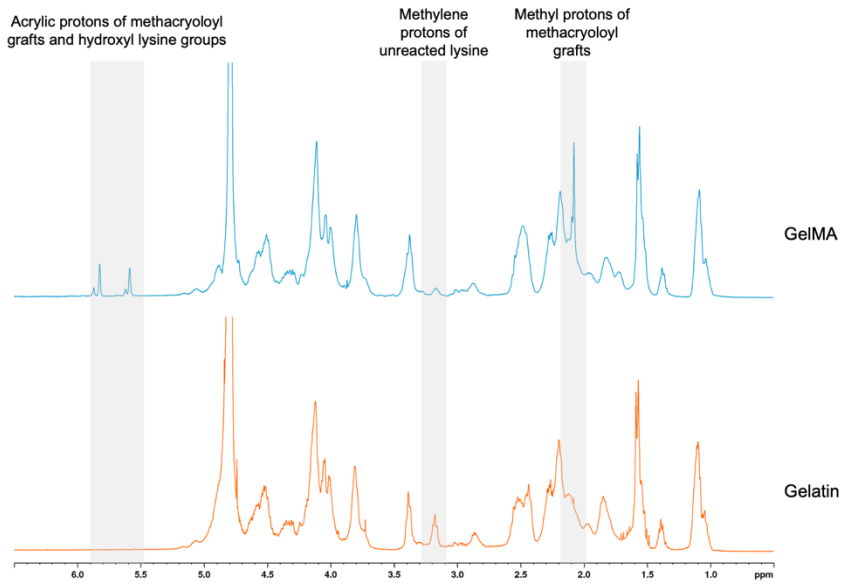


***Figure 6.2** – [1]H-NMR spectra of GelMA (top) and unfunctionalised gelatine (bottom).*

As previously mentioned in Chapter 4, the degree of methacrylation of SilkMA was 35-40% after a 3h reaction with GMA. On the other hand, the ^{1}H-NMR of GelMA displays peaks in the 5–6 ppm range and at ~ 1.8 ppm, corresponding to the acrylic protons of methacryloyl of lysine and hydroxyl lysine groups and the methyl proton of methacryloyl grafts, respectively [163,315,316]. These groups are absent in the spectra of unmodified gelatine, indicating the covalent functionalisation of gelatine with the methacryloyl groups (**Figure 6.2**). The marked decrease in the free lysine signal at 3.1–3.2 ppm indicated that the DF% was 60% after 2 h reaction with 6% (*v*/*v*) MA.

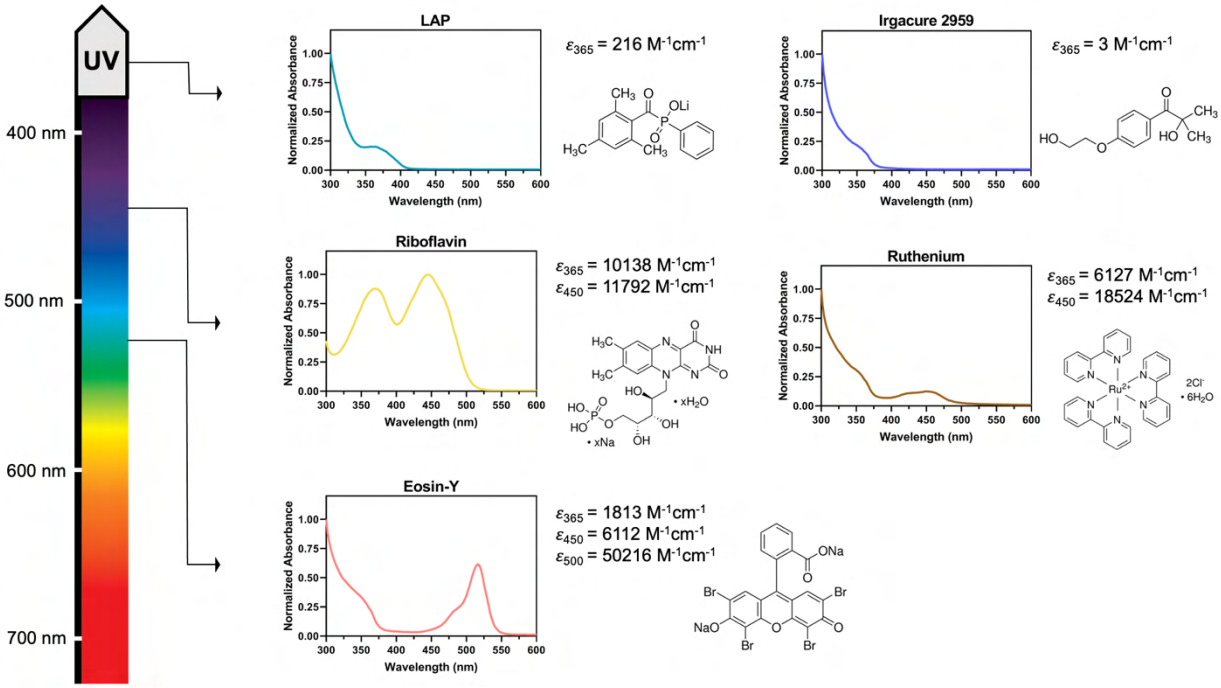


Figure 6.3 *– Absorption spectra and molar extinction coefficients of commonly used type I (LAP and Irgacure 2959) and type II (RF, ruthenium and eosin-Y) photoinitiators.*

6.3.2 Molar extinction coefficient of different photoinitiators

To achieve efficient curing reactions, it is essential to consider the photoinitiator absorption spectra and its molar extinction coefficient (ε) at the used light range. Herein, we characterised several type I (LAP and I2959) and type II (RF, Eosin Y and Ru) photoinitiators (**Figure 6.3**). As shown in **Table 6.1**, the studied molecules absorb light differently in the 365-550 nm range. For example, LAP showed a 72-fold higher molar extinction coefficient in the UV when compared to Irgacure 2959, another type II photoinitiator. Similarly, RF exhibits higher ε in the UV than Eosin Y and Ru by approximately 6 and 2-fold, respectively. However, despite RF exhibiting a higher ε than Eosin Y by approximately 3 and 2-fold at 405 and 450 nm, respectively, Ru showed the highest ε in that range.

***Table 6.1** – Comparison between different biocompatible photoinitiators: toxicity, water solutibility and molar extinction coefficient at different wavelenghts (365, 405, 450, 500 and 550 nm).*

Photoinitiator		Toxicity LC_{50} (mg/kg)	Water solubility (mg/mL)	Molar extinction coefficient (ε, M^{-1} cm^{-1})				
				ε_{365}	ε_{405}	ε_{450}	ε_{500}	ε_{550}
Type I	LAP	N/A	29.4	216	19	-	-	-
	I2959	2000 (rat oral)	1	2.97	-	-	-	-
Type II	Riboflavin	10000 (rat oral)	100	10138	6799	11792	1793	-
	Eosin Y	2344 (rat oral)	100	1813	2211	6112	50216	3042
	Ruthenium	1999 (mouse intravenous)	soluble	6127	9326	18524	2771	-

6.3.3 Fabrication of SilkMA hydrogels

SilkMA hydrogels were prepared using two distinct photoinitiating systems: LAP and RF/SPS. As shown is **Figure 6.4**a, SilkMA-LAP hydrogels could be prepared within 1 min using a UV-light intensity of 30 mW/cm^2 and within 3 min using 3 mW/cm^2 UV under argon atmosphere. SilkMA-LAP hydrogels were optically clear and easily handled. However, as shown in **Figure 6.4**b, when using RF/SPS, 15% SilkMA hydrogels required a minimum photocrosslinking time of 2 min if visible light was used and 5 min for UV-light. Further, while a minimum irradiation time of 3 min was needed to obtain optically clear hydrogels using visible light, SilkMA-RF/SPS hydrogels photocrosslinked using UV-light were opaque. Since SilkMA-LAP hydrogels showed improved transparency, were more easily handled, and required shorter irradiation times when compared with SilkMA-RF/SPS hydrogels, SilkMA-LAP hydrogels were selected for further characterisation.

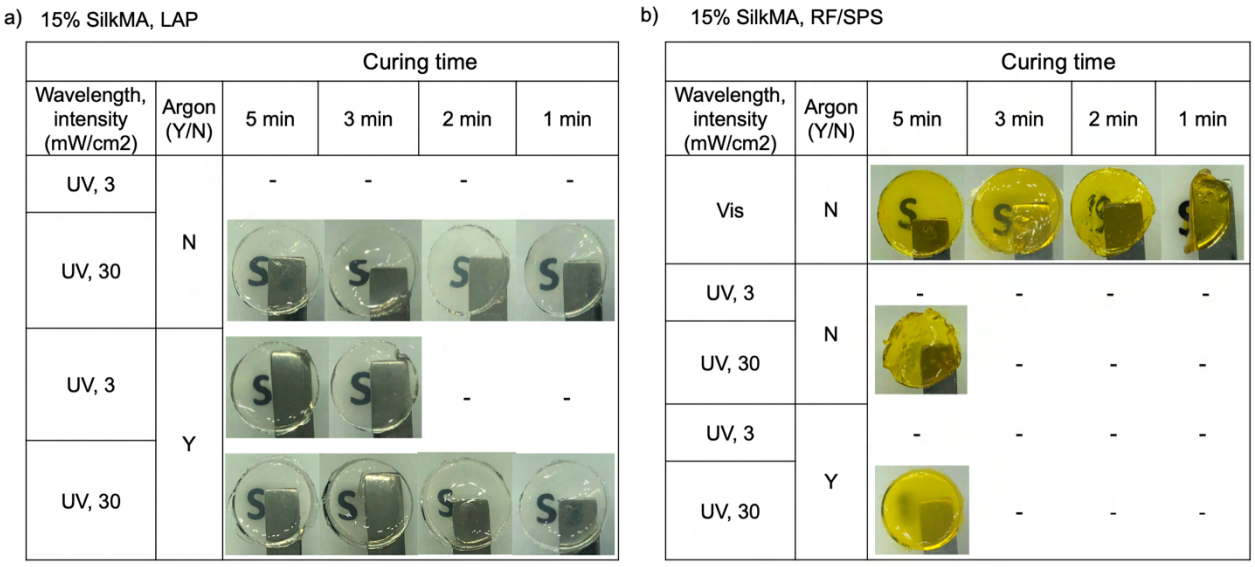


Figure 6.4 *– Appearance of 15% SilkMA hydrogels prepared using different light conditions (wavelength and intensity), curing times and photoinitiators: a) LAP and b) RF and SPS.*

Next, the ability of SilkMA-LAP hydrogels to fill corneal injuries and adhere to the stromal bed was investigated. After creating a 5 mm corneal defect (~ 50% deep), 20 μL of 15% SilkMA-LAP precursor solution was added to the injury and UV-crosslinked for 5 min. As shown by the OCT intensity contrast images (**Figure 6.5**a), the hydrogels appear to fill the defect without any obvious voids between the hydrogel and the porcine cornea. The relative stiffness of the *in situ* cured hydrogels (**Figure 6.5**b) is in agreement with the rheology data (**Figure 6.5**c), with 20% SilkMA hydrogels exhibiting a significantly higher relative stiffness and storage modulus ($p< 0.01$). However, the stiffness maps of *in situ* cured SilkMA-LAP hydrogels showed evidence of uncured prepolymer solution (**Figure 6.5**a, white arrows). To calculate the percentage of uncured solution after photocrosslinking, the weight of the prepolymer solution and the weight of the photocrosslinked hydrogels have been measured. As shown in **Figure 6.5**d, the residual mass of 15% SilkMA-LAP gels (34 ± 1%) was significantly higher than 20% SilkMA-LAP (6 ± 1%), 15% GelMA-LAP (4 ± 1%) and 20% GelMA-LAP (2 ± 1%)

crosslinked in the same conditions ($p < 0.0001$). The residual mass of 20% SilkMA-LAP hydrogels follows the same trend, with 15% ($p < 0.01$) and 20% GelMA-LAP hydrogels ($p<0.001$) exhibiting significantly lower values. Lastly, the residual mass of 20% hydrogels with different formulations was studied (**Figure 6.5**e). SilkMA-LAP exhibited a 3-fold higher residual mass than GelMA-LAP and GelMA/SilkMA-LAP blend in a 1:1 and 3:1 ratio ($p < 0.001$).

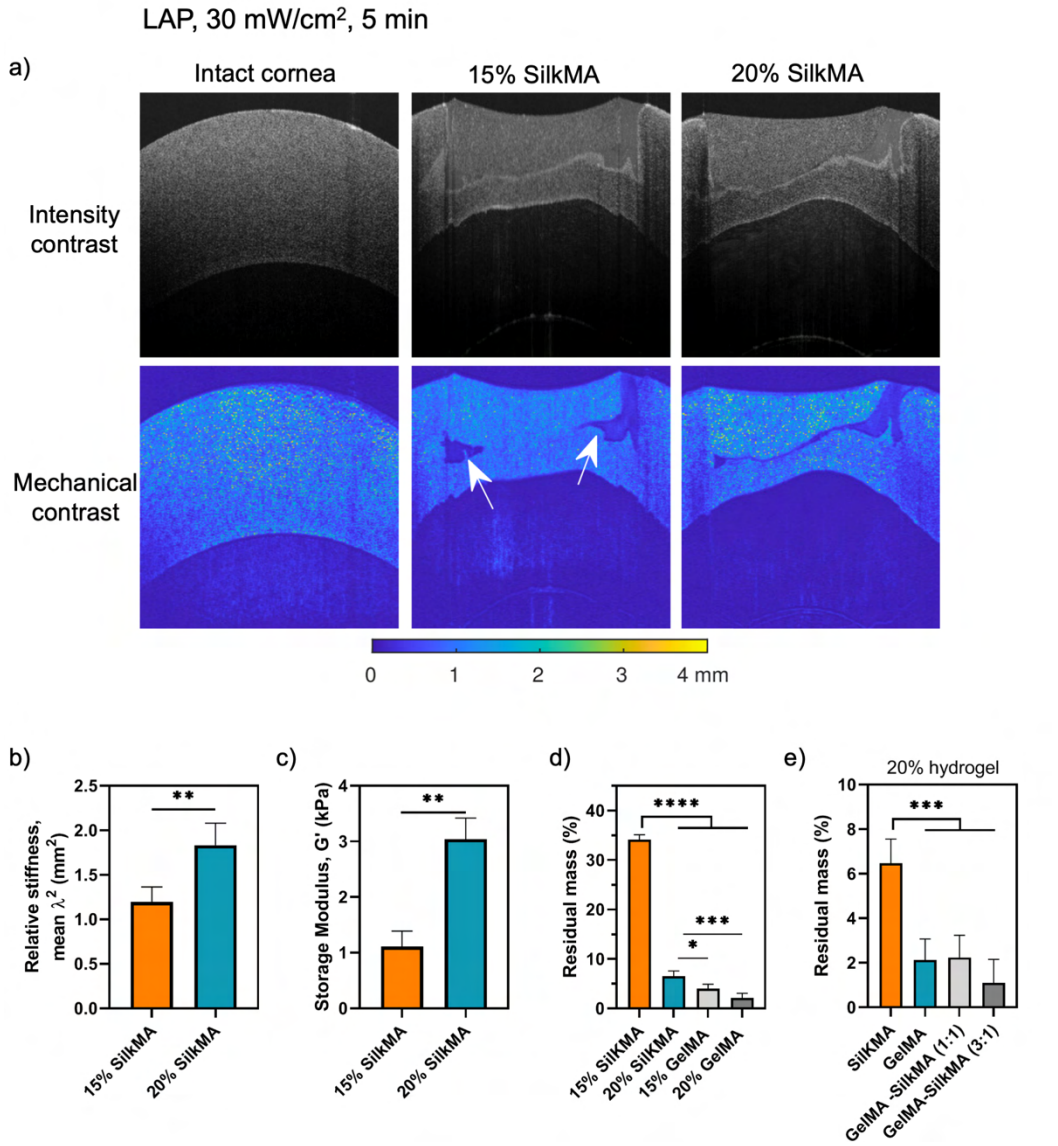


Figure 6.5 *– SilkMA-LAP hydrogel performance: a) Ex vivo optical coherence tomography images of the native porcine cornea: intensity and mechanical contrast of porcine corneas before and after in situ curing of 15 and 20% SilkMA hydrogels. The stiffness map ranges from dark blue (soft) to yellow (stiff). The arrows indicate areas of uncured gel. b) Relative stiffness of 15 and 20% SilkMA hydrogels calculated from OCT*

*scans. b) Storage modulus of 15 and 20% SilkMA hydrogels. d) Residual mass after photocrosslinking of 15 and 20% SilkMA and GelMA hydrogels. e) Residual mass after photocrosslinking of 20% hydrogels with different formulations: SilkMA, GelMA and different ratios of both polymers. Data presented as mean value ± SD (*p<0.05, **p<0.01, ***p< 0.001, ****p<0.0001).*

6.3.4 Fabrication of GelMA hydrogels

Subsequently, we tested the preparation of GelMA adhesives using LAP and RF/SPS. As shown in **Figure 6.6**a, 15% GelMA-LAP gels crosslinked for 5 min using UV-light successfully filled the corneal injury and remained *in situ* after incubation in PBS for 5 days, whilst with 15% GelMA/SilkMA-LAP (1:1) voids were observed after 24h incubation in PBS (yellow arrows). To assess the ability of these hydrogels to act as tissue adhesives, 2-mm full-thickness corneal perforations were created at the centre of the porcine cornea. After the gels were photocrosslinked *in situ*, the porcine cornea was mounted on an AAC. During the test, a PBS solution was continuously injected in the chamber and the intraocular pressure was monitorised with a pressure sensor until the bursting (**Figure 6.6**b). The difference between the burst pressure of 15% (10 ± 5 kPa) and 20% GelMA-LAP (12 ± 4 kPa) was not significant, however GelMA-LAP gels exhibited significantly higher burst pressures than blended GelMA/SilkMA-LAP formulations at different ratios ($p < 0.05$, **Figure 6.6**c).

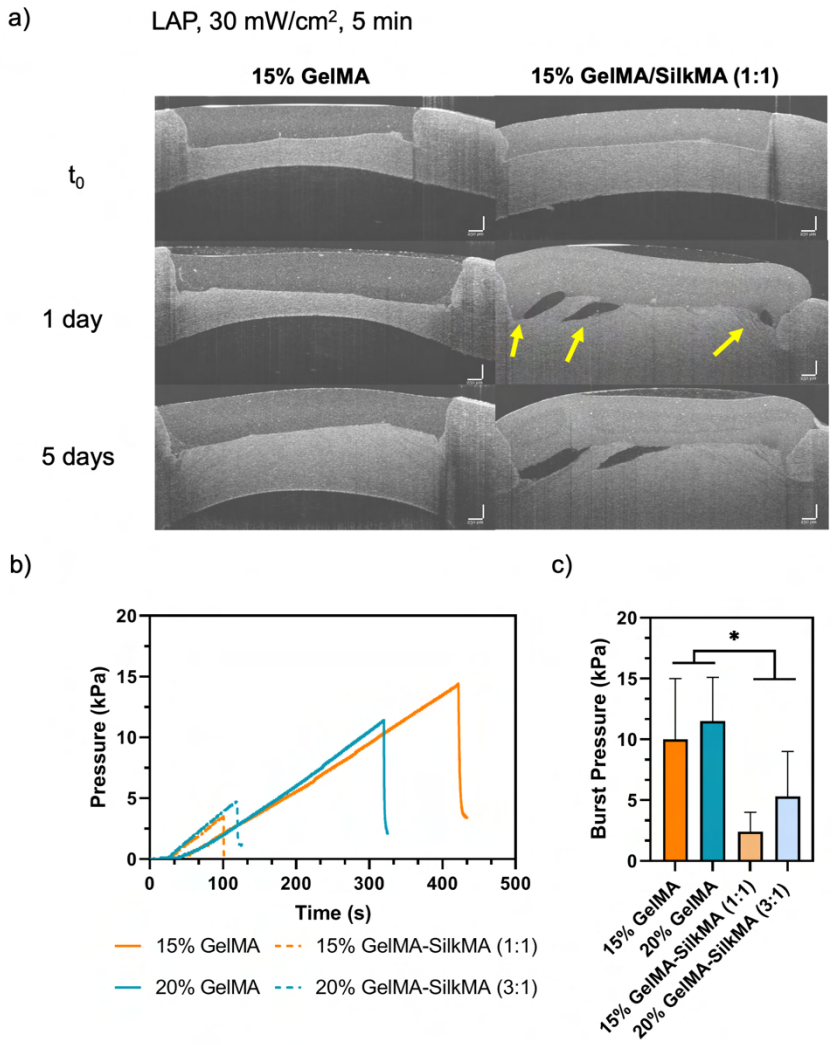


Figure 6.6 *– GelMA-LAP and GelMA/SilkMA-LAP hydrogel performance: a) Ex vivo optical coherence tomography images of the native porcine cornea with 15% GelMA and 15% GelMA:SilkMA (1:1) immediately after photocrosslinking (t_0) and after 1 and 5 days. The darker areas below the hydrogel indicate the presence of voids (yellow arrows). b) Representative pressure curves of the studied groups. c) Ex vivo burst pressure of GelMA and GelMA:SilkMA adhesives on the artificial anterior chamber (n=8). Data presented as mean value ± SD (*p<0.05).*

When GelMA hydrogels were prepared using RF/SPS and visible light, it was observed that only 15 seconds were needed to obtain a hydrogel that could be handled without leaving uncured residues in the mould (**Figure 6.7**a). The hydrogels did not dissolve after incubation at 37°C for 24h, confirming the chemical crosslinking. Next, the burst pressure of 15% GelMA hydrogels prepared using RF/SPS photoinitiating system was investigated and compared with

the 15% GelMA-LAP results (**Figure 6.7**b, c). As shown in **Figure 6.7**b, 15% GelMA-RF/SPS photocrosslinked using visible light for 2 min exhibited a burst pressure of 46 ± 8 kPa, whilst 15% GelMA-LAP cured using UV-light for 5 minutes had a burst pressure of 10 ± 5 kPa, a 5-fold difference ($p < 0.0001$). Similarly, the burst pressure of 20% GelMA-RF/SPS and 20% GelMA-LAP was 50 ± 1 kPa and 12 ± 4 kPa, respectively ($p < 0.0001$).

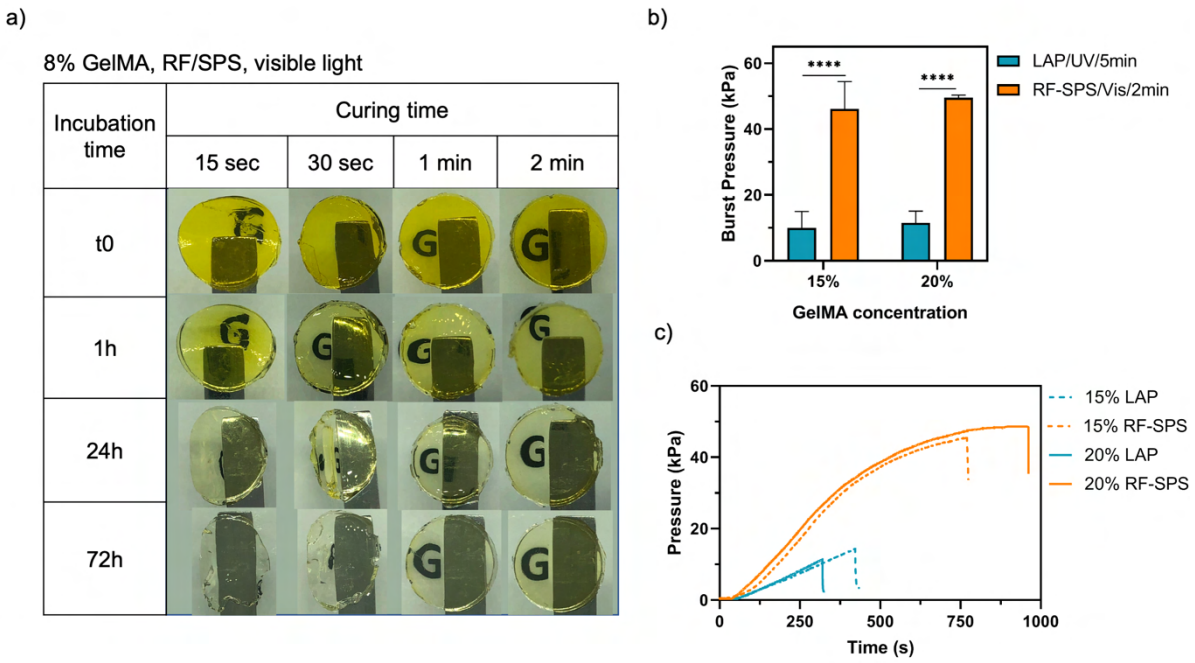


Figure 6.7 *– GelMA-LAP and GelMA-RF/SPS hydrogel performance: a) Appearance of GelMA hydrogels prepared using a RF/SPS photoinitiating system and different curing times, immediately after curing and after incubation in PBS for 1, 24 and 72 h. b) Mean burst pressure of GelMA adhesives photocrosslinked using LAP and UV light or RF/SPS and visible light in the AAC (n=8). c) Representative pressure curves of the studied groups. Data presented as mean value ± SD (****p<0.0001).*

After measuring the GelMA-RF/SPS adhesive burst pressure on the AAC, the burst pressure of GelMA-RF/SPS formulations with different polymer concentrations, crosslinking times and light intensity/wavelength was measured on the porcine eye. As shown in **Figure 6.8**a, the burst release pressure of GelMA-RF/SPS adhesives in the porcine eye showed a positive correlation with the polymer concentration. However, the difference is only significant between 12%

GelMA-RF/SPS (14 ± 6 kPa) and 15 and 20% GelMA-RF/SPS (33 ± 13 kPa and 38 ± 17 kPa, respectively) adhesives crosslinked for 1 min, and between 12% (24 ± 9 kPa) and 20% GelMA-RF/SPS (44 ± 9 kPa) gels crosslinked for 2 min ($p < 0.05$). For a given polymer concentration, no differences were observed between the burst pressure of adhesives crosslinked for 1 and 2 min. Next, the impact of using different light energy (visible or UV) and UV-intensity (3 and 30 mW/cm^2) was studied. As shown in **Figure 6.8**b, the results showed no differences in the burst pressure of adhesives crosslinked used visible light or UV-light with an intensity of 30 mW/cm^2. However, independently of the polymer concentration, 3 mW/cm^2 UV-light intensity yields significantly lower burst pressures when compared with visible and 30 mW/cm^2 UV-light (**Figure 6.8**b).

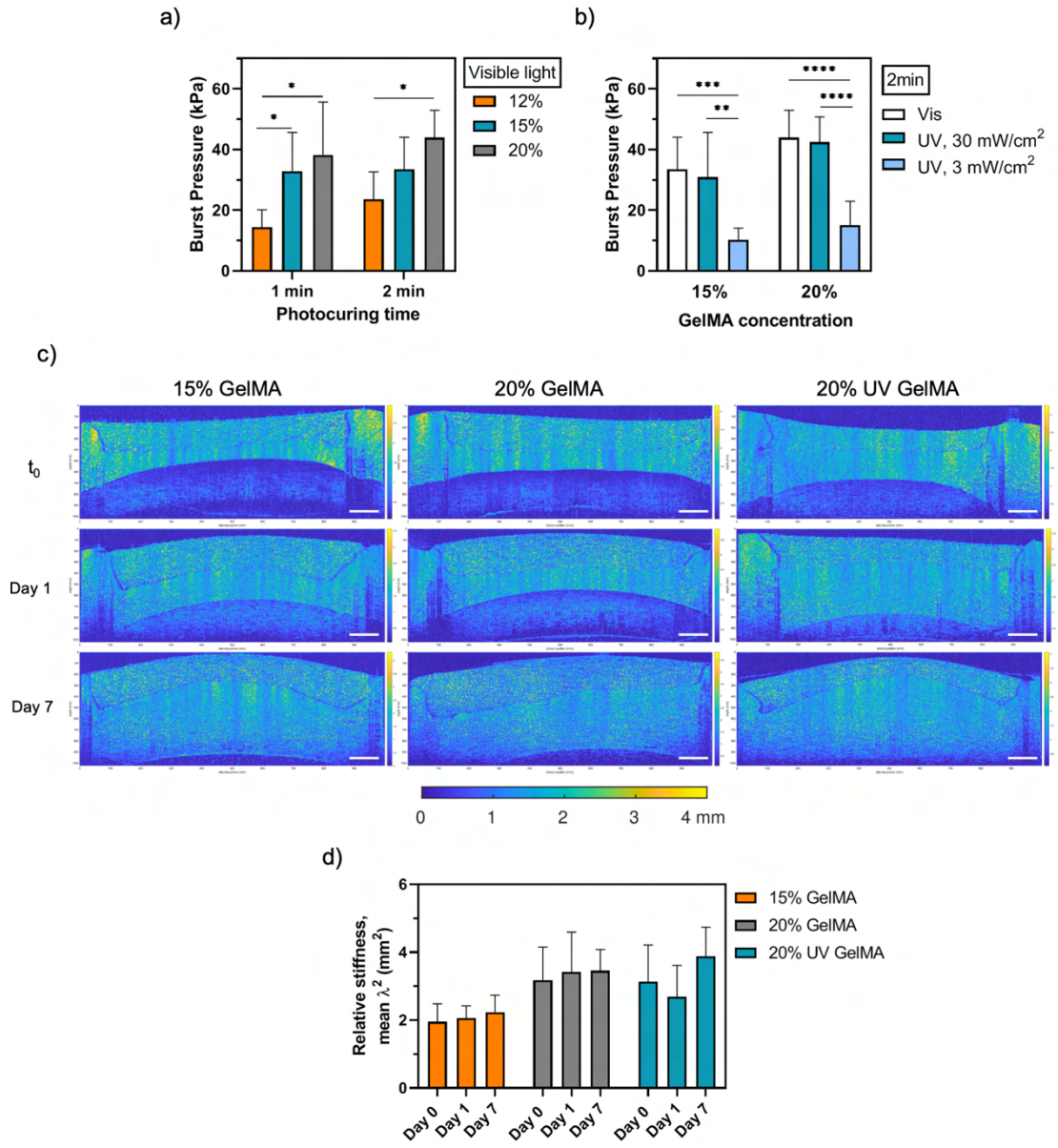


Figure 6.8 *– GelMA-RF/SPS adhesives mean ocular burst pressure optimisation: a) polymer concentration and curing time and b) light energy and intensity. c) Wavelength maps generated by a self-developed algorithm for optical coherence elastography analysis* [314]*. The stiffness of the tissue increases from dark blue (soft) to yellow (stiff). d) Relative stiffness of the studied groups overtime (day 0, 1 and 7). Data presented as mean value ± SD (*p<0.05, **p<0.01, ***p< 0.001, ****p<0.0001).*

Finally, the ability of GelMA-RF/SPS adhesives fill the corneal injury, restore the corneal curvature and remain *in situ* after incubation in PBS was studied. As shown in **Figure 6.8**c, GelMA-RF/SPS adhesives were able to fill the defect without any uncured solution being

observed at the cornea-adhesive interface. Moreover, the adhesives remained *in situ* for 7 days without any significant changes in stiffness (**Figure 6.8**d).

6.4 Discussion

To tailor the properties of photosensitive proteins, several key parameters can be adjusted to yield substantially different materials: the protein type (different ratio of amino acids), degree of functionalisation, polymer concentration, light parameters (intensity and wavelength) and photoinitiating system.

Overall, the success of a corneal adhesive depends on three main functional requirements: 1) fast *in situ* sol-gel transition for usability purposes since it prevents glue dilution and decreases the clinical intervention time; 2) strong adhesion to corneal collagen for efficient sealing and 3) physical and mechanical characteristics matching the corneal properties (**Table 2.1**). Importantly, both the crosslinking time and the mechanical properties depend on the photocrosslinking reaction efficiency. In order to improve the reaction kinetics and circumvent low reaction efficiencies, previous studies have used longer exposure times or increased the light intensity or the photoinitiator concentration [157]. However, for this application, none of these approaches are suitable due to requirement 1) and risks related with retinal light toxicity and cytocompatibility.

Therefore, in this work different strategies have been used to improve the photocrosslinking efficiency. Firstly, we have chemically modified silk and gelatine with GMA and MA, respectively, to form SilkMA and GelMA. This reaction introduced vinyl groups into the protein backbone through the primary amines on lysine residues. The double bonded carbons

in these groups are highly reactive and promote fast free-radical polymerisation reactions in the presence of a photoinitiator and light [193,310]. The maximum DF% obtained for SilkMA was approximately 35-40%, while for GelMA we have obtained values from 55-75%. Since GelMA is a semi-synthetic polymer, we optimised our reaction parameters to yield a DF% of 60% with objective of preserving the biopolymer characteristics. Previous studies reported a DF% of 100 and 42% for GelMA and SilkMA, respectively [151,315]. Gelatine exhibits a lysine content (2.65 mol%) that is 13-fold higher than silk (0.2 mol%), which might explain the higher DF% observed [151,317]. However, another important difference between the reaction Gelatine-MA and Silk-GMA is that two molecules of GMA can react with one free amino residue, while MA only reacts with one [318]. Despite the differences in the DF%, both polymers yielded robust hydrogels (**Figure 6.4**a, **Figure 6.7**a).

Secondly, since high compatibility between the initiator and the light source is essential to obtain efficient crosslinking reactions, the absorption spectrum and the molar extinction coefficient of several photoinitiators at different wavelengths were studied [157]. As shown in **Figure 6.3** and **Table 6.1**, each photoinitiator shows a different absorption profile, water-solubility and toxicity. Despite being one of the most used photoinitiators in the field due to its low cytotoxicity, I2959 shows limited initiation efficiency due to low water-solubility and absorption in the UV (ε_{365}= 3 $M^{-1}cm^{-1}$) [305]. As retinal light toxicity is reported to be dose dependent and cumulative, the objective of this work was to develop corneal adhesives that could be quickly photocured *in situ* using low light intensities [319]. Therefore, I2959 was not considered for this work. In contrast, LAP is reported to be more efficient, less cytotoxic and more soluble in water than I2959, avoiding the use of toxic organic solvents [157,305]. In addition to performing better with UV-light than I2959 (ε_{365}= 216 $M^{-1}cm^{-1}$), it also shows some light

absorption in the visible (ε_{405}= 19 $M^{-1}cm^{-1}$), however in this range the crosslinking efficiency would be lower, requiring longer curing times. Finally, when considering using a light source within the visible range, type II photoinitiators are more suitable as they exhibit higher extinction coefficients (**Table 6.1**). RF was used in this study (vitamin B2) due to its biocompatibility, strong absorption in both visible (ε_{450} = 11792 M^{-1}) and UV range (ε_{365}= 10138 M^{-1}) and, most importantly, because it is currently used in corneal crosslinking (CXL), a FDA-approved method to stiffen the cornea [289,307].

Lastly, the efficiency of the RF-mediated crosslinking was improved by using a co-initiator. RF mediated photo-crosslinking of silk and gelatine is achieved by the oxidation of tyrosine residues [193]. The RF exposure to visible light produces an excited RF state (RF*) able to strip electrons from tyrosine residues forming tyrosyl radicals. The coupling of two tyrosyl radicals via carbon-carbon bonds forms di-tyrosine bonds [193,211,212,320]. However, previous studies have demonstrated that the photocrosslinking of silk (4.8 mol% tyrosine) [186] and gelatine (0.9 mol% tyrosine) [164] using solely RF is slow. For example, silk-RF solutions were irradiated for 1 h to achieve the complete crosslinking 40 μm thick films [307], while 6 wt% gelatine-RF hydrogels were firstly physically crosslinked at 4 °C for 20 min and posteriorly irradiated for 2 h to chemically crosslink the hydrogel [321]. As previously mentioned, the success of an ocular adhesive depends not only on its adhesion strength to the corneal tissue but also on the time required for *in situ* crosslinking. In cases of full-thickness corneal perforations, the eye is leaking aqueous fluid from the anterior chamber. Consequently, if gelation is not achieved within a few seconds to minutes, the adhesive solution will be diluted and a liquid layer will be formed between the adhesive and corneal surface potentially compromising its performance. The crosslinking efficiency of type II photoinitiators might increase if they are used together

with a co-initiator (e.g. SPS, TEA), thereby decreasing the reaction time and the light intensity needed [199]. In this study, RF was used together with SPS, which continuously boosts the generation of free radicals, accelerating gelation [193]. To our knowledge, this was the first study to investigate the GelMA hydrogel formation via RF/SPS mediated crosslinking.

Hence, in this work we studied the suitability of SilkMA and GelMA hydrogels to be used as corneal adhesives. The materials were photocrosslinked using different light conditions (UV, visible), photoinitiation systems (LAP, RF-SPS) and curing times (15 s to 5 min) and its performance as tissue adhesives was assessed *ex vivo*.

One major issue observed with SilkMA-LAP hydrogels was oxygen inhibition, as this molecule can scavenge radicals required for the crosslinking reaction [155,159]. This issue can be overcome by photocrosslinking the hydrogels under inert conditions (e.g. argon or nitrogen atmosphere). However, these conditions might be difficult to implement and would likely negatively affect cell viability. Another strategy to overcome oxygen inhibition is to increase light intensity and photoinitiator concentration [155]. As shown in **Figure 6.5**a, SilkMA hydrogels could not be prepared using 3 mW/cm^2 UV-light in 5 min, however, when a 10-times higher intensity was used, hydrogels could be photocured within 1 min. When crosslinking the hydrogels in an inert atmosphere, hydrogels were successfully prepared using 3 mW/cm^2 UV-light in a minimum time of 3 min.

However, despite exhibiting excellent mechanical properties (**Figure 6.5**c), both 15 and 20% SilkMA hydrogels could not completely fill an ocular injury. As shown in **Figure 6.5**a, a volume of uncured prepolymer solution remained between the hydrogel and the corneal tissue after photocrosslinking, preventing tissue sealing. A negative correlation between the polymer

concentration and the residual mass was observed (**Figure 6.5**d). Further, when comparing the residual mass of 15 and 20% SilkMA-LAP and GelMA-LAP hydrogels photocrosslinked in the same conditions, the former exhibits a significantly higher residual mass independently of the concentration. We hypothesise that the lower degree of crosslinking may be due to the lower content of methacrylate groups grafted into the silk backbone when compared to gelatine, since the first only contains 0.2 mol% of lysine residues (DF= 35-40%), while gelatine contains 13 times more of lysine residues (2.65 mol%) from which 60% were modified [151,317].

Next, we tested the *ex vivo* burst resistance of GelMA-LAP and SilkMA/GelMA-LAP blends. GelMA-LAP adhesives exhibited a burst pressure of approximately 10 kPa, which is 5-fold higher than the human physiological IOP (2 ± 0.2 kPa) [51]. However, when GelMA was blended with SilkMA, the IOP that the adhesives could withstand was significantly lower ($p < 0.05$), with the OCT images revealing voids between the hydrogel and the corneal tissue after 1 day of incubation (**Figure 6.6**). After failing to seal the corneal injuries by itself, these results also suggest that SilkMA had a negative impact on the performance of the GelMA/SilkMA blends and, therefore, this polymer was considered not suitable for this application.

When GelMA hydrogels were photocured using the RF-SPS photoinitiation system, a higher reaction efficiency was observed compared to LAP. As shown in **Figure 6.7**a, 8% GelMA-RF hydrogels photocured for 1 min did not degrade within 72 h. Moreover, GelMA-RF/SPS hydrogels crosslinked for 2 min exhibited a 5-fold higher burst pressure than GelMA-LAP bioadhesives crosslinked for 5 min (**Figure 6.7**b, $p < 0.0001$), which demonstrates the superior cohesive strength and adhesion to the stromal bed of GelMA-RF/SPS adhesives. Goto et al. photocured 20% GelMA-RF/TEA hydrogels in 1 min obtaining a compressive modulus of approximately 17 kPa [322]. In this work, 20% GelMA-RF/SPS crosslinked for 2 min exhibited a

13-fold higher compressive modulus (**Figure 7.6**f). Further, we have successfully prepared 8% GelMA-RF/SPS hydrogels within 15 s that could be handled and did not degrade completely after 72h (**Figure 6.7**a), while in the previously mentioned study, 15% GelMA-RF/TEA gels could not be removed from the mould due to uncrosslinked polymer [322]. These results demonstrate the efficiency and relevance of the RF/SPS photoinitiation system used in this work.

Finally, different GelMA concentrations, light characteristics and curing times were tested *ex vivo* to define which GelMA-RF/SPS formulations would yield a better adhesive performance (**Figure 6.8**). As expected, a positive correlation between the burst pressure and the polymer concentration and radiation dose (time and intensity) was observed (**Figure 6.8**a, b). Due to the higher bust pressures obtained, 15 and 20% GelMA-RF/SPS crosslinked using visible or UV-light (30 mW/cm^2) were selected for further characterisation. A minimum photocrosslinking time of 2 min was chosen to reduce performance variability since bioadhesives photocured for 1 min exhibited greater standard deviations (**Figure 6.8**a). As shown in **Figure 6.8**c, GelMA-RF/SPS bioadhesives were able to fill the corneal injury and exhibited excellent adhesion to corneal collagen. After 7 days of incubation in PBS, no signs of detachment can be observed despite the increased pressure applied on the adhesive due to corneal swelling [32]. The bioadhesives did not show any significant changes in stiffness during incubation in PBS at 37ºC, suggesting minimal degradation in PBS (**Figure 6.8**d).

6.5 Conclusion

In this chapter, the performance of photosensitive silk and gelatine-based gels as corneal adhesives was investigated. The *ex vivo* burst pressure of SilkMA and GelMA hydrogels crosslinked using different photoinitiation systems and light conditions was measured. GelMA-

RF/SPS hydrogels showed promising results due to its fast *in situ* gelation, transparency, cohesive strength, and strong adhesion to corneal collagen. The optimised formulations will be further characterised in the next chapter.

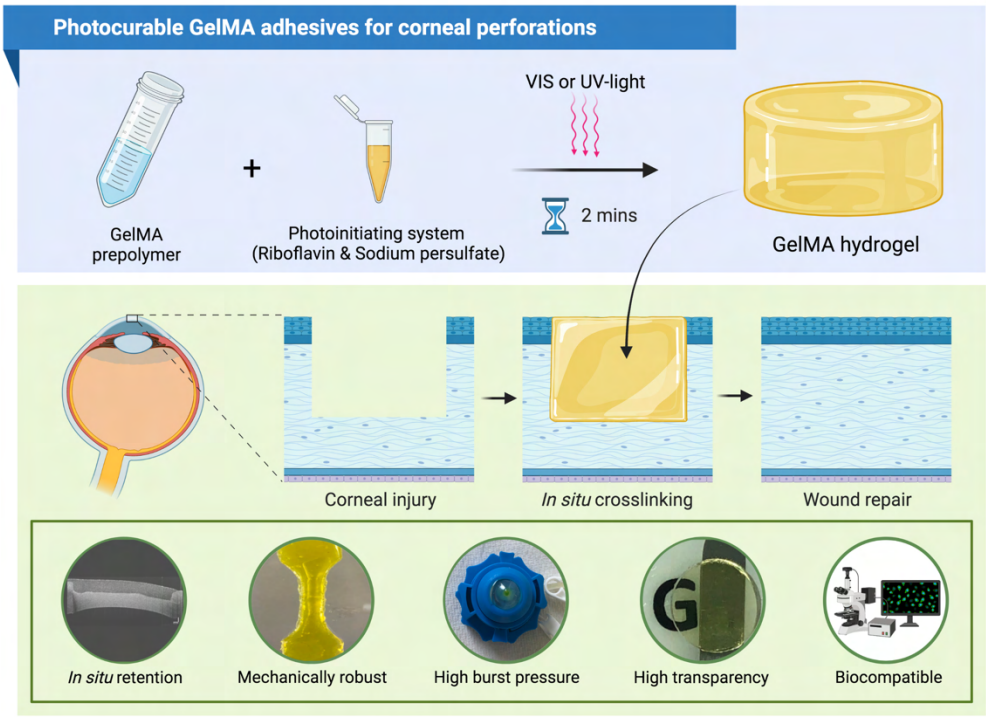
CHAPTER SEVEN

7 Photocurable GelMA Adhesives for Corneal Perforations

Data in this chapter is also presented in the published article found in Appendix B:

Inês A. Barroso, Kenny Man, Thomas E. Robinson, Sophie C. Cox, and Anita K. Ghag. "*Photocurable GelMA Adhesives for Corneal Perforation*s", Bioengineering 9, no. 2: 53. DOI: 10.3390/bioengineering9020053 (2022)

The current treatments for the management of corneal and scleral perforations include sutures and adhesives. While sutures are invasive, induce astigmatism and carry a risk of infection, cyanoacrylate glues are toxic, proinflammatory and form an opaque and rough surface that precludes vision. Consequently, the clinical need for a fast curing and strong tissue adhesive with minimised cytotoxicity and host inflammation remains unmet. In this paper, we engineer a GelMA adhesive that can be crosslinked *in situ* within 2 min using UV or visible light and a RF/SPS system. OCT images demonstrated that the flowable GelMA adhesive could completely fill corneal wounds and restore the ocular curvature by forming a smooth contour on the ocular surface. Further, *ex vivo* studies in porcine eyes showed that GelMA bioadhesives exhibited burst pressures that were comparable to cyanoacrylates (49 ± 9 kPa), with the hydrogels exhibiting a transmittance (90%), water content (85%) and storage modulus (5 kPa) similar to the human cornea. Finally, using human dermal fibroblasts, we showed that our GelMA adhesive was non-toxic and could effectively support cell adhesion and proliferation. Taken together, the adhesive's performance, injectability and ease of administration, together with gelatine's availability and cost-effectiveness, make it a potential stromal filler or sealant for corneal and conjunctival applications.



7.1 Introduction

Globally, corneal blindness is estimated to affect approximately 23 million people, with an estimated 1.5 million new cases per year [4,323]. Corneal wounds and perforations can arise from infections, traumatic injuries, surgical procedures (e.g., cataract surgery), autoimmune diseases (e.g., ulcerative keratitis) or degenerative disorders [11,324]. Full-thickness corneal injuries can leak and allow the ingress of pathogens into the eye. Therefore, given the risk of ocular morbidity and vision loss, corneal perforations are considered surgical emergencies [8]. Currently, the sealing of corneal wounds remains challenging for surgeons and sutures are still the gold standard treatment for the closure of ocular wounds due to their high tensile strength [8,325]. However, sutures are time consuming to position, inflict additional trauma to the tissues, can act as a nidus for infection, induce astigmatism and often require secondary removal procedures [4,9,10].

In contrast, tissue adhesives are an appealing alterative to the use of sutures. Tissue adhesives exhibit lower infection rates, can be delivered through small applicators and form a continuous seal, adapting to the wound morphology and distributing the load, thereby decreasing scarring [6,7]. The development of an effective and safe tissue adhesive could reduce surgical and hospitalisation time, lower the incidence of complications and reduce leakage from wounds [4]. Specifically, the ideal material to repair corneal perforations must be optically clear to allow vision, exhibit strong adhesive properties to the naturally moist ocular surface, provide healing enhancement without scarring or vascularisation and have a rapid *in situ* crosslinking after application [1,4,7,58,184,326]. Nowadays, ocular adhesives can be divided into two main groups: naturally derived (e.g., fibrin-based) and synthetic adhesives (e.g., cyanoacrylate and PEG-based) [11].

In ocular surgery, fibrin sealants have been used to seal corneal perforations (with and without an amniotic membrane), lens capsule lacerations and to repair leaking blebs [11,22]. Fibrin glues are biodegradable, easy to apply and show minimal toxicity together with improved comfort. The main drawbacks of these bioinspired glues are the potential risk of disease transmission and fast degradation *in vivo* (within days to weeks), which limits its use and/or requires re-application. Currently, fibrin-based adhesives are mainly used for amniotic membrane fixation [11,22,23]. Although cyanoacrylate-based adhesives (CAs) are not FDA approved for ophthalmic use, these adhesives have been used off-label in the eye for several decades [66,86]. In ocular surgery, CAs are reported to be toxic, proinflammatory and are associated with many postoperative complications, such as keratitis [18,19], unintentional entry into the anterior chamber [20,21], corneal neovascularisation and scar formation [11,23,327]. Nonetheless, CAs remain a useful tool in the treatment of ocular surgical emergencies due to their quick preparation, easy application and effective and secure performance. Another class of synthetic tissue adhesives

are based on the FDA-approved polymer PEG. PEG-based adhesives are safe, well tolerated, elastic and biodegradable, work independently of the clotting cascade, do not carry risks of disease transmission and some formulations remain *in situ* longer than fibrin sealants [24,85]. ReSure (Ocular Therapeutix, Bedford, MA, USA) and OcuSeal (BD Medical, Le Pont de Claix, France) are approved for sealing corneal incisions. However, despite being useful to reinforce suture sealing and close corneal incisions, these adhesives are not appropriate to function as stromal fillers due to poor mechanical properties, high swelling rates and short *in vivo* retention [85,90,91].

Over the last decade, several polymers have been studied in an effort to develop novel tissue adhesives, such as alginate [328,329], chondroitin sulphate [330], chitosan [328,331,332], tropoelastin [278], gelatine [58,152,164,184,206,333], poly(acrylamide-methyl acrylate-acrylic acid) [334] and N-iso-propylacrylamide copolymerised with butylacrylate [335]. However, currently the clinical needs are still unmet with no materials specifically approved for the filling and repair of corneal defects [270].

Gelatine is a promising biomaterial for the repair of corneal defects given its availability, cost-effectiveness, water solubility and presence of both cell-binding sites (e.g., RGD peptide sequence) and matrix metalloproteinase motifs that promote cellular adhesion and allow enzymatic degradation, respectively [309,336]. However, it requires modification to enable mechanical tailoring via chemical crosslinking. Once methacrylic/methacryloyl groups (GelMA) are introduced, these bioadhesives can be photocrosslinked under physiological conditions within seconds. The final adhesive properties can be tailored by changing the initial gel strength of raw gelatine (Bloom factor), the degree of methacryloyl functionalisation (DF%), polymer concentration, light characteristics and time. Recently, GelMA-based

adhesives photocrosslinked using type I photoinitiators, such as LAP (Lithium phenyl-2,4,6 trimethylbenzoylphosphinate)[333] and Irgacure-2959[58,152,184,337], or type II photoinitiators, such as ruthenium/SPS [164], RF/TEA [322] and Eosin Y/VC/TEA [126,150,154,205,206], have been investigated for different applications. In ocular surgery, there have been studies on the development of GelMA adhesives/hydrogels to be photocrosslinked *in situ* [58,126,154,206] or implanted after curing [152].

In this paper, we develop an optically clear and injectable gelatine-based adhesive that can seal corneal defects. In this work, we use RF as a photoinitiator since it is already being used in corneal crosslinking (CXL), an FDA-approved procedure to treat patients with post laser *in situ* keratomileusis (LASIK) ectasia and progressive corneal thinning (keratoconus) [133,134]. Furthermore, RF is a naturally occurring photosensitive molecule (vitamin B2) and absorbs light in both the UV (365 nm) and visible range [274].

Chapter 7 aims to assess the ability of GelMA-RF/SPS hydrogels to cure *in situ* in a timely manner, seal full-thickness corneal perforations by adhering to the corneal collagen, restore the corneal curvature, withstand high interocular pressures and remain *in situ* after incubation in PBS while keeping its optical clarity. In this study, GelMA bioadhesives of different polymer concentrations are crosslinked using UV or visible light and a photoinitiator system composed by RF and SPS: 15 (*w*/*v*)% and 20 (*w*/*v*)% GelMA crosslinked with visible light (referred as 15% and 20%, respectively) and 20 (*w*/*v*)% GelMA crosslinked with UV light (20% UV).

To our knowledge, this is the first work investigating GelMA hydrogel formation via RF/SPS mediated photocrosslinking. As shown in **Figure 7.1**, the physicochemical, adhesive, and biological properties of GelMA bioadhesives are characterised. Briefly, we conclude that GelMA bioadhesives can be injected *in situ* and rapidly seal full-thickness corneal perforations (≤2 min). The adhesives restored the corneal curvature by forming a smooth and transparent

seal, while withstanding intraocular pressures comparable to Histoacryl (33–50 kPa). The versatility of the semi-synthetic bioadhesives developed in this study to function on dry, semi-dry and wet substrates make them suitable to be applied not only for sealing corneal and conjunctival lacerations, but also in different physiological conditions (e.g., skin).

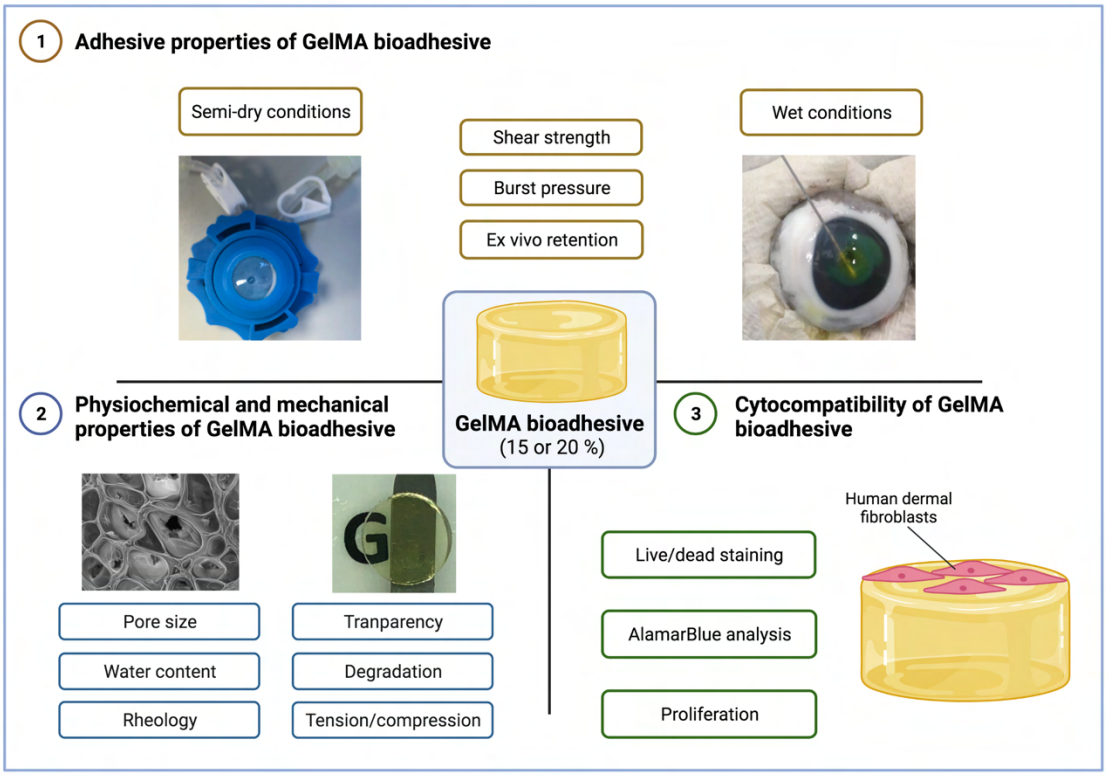


Figure 7.1 *– Schematic outline investigating the properties of GelMA bioadhesives.*

7.2 Methods

7.2.1 *Ex vivo* retention time

Freshly enucleated porcine eyes were obtained from a local butcher. After the creation of a 5 mm corneal defect with a biopsy punch (50% deep), 10 µL of prepolymer solution were applied to the defect site and photocrosslinked. OCT imaging was used to assess the ability of the engineered adhesives to fill the corneal defect and adhere to the corneal stroma immediately after photocrosslinking (t_0) and to study the dimensional stability and retention time of the

hydrogels after incubation. Samples were imaged with a Telesto II SD-OCT System (Thorlabs, Germany) at t_0 and after 1, 3 and 7 days of incubation in 20 mL of PBS with 5% penicillin/streptomycin (Sigma-Aldrich, UK) at 4 °C.

7.2.2 2D cell seeding on GelMA gels

GelMA pre-polymer solutions were prepared, UV sterilised and photocrosslinked as previously described in 48-well suspension cell culture plates (Sarstedt, Germany). After curing, 100 µL of DMEM was added to the hydrogels to prevent dehydration. One hour before cell seeding, the hydrogel matrices were partially dried to potentiate cell penetration. Then, 60 µL of cell suspension was added dropwise onto each hydrogel (9×10^3 cells per scaffold) and samples were incubated for 1 h at 37 °C with 5% CO_2 to bolster cell adhesion. After 1 h, DMEM was carefully added to the wells without disturbing the cell-laden hydrogels [247]. The culture medium was changed every two days.

7.3 Results

7.3.1 Adhesive properties of GelMA bioadhesives

The success of a bioadhesive depends on its adhesion and retention at the wound site [329]. In this study, burst pressure and lap shear tests were performed to characterise the GelMA bioadhesive properties in semi-dry and wet conditions. A cyanoacrylate-based adhesive (Histoacryl, B. Braun Surgical S.A., Barcelona, Spain) was used as a positive control due to its off-label application in surgical emergencies involving corneal perforations. To quantitively assess the mechanical adhesion of GelMA bioadhesives to the corneal tissue under liquid pressure, GelMA formulations were tested using two different set-ups: an AAC and a porcine eye (**Figure 3.2**, **Figure 7.2**e).

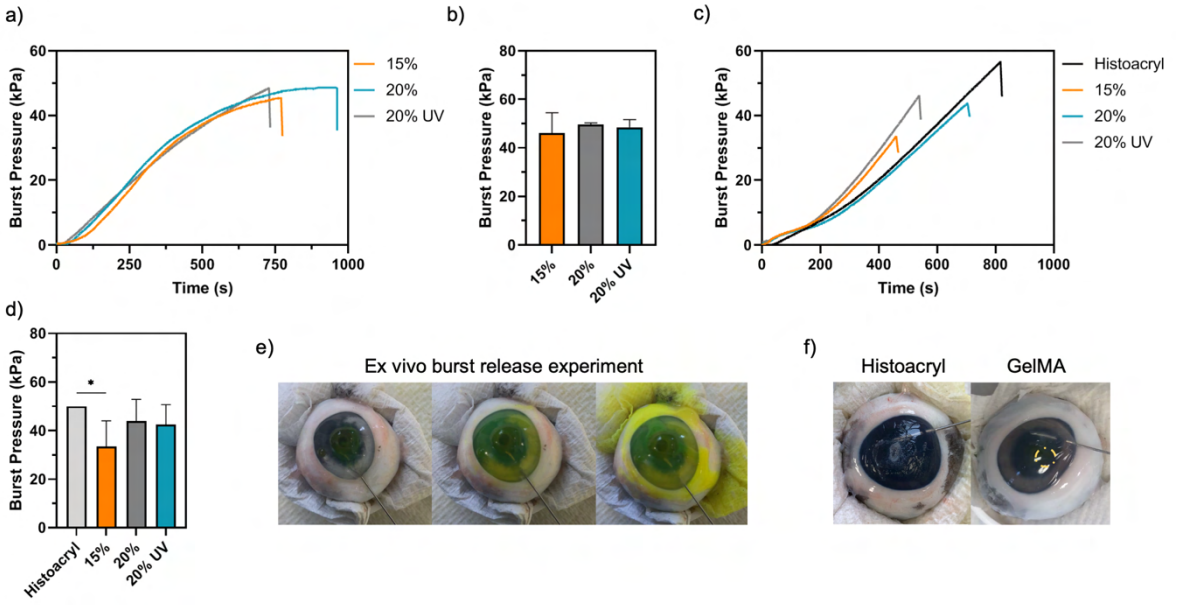


Figure 7.2 *– Ex vivo burst pressure of GelMA bioadhesives: a) representative pressure curves of the studied groups when the cornea was mounted in the artificial anterior chamber; b) mean burst pressure of GelMA adhesives in the artificial anterior chamber (n = 8); c) representative pressure curves of the studied groups and Histoacryl glue in the porcine eyeball; d) mean burst pressure of GelMA adhesives and Histoacryl glue in the porcine eyeball (n = 8); e) porcine eyeball before, during and after the burst pressure experiment; f) appearance of full-thickness corneal injuries sealed with Histoacryl and GelMA. Data presented as mean value ± SD (* $p < 0.05$).*

In the first method, after making a 2 mm full-thickness central injury, the cornea is removed with a scalpel and mounted on the AAC. As only the cornea is mounted on the AAC, this method tests the corneal adhesive performance in a semi-dry environment. However, since liquids at the wound–adhesive interface are a barrier to strong surface bonding and, in case of a corneal perforation, the eye leaks aqueous humour, the performance of GelMA bioadhesives was also studied in the porcine eyeball with a full-thickness perforation. This experimental setup is closer to the real situation and represents the worst-case scenario. In both systems, a fluorescein solution was progressively injected until bursting or reaching the pump's maximum pressure of 50 kPa. The average burst pressure of GelMA bioadhesives on the AAC was between 46 ± 8 and 50 ± 1 kPa. The difference was not statistically significant between the

groups ($p > 0.05$) (**Figure 7.2**a,b). As expected, the burst pressures obtained when sealing corneal injuries on the porcine eyeball were lower than in the AAC, with 15%, 20% and 20% UV GelMA bioadhesives exhibiting burst pressures of 33 ± 11, 49 ± 9 and 48 ± 8 kPa, respectively, while Histoacryl had a burst pressure superior to 50 kPa (**Figure 7.2**c,d). However, only 15% GelMA and the control were statistically significantly different ($p < 0.05$). Despite showing high adhesive strength on wet substrates, Histoacryl showed no adhesion onto semi-dry corneal tissue. Furthermore, when this glue was used an opaque and rough patch formed, while GelMA formed a smooth and transparent seal that could restore the curvature of the cornea (**Figure 7.2**f). Finally, we observed that the bioadhesive failure position was generally on the interface between the hydrogel and the cornea, suggesting that the adhesion force is lower than the adhesive strength.

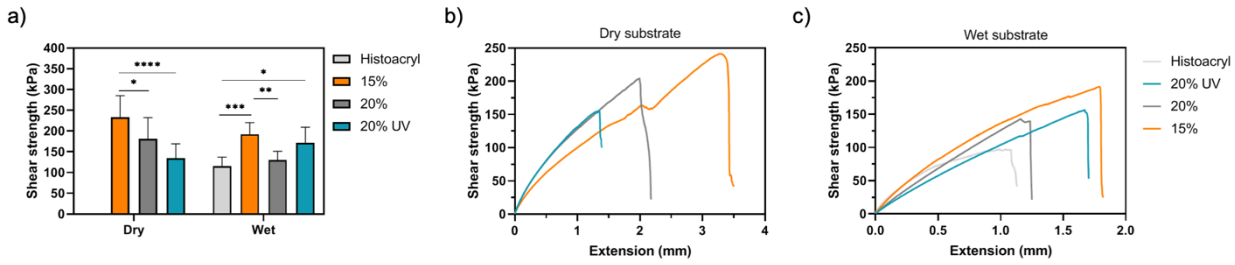


Figure 7.3 *– In vitro shear strength of GelMA adhesives: a) mean shear strength of GelMA bioadhesives and Histoacryl in wet and dry conditions; c,d) Representative stress–strain curves of GelMA hydrogels and Histoacryl in dry and wet substrates, respectively. Data presented as mean value ± SD (* $p < 0.05$, ** $p < 0.01$, *** $p < 0.001$, **** $p < 0.0001$).*

Next, lap shear tests were used to investigate the adhesion strength of GelMA bioadhesives to wet and dry substrates (**Figure 3.3**). In line with the results obtained in the burst pressure experiment, when a liquid layer is present on the interface between the substrate and the adhesive, lower shear strengths were obtained for all the groups tested (**Figure 7.3**a). However,

the minimum strength at break was around 130 kPa for both conditions tested. More specifically, the highest shear strength on dry conditions was obtained for 15% (233 ± 52 kPa), which was significantly higher than 20% (181 ± 51 kPa, $p < 0.05$) and 20% UV (134 ± 35 kPa, $p < 0.0001$). Histoacryl failed to glue the dry gelatine-coated glass slides (**Figure 7.3**a,b). On a wet substrate, Histoacryl exhibited a shear strength of 115 ± 22 kPa, which was significantly lower than the results obtained for 15% (192 ± 28 kPa, $p < 0.001$) and 20% UV (171 ± 38 kPa, $p < 0.05$) (**Figure 7.3**a,c). Finally, the GelMA bioadhesive failure was caused by hydrogel detachment from the gelatine coating as residual GelMA could be found on one side of the gelatine-coated glass slide after the test (delamination).

7.3.2 Physicochemical characterisation of GelMA bioadhesives

The optical transparency of GelMA bioadhesives over time is shown in **Figure 7.4**a. After photocrosslinking, 15 and 20% GelMA adhesives were macroscopically clear and lightly yellow, with an optical transmittance of ~ 62 ± 0.5% (**Figure 7.4**b). As RF leaches out from the matrices, the transmittance of GelMA adhesives progressively increased and, after 3 and 24 h, it was approximately 86 ± 0.5% and 91 ± 0.5%, respectively, for both 15 and 20% GelMA adhesives. However, 20% UV samples were not optically clear, showing a maximum transparency of 64.2 ± 11% (**Figure 7.4**a,b). The optical transmittance of 20% UV was significantly lower than 15 and 20% at all time points ($p < 0.0001$).

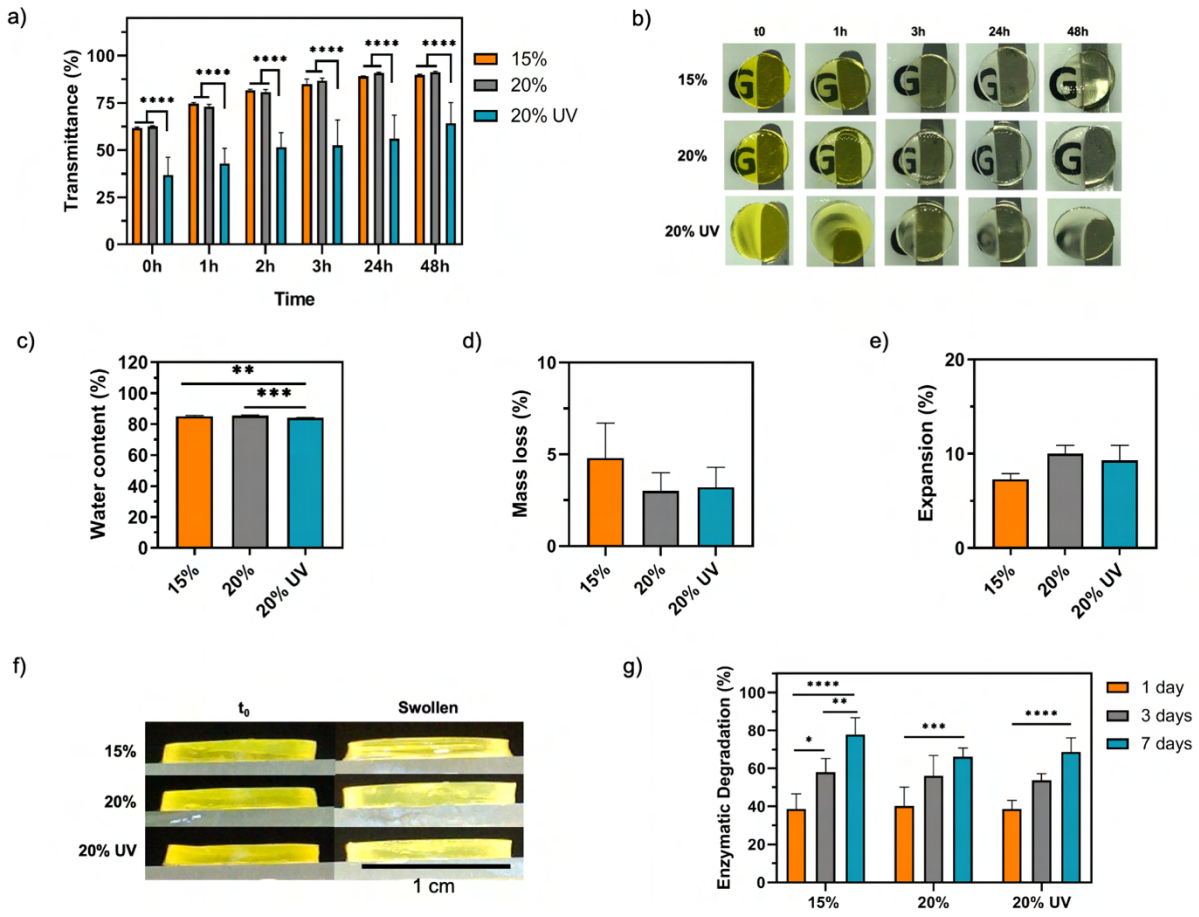


Figure 7.4 *– In vitro characterisation of GelMA bioadhesives. GelMA hydrogels transmittance in the visible range: a) average optical transmittance and b) optical transparency of the hydrogels overtime. Hydrogel diameter = 1 cm. Swelling properties of GelMA hydrogels in PBS at 32 °C: c) equilibrium water content (%), d) mass loss (%), e) expansion (%) in PBS and f) lateral image of the hydrogels after photocrosslinking (t_0) and after 24 h incubation in PBS (swollen). g) In vitro degradation of GelMA hydrogels incubated in 1 U/mL collagenase II at 32 °C for 1, 3 and 7 days. Data are presented as mean value ± SD (* $p < 0.05$, ** $p < 0.01$, *** $p < 0.001$, **** $p < 0.0001$).*

To determine the water content, mass loss and the percentage of expansion, 15, 20 and 20% UV GelMA bioadhesives were incubated in PBS at the ocular temperature for 24 h. The water content was shown to be higher than 84% throughout all groups studied; however, 20% UV (84.1 ± 0.3%) displayed a significantly lower water content than 15% (85.1 ± 0.5%, $p < 0.01$) and 20% (85.5 ± 0.3%, $p < 0.001$) samples (**Figure 7.4**c). Moreover, regardless of polymer concentration or light source used, no significant differences were observed in the percentage

of uncrosslinked monomers within the hydrogel network (mass loss = 3–5%) (**Figure 7.4**d). This result, together with the fact that the material was easily handled in the swollen state (**Figure 7.4**b) and no residual uncured solution could be observed in the mould after curing, suggest complete crosslinking [215]. The expansion of GelMA bioadhesives in PBS was not statistically different between groups, despite ranging from 7.3 ± 0.6% to 10.0 ± 0.9% for 15 and 20% GelMA bioadhesives, respectively ($p > 0.05$) (**Figure 7.4**e). Finally, as shown in **Figure 7.4**f, GelMA bioadhesives displayed minimal volume changes and high dimensional stability in the swollen state.

The susceptibility of GelMA bioadhesives to enzymatic degradation was studied *in vitro* by incubating the hydrogels in 1 U/mL collagenase II for up to 7 days. As shown in **Figure 7.4**g, our results show that there was a time-dependent increase in degradation. After 1 and 2 days, the GelMA bioadhesive degradation was around 39% and 55%, respectively. Although no significant differences were observed between the studied groups, after 7 days, 15% bioadhesives (78 ± 9%) showed a degradation that was around ~10% higher than 20% (66 ± 5%) and 20% UV (68 ± 7%) samples.

The microstructure of GelMA bioadhesives was investigated using SEM and micro-CT analysis. SEM images of the adhesive's surface revealed a uniform and interconnected pore structure for all studied groups (**Figure 7.5**a). Since SEM images suggest that 20% UV bioadhesives have a smaller pore size than 15 and 20% samples, micro-CT was subsequently used to investigate the internal structure of the bioadhesives. As shown in **Figure 7.5**b–d, the pore size distribution was different between the studied groups. The narrower size distribution observed for 20% bioadhesives suggests a negative correlation between polymer concentration and size distribution. Likewise, the light wavelength and intensity used also seem to affect size

distribution as 20% UV bioadhesives showed a narrower size distribution compared to 20%. We observed that, for 20% samples, 19 ± 5% and 20 ± 2% of the pores had 50 and 100 μm, respectively, while the prevalence of 50 and 100 μm pores in 20% UV adhesives was 35 ± 5% and 16 ± 3%, respectively (**Figure 7.5**c,d). As shown in **Figure 7.5**e, the total porosity of 15, 20 and 20% UV bioadhesives was 67 ± 4, 59 ± 6 and 25 ± 3%, respectively. The porosity of 20% UV samples was significantly lower than 15% ($p < 0.0001$) and 20% ($p < 0.001$). Likewise, the structure thickness of 20% UV samples (142 ± 10 μm) was significantly higher than 15% (79 ± 16 μm, $p < 0.01$) and 20% (91 ± 8 μm, $p < 0.01$) bioadhesives (**Figure 7.5**f). Finally, the average pore size of 15, 20 and 20% UV samples was significantly different and equal to 167 ± 24, 118 ± 11 and 74 ± 6 μm, respectively (**Figure 7.5**g).

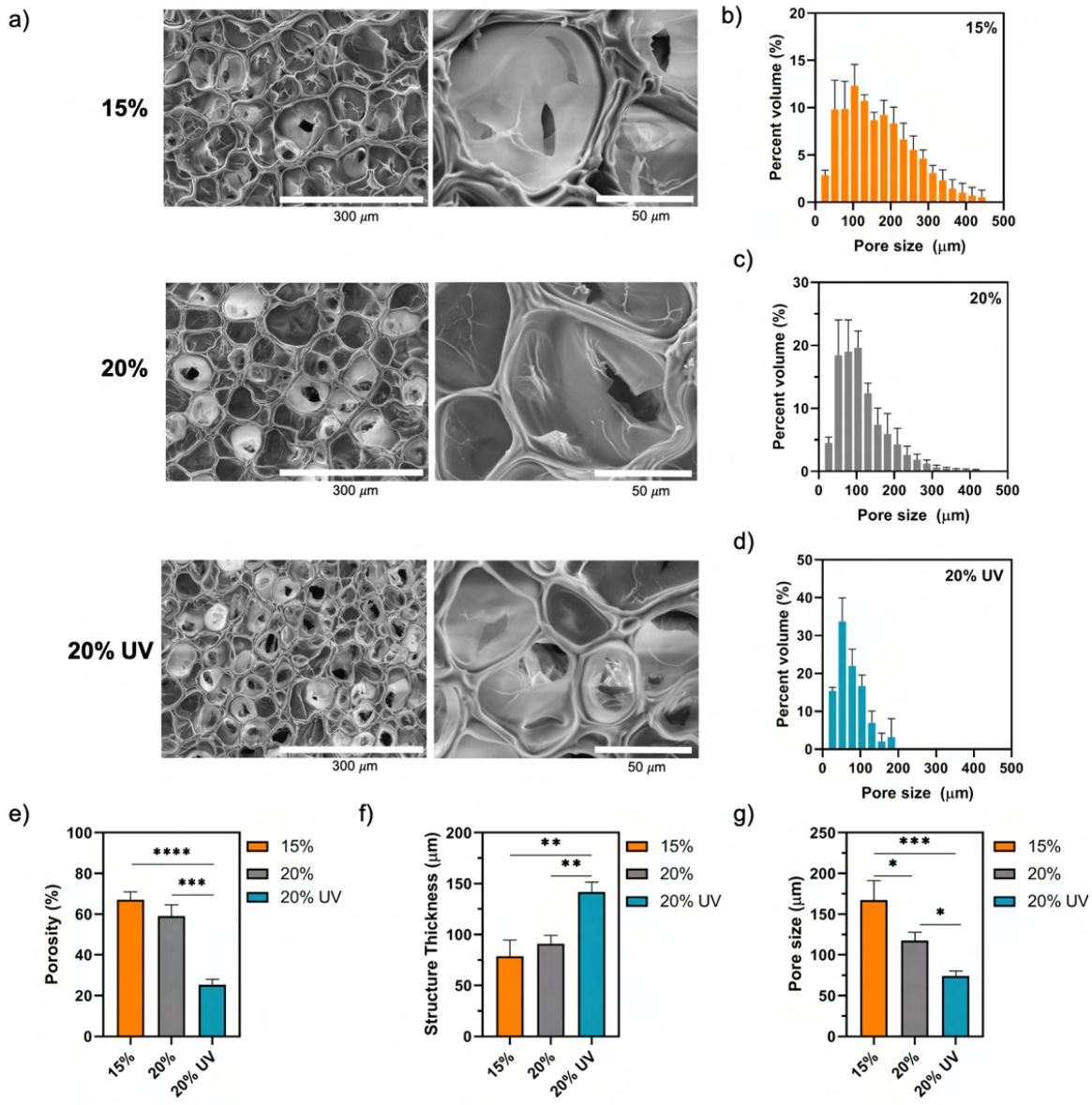


Figure 7.5 *– GelMA bioadhesives morphology and microstructure analysis after freeze drying. a) Representative SEM images of GelMA scaffolds at different magnifications. Quantitative analysis of porosity by micro-CT: b-d) pore size distribution in the hydrogels, e) total porosity, f) mean pore wall thickness and g) mean pore size. Data are presented as mean value ± SD (* $p < 0.05$, ** $p < 0.01$, *** $p < 0.001$ and **** $p < 0.0001$).*

The viscoelastic properties of GelMA bioadhesives were studied via oscillatory rheometry. G' and G'' modulus represent the elastic and reversible response of the material and the viscous and irreversible rearrangement of its polymeric structure, respectively [284,338]. As shown in **Figure 7.6**a,b, a positive correlation between G' and the polymer concentration was observed. 15% bioadhesives (3.4 ± 0.1 kPa) had a 55% lower G' than 20% (5.5 ± 0.9 kPa, $p < 0.05$) and 20% UV (5.2 ± 1.1 kPa, $p < 0.05$). The G'' values were not statistically different between groups, ranging from 107 and 163 kPa (**Figure 7.6**c). Moreover, the damping factor (G''/G') was lower than 0.03 for all the samples (**Figure 7.6**d). Then, the mechanical performance of GelMA bioadhesives was assessed by compressive and tensile mechanical testing (**Figure 7.6**e,g). In agreement with the rheology data, statistical analysis showed a significant effect of polymer concentration on the compressive and tensile moduli (**Figure 7.6**f,h). The compressive modulus of 15% bioadhesives (84 ± 4 kPa) was significantly lower than 20% (207 ± 9 kPa, $p < 0.0001$) and 20% UV (255 ± 25 kPa, $p < 0.0001$) samples, a difference of approximately 3-fold (**Figure 7.6**f). Despite this difference, all groups resisted 8 cycles of 60% strain without apparent damage, demonstrating the mechanical stability of GelMA bioadhesives. Additionally, our results showed that 15% samples (34 ± 9 kPa) exhibited lower tensile modulus than 20% (51 ± 6 kPa, $p < 0.01$) and 20% UV (60 ± 7 kPa, $p < 0.001$) adhesives (**Figure 7.6**h). Higher compressive and tensile moduli were observed for 20% UV samples when compared to 20%; however, only the difference in the compressive moduli was significant ($p < 0.01$). Finally, the ultimate tensile strength of 15, 20 and 20% UV bioadhesives was 36 ± 5, 50 ± 10 and 47 ± 10 kPa, respectively ($p > 0.05$, **Figure 7.6**i), and the maximum elongation was between 130–150% ($p > 0.05$, **Supplementary Figure A.1**).

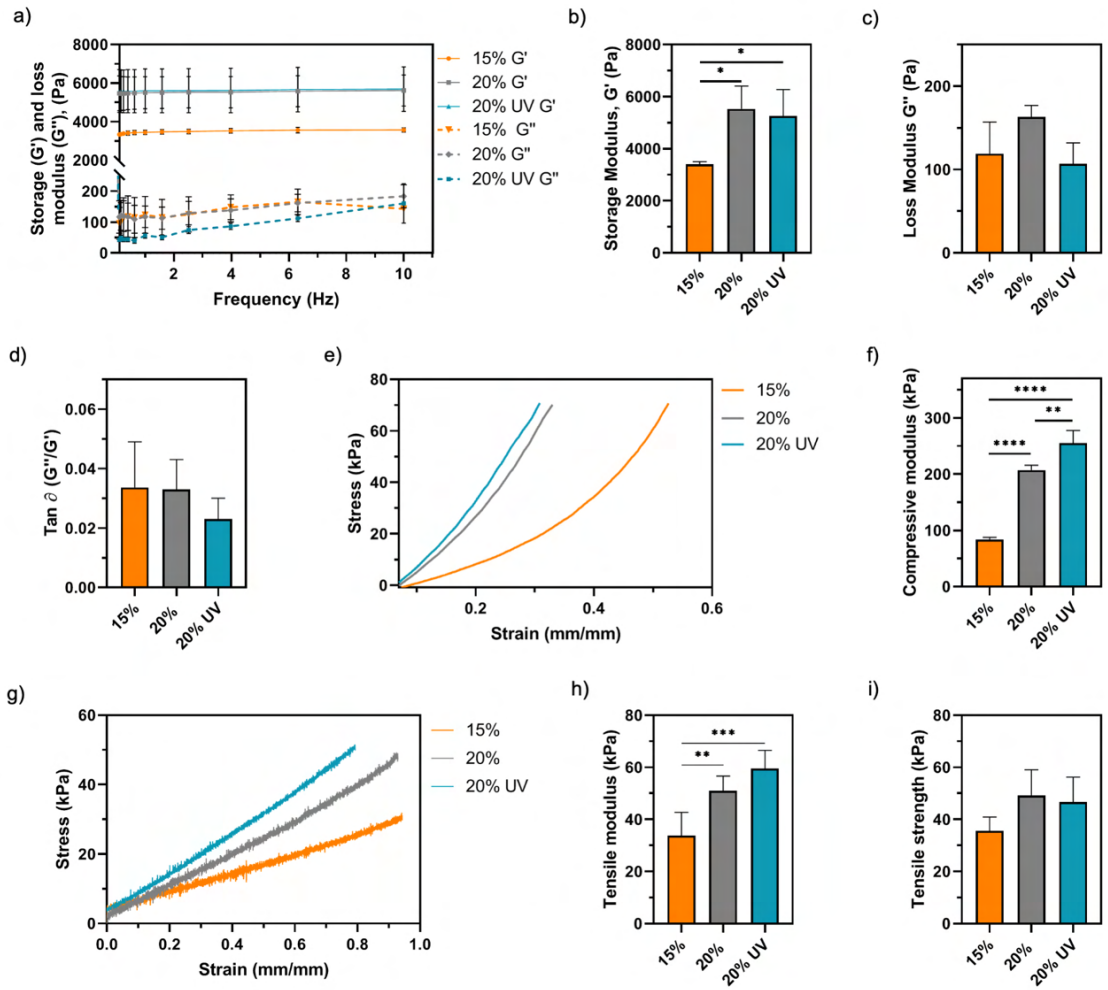


Figure 7.6 *– Rheological properties of GelMA bioadhesives: a) frequency sweep, b) storage modulus (G'), c) loss modulus (G'') and d) damping factor (tan δ). Cyclic compressive mechanical testing of GelMA hydrogels: e) representative compressive stress–strain curves and f) compressive moduli. Tensile mechanical testing of GelMA hydrogels: g) representative tensile stress–strain curves, h) tensile moduli and i) maximum tensile strength. Data are presented as mean value ± SD (* $p < 0.05$, ** $p < 0.01$, *** $p < 0.001$, **** $p < 0.0001$).*

7.3.3 *Ex vivo* retention of GelMA bioadhesives

Next, *ex vivo* analysis was carried out to assess if the GelMA bioadhesive could fill a partial-thickness corneal injury and restore the corneal curvature. We observed that GelMA could be administered to the wound bed as a flowable liquid, fill the injury and adapt to the wound shape

prior to physical crosslinking. As shown in **Figure 7.7**, GelMA bioadhesives formed a smooth contour on the corneal surface. The hydrogel remained optically clear after placement and exhibited excellent adhesion to the corneal tissue. After 24 h, stromal swelling could be observed due to absorption of water by the *ex vivo* cornea. Despite the increasing stromal pressure, all studied groups were retained *in situ*, without any signs of detachment, degradation, or shape loss at day 7.

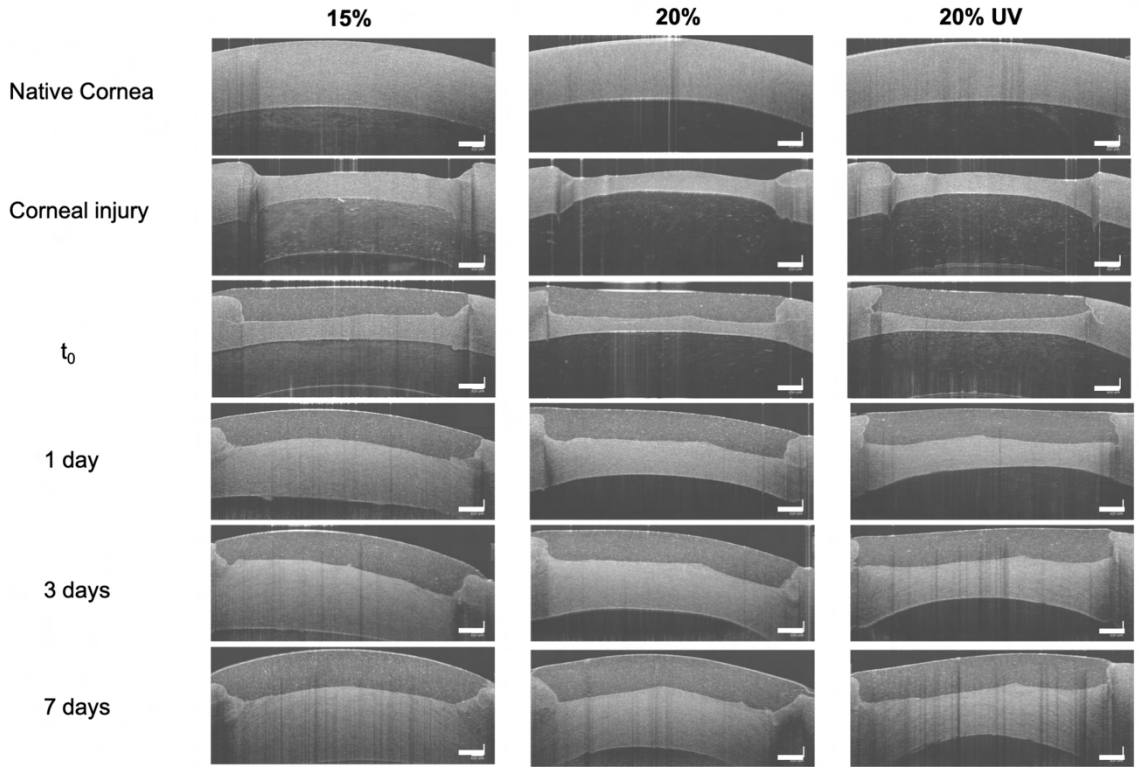


***Figure 7.7** – Ex vivo optical coherence tomography images of the native porcine cornea, partial-thickness corneal injury (≃ 50% deep) and GelMA bioadhesives immediately after photocrosslinking (t_0) and after 1, 3 and 7 days. Scale bar = 500 µm.*

7.3.4 *In vitro* assessment of cytocompatibility

The viability, metabolic activity and proliferation of HDFs seeded on GelMA bioadhesives were evaluated. As shown in **Figure 7.8**a, live/dead images indicate high-cell viability for all tested conditions, with cells exhibiting a fibroblast-like morphology suggesting that GelMA

bioadhesives did not induce toxicity. All groups could support cell attachment and proliferation, with cell confluency being reached within 7 days. Since no dead cells were observed in the live/dead images, the proliferation of cells on the hydrogels was subsequently quantified. The DNA-normalised metabolic activity of HDFs cells seeded on 20% and 20% UV GelMA bioadhesives was slightly higher than 15% samples throughout the experiment (**Figure 7.8**b). However, the difference was only significant between 15 and 20% GelMA bioadhesives at day 7 ($p < 0.05$).

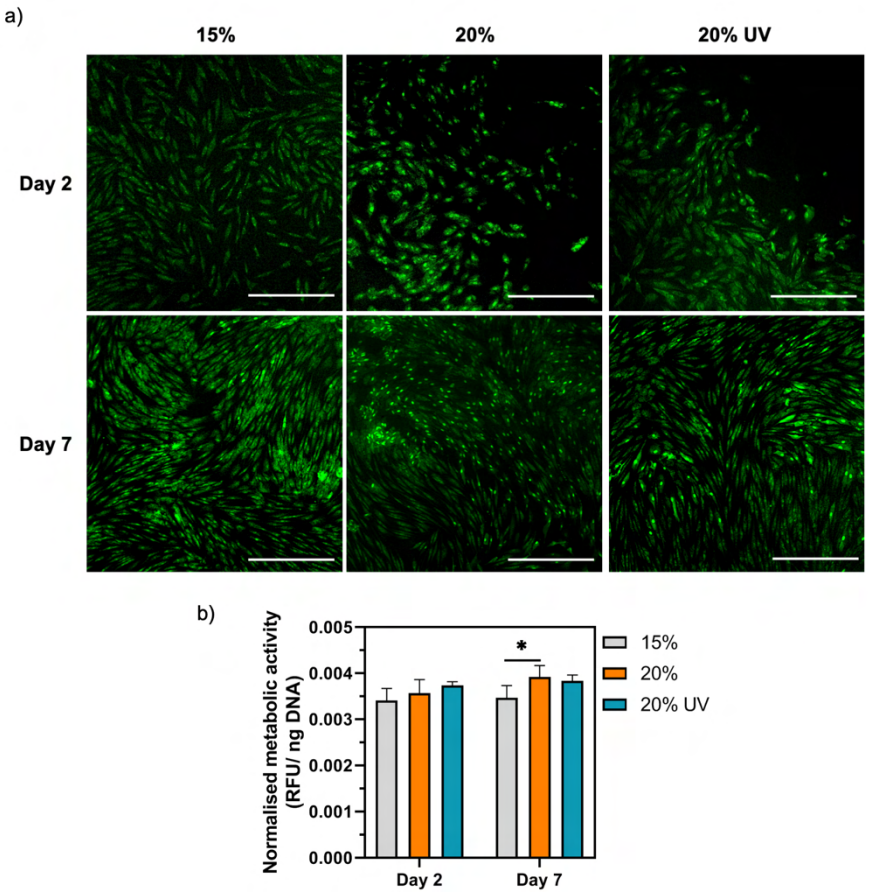


***Figure 7.8** – Cytotoxicity of GelMA hydrogels. a) Live/Dead images of HDFs seeded on GelMA adhesives. Scale bar = 45 µm. b) Normalised metabolic activity 2 and 7 days after cell seeding. Data are presented as mean value ± SD (* $p < 0.05$).*

7.4 Discussion

Currently, there is a clinical need to develop strong and leak-free tissue adhesives that preserve corneal tissue function, decreasing postoperative morbidity and improving patient comfort [4]. While CA glues are toxic and associated with a range of complications, biocompatible fibrin and PEG-based adhesives are weak and degrade quickly making them ineffective to be applied as stromal fillers and for long-term treatments. This study aims to engineer a biocompatible and optically clear GelMA-based stromal filler with the adequate mechanical and adhesive properties to seal full-thickness corneal perforations.

Ease of use and rapid gelation times are essential characteristics for the clinical suitability, acceptance and success of an adhesive. To achieve fast gelation (≤2 min), the photosensitive GelMA prepolymer solution was mixed with RF and SPS. As shown in **Figure 6.3**, RF is a naturally occurring photosensitive molecule with a distinct absorption peak in the UV ($\lambda = 375\,nm$) and visible ($\lambda = 450\,nm$) range, which have high molar extinction coefficients (**Table 6.1**). Photoinitiators with lower extinction coefficients would require longer irradiation times or higher photoinitiators/accelerators concentrations that are incompatible with the desired application given the increased photocrosslinking time and possible cytotoxic effects. In addition, the fact that both visible and UV can trigger the free-radical crosslinking reaction allows the photocrosslinking capability testing of both wavelengths. Since light is a form of electromagnetic energy, depending on its intensity, both UV, visible and infrared light can cause ocular damage [339]. Nevertheless, several ocular structures absorb or scatter some of the light entering the eye, protecting the retina from damage [319]. In this study, the UV wavelength (365 nm) and RF (2.66 mM) concentration were chosen in agreement with CXL therapy [247]. Li et al. used UV radiation (365 nm, 35 mW/cm^2, 2 min) to crosslink a thiol-acrylate hydrogel on a

rabbit's cornea. Post-implantation histological examination did not find any signs of inflammation or tissue damage on the corneal epithelium, stroma or endothelium [58]. Importantly, the photocrosslinking parameters used by Li et al. were very similar to the conditions used in this study to cure 20% UV GelMA (365 nm, 30 mW/cm^2, 2 min). In this study, the photocrosslinking capability of visible light (lower energy) was also assessed through the preparation of 15 and 20% GelMA bioadhesives. Lastly, RF's slow gelation kinetics would be incompatible with the desired application [211]. To overcome this issue, we utilised SPS, an electron acceptor that is reported to enable the fast and safe photocrosslinking of polymers [211,340]. The 15, 20% and 20% UV GelMA bioadhesives were crosslinked under physiological conditions since all components are water soluble and the system RF/SPS is not susceptible to oxygen inhibition. Taken together, we showed the importance of employing the appropriate photoinitiator/curing system on the utility of the corneal adhesive in the clinical setting.

The burst pressure is the most relevant parameter to assess the efficacy of GelMA bioadhesives in sealing full-thickness corneal perforations under liquid pressure. Thus, the mechanical adhesion of GelMA formulations was assessed in porcine eyes and compared with Histoacryl (CA). CA adhesives are proinflammatory, induce corneal vascularisation and scarring, and inhibit corneal tissue regeneration [327]. Still, given its strong adhesion strength, fast polymerisation and ease of use, these adhesives are currently used 'off-label' by ophthalmologists to seal ocular wounds [86]. In this work, no significant differences in the burst pressure were observed between 20 and 20% UV GelMA samples and the control, even though 15% bioadhesives showed a significantly lower burst pressure than Histoacryl. GelMA bioadhesives could withstand on average an IOP between 33 and 49 kPa without leakages, values that are at least 17-fold higher than the human physiological IOP range (2 ± 0.4 kPa, **Figure 7.2**d) [51]. Recently, several different photoinitiator systems have been combined with

GelMA, drastically affecting the final properties of the hydrogels [58,126,150,152,154,164,184,205,206,333,337]. As shown in **Figure 6.7**, the ocular burst pressure obtained using LAP (~11 kPa) was around 4-times lower than RF/SPS (~48 kPa, $p < 0.0001$), highlighting the advantages of using this system when crosslinking GelMA hydrogels.

After surgery and during the healing process the adhesives will be subjected to shear forces due to eyelid and eyeball movements. This will likely cause patient discomfort and potentially result in implant failure. Therefore, we evaluated the physical robustness of our GelMA bioadhesive in satisfying these critical parameters. We employed the *in vitro* lap shear tests to investigate the adhesive's performance on wet and dry substrates. The average shear strength of GelMA bioadhesives was higher than Histoacryl, which was only not significantly lower than 20% GelMA (**Figure 7.3**a). Moreover, GelMA achieved strong adhesion in dry (gelatine-coated glass slides), semi-wet (porcine cornea mounted on ACC) and wet (full-thickness injury in eye) substrates, while Histoacryl was only effective to glue wet substrates. This highlights the versatility of GelMA bioadhesives and supports their suitability to be applied in dynamic *in vivo* conditions.

CAs are reported to fail in adhering to wet surfaces due to their solidification immediately upon exposure to water [333]. The moisture on the ocular surface needs to be carefully controlled and the adhesive rapidly applied, as it might polymerise before entering in contact with the wound bed. Due to this fast (10–60 s) but uncontrolled polymerisation, together with a very low viscosity, the successful application of CA glues remains a challenge and specialised training is required [86]. Nonetheless, fast sealing is of utmost importance as it avoids glue dilution due to continuous fluid egress from the wound. In this study, once the GelMA bioadhesive is heated to 37 °C, the flowable polymer can be added to the ocular injury. After filling the wound bed,

the solution will physically crosslink upon cooling since the ocular temperature is around 32 °C, forming an adhesive plug within seconds. Then, this reversible seal can be chemically crosslinked with light.

As shown in **Supplementary Figure A.2**b, in addition to fail as a stromal filler, Histoacryl also creates a rough and opaque seal that precludes vision and makes the visualisation of infectious infiltrates and wound healing assessment challenging (**Figure 7.2**f) [11]. Usually, a bandage contact lens is often needed to improve patient comfort [86]. In contrast, GelMA adhesives formed a smooth contour and restored the ocular curvature (**Figure 7.7**). The 15 and 20% GelMA adhesives were macroscopically clear with a light-yellow colour after curing and exhibited a transmittance of ~63% (**Figure 7.4**a,b). This lower transmittance value was due to the RF being trapped within the gel absorbing light in the 400–500 nm range (**Supplementary Figure A.3**). Since RF does not participate in the crosslinking reaction, the optical transmittance increases to ~85% after 2–3 h as RF diffuses out of the hydrogel. This value is higher than the reported human corneal transmittance (78–80%) [47,290]. Although the filler will suffer degradation and remodelling *in vivo*, the bioadhesive needs to have similar transmittance to the human cornea to replicate visual acuity. However, 20% UV bioadhesives were opaque with an average transmittance of ~64% (**Figure 7.4**a,b). We observed a 2-fold decrease in the porosity and a significant pore size decrease (~37%) when UV light was used to crosslink 20% GelMA, which are thought to cause light scattering, affecting transparency. Together, our findings indicate the 15 and 20% GelMA bioadhesives show suitable optical properties for corneal engineering applications. Further, as previously reported by Gorth et al., we observed a negative correlation between the porosity and pore size and the tensile and compressive moduli of the adhesive (**Figure 7.6**f,h) [341]. However, the pore structure did not influence the adhesive's burst pressure (**Figure 7.2**b,d).

Lastly, CA adhesives form a water-tight, but inflexible, bond to tissue, which makes its application inadequate for tissues with physiological movement. In the management of ocular perforations, CA glue patching is reported to be successful only when the perforation is smaller than 1 mm and, in 30 to 50% of the cases, the glue needs to be reapplied due to leaks [86,327]. Consequently, an ideal adhesive for corneal perforations needs to be tough, but pliable. Hatami-Marbini studied the dynamic shear properties of corneal stroma using oscillatory experiments, showing that corneal G' and G'' varied from 2 to 8 kPa and 0.3 to 1.2 kPa, respectively [49]. In this work, all formulations exhibited a G' within the mentioned range (3.4 to 5.5 kPa); however, the G'' of our hydrogels was out of range (~0.1 kPa). Importantly, the hydrogels showed a G'' that was an order of magnitude lower than G', confirming the viscoelastic behaviour of GelMA bioadhesives (**Figure 7.6**b,c) [151].

Whilst commercially available fibrin and CA-based adhesives are not approved for ocular use, some PEG-based sealants were granted approval for corneal incision sealing [87,88]. However, it is important to note that these adhesives have not been designed for long-term integration in the cornea. Despite being useful in reinforcing suture sealing, these materials are inappropriate to function as stromal fillers due to poor adhesion, high swelling rates and short retention times (few hours to a couple days). ReSure is the only FDA-approved sealant for intraoperative management of corneal incisions, while OcuSeal is the only option approved in Europe [87,89,342]. Since these sealants are composed by 89% of water, they form a smooth and lubricious surface, avoiding the use of a bandage contact lens for improved comfort [95]. However, they are reported to be sloughed off in tears within 1–4 days due to eyelid movement and PEG hydrolysis/enzymatic degradation [25,86,87,94,342,343]. Additionally, despite exhibiting lower swelling than other PEG-adhesives, the weight increase in ReSure is approximately 35% [89]. Hydrophilic

hydrogels are 3D water-swellable networks. High swelling ratios weaken the mechanical properties, potentiate degradation and impact the overall shape of the adhesives, which might influence sealing and induce pressure on the surrounding tissues. GelMA adhesives showed high dimensional stability with an expansion between 7 and 10%, thereby reducing the risk of implant mismatch (**Figure 7.4**e,f). Additionally, all studied formulations exhibited water content values similar to the human cornea (72–85%) [48,344,345].

Strong adhesion to the host tissue and *in situ* retention are paramount for the success of a bioadhesive [328]. The *ex vivo* retention of GelMA bioadhesives was studied by making a 50% deep corneal injury in porcine corneas. The average thickness of the porcine cornea is approximately 1400 μm, whilst the human cornea is on average 500–700 μm thick (**Supplementary Figure A.2**a) [33]. OCT images show negligible bioadhesive degradation in PBS over the course of the experiment (**Figure 7.7**). Corneal swelling and loss of corneal transparency was observed after 24 h due to *ex vivo* absorption of large amounts of water by the stromal proteoglycans [32,35]. Importantly, 15 and 20% GelMA bioadhesives remained optically clear throughout the experiment. Despite the increased stromal swelling pressure, GelMA bioadhesives remained attached to the cornea demonstrating a strong tissue bond.

The GelMA adhesive strength depends on its cohesion (crosslinking density) and interfacial adhesiveness to the wound bed [328]. Such strong adhesion to the tissue is expected to arise from a synergistic effect between physical interaction (mechanical interlocking to the ECM), covalent bonding, hydrogen bonding and electrostatic and hydrophobic interactions [206,278,334]. As previously reported, the methacrylic/methacryloyl groups on GelMA can react with the thiol and amine groups on the tissue, imparting tissue adhesion due to the formation of chemical bonds between the two surfaces [205]. Furthermore, functional groups on GelMA backbone (e.g.,

-OH, -NH_2) can also form hydrogen bonds with the corresponding component on the tissue interface [330]. Taken together, our results show that GelMA adhesives are dimensionally stable and restore the corneal curvature, while showing a strong adhesion and retained transparency *in vitro*.

As with CAs, the rapid and uncontrollable polymerisation of ReSure and OcuSeal works both in favour and against them. Since these sealants polymerise within 10–20 s after mixing, a late application might result in polymer hardening within the applicator [278]. Conversely, if the adhesive is applied too early, the wound will not be properly sealed due to the low viscosity of the material [25,95]. Before exposure to light, GelMA forms a plug within the wound, but the adhesive is soft and can still be easily removed. The use of light to crosslink GelMA bioadhesives hardens the polymer and allows tuning over the polymerisation rate depending on the desired mechanical properties (chemical crosslinking).

The synergy between the mechanical and biological adhesive characteristics is of utmost importance in the adhesive's success by preventing corneal scarring and vascularisation. Consequently, the absence of cell adhesion moieties in CAs and PEG-based adhesives halts its application as stromal fillers since cell adhesion is an essential step for successful tissue regeneration [89,206]. In this work, a protein-based polymer was chosen due to its biocompatibility, biodegradability and presence of cell adhesion sites (e.g., RGD sequences). Albeit having a negligible degradation in PBS, a time-dependent degradation in the presence of collagenase II was observed, demonstrating the biodegradability of the GelMA adhesives (**Figure 7.4**g). The fact that the bioadhesive can be enzymatically degraded, allowing cells to remodel their environment, is essential for wound repair. According to our results, the engineered hydrogels were not toxic and could support the adhesion and proliferation of HDFs over 7 days,

confirming the cytocompatibility of the adhesive (**Figure 7.8**). These results also confirm that the reagents used in the photocrosslinking reaction (RF/SPS) were not cytotoxic at the concentrations used in this study. Previous studies using similar concentrations of SPS reported that this molecule is rapidly consumed during the photocrosslinking reaction to levels that are not cytotoxic to cells (<20 μM) [164,211].

Recently, some authors have used the Eosin Y/TEA/VC system to photocrosslink GelMA (GelCORE) [126,154] and glycidyl methacrylate-modified gelatine (GELGYM) bioadhesive hydrogels [206]. Both adhesives supported cell adhesion and proliferation. GelCORE effectively sealed corneal defects and induced stromal regeneration and re-epithelisation in a rabbit stromal defect model [126]. Sani et al. compared the burst pressures of ReSure and GelCORE (20% GelMA, Eosin Y, TEA, VC, 100 mW/cm^2, visible light, 4 min) on 2 mm full-thickness injuries on rabbit eyes. The authors obtained a burst pressure of 30 ± 4 and 15 ± 6 kPa for GelCORE and ReSure, respectively [126]. In this study, the average burst pressure GelMA (visible light, 2 min) on a 2 mm full-thickness injury on a porcine cornea was 49 ± 9 kPa (**Figure 7.2**b). Shorter gelling times improve the clinical usability of these adhesives given the importance of rapid polymerisation on the performance and overall acceptance of tissue adhesives [126,154].

To our knowledge, this is the first study to investigate GelMA hydrogel formation via RF/SPS mediated photocrosslinking. We demonstrated that GelMA bioadhesives are effective on both wet and dry substrates, highlighting its versatility and potential to be applied in different physiological conditions. Considering that our optimised formulation (20% GelMA) showed an averaged burst pressure of 49 ± 9 kPa and knowing that the normal physiological and hypertensive blood pressures are approximately 8–19 and 40 kPa, respectively, we hypothesise that GelMA bioadhesives could meet the criteria for vascular sealants [333]. Moreover, GelMA

adhesives could also be assessed as stromal fillers replacing the need for donor corneas in keratoplasty. Finally, the main limitation of GelMA bioadhesives is related with the usability, as both the polymer and RF/SPS need to be reconstituted in PBS and heated to 37 °C and an external light source is required to crosslink the bioadhesive. Due to the difficulty in replicating *in vitro* the ocular complex physiological environment, long-term experiments in an *ex vivo* ocular model or *in vivo* will be required to further evaluate the intrinsically linked physical and biological attributes of these photocurable bioadhesives, such as light effect in retinal toxicity, cytotoxicity, host response and the adhesive performance and degradation in the eye (ocular movements, blinking and tear film). The delivery of antibiotics, growth factors or anti-inflammatory agents from GelMA bioadhesives should be considered in the future since the biopolymer hydrophilic nature provides a solubilising environment for the incorporation of many bioactive molecules.

7.5 Conclusion

This work describes the synthesis and characterisation of a novel protein-based bioadhesive for the treatment of corneal perforations. The injectable bioadhesive, composed of GelMA and a RF/sodium persulfate photoinitiator system, can be photocrosslinked *in situ* within 2 min using either UV or visible light. *Ex vivo* experiments in porcine eyes demonstrated complete sealing of full-thickness corneal perforations in the absence of sutures. The engineered adhesive has high translational potential due to its superior adhesion to both wet and dry substrates, outstanding physical properties, viscoelasticity and cytocompatibility in comparison to the commercially available options (e.g., fibrin glue, ReSure and cyanoacrylates).

CHAPTER EIGHT

8 Conclusions and Future Work

8.1 General overview

Due to a worldwide corneal tissue shortage and off-label use of toxic tissue adhesives, tissue-engineered hydrogels are being investigated as an alternative source. While biosynthetic corneal substitutes can be implanted reducing the demand for donor human corneal tissue, stromal fillers and tissue adhesives can be cured *in situ* preventing corneal scarring and vascularisation caused by toxic adhesives. Ideally, these materials should be transparent, mechanically strong, allow the diffusion of oxygen and nutrients and be compatible with cell encapsulation. In addition, tissue adhesives must be injectable, crosslink *in situ* within seconds to a few minutes without heat production and strongly adhere to the corneal tissue.

Biopolymers are very attractive materials for tissue engineering and bioink ink development due to their proven biocompatibility, biodegradation and tailorable physicochemical properties. However, the challenge of developing semi-synthetic polymers that exhibit suitable mechanical properties while preserving their advantageous biological cues due to minimal usage of synthetic additives and chemical modifications remains unmet.

In this thesis, the development and characterisation of silk and gelatine-based photosensitive hydrogels for corneal tissue engineering applications have been reported. Inspired by the importance of pH changes during silk's *in vivo* processing, chapter 4 builds a fundamental understanding of the prepolymer solution pH on the impact of the initial protein secondary

structure and studies the spontaneous conformation transitions under physiological conditions and the mechanical toughening impact of β-sheet crystallinity. This chapter highlights the need to strictly control the pH of SilkMA prepolymer solutions to enhance reproducible manufacture, thereby increasing the potential clinical adoption of chemically crosslinked silk-based hydrogels. Further, silk-based materials are very attractive for ocular tissue engineering applications due to the outstanding mechanical and optical properties of silk proteins. Chapter 5 details the characterisation of gentamicin-loaded SilkMA hydrogels for corneal repair. It was been confirmed that the chemical modification of silk fibroin with vinyl groups did not have a detrimental effect on the biodegradability and cytocompatibility of the material. Then, the efficacy SilkMA hydrogels against clinically relevant bacteria were tested *in vitro*. SilkMA hydrogels were optically transparent, mechanically robust, showed water content values similar to the human cornea and could successfully inhibit bacterial growth. Taken together, our results demonstrate the potential of SilkMA-LAP systems for tissue engineering applications since it allows crosslinking of hydrophilic and strong hydrogels within minutes under mild environmental conditions.

Finally, in an effort to develop a corneal adhesive (chapter 6), different SilkMA and GelMA prepolymer solutions were tested in combination with several photoinitiators and photocrosslinking conditions (wavelength, intensity and exposure times). The adhesive strength, and ability to fill the injury and restore the corneal curvature were studied *ex vivo* after creating 2-mm full-thickness corneal perforation on a porcine eyeball. While SilkMA hydrogels failed as tissue sealants, GelMA-RF/SPS hydrogels exhibited strong adhesion to corneal collagen together with minimal degradation in PBS at 37°C over 7 days. Lastly, chapter 7 focused on the characterisation of the formulations previously optimised. Similarly to SilkMA, GelMA hydrogels were non-toxic and could support cell adhesion and proliferation. Before

exposure to light, GelMA forms a plug within the wound due to physical crosslinking, however, at this point, the hydrogel can still be easily removed. The use of light chemically crosslinks the polymer and allows tuning over the polymerisation rate. The optimal formulation (20% GelMA-RF/SPS, visible light, 2 minutes) formed a smooth and transparent seal that showed superior adhesion to both wet and dry substrates, exhibiting an average burst pressure of 49 ± 9 kPa on the porcine eyeball. In contrast, a cyanoacrylate-based adhesive (Histoacryl) formed an opaque and rough patch and showed no adhesion onto semi-dry corneal tissue, despite showing a burst pressure higher than 50 kPa on the eyeball. Considering these properties, GelMA-RF/SPS hydrogels might be used for several ophthalmologic applications:

i. Ocular adhesive for corneal, corneoscleral or scleral injuries;
ii. Corneal glue to reinforce sutures or facilitate sutureless grafting in keratoplasties;
iii. Stromal substitutes replacing the need for human corneal tissue.

Finally, the injectability and the high burst pressures obtained on a leaking corneal injury, suggest that these bioadhesives could also be applied in different physiological conditions, such as cosmetic and vascular surgery.

8.2 Overarching future work

8.2.1 *Ex vivo* and *in vivo* studies

In this work, the cytocompatibility of the SilkMA solutions and photocrosslinked SilkMA and GelMA hydrogels was assessed *in vitro* using HDFs. However, the *in vitro* set-up used is not representative of the ocular complex physiological environment that includes the presence of tear film and shear forces due to ocular movements and blinking. Therefore, to further evaluate the physical and biological attributes of SilkMA and GelMA hydrogels, such as the effect of

the curing light on retinal toxicity, cytotoxicity, host response and hydrogel behaviour and degradation, these materials need to be tested using an *ex vivo* model (e.g. porcine model [346]) or *in vivo* [126]. While *ex vivo* studies would be useful to study the biocompatibility of the constructs using corneal cells (e.g. epithelial adhesion and migration over the hydrogel), only *in vivo* experiments are representative of the dynamic ocular environment and, therefore, suitable to assess *in situ* retention time and hydrogel degradation. Rabbits are currently the most commonly used animals to study *in vivo* corneal wound healing, however, the rabbit cornea lacks the Bowman's membrane, which limits the utility of the studies for epithelial wound healing or topical drug delivery [324,347]. Consequently, in the future, the chicken cornea (White Leghorn Chicken) might be used since it is more representative of corneal morphology and physiology [324].

8.2.2 Drug delivery

The hydrophilic character of SilkMA and GelMA hydrogels provides a solubilizing environment for the incorporation of bioactive molecules, such as antibiotics and growth factors. Herein, the *in vitro* antimicrobial activity of gentamicin-loaded SilkMA hydrogels against *Staphylococcus aureus* and *Pseudomonas aeruginosa* was studied. However, in addition to possessing antimicrobial activity, an ideal corneal substitute/adhesive must be able to prevent vascularisation, scarring and corneal melting. Therefore, future investigations might consider incorporating:

i. Anti-VEGF agents used to treat ocular angiogenesis (e.g. pegaptanib, ranibizumab, and aflibercept) [348–350];
ii. Decorin, a small leucine-rich proteoglycan and anti-scarring agent that attenuates scarring by regulating TGFβ activity and collagen fibril spacing [351,352];
iii. Enzyme inhibitors (e.g. anti-collagenases, anti-MMPs) to prevent corneal melting [353,354].

The water solubility, drug quantity necessary to observe a therapeutic effect and the impact of the substance on the hydrogel optical transmittance should be considered.

8.2.3 3D printing

3D printing technology aims to deposit biomaterials laden with cells and bioactive molecules in a precise layer-by-layer fashion, in order to bioengineer tissues and organs [355]. In particular, lithography-based techniques, enable the fabrication of complex and patterned structures that cannot be produced by extrusion-based bioprinting with significantly greater resolution (25- 50 μm) [157]. Given the prepolymer flowability, fast curing kinetics and robust mechanical properties of SilkMA and GelMA hydrogels future studies might investigate the suitability of these formulations for corneal bioprinting by:

i. Developing a human corneal digital model (g-code);
ii. Testing the printability of cell-laden SilkMA and GelMA using different formulations (e.g. photoinitiator type and concentration) and fabrication settings (e.g. light energy, exposure time and resolution);
iii. Understanding of the prepolymer composition effect and fabrication settings on the overall physical, mechanical and biological properties of the constructs.

8.3 SilkMA hydrogel development

8.3.1 Main limitations

SF is a natural fibrous protein that has been recently studied for several tissue engineering applications due to its outstanding mechanical properties, aqueous processing, ease of modification and biocompatibility. In recent years, the chemically crosslinked silk-based hydrogels via light-mediated (e.g. di-tyrosine bond formation [215], methacrylation [151]) or

enzymatic-based crosslinking [194] allowed a wider application of silk-based hydrogels in the field. Contrary to physically crosslinked silk-hydrogels, chemically crosslinked polymers can be quickly prepared under physiological conditions as no harsh environmental conditions (e.g. vortexing, methanol treatment, low pH) are required to induce gelation. However, SilkMA hydrogels show several drawbacks related to the intrinsic properties of the protein and crosslinking mechanism used, such as:

8.3.1.1 Limited biological activity

Bombyx mori silk contains a fibroblast growth-promoting peptide in the N terminal, however, due to the absence of cell-binding RGD sequences that are involved in cell-substrate attachment, *B.mori* silk shows limited initial cellular response [185]. Therefore, silkworm silks containing this sequence, such as the non-mulberry silkworms *Antheraea mylitta* and *Philosamia ricini* together with other polymers, such as gelatine or collagen, show enhanced cellular adhesion and viability in comparison to *B.mori* silk [185,250].

8.3.1.2 Low content of lysine residues

As previously reported, SF contains 0.2 mol% of lysine residues which are likely the main site for the introduction of GMA into the protein backbone [151]. ^{1}H-NMR spectroscopy revealed that GMA was successfully grafted to 35-40% of these residues. On the other hand, gelatine exhibits a 13-fold higher lysine content (2.65 mol%) and 60% of those residues were functionalised with MA [151,317]. Even though both SilkMA and GelMA yielded robust hydrogels, the number of methacrylate groups grafted into the polymer affects the final physical and mechanical properties of the hydrogel. Indeed, 15% GelMA hydrogels exhibited a 4-fold higher compressive modulus (84 ± 4 kPa**, Figure 7.6**f) together with a 4 times lower expansion in PBS

(7 ± 1%, **Figure 7.4**e) when compared to 15% SilkMA (21 ± 2 kPa**, Figure 5.4**d and 29 ± 7%, **Figure 5.2**f, respectively), suggesting a higher crosslink density.

8.3.1.3 Free-radical polymerisation reaction inhibition by oxygen

Oxygen is reported to inhibit photo-initiated polymerization of acrylamide and acrylate-based chemistries [157,159]. This effect can be avoided by increasing the irradiation dosage, photoinitiator concentration or by photocuring the samples in a closed mould or an oxygen-free atmosphere (e.g. nitrogen, argon) [157]. Despite not observing any oxygen inhibition issues when photocuring GelMA/RF-SPS hydrogels using visible light, SilkMA-LAP hydrogels could only be prepared using a low UV intensity (3 mW/cm^2) under an inert atmosphere. When 10 times higher intensity was used (30 mW/cm^2) no inhibitory effect was observed.

Consequently, this oxygen inhibitory effect represents a limitation to the use of SilkMA gels in situations that require UV light intensity to be minimised (e.g. *in situ* cured corneal scaffolds). Importantly, this effect is not observable when the hydrogels are placed in a closed mould or 3D printed using DLP.

8.3.1.4 Transparency decrease overtime

Silk fibroin films have been extensively explored for ocular applications due to their transparent nature. Herein, we developed SilkMA hydrogels that exhibited a light transmittance between 82-92% depending on the prepolymer solution pH (**Figure 4.2**b). However, we have demonstrated that SilkMA hydrogels become increasing opaque over time as the protein crystallinity increases due to a hydrophobic β-sheet content rise (**Figure 4.5**b). Even though this effect can be delayed by using a prepolymer solution with a slightly basic pH (**Figure 4.5**a),

the decrease in the optical clarity of the constructs represents a drawback for the application of SilkMA hydrogels as long-term corneal substitutes.

8.3.2 Future applications

8.3.2.1 Cartilage tissue engineering

In addition to increasing the opacity of the gels, the increasing beta-sheet content also has a toughening impact that might be advantageous to engineer stiffer tissues. The compressive modulus of SilkMA pH 5 hydrogels rose from 40 kPa to 1.1 MPa in 2 weeks **(Figure 4.5**c). Since recent studies have demonstrated that HRP-crosslinked and light crosslinked (Ru/SPS) silk-based hydrogels can support the long-term culture of human chondrocytes, future studies could investigate the suitability of SilkMA hydrogels for cartilage tissue engineering [215].

8.3.2.2 Hydrogel adhesives

SilkMA-LAP hydrogels were optically clear, stretchable and sticky, exhibiting high shear strength on both wet and dry conditions. As shown in **Figure 8.1**, the shear strength of SilkMA hydrogels was significantly higher than Histoacryl, ranging from 192-245 kPa and 272-398 kPa on wet and dry substrates, respectively. Therefore, future studies might investigate the application of transparent SilkMA hydrogels for tissue engineering applications that require adhesion between hydrogel surfaces, coatings for medical devices or skin adhesives.

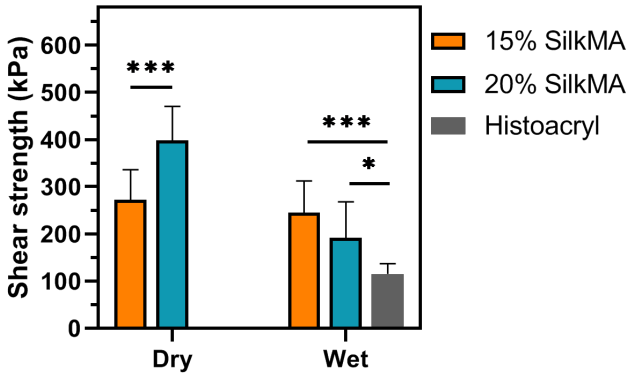


Figure 8.1 *- In vitro shear strength of 15 and 20% SilkMA hydrogels (3 mW/cm² UV-light, 5 min) and Histoacryl in wet and dry conditions (n=7). Data presented as mean value ± SD (* $p < 0.05$, *** $p < 0.001$).*

8.4 GelMA adhesive development

8.4.1 Curing time optimisation

In this work, the *in situ* burst pressure of different SilkMA and GelMA prepolymer solutions photocrosslinked using different light energy, intensity and curing time was measured *ex vivo*. The selected optimised formulations exhibited high burst pressures since this property is a measure of the cohesive strength of the hydrogel. However, future investigations should assess the kinetics of gelation for different GelMA/RF-SPS formulations using *in situ* photorheology as this technique allows monitoring of the crosslinking reaction mechanics over time. Upon irradiation, the storage modulus increases due to the gelation of the prepolymer solution into an elastic hydrogel. Therefore, different light intensities and polymer and initiating systems can be compared. For each system, the gelation point is defined as the G' cross over G'', while complete crosslinking occurs when a plateau in the storage modulus is observed [211]. Consequently, photorheology allows *in situ* determination of the maximum G' and the minimum time (optimal curing time) required to reach this value. The determination of the

minimal irradiation time is essential to increase the clinical acceptance since shorter gelling times improve the usability and performance of these adhesives.

8.4.2 Burst pressure for different wound sizes and locations in the cornea and sclera

The burst pressure is the primary efficacy test relevant to studying the hydrogel capacity to withstand relevant physiological pressures. In this work, circular penetrating wounds were made by inserting a 2-mm trephine perpendicularly to the central cornea. Future studies should consider testing the GelMA adhesive performance in linear (using scalpel blades) and circular open wounds in corneal, corneoscleral and scleral regions. Further, it has been previously reported that the burst pressure is inversely proportional to the perforation size [123,206]. Consequently, the minimum and maximum full-thickness perforation sizes that GelMA adhesives can seal should be investigated. A successful repair is defined as a sealed defect that allows ocular pressurization to 4.5 kPa or greater since the normal IOP is lower than 2.8 kPa and the ocular hypertension values range from 2.9 to 4.4 kPa [356,357].

8.4.3 Potential application of GelMA-RF/SPS hydrogels for vascular and lung sealing

The obtained burst pressure of GelMA bioadhesives was higher than the human hypertensive blood pressure (40 kPa) and the maximum pressure exerted on the lung during breathing (0.13-0.27 kPa) [278,333]. This result, together with GelMA's wet tissue adhesion and flexibility, suggests that GelMA bioadhesives could fulfil the requirements of vascular adhesives and lung sealants. In vascular surgery, it is of utmost importance that tissue adhesives also act as hemostats thereby preventing blood loss by facilitating clot formation [332]. Thus, combined with a haemostatic agent, GelMA adhesives could be effective to stop bleeding and quickly seal the vascular injuries, reducing the surgical time, invasiveness and failure associated with suture and staples

application in friable and elastic tissues [332]. On the other hand, lung sealants should be highly elastic with a modulus in the range of 5-30 kPa when deformed at physiologically relevant rates [278,358]. The high tensile modulus (34-60 kPa, **Figure 7.6**h) and elongation (130-150%, **Supplementary Figure A.1**) of GelMA/RF-SPS adhesives suggest that these materials could be suitable for lung incision sealing. Progel, an FDA-approved pleural air leak sealant approved to be used in conjunction with sutures, is reported to have a low burst pressure (4.3 kPa) and a tensile strength (42 kPa) comparable to GelMA (36-50 kPa, **Figure 7.6**i) [278]. However, to accurately compare the performance of these materials, the same setup and polymer volume should be used.

LIST OF REFERENCES

1. Mehdizadeh, M. & Yang, J. Design Strategies and Applications of Tissue Bioadhesives. *Macromol. Biosci.* **13,** 271–288 (2013).
2. Singer, A. J. & Thode, H. C. A review of the literature on octylcyanoacrylate tissue adhesive. *Am. J. Surg.* **187,** 238–248 (2004).
3. Antonio Lauto, D. M. and L. J. F. Adhesive biomaterials for tissue reconstruction. *J. Chem. Technol. Biotechnol.* **83,** 1163–1169 (2008).
4. Bhatia, S. K. *Biomaterials for Clinical Applications. Springer* (Springer, 2010).
5. Assmann, A., Vegh, A., Ghasemi-Rad, M., Bagherifard, S., Cheng, G., Sani, E. S., Ruiz-Esparza, G. U., Noshadi, I., Lassaletta, A. D., Gangadharan, S., Tamayol, A., Khademhosseini, A. & Annabi, N. A highly adhesive and naturally derived sealant. *Biomaterials* **140,** 115–127 (2017).
6. Annabi, N., Yue, K., Tamayol, A. & Khademhosseini, A. Elastic sealants for surgical applications. *Eur. J. Pharm. Biopharm.* **95,** 27–39 (2015).
7. Petrie, E. M. Cyanoacrylate adhesives in surgical applications: A critical review. *Rev. Adhes. Adhes.* **2,** 253–310 (2014).
8. Tan, J., Foster, L. J. R. & Watson, S. L. Corneal Sealants in Clinical Use: A Systematic Review. *Curr. Eye Res.* **00,** 1–6 (2020).
9. Hashemi, H. & Dadgostar, A. Automated lamellar therapeutic keratoplasty with fibrin adhesive in the treatment of anterior corneal opacities. *Cornea* **30,** 655–659 (2011).
10. Kaufman, H. E., Insler, M. S., Ibrahim-Elzembely, H. A. & Kaufman, S. C. Human Fibrin Tissue Adhesive for Sutureless Lamellar Keratoplasty and Scleral Patch Adhesion: A Pilot Study. *Ophthalmology* **110,** 2168–2172 (2003).
11. Bhatia, S. S. Ocular surface sealants and adhesives. *Ocul. Surf.* **4,** 146–154 (2006).
12. Webster Jr., R. G., Slansky, H. H., Refojo, M. F., Boruchoff, S. A. & Dohlman, C. H. The Use of Adhesive for the Closure of Corneal Perforations: Report of Two Cases. *Arch. Ophthalmol.* **80,** 705–709 (1968).
13. Meskin, S. W., Ritterband, D. C., Shapiro, D. E., Kusmierczyk, J., Schneider, S. S., Seedor, J. A. & Koplin, R. S. Liquid bandage (2-octyl cyanoacrylate) as a temporary wound barrier in clear corneal cataract surgery. *Ophthalmology* **112,** 2015–2021 (2005).

14. Shigemitsu, T. & Majima, Y. The utilization of a biological adhesive for wound treatment: Comparison of suture, self-sealing sutureless and cyanoacrylate closure in the tensile strength test. *Int. Ophthalmol.* **20,** 323–328 (1997).
15. Leung, G. Y. S., Peponis, V., Varnell, E. D., Lam, D. S. C. & Kaufman, H. E. Preliminary in vitro evaluation of 2-octyl cyanoacrylate (Dermabond®) to seal corneal incisions. *Cornea* **24,** 998–999 (2005).
16. Zalta, A. H. & Wieder, R. H. Closure of leaking filtering blebs with cyanoacrylate tissue adhesive. *Br. J. Ophthalmol.* **75,** 170–173 (1991).
17. Leahey, A. B., Gottsch, J. D. & Stark, W. J. Clinical Experience with N-butyl Cyanoacryiate (Nexacryl) Tissue Adhesive. *Ophthalmology* **100,** 173–180 (1993).
18. Cavanaugh, T. B. & Gottsch, J. D. Infectious keratitis and cyanoacrylate adhesive. *Am. J. Ophthalmol.* **111,** 466–472 (1991).
19. Ferry, A. P. & Barnert, A. H. Granulomatous Keratitis Resulting From use of Cyanoacrylate Adhesive for Closure of Perforated Corneal Ulcer. *Am. J. Ophthalmol.* **72,** 538–541 (1971).
20. Gary D Markowitz, MD; Stephen E Orlin, MD; William C Frayer, MD; Anthony P Andrews, MD; Richard B Prince, M. Corneal Endothelial Polymerization of Histoacryl Adhesive: A Report of a New Intraocular Complication. *Ophthalmic Surgery, Lasers Imaging Retin.* **26(3),** 256–258 (1995).
21. Siegal, J. E. & Zaidman, G. W. Surgical removal of cyanoacrylate adhesive after accidental instillation in the anterior chamber. *Ophthalmic Surg.* **20,** 179–181 (1989).
22. Panda, A., Kumar, S., Kumar, A., Bansal, R. & Bhartiya, S. Fibrin glue in ophthalmology. *Indian J. Ophthalmol.* **57,** 371 (2009).
23. Jhanji, V., Young, A. L., Mehta, J. S., Sharma, N., Agarwal, T. & Vajpayee, R. B. Management of Corneal Perforation. *Surv. Ophthalmol.* **56,** 522–538 (2011).
24. Natour, E., Suedkamp, M. & Dapunt, O. E. Assessment of the effect on blood loss and transfusion requirements when adding a polyethylene glycol sealant to the anastomotic closure of aortic procedures: a case-control analysis of 102 patients undergoing Bentall procedures. *J. Cardiothorac. Surg.* **7,** 1 (2012).
25. Uy, H. S. & Kenyon, K. R. Surgical outcomes after application of a liquid adhesive ocular bandage to clear corneal incisions during cataract surgery. *J. Cataract Refract. Surg.* **39,** 1668–1674 (2013).
26. Brunette, I., Roberts, C. J., Vidal, F., Harissi-Dagher, M., Lachaine, J., Sheardown, H.,

Durr, G. M., Proulx, S. & Griffith, M. Alternatives to eye bank native tissue for corneal stromal replacement. *Prog. Retin. Eye Res.* **59,** 97–130 (2017).

27. Meek, K. M. & Knupp, C. Corneal structure and transparency. *Prog. Retin. Eye Res.* **49,** 1–16 (2015).
28. Mobaraki, M., Abbasi, R., Vandchali, S. O., Ghaffari, M., Moztarzadeh, F. & Mozafari, M. Corneal repair and regeneration: Current concepts and future directions. *Front. Bioeng. Biotechnol.* **7,** 1–20 (2019).
29. Jhanji, V., Young, A. L., Hons, M., Mehta, J. S., Sharma, N., Agarwal, T., Vajpayee, R. B. & Edin, F. Management of Corneal Perforation. *Surv. Ophthalmol.* **56,** 522–538 (2011).
30. Rana, M. & Savant, V. Contact Lens & Anterior Eye A brief review of techniques used to seal corneal perforation using cyanoacrylate tissue adhesive. *Contact Lens Anterior Eye* **36,** 156–158 (2013).
31. Leonard A Levin MD PhD, Siv F. E. Nilsson PhD, James Ver Hoeve MD, Samuel Wu MD, Paul L. Kaufman MD, A. A. M. *Adler's Physiology of the Eye:* (Saunders, 2011).
32. Oie, Y. & Nishida, K. Corneal regenerative medicine. *Regen. Ther.* **5,** 40–45 (2016).
33. Frederick S. Brightbill MD, Peter J. McDonnell MD, Charles N. J. McGhee MB PhD, Ayad A. Farjo MD, O. S. M. *Corneal Surgery: Theory Technique and Tissue. Mosby* (2009).
34. Khosravimelal, S., Mobaraki, M., Eftekhari, S., Ahearne, M., Seifalian, A. M. & Gholipourmalekabadi, M. Hydrogels as Emerging Materials for Cornea Wound Healing. *Small* **2006335,** (2021).
35. Huang, Y. X. Corneal tissue engineering. *Biointegration Med. Implant Mater. Sci. Des.* 86–115 (2010).
36. Chen, Z., You, J., Liu, X., Cooper, S., Hodge, C., Sutton, G., Crook, J. M. & Wallace, G. G. Biomaterials for corneal bioengineering. *Biomed. Mater.* **13,** (2018).
37. Espana, E. M. & Birk, D. E. Composition, structure and function of the corneal stroma. *Exp. Eye Res.* **198,** 108137 (2020).
38. Matthyssen, S., Bogerd, B. Van Den, Ní, S., Koppen, C. & Zakaria, N. Corneal regeneration : A review of stromal replacements. *Acta Biomater.* **69,** 31–41 (2018).
39. Maurice, B. Y. D. M. The structure and transparency of the cornea. *J. Physiol.* 263–286 (1957).
40. Kotecha, A. What Biomechanical Properties of the Cornea Are Relevant for the

Clinician? *Surv. Ophthalmol.* **52,** 109–114 (2007).

41. Wilson, S. E., Mohan, R. R., Mohan, R. R., Ambro, R., Hong, J. & Lee, J. Corneal wound healing response - cytokine mediated interaction of epithelium stroma and inflammatory cells. **20,** 625–637 (2001).
42. Ljubimov, A. V. & Saghizadeh, M. Progress in corneal wound healing. *Prog. Retin. Eye Res.* **49,** 17–45 (2015).
43. Chaurasia, S., Lim, R., Lakshminarayanan, R. & Mohan, R. Nanomedicine Approaches for Corneal Diseases. *J. Funct. Biomater.* **6,** 277–298 (2015).
44. Kamil, S. & Mohan, R. R. Corneal stromal wound healing: Major regulators and therapeutic targets. *Ocul. Surf.* **19,** 290–306 (2021).
45. Tan, J. H., Ng, E. Y. K., Rajendra Acharya, U. & Chee, C. Infrared thermography on ocular surface temperature: A review. *Infrared Phys. Technol.* **52,** 97–108 (2009).
46. Coles, W. H. & Jaros, P. A. Dynamics of ocular surface pH. *Br. J. Ophthalmol.* **68,** 549–552 (1984).
47. Rafat, M., Li, F., Fagerholm, P., Lagali, N. S., Watsky, M. A., Munger, R., Matsuura, T. & Griffith, M. PEG-stabilized carbodiimide crosslinked collagen-chitosan hydrogels for corneal tissue engineering. *Biomaterials* **29,** 3960–3972 (2008).
48. Taylor, Z. D., Garritano, J., Sung, S., Bajwa, N., Bennett, D. B., Nowroozi, B., Tewari, P., Sayre, J. W., Hubschman, J.-P., Deng, S. X., Brown, E. R. & Grundfest, W. S. THz and mm-Wave Sensing of Corneal Tissue Water Content: Electromagnetic Modeling and Analysis. *Physiol. Behav.* **176,** 139–148 (2016).
49. Hatami-Marbini, H. Viscoelastic shear properties of the corneal stroma. *J. Biomech.* **47,** 723–8 (2014).
50. Elsheikh, A., Wang, D., Brown, M., Rama, P., Campanelli, M. & Pye, D. Assessment of corneal biomechanical properties and their variation with age. *Curr. Eye Res.* **32,** 11–19 (2007).
51. Wang, Y. X., Xu, L., Wei, W. Bin & Jonas, J. B. Intraocular pressure and its normal range adjusted for ocular and systemic parameters. The Beijing eye study 2011. *PLoS One* **13,** 1–16 (2018).
52. Spotnitz, W. D. & Burks, S. Hemostats, sealants, and adhesives: Components of the surgical toolbox. *Transfusion* **48,** 1502–1516 (2008).
53. Zheng, K., Gu, Q., Zhou, D., Zhou, M. & Zhang, L. Recent progress in surgical adhesives for biomedical applications. *Smart Mater. Med.* **3,** 41–65 (2022).

54. Spotnitz, W. D. Fibrin Sealant: The Only Approved Hemostat, Sealant, and Adhesive—a Laboratory and Clinical Perspective. *ISRN Surg*. **2014,** 1–28 (2014).
55. Burks, S. & Spotnitz, W. Safety and usability of hemostats, sealants, and adhesives. *AORN J*. **100,** 160–176 (2014).
56. Qiu, L., See, A. A. Q., Steele, T. W. J. & King, N. K. K. Bioadhesives in neurosurgery: a review. *J. Neurosurg. JNS* **133,** 1928–1938 (2020).
57. Schmidt-Erfurth, U. & Thomas Kohnen. *Encyclopedia of Ophthalmology. Encycl. Ophthalmol*. (Springer, 2018). doi:10.1007/978-3-642-35951-4
58. Li, L., Lu, C., Wang, L., Chen, M., White, J., Hao, X., McLean, K. M., Chen, H. & Hughes, T. C. Gelatin-Based Photocurable Hydrogels for Corneal Wound Repair. *ACS Appl. Mater. Interfaces* **10,** 13283–13292 (2018).
59. Bloomfield, S., Barnert, A. H. & Kanter, P. D. The use of Eastman 910 monomer as an adhesive in ocular surgery. I. Biologic effects on ocular tissues. *Am. J. Ophthalmol*. **55,** 742–748 (1963).
60. Nathan, H. S., Nachlas, M. M., Solomon, R. D., Halpern, B. D. & Seligman, A. M. Nonsuture Closure of Arterial Incisions Using a Rapidly-Polymerizing Adhesive. *Ann. Surg*. **152,** (1960).
61. Toriumi, D. M., O'Grady, K., Desai, D. & Bagal, A. Use of octyl-2-cyanoacrylate for skin closure in facial plastic surgery. *Plast. Reconstr. Surg*. **102,** 2209—2219 (1998).
62. Duarte, A. P., Coelho, J. F., Bordado, J. C., Cidade, M. T. & Gil, M. H. Surgical adhesives: Systematic review of the main types and development forecast. *Prog. Polym. Sci*. **37,** 1031–1050 (2012).
63. Ebnesajjad, S. & Landrock, A. H. *Adhesives for Medical and Dental Applications. Adhes. Technol. Handb*. (2015). doi:10.1016/b978-0-323-35595-7.00010-3
64. Leonard, F., Kulkarni, R. K., Brandes, G., Nelson, J. & Cameron, J. J. Synthesis and degradation of poly (alkyl α-cyanoacrylates). *J. Appl. Polym. Sci*. **10,** 259–272 (1966).
65. Robertson, F. P., Magill, L. J., Davidson, C., Mitchell, H. & Davidson, B. R. *Cyanoacrylate tissue glues for cutaneous wound closure. Wound Heal. Biomater*. **2,** (Elsevier Ltd, 2016).
66. Oelker, A. M. & Grinstaff, M. W. Ophthalmic adhesives: A materials chemistry perspective. *J. Mater. Chem*. **18,** 2521–2536 (2008).
67. Duffy, C., Zetterlund, P. B. & Aldabbagh, F. Radical polymerization of alkyl 2-cyanoacrylates. *Molecules* **23,** (2018).

68. García Cerdá, D., Ballester, A. M., Aliena-Valero, A., Carabén-Redaño, A. & Lloris, J. M. Use of cyanoacrylate adhesives in general surgery. *Surg. Today* **45,** 939–956 (2015).
69. Pani, K. C., Gladieux, G., Brandes, G., Kulkarni, R. K. & Leonard, F. The degradation of n-butyl alpha-cyanoacrylate tissue adhesive. II. *Surgery* **63,** 481—489 (1968).
70. Woodward, S. C., Herrman, J. B., Cameron, J. L., Brandes, G., Pulaski, E. J. & Leonard, F. Histotoxicity of cyanoacrylate tissue adhesive in the rat. *Ann. Surg.* **162,** 113–122 (1965).
71. Ethicon. Dermabond Advanced Topical Skin Adhesive. (2015).
72. Biomedical, A. SurgiSeal Topical Skin adhesive Brochure.
73. Ge, L. & Chen, S. Recent advances in tissue adhesives for clinical medicine. *Polymers (Basel).* **12,** (2020).
74. Nam, S. & Mooney, D. Polymeric Tissue Adhesives. *Chem. Rev.* (2021). doi:10.1021/acs.chemrev.0c00798
75. Dermabond [package insert]. *Ethicon, Johnson & Johnson* (1998).
76. Liquiband Flex [instructions for use]. *Adv. Med. Solut.* (2011).
77. *Surgiseal [professional use reference]. Adhezion Biomed.* (2010).
78. Histoacryl and Histoacryl Blue [package insert]. *Tissueseal* (2008).
79. Indermil [package insert]. *US Surg. Tyco*
80. Koonce, S. L., Eck, D. L., Shaddix, K. K. & Perdikis, G. A prospective randomized controlled trial comparing N-butyl-2 cyanoacrylate (Histoacryl), octyl cyanoacrylate (Dermabond), and subcuticular suture for closure of surgical incisions. *Ann. Plast. Surg.* **74,** 107—110 (2015).
81. Cho, E., Jun, C. H., Cho, S. B., Park, C. H., Kim, H. S., Choi, S. K. & Rew, J. S. Endoscopic variceal ligation-induced ulcer bleeding: What are the risk factors and treatment strategies? *Medicine (Baltimore).* **96,** (2017).
82. Liew, W., Wai, Y. Y., Kosai, N. R. & Gendeh, H. S. Tackers versus glue mesh fixation: an objective assessment of postoperative acute and chronic pain using inflammatory markers. *Hernia* **21,** 549–554 (2017).
83. Loffroy, R., Guiu, B., Cercueil, J.-P. & Krause, D. Endovascular Therapeutic Embolisation: An Overview of Occluding Agents and their Effects on Embolised Tissues. *Curr. Vasc. Pharmacol.* **7,** 250–263 (2009).
84. Loffroy, R. Glubran2®, Histoacryl® or Trufill®: Which cyanoacrylate glue for endovascular use? *Diagn. Interv. Imaging* **97,** 119 (2016).

85. Bouten, P. J. M., Zonjee, M., Bender, J., Yauw, S. T. K., Van Goor, H., Van Hest, J. C. M. & Hoogenboom, R. The chemistry of tissue adhesive materials. *Prog. Polym. Sci.* **39,** 1375–1405 (2014).
86. Trujillo-de Santiago, G., Sharifi, R., Yue, K., Sani, E. S., Kashaf, S. S., Alvarez, M. M., Leijten, J., Khademhosseini, A., Dana, R. & Annabi, N. Ocular adhesives: Design, chemistry, crosslinking mechanisms, and applications. *Biomaterials* **197,** 345–367 (2019).
87. BD. BD Ocuseal Liquid Bandage leaflet. Le Pont de Claix, France (2009).
88. Ocular Therapeutix, I. ReSure Sealant Instructions for Use. Bedford, MA, USA (2014).
89. FDA. ReSure Summary of Safety and Effectiveness Data. Bedford, MA, USA (2014).
90. International, B. CoSeal Package Insert. Glattpark, Switzerland (2006).
91. Covidien. DuraSeal Package Insert. Mansfield, MA, USA (2005).
92. Corporation, G. FocalSeal Package Insert. (2000).
93. Neomend. ProGel Package Insert. (2010).
94. Lerit, S. J. T. & Abano, J. M. R. Comparison of Tensile Strength of Fibrin Glue, 2-Octyl Cyanoacrylate, Liquid Ocular Bandage, and Conventional Nylon 10-0 Sutures in Corneal Laceration Repair in an Animal Model. *Philipp. Acad. Opthamlmology* 52–58 (2012).
95. Potvin, R. & Makari, S. Cataract surgery and methods of wound closure: A review. *Clin. Ophthalmol.* **9,** 921–928 (2015).
96. Maddula, S., Davis, D. K., Ness, P. J., Burrow, M. K. & Olson, R. J. Comparison of wound strength with and without a hydrogel liquid ocular bandage in human cadaver eyes. *J. Cataract Refract. Surg.* **36,** 1775–1778 (2010).
97. Bondalapati, S. & Ambati, B. Minimally Invasive Pterygium Surgery: Sutureless Excision with Amniotic Membrane and Hydrogel Sealant. *Case Rep. Ophthalmol.* **7,** 79–84 (2016).
98. Masket, S., Hovanesian, J. A., Levenson, J., Tyson, F., Flynn, W., Endl, M., Majmudar, P. A., Modi, S., Chu, R., Raizman, M. B., Lane, S. S. & Kim, T. Hydrogel sealant versus sutures to prevent fluid egress after cataract surgery. *J. Cataract Refract. Surg.* **40,** 2057–2066 (2014).
99. Taboada, G. M., Yang, K., Pereira, M. J. N., Liu, S. S., Hu, Y., Karp, J. M., Artzi, N. & Lee, Y. Overcoming the translational barriers of tissue adhesives. *Nat. Rev. Mater.* **5,** 310–329 (2020).

100. Tisseel [package insert]. *Baxter* (2009).
101. Evicel [package insert]. *Ethicon, Johnson & Johnson* (2008).
102. Vitagel [instructions for use]. *Orthovita (Stryker)* (2012).
103. Tachosil [package insert]. *Baxter* (2010).
104. Panda, A., Kumar, S., Kumar, A., Bansal, R. & Bhartiya, S. Current Ophthalmology Fibrin glue in ophthalmology. (2009). doi:10.4103/0301-4738.55079
105. Lacaze, L., Le Dem, N., Bubenheim, M., Tsilividis, B., Mezghani, J., Schwartz, L., Francois, A., Ertaud, J. Y., Bagot D'Arc, M. & Scotté, M. Tensile strength of biological fibrin sealants: A comparative study. *J. Surg. Res.* **176,** 455–459 (2012).
106. Zhou, A. X. & Ambati, B. K. Sutureless Lamellar Corneoscleral Patch Graft With Fibrin Sealant for Limbal Dermoid Removal. *J. Pediatr. Ophthalmol. Strabismus* **53 Online,** e22–e25 (2016).
107. Chan, S. M. & Boisjoly, H. Advances in the use of adhesives in ophthalmology. *Curr. Opin. Ophthalmol.* **15,** 305–310 (2004).
108. Rashmi Deshmukh, L. J. S. & Rasik Vajpayee. Management of corneal perforations: An update. *Indian J. Ophthalmol.* **68,** (2019).
109. Lekskul, M., Fracht, H. U., Cohen, E. J., Rapuano, C. J. & Laibson, P. R. Nontraumatic corneal perforation. *Cornea* **19,** 313–319 (2000).
110. Yin, J., Singh, R. B., Al Karmi, R., Yung, A., Yu, M. & Dana, R. Outcomes of Cyanoacrylate Tissue Adhesive Application in Corneal Thinning and Perforation. *Cornea* **38,** 668–673 (2019).
111. Portnoy, S. L., Insler, M. S. & Kaufman, H. E. Surgical management of corneal ulceration and perforation. *Surv. Ophthalmol.* **34,** 47–58 (1989).
112. Grau, A. E. & Durán, J. A. Treatment of a large corneal perforation with a multilayer of amniotic membrane and TachoSil. *Cornea* **31,** 98–100 (2012).
113. Guhan, S., Peng, S. L., Janbatian, H., Saadeh, S., Greenstein, S., Al Bahrani, F., Fadlallah, A., Yeh, T. C. & Melki, S. A. Surgical adhesives in ophthalmology: History and current trends. *Br. J. Ophthalmol.* **102,** 1328–1335 (2018).
114. Chen, S. C., Telinius, N., Lin, H. T., Huang, M. C., Lin, C. C., Chou, C. H. & Hjortdal, J. Use of fish scale-derived BioCornea to seal full-thickness corneal perforations in pig models. *PLoS One* **10,** (2015).
115. Sharma, N., Singhal, D., Maharana, P. K. & Vajpayee, R. B. Tuck-In Tenon Patch Graft in Corneal Perforation. *Cornea* **38,** 951–954 (2019).

116. Refojo, M. F., Dohlman, C. H., Ahmad, B., Carroll, J. M. & Allen, J. C. Evaluation of Adhesives for Corneal Surgery. *Arch. Ophthalmol.* **80,** 645–656 (1968).
117. Al-Shahwan, S., Al-Torbak, A. A., Al-Jadaan, I., Omran, M. & Edward, D. P. Long-term Follow Up of Surgical Repair of Late Bleb Leaks After Glaucoma Filtering Surgery. *J. Glaucoma* **15,** (2006).
118. Haslinda, A. R., Azhany, Y., Noor-Khairul, R., Zunaina, E. & Liza-Sharmini, A. T. Cyanoacrylate tissue glue for wound repair in early posttrabeculectomy conjunctival bleb leak: A case series. *Int. Med. Case Rep. J.* **8,** 145–150 (2015).
119. Loane, M. E. & Galanopoulos, A. The surgical management of leaking filtering blebs. *Curr. Opin. Ophthalmol.* **10,** (1999).
120. Setlik, D. E., Seldomridge, D. L., Adelman, R. A., Semchyshyn, T. M. & Afshari, N. A. The effectiveness of isobutyl cyanoacrylate tissue adhesive for the treatment of corneal perforations. *Am. J. Ophthalmol.* **140,** 920–921 (2005).
121. Taravella, M. J. & Chang, C. D. 2-Octyl cyanoacrylate medical adhesive in treatment of a corneal perforation. *Cornea* **20,** 220–221 (2001).
122. Fogle, J. A., Kenyon, K. R. & Foster, C. S. Tissue adhesive arrests stromal melting in the human cornea. *Am. J. Ophthalmol.* **89,** 795–802 (1980).
123. Sharma, A., Kaur, R., Kumar, S., Gupta, P., Pandav, S., Patnaik, B. & Gupta, A. Fibrin glue versus N-butyl-2-cyanoacrylate in corneal perforations. *Ophthalmology* **110,** 291–298 (2003).
124. Lagoutte, F. M., Gauthier, L. & Comte, P. R. M. A fibrin sealant for perforated and preperforated corneal ulcers. *Br. J. Ophthalmol.* **73,** 757–761 (1989).
125. Sharma, A. & K, M. Scleral Patch Graft Augmented Cyanoacrylate Tissue. *Cornea* **32,** 1326–1330 (2013).
126. Shirzaei Sani, E., Kheirkhah, A., Rana, D., Sun, Z., Foulsham, W., Sheikhi, A., Khademhosseini, A., Dana, R. & Annabi, N. Sutureless repair of corneal injuries using naturally derived bioadhesive hydrogels. *Sci. Adv.* **5,** (2019).
127. Garcia-Porta, N., Fernandes, P., Queiros, A., Salgado-Borges, J., Parafita-Mato, M. & González-Méijome, J. M. Corneal Biomechanical Properties in Different Ocular Conditions and New Measurement Techniques. *ISRN Ophthalmol.* **2014,** 1–19 (2014).
128. Raiskup, F. & Spoerl, E. Corneal crosslinking with riboflavin and ultraviolet A. I. principles. *Ocul. Surf.* **11,** 65–74 (2013).
129. Bykhovskaya, Y., Li, X., Epifantseva, I., Haritunians, T., Siscovick, D., Aldave, A.,

Szczotka-Flynn, L., Iyengar, S. K., Taylor, K. D., Rotter, J. I. & Rabinowitz, Y. S. Variation in the lysyl oxidase (LOX) gene is associated with keratoconus in family-based and case-control studies. *Investig. Ophthalmol. Vis. Sci.* **53,** 4152–4157 (2012).

130. Zhang, Y., Conrad, A. H. & Conrad, G. W. Effects of ultraviolet-A and riboflavin on the interaction of collagen and proteoglycans during corneal cross-linking. *J. Biol. Chem.* **286,** 13011–13022 (2011).
131. Kamiya, K., Kanayama, S., Takahashi, M. & Shoji, N. Visual and topographic improvement with epithelium-on, oxygen-supplemented, customized corneal cross-linking for progressive keratoconus. *J. Clin. Med.* **9,** 1–10 (2020).
132. Ambrósio, R. & Wilson, S. E. LASIK vs LASEk vs PRK: Advantages and indications. *Semin. Ophthalmol.* **18,** 2–10 (2003).
133. Jeng, B. H. *Advances in Medical and Surgical Cornea*. (Springer-Verlag Berlin Heidelberg, 2014). doi:10.1007/978-3-662-44888-5
134. Randleman, J. B., Khandelwal, S. S. & Hafezi, F. Corneal cross-linking. *Surv. Ophthalmol.* **60,** 509–523 (2015).
135. Jeng, B. H. *Advances in Medical and Surgical Cornea: From Diagnosis to Procedure*. (2014). doi:10.1007/978-3-662-44888-5
136. Kamaev, P., Friedman, M. D., Sherr, E. & Muller, D. Photochemical kinetics of corneal cross-linking with riboflavin. *Investig. Ophthalmol. Vis. Sci.* **53,** 2360–2367 (2012).
137. Meek, K. M. & Hayes, S. Corneal cross-linking - a review. *Ophthalmic Physiol. Opt.* **33,** 78–93 (2013).
138. Hayes, S., Morgan, S. R. & Meek, K. M. Keratoconus: cross-linking the window of the eye. *Ther. Adv. Rare Dis.* **2,** 263300402110035 (2021).
139. Scott McCall, A., Kraft, S., Edelhauser, H. F., Kidder, G. W., Lundquist, R. R., Bradshaw, H. E., Dedeic, Z., Dionne, M. J. C., Clement, E. M. & Conrad, G. W. Mechanisms of corneal tissue cross-linking in response to treatment with topical riboflavin and Long-Wavelength Ultraviolet Radiation (UVA). *Investig. Ophthalmol. Vis. Sci.* **51,** 129–138 (2010).
140. Mencucci, R., Paladini, I., Sarchielli, E., Favuzza, E., Vannelli, G. B. & Marini, M. Transepithelial riboflavin/ultraviolet. A corneal cross-linking in keratoconus: Morphologic studies on human corneas. *Am. J. Ophthalmol.* **156,** 874-884.e1 (2013).
141. Hashemi, H., Mohebbi, M. & Asgari, S. Standard and accelerated corneal cross-linking long-term results: A randomized clinical trial. *Eur. J. Ophthalmol.* **30,** 650–657 (2020).

142. Hashemi, H., Fotouhi, A., Miraftab, M., Bahrmandy, H., Seyedian, M. A., Amanzadeh, K., Heidarian, S., Nikbin, H. & Asgari, S. Short-term comparison of accelerated and standard methods of corneal collagen crosslinking. *J. Cataract Refract. Surg.* **41,** 533–540 (2015).

143. Shetty, R., Pahuja, N. K., Nuijts, R. M. M. A., Ajani, A., Jayadev, C., Sharma, C. & Nagaraja, H. Current Protocols of Corneal Collagen Cross-Linking: Visual, Refractive, and Tomographic Outcomes. *Am. J. Ophthalmol.* **160,** 243–249 (2015).

144. Decker, C. The use of UV irradiation in polymerization. *Polym. Int.* **45,** 133–141 (1998).

145. Bryant, S. J., Nuttelman, C. R., Anseth, K. S., Bryant, S. J., Nuttelman, C. R., Anseth, K. S., Bryant, S. J. & Nuttelman, C. R. Cytocompatibility of UV and visible light photoinitiating systems on cultured NIH / 3T3 fibroblasts in vitro systems on cultured NIH / 3T3 broblasts in vitro. **5063,** (2012).

146. Sudhakar, C. K., Upadhyay, N., Jain, A., Verma, A., Narayana Charyulu, R. & Jain, S. *Hydrogels-Promising Candidates for Tissue Engineering. Nanotechnol. Appl. Tissue Eng.* (Elsevier Inc., 2015). doi:10.1016/B978-0-323-32889-0.00005-4

147. Monteiro, N., Thrivikraman, G., Athirasala, A., Tahayeri, A., França, C. M., Ferracane, J. L. & Bertassoni, L. E. Photopolymerization of cell-laden gelatin methacryloyl hydrogels using a dental curing light for regenerative dentistry. *Dent. Mater.* **34,** 389–399 (2018).

148. Guvendiren, M., Purcell, B. & Burdick, J. A. *Photopolymerizable Systems. Polym. Sci. A Compr. Ref. 10 Vol. Set* **9,** (Elsevier B.V., 2012).

149. Shirzaei Sani, E., Portillo-Lara, R., Spencer, A., Yu, W., Geilich, B. M., Noshadi, I., Webster, T. J. & Annabi, N. Engineering Adhesive and Antimicrobial Hyaluronic Acid/Elastin-like Polypeptide Hybrid Hydrogels for Tissue Engineering Applications. *ACS Biomater. Sci. Eng.* **4,** 2528–2540 (2018).

150. Annabi, N., Rana, D., Shirzaei Sani, E., Portillo-Lara, R., Gifford, J. L., Fares, M. M., Mithieux, S. M. & Weiss, A. S. Engineering a sprayable and elastic hydrogel adhesive with antimicrobial properties for wound healing. *Biomaterials* **139,** 229–243 (2017).

151. Kim, S. H., Yeon, Y. K., Lee, J. M., Chao, J. R., Lee, Y. J., Seo, Y. B., Sultan, M. T., Lee, O. J., Lee, J. S., Yoon, S. Il, Hong, I. S., Khang, G., Lee, S. J., Yoo, J. J. & Park, C. H. Precisely printable and biocompatible silk fibroin bioink for digital light processing 3D printing. *Nat. Commun.* **9,** 1–14 (2018).

152. Kilic Bektas, C., Burcu, A., Gedikoglu, G., Telek, H. H., Ornek, F. & Hasirci, V.

Methacrylated gelatin hydrogels as corneal stroma substitutes: in vivo study. *J. Biomater. Sci. Polym. Ed.* **30,** 1803–1821 (2019).

153. Duarte Campos, D. F., Rohde, M., Ross, M., Anvari, P., Blaeser, A., Vogt, M., Panfil, C., Yam, G. H. F., Mehta, J. S., Fischer, H., Walter, P. & Fuest, M. Corneal bioprinting utilizing collagen-based bioinks and primary human keratocytes. *J. Biomed. Mater. Res. - Part A* **107,** 1945–1953 (2019).
154. Khalil, I. A., Saleh, B., Ibrahim, D. M., Jumelle, C., Yung, A., Dana, R. & Annabi, N. Ciprofloxacin-loaded Bioadhesive Hydrogels for Ocular Applications. *Biomater. Sci.* (2020).
155. Lim, K. S., Schon, B. S., Mekhileri, N. V., Brown, G. C. J., Chia, C. M., Prabakar, S., Hooper, G. J. & Woodfield, T. B. F. New Visible-Light Photoinitiating System for Improved Print Fidelity in Gelatin-Based Bioinks. *ACS Biomater. Sci. Eng.* **2,** 1752–1762 (2016).
156. Andrzejewska, E. *Chapter 2 - Free Radical Photopolymerization of Multifunctional Monomers A2 - Baldacchini, Tommaso. Three-Dimensional Microfabr. Using Two-phot. Polym.* (Elsevier Inc., 2016). doi:10.1016/B978-0-323-35321-2/00004-2
157. Lim, K. S., Galarraga, J. H., Cui, X., Lindberg, G. C. J., Burdick, J. A. & Wood, T. B. F. Fundamentals and Applications of Photo-Cross-Linking in Bioprinting. *Chem. Rev.* **120,** 10662–10694 (2020).
158. Bagheri, A. & Jin, J. Photopolymerization in 3D Printing. *ACS Appl. Polym. Mater.* **1,** 593–611 (2019).
159. Loessner, D., Meinert, C., Kaemmerer, E., Martine, L. C., Yue, K., Levett, P. A., Klein, T. J., Melchels, F. P. W., Khademhosseini, A. & Hutmacher, D. W. Functionalization, preparation and use of cell-laden gelatin methacryloyl-based hydrogels as modular tissue culture platforms. *Nat. Protoc.* **11,** 727–746 (2016).
160. Nichol, J. W., Koshy, S. T., Bae, H., Hwang, C. M., Yamanlar, S. & Khademhosseini, A. Cell-laden microengineered gelatin methacrylate hydrogels. *Biomaterials* **31,** 5536–5544 (2010).
161. Goodarzi, H., Jadidi, K., Pourmotabed, S., Sharifi, E. & Aghamollaei, H. Preparation and in vitro characterization of cross-linked collagen–gelatin hydrogel using EDC/NHS for corneal tissue engineering applications. *Int. J. Biol. Macromol.* **126,** 620–632 (2019).
162. Rose, J. B., Pacelli, S., El Haj, A. J., Dua, H. S., Hopkinson, A., White, L. J. & Rose, F. R. A. J. Gelatin-based materials in ocular tissue engineering. *Materials (Basel).* **7,** 3106–

3135 (2014).

163. Pahoff, S., Meinert, C., Bas, O., Nguyen, L., Klein, T. J. & Hutmacher, D. W. Effect of gelatin source and photoinitiator type on chondrocyte redifferentiation in gelatin methacryloyl-based tissue-engineered cartilage constructs. *J. Mater. Chem. B* **7,** 1761–1772 (2019).

164. Elvin, C. M., Vuocolo, T., Brownlee, A. G., Sando, L., Huson, M. G., Liyou, N. E., Stockwell, P. R., Lyons, R. E., Kim, M., Edwards, G. A., Johnson, G., McFarland, G. A., Ramshaw, J. A. M. & Werkmeister, J. A. A highly elastic tissue sealant based on photopolymerised gelatin. *Biomaterials* **31,** 8323–8331 (2010).

165. Hafidz, R. N. R. M., Yaakob, C. M., Amin, I. & Noorfaizan, A. Chemical and functional properties of bovine and porcine skin gelatin. *Int. Food Res. J.* **18,** (2011).

166. Ahearne, M., Fernández-Pérez, J., Masterton, S., Madden, P. W. & Bhattacharjee, P. Designing Scaffolds for Corneal Regeneration. *Adv. Funct. Mater.* **30,** (2020).

167. Ludwig, P. E., Huff, T. J. & Zuniga, J. M. The potential role of bioengineering and three-dimensional printing in curing global corneal blindness. *J. Tissue Eng.* **9,** 204173141876986 (2018).

168. Gorgieva Selestina; Kokol Vanja; Pignatello Rosario. Collagen- vs. Gelatine-Based Biomaterials and Their Biocompatibility: Review and Perspectives, Biomaterials Applications for Nanomedicine. *IntechOpen* 1–36 (2011).

169. Lynn, A. K., Yannas, I. V. & Bonfield, W. Antigenicity and immunogenicity of collagen. *J. Biomed. Mater. Res. - Part B Appl. Biomater.* **71,** 343–354 (2004).

170. Kilic Bektas, C. & Hasirci, V. Mimicking corneal stroma using keratocyte-loaded photopolymerizable methacrylated gelatin hydrogels. *J. Tissue Eng. Regen. Med.* **12,** e1899–e1910 (2018).

171. Mimura, T., Amano, S., Yokoo, S., Uchida, S., Yamagami, S., Usui, T., Kimura, Y. & Tabata, Y. Tissue engineering of corneal stroma with rabbit fibroblast precursors and gelatin hydrogels. *Mol. Vis.* **14,** 1819–1828 (2008).

172. Yamamoto, S., Hirata, A., Ishikawa, S., Ohta, K., Nakamura, K. I. & Okinami, S. Feasibility of using gelatin-microbial transglutaminase complex to repair experimental retinal detachment in rabbit eyes. *Graefe's Arch. Clin. Exp. Ophthalmol.* **251,** 1109–1114 (2013).

173. Chen, T., Embree, H. D., Brown, E. M., Taylor, M. M. & Payne, G. F. Enzyme-catalyzed gel formation of gelatin and chitosan: Potential for in situ applications. *Biomaterials* **24,**

2831–2841 (2003).

174. Albes, J. M., Krettek, C., Hausen, B., Rohde, R., Haverich, A. & Borst, H. G. Biophysical properties of the gelatin-resorcinformaldehyde/glutaraldehyde adhesive. *Ann. Thorac. Surg.* **56,** 910–915 (1993).

175. Suzuki, S. & Ikada, Y. Adhesion of cells and tissues to bioabsorbable polymeric materials: Scaffolds, surgical tissue adhesives and anti-adhesive materials. *J. Adhes. Sci. Technol.* **24,** 2059–2077 (2010).

176. Tonelli, E., De Almeida, H. C. & Bambirra, E. A. Tissue adhesives for a sutureless fadenoperation: An experimental study in a rabbit model. *Investig. Ophthalmol. Vis. Sci.* **45,** 4340–4345 (2004).

177. Chen, T., Janjua, R., McDermott, M. K., Bernstein, S. L., Steidl, S. M. & Payne, G. F. Gelatin-based biomimetic tissue adhesive. Potential for retinal reattachment. *J. Biomed. Mater. Res. - Part B Appl. Biomater.* **77,** 416–422 (2006).

178. McDermott, M. K., Chen, T., Williams, C. M., Markley, K. M. & Payne, G. F. Mechanical properties of biomimetic tissue adhesive based on the microbial transglutaminase-catalyzed crosslinking of gelatin. *Biomacromolecules* **5,** 1270–1279 (2004).

179. Rizwan, M., Peh, G. S. L., Ang, H. P., Lwin, N. C., Adnan, K., Mehta, J. S., Tan, W. S. & Yim, E. K. F. Sequentially-crosslinked bioactive hydrogels as nano-patterned substrates with customizable stiffness and degradation for corneal tissue engineering applications. *Biomaterials* **120,** 139–154 (2017).

180. Van Den Bulcke, A. I., Bogdanov, B., De Rooze, N., Schacht, E. H., Cornelissen, M. & Berghmans, H. Structural and Rheological Properties of Methacrylamide Modified Gelatin Hydrogels. *Biomacromolecules* **1,** 31–38 (2000).

181. Uyanlklar, M., Günal, G., Tevlek, A., Hosseinian, P. & Aydin, H. M. Hybrid Cornea: Cell Laden Hydrogel Incorporated Decellularized Matrix. *ACS Biomater. Sci. Eng.* **6,** 122–133 (2020).

182. Sun, W. & Mi, S. Fiber reinforced GelMA hydrogel to induce the regeneration of corneal stroma. 1–12

183. Soucy, J. R., Shirzaei Sani, E., Portillo Lara, R., DIaz, D., DIas, F., Weiss, A. S., Koppes, A. N., Koppes, R. A. & Annabi, N. Photocrosslinkable Gelatin/Tropoelastin Hydrogel Adhesives for Peripheral Nerve Repair. *Tissue Eng. - Part A* **24,** 1393–1405 (2018).

184. Assmann, A., Vegh, A., Ghasemi-Rad, M., Bagherifard, S., Cheng, G., Sani, E. S., Ruiz-

Esparza, G. U., Noshadi, I., Lassaletta, A. D., Gangadharan, S., Tamayol, A., Khademhosseini, A. & Annabi, N. A highly adhesive and naturally derived sealant. *Biomaterials* **140,** 115–127 (2017).

185. Holland, C., Numata, K., Rnjak-Kovacina, J. & Seib, F. P. The Biomedical Use of Silk: Past, Present, Future. *Adv. Healthc. Mater.* **8,** (2019).
186. Galateanu, B., Hudita, A., Zaharia, C., Bunea, M., Vasile, E. & Buga, M. Silk-Based Hydrogels for Biomedical Applications. 1791–1817 (2019).
187. Helena S. Azevedo, R. M. . da S. *Self-Assembling Biomaterials*. (Woodhead Publishing Limited, 2018).
188. Rockwood, D. N., Preda, R. C., Yücel, T., Wang, X., Lovett, M. L. & Kaplan, D. L. Materials fabrication from Bombyx mori silk fibroin. *Nat. Protoc.* **6,** 1612–1631 (2011).
189. Greving, I., Dicko, C., Terry, A., Callow, P. & Vollrath, F. Small angle neutron scattering of native and reconstituted silk fibroin. *Soft Matter* **6,** 4389–4395 (2010).
190. Foo, C. W. P., Bini, E., Hensman, J., Knight, D. P., Lewis, R. V. & Kaplan, D. L. Role of pH and charge on silk protein assembly in insects and spiders. *Appl. Phys. A Mater. Sci. Process.* **82,** 223–233 (2006).
191. Matthyssen, S., Van den Bogerd, B., Dhubhghaill, S. N., Koppen, C. & Zakaria, N. Corneal regeneration: A review of stromal replacements. *Acta Biomater.* **69,** 31–41 (2018).
192. Floren, M., Migliaresi, C. & Motta, A. Processing Techniques and Applications of Silk Hydrogels in Bioengineering. *J. Funct. Biomater.* **7,** 26 (2016).
193. Mu, X., Sahoo, J. K., Cebe, P. & Kaplan, D. L. Photo-crosslinked silk fibroin for 3d printing. *Polymers (Basel).* **12,** 1–18 (2020).
194. Partlow, B. P., Hanna, C. W., Rnjak-Kovacina, J., Moreau, J. E., Applegate, M. B., Burke, K. A., Marelli, B., Mitropoulos, A. N., Omenetto, F. G. & Kaplan, D. L. Highly tunable elastomeric silk biomaterials. *Adv. Funct. Mater.* **24,** 4615–4624 (2014).
195. Li, Q., Wang, D. A. & Elisseeff, J. H. Heterogeneous-phase reaction of glycidyl methacrylate and chondroitin sulfate: Mechanism of ring-opening-transesterification competition. *Macromolecules* **36,** 2556–2562 (2003).
196. Reis, A. V., Reis, A. V, Rubira, A. F. & Muniz, E. C. Reaction of Glycidyl Methacrylate at the Hydroxyl and Carboxylic Groups of Poly(vinyl alcohol) and Poly(acrylic acid): Is this Reaction Mechanism Still Unclear ? 3750–3757 (2009). doi:10.1021/jo900033c
197. Hong, H., Seo, Y. B., Kim, D. Y., Lee, J. S., Lee, Y. J., Lee, H., Ajiteru, O., Sultan, M.

T., Lee, O. J., Kim, S. H. & Park, C. H. Digital light processing 3D printed silk fibroin hydrogel for cartilage tissue engineering. *Biomaterials* **232,** 119679 (2020).

198. Kim, S. H., Seo, Y. B., Yeon, Y. K., Lee, Y. J., Park, H. S., Sultan, M. T., Lee, J. M., Lee, J. S., Lee, O. J., Hong, H., Lee, H., Ajiteru, O., Suh, Y. J., Song, S.-H., Lee, K.-H. & Park, C. H. 4D-bioprinted silk hydrogels for tissue engineering. *Biomaterials* **260,** 120281 (2020).
199. Tomal, W. & Ortyl, J. Water-soluble photoinitiators in biomedical applications. *Polymers (Basel)*. **12,** 1–30 (2020).
200. Fouassier, J. P., Morlet-Savary, F., Lalevée, J., Allonas, X. & Ley, C. Dyes as photoinitiators or photosensitizers of polymerization reactions. *Materials (Basel)*. **3,** 5130–5142 (2010).
201. Fairbanks, B. D., Schwartz, M. P., Bowman, C. N. & Anseth, K. S. Photoinitiated polymerization of PEG-diacrylate with lithium phenyl-2,4,6-trimethylbenzoylphosphinate: polymerization rate and cytocompatibility. *Biomaterials* **30,** 666 (2009).
202. Majima, T., Schnabel, W. & Weber, W. Phenyl-2,4,6-trimethylbenzoylphosphinates as water-soluble photoinitiators. Generation and reactivity of O=P(C6H5)(O–) radical anions. *Die Makromol. Chemie* **192,** 2307–2315 (1991).
203. Ligon, S. C., Liska, R., Stampfl, J., Gurr, M. & Mülhaupt, R. Polymers for 3D Printing and Customized Additive Manufacturing. *Chem. Rev.* **117,** 10212–10290 (2017).
204. Jasinski, F., Zetterlund, P. B., Braun, A. M., Chemtob, A., Jasinski, F., Zetterlund, P. B., Braun, A. M. & Chemtob, A. Photopolymerization in dispersed systems. *Prog. Polym. Sci.* **84,** 47–88 (2019).
205. Tavafoghi, M., Sheikhi, A., Tutar, R., Jahangiry, J., Baidya, A., Haghniaz, R. & Khademhosseini, A. Engineering Tough, Injectable, Naturally Derived, Bioadhesive Composite Hydrogels. *Adv. Healthc. Mater.* **9,** (2020).
206. Sharifi, S., Islam, M. M., Sharifi, H., Islam, R., Koza, D., Reyes-Ortega, F., Alba-Molina, D., Nilsson, P. H., Dohlman, C. H., Mollnes, T. E., Chodosh, J. & Gonzalez-Andrades, M. Tuning gelatin-based hydrogel towards bioadhesive ocular tissue engineering applications. *Bioact. Mater.* **6,** 3947–3961 (2021).
207. Noshadi, I., Hong, S., Sullivan, K. E., Shirzaei Sani, E., Portillo-Lara, R., Tamayol, A., Shin, S. R., Gao, A. E., Stoppel, W. L., Black, L. D., Khademhosseini, A. & Annabi, N. In vitro and in vivo analysis of visible light crosslinkable gelatin methacryloyl (GelMA)

hydrogels. *Biomater. Sci.* **5,** 2093–2105 (2017).

208. Yang, K. H., Lindberg, G., Soliman, B., Lim, K., Woodfield, T. & Narayan, R. J. Effect of photoinitiator on precursory stability and curing depth of thiol-ene clickable gelatin. *Polymers (Basel).* **13,** (2021).
209. Lim, K. S., Klotz, B. J., Lindberg, G. C. J., Melchels, F. P. W., Hooper, G. J., Malda, J., Gawlitta, D. & Woodfield, T. B. F. Visible Light Cross-Linking of Gelatin Hydrogels Offers an Enhanced Cell Microenvironment with Improved Light Penetration Depth. *Macromol. Biosci.* **19,** 1–14 (2019).
210. Lim, K. S., Levato, R., Costa, P. F., Castilho, M. D., Alcala-Orozco, C. R., Van Dorenmalen, K. M. A., Melchels, F. P. W., Gawlitta, D., Hooper, G. J., Malda, J. & Woodfield, T. B. F. Bio-resin for high resolution lithography-based biofabrication of complex cell-laden constructs. *Biofabrication* **10,** (2018).
211. Piluso, S., Flores Gomez, D., Dokter, I., Moreira Texeira, L., Li, Y., Leijten, J., Van Weeren, R., Vermonden, T., Karperien, M. & Malda, J. Rapid and cytocompatible cell-laden silk hydrogel formation: Via riboflavin-mediated crosslinking. *J. Mater. Chem. B* **8,** 9566–9575 (2020).
212. Navarro, J., Swayambunathan, J., Lerman, M., Santoro, M. & Fisher, J. P. Development of keratin-based membranes for potential use in skin repair. *Acta Biomater.* **83,** 177–188 (2019).
213. Greene, T., Lin, T. Y., Andrisani, O. M. & Lin, C. C. Comparative study of visible light polymerized gelatin hydrogels for 3D culture of hepatic progenitor cells. *J. Appl. Polym. Sci.* **134,** 1–10 (2017).
214. Wang, Z., Tian, Z., Menard, F. & Kim, K. Comparative study of gelatin methacrylate hydrogels from different sources for biofabrication applications. *Biofabrication* **9,** (2017).
215. Cui, X., Soliman, B. G., Alcala-Orozco, C. R., Li, J., Vis, M. A. M., Santos, M., Wise, S. G., Levato, R., Malda, J., Woodfield, T. B. F., Rnjak-Kovacina, J. & Lim, K. S. Rapid Photocrosslinking of Silk Hydrogels with High Cell Density and Enhanced Shape Fidelity. *Adv. Healthc. Mater.* **9,** 1–15 (2020).
216. Piras, C. C. & Smith, D. K. Multicomponent polysaccharide alginate-based bioinks. *J.Mater.Chem.B* **8,** (2020).
217. Sun, M., Sun, X., Wang, Z., Guo, S., Yu, G. & Yang, H. Synthesis and properties of gelatin methacryloyl (GelMA) hydrogels and their recent applications in load-bearing

tissue. *Polymers (Basel)*. **10,** (2018).

218. Yan, L. P., Silva-Correia, J., Ribeiro, V. P., Miranda-Goncąlves, V., Correia, C., Da Silva Morais, A., Sousa, R. A., Reis, R. M., Oliveira, A. L., Oliveira, J. M. & Reis, R. L. Tumor Growth Suppression Induced by Biomimetic Silk Fibroin Hydrogels. *Sci. Rep.* **6,** 1–11 (2016).
219. Tabatabai, A. P., Kaplan, D. L. & Blair, D. L. Rheology of reconstituted silk fibroin protein gels: The epitome of extreme mechanics. *Soft Matter* **11,** 756–761 (2015).
220. Costa, J. B., Silva-Correia, J., Oliveira, J. M. & Reis, R. L. Fast Setting Silk Fibroin Bioink for Bioprinting of Patient-Specific Memory-Shape Implants. *Adv. Healthc. Mater.* **6,** 1–8 (2017).
221. Qi, Y., Wang, H., Wei, K., Yang, Y., Zheng, R. Y., Kim, I. S. & Zhang, K. Q. A review of structure construction of silk fibroin biomaterials from single structures to multi-level structures. *Int. J. Mol. Sci.* **18,** (2017).
222. Kim, U. J., Park, J., Li, C., Jin, H. J., Valluzzi, R. & Kaplan, D. L. Structure and properties of silk hydrogels. *Biomacromolecules* **5,** 786–792 (2004).
223. Matsumoto, A., Chen, J., Collette, A. L., Kim, U., Altman, G. H., Cebe, P. & Kaplan, D. L. Mechanisms of Silk Fibroin Sol - Gel Transitions. **110,** 21630–21638 (2006).
224. Wray, L. S., Hu, X., Gallego, J., Georgakoudi, I., Omenetto, F. G., Schmidt, D. & Kaplan, D. L. Effect of processing on silk-based biomaterials: Reproducibility and biocompatibility. *J. Biomed. Mater. Res. - Part B Appl. Biomater.* **99 B,** 89–101 (2011).
225. Kundu, B., Kurland, N. E., Bano, S., Patra, C., Engel, F. B., Yadavalli, V. K. & Kundu, S. C. Silk proteins for biomedical applications: Bioengineering perspectives. *Prog. Polym. Sci.* **39,** 251–267 (2014).
226. Terry, A. E., Knight, D. P., Porter, D. & Vollrath, F. pH induced changes in the rheology of silk fibroin solution from the middle division of Bombyx mori silkworm. *Biomacromolecules* **5,** 768–772 (2004).
227. Fini, M., Motta, A., Torricelli, P., Giavaresi, G., Nicoli Aldini, N., Tschon, M., Giardino, R. & Migliaresi, C. The healing of confined critical size cancellous defects in the presence of silk fibroin hydrogel. *Biomaterials* **26,** 3527–3536 (2005).
228. Nagarkar, S., Nicolai, T., Chassenieux, C. & Lele, A. Structure and gelation mechanism of silk hydrogels. *Phys. Chem. Chem. Phys.* **12,** 3834 (2010).
229. Luo, K., Yang, Y. & Shao, Z. Physically Crosslinked Biocompatible Silk-Fibroin-Based Hydrogels with High Mechanical Performance. *Adv. Funct. Mater.* **26,** 872–880 (2016).

230. Dong, T., Mi, R., Wu, M., Zhong, N., Zhao, X., Chen, X. & Shao, Z. The regenerated silk fibroin hydrogel with designed architecture bioprinted by its microhydrogel. *J. Mater. Chem. B* **7,** 4328–4337 (2019).

231. Hofmann, S., Wong Po Foo, C. T., Rossetti, F., Textor, M., Vunjak-Novakovic, G., Kaplan, D. L., Merkle, H. P. & Meinel, L. Silk fibroin as an organic polymer for controlled drug delivery. *J. Control. Release* **111,** 219–227 (2006).

232. Gil, E. S., Spontak, R. J. & Hudson, S. M. Effect of β-sheet crystals on the thermal and rheological behavior of protein-based hydrogels derived from gelatin and silk fibroin. *Macromol. Biosci.* **5,** 702–709 (2005).

233. Alessandrino, A., Marelli, B., Arosio, C., Fare, S., Tanzi, M. C. & Freddi, G. Electrospun silk fibroin mats for tissue engineering. *Eng. Life Sci.* **8,** 219–225 (2008).

234. Ghosh, S., Parker, S. T., Wang, X., Kaplan, D. L. & Lewis, J. A. Direct-write assembly of microperiodic silk fibroin scaffolds for tissue engineering applications. *Adv. Funct. Mater.* **18,** 1883–1889 (2008).

235. Zhang, X. & Pan, Z. Microstructure transitions and dry-wet spinnability of Silk fibroin protein from Waste silk quilt. *Polymers (Basel).* **11,** (2019).

236. Leisk, G. G., Lo, T. J., Yucel, T., Lu, Q. & Kaplan, D. L. Electrogelation for protein adhesives. *Adv. Mater.* **22,** 711–715 (2010).

237. Wang, S. D. & Zhang, K. Q. Electrogelation and rapid prototyping of Bombyx mori silk fibroin. *Mater. Lett.* **169,** 5–9 (2016).

238. Wang, X., Kluge, J. A., Leisk, G. G. & Kaplan, D. L. Sonication-induced gelation of silk fibroin for cell encapsulation. *Biomaterials* **29,** 1054–1064 (2008).

239. Yucel, T., Cebe, P. & Kaplan, D. L. Vortex-induced injectable silk fibroin hydrogels. *Biophys. J.* **97,** 2044–2050 (2009).

240. Mazzocchi, A., Devarasetty, M., Huntwork, R., Soker, S. & Skardal, A. Optimization of collagen type I-hyaluronan hybrid bioink for 3D bioprinted liver microenvironments. *Biofabrication* **11,** (2019).

241. Lim, K. S., Abinzano, F., Bernal, P. N., Albillos Sanchez, A., Atienza-Roca, P., Otto, I. A., Peiffer, Q. C., Matsusaki, M., Woodfield, T. B. F., Malda, J. & Levato, R. One-Step Photoactivation of a Dual-Functionalized Bioink as Cell Carrier and Cartilage-Binding Glue for Chondral Regeneration. *Adv. Healthc. Mater.* **9,** 1–13 (2020).

242. Kimberly A. Smeds, Anne Pfister-Serres, Daijiro Miki, Kourosh Dastgheib, M. I. & Diane L. Hatchell, M. W. G. Photocrosslinkable polysaccharides for in situ hydrogel

formation. *J Biomed Mater Res* **55,** 254–255 (2000).

243. Kesti, M., Müller, M., Becher, J., Schnabelrauch, M., D'Este, M., Eglin, D. & Zenobi-Wong, M. A versatile bioink for three-dimensional printing of cellular scaffolds based on thermally and photo-triggered tandem gelation. *Acta Biomater*. **11,** 162–172 (2015).
244. Pescosolido, L., Schuurman, W., Malda, J., Matricardi, P., Alhaique, F., Coviello, T., Van Weeren, P. R., Dhert, W. J. A., Hennink, W. E. & Vermonden, T. Hyaluronic acid and dextran-based semi-IPN hydrogels as biomaterials for bioprinting. *Biomacromolecules* **12,** 1831–1838 (2011).
245. Dubbin, K., Tabet, A. & Heilshorn, S. C. Quantitative criteria to benchmark new and existing bio-inks for cell compatibility. *Biofabrication* **9,** 044102 (2017).
246. Hu, X., Kaplan, D. & Cebe, P. Determining Beta-Sheet Crystallinity in Fibrous Proteins by Thermal Analysis and Infrared Spectroscopy. 6161–6170 (2006).
247. Bhattacharjee, P., Fernández-Pérez, J. & Ahearne, M. Potential for combined delivery of riboflavin and all-trans retinoic acid, from silk fibroin for corneal bioengineering. *Mater. Sci. Eng. C* **105,** 110093 (2019).
248. Guimarães, C. F., Gasperini, L., Marques, A. P. & Reis, R. L. The stiffness of living tissues and its implications for tissue engineering. *Nat. Rev. Mater.* (2020).
249. Buitrago, J. O., Patel, K. D., El-Fiqi, A., Lee, J. H., Kundu, B., Lee, H. H. & Kim, H. W. Silk fibroin/collagen protein hybrid cell-encapsulating hydrogels with tunable gelation and improved physical and biological properties. *Acta Biomater*. **69,** 218–233 (2018).
250. Singh, Y. P., Bandyopadhyay, A. & Mandal, B. B. 3D Bioprinting Using Cross-Linker-Free Silk-Gelatin Bioink for Cartilage Tissue Engineering. *ACS Appl. Mater. Interfaces* **11,** 33684–33696 (2019).
251. Ribeiro, V. P., Silva-Correia, J., Gonçalves, C., Pina, S., Radhouani, H., Montonen, T., Hyttinen, J., Roy, A., Oliveira, A. L., Reis, R. L. & Oliveira, J. M. Rapidly responsive silk fibroin hydrogels as an artificial matrix for the programmed tumor cells death. *PLoS One* **13,** 1–21 (2018).
252. Qiao-Na Wei, Ai-Min Huang, Lin Ma, Zilun Huang, Xi Huang, Pan-Pan Qiang, Zhu-Ping Gong, L. Z. Structure Regulation of Silk Fibroin Films for Controlled Drug Release. *J. Appl. Polym. Sci.* (2012). doi:10.1002/app
253. Chen, X., Shao, Z., Marinkovic, N. S., Miller, L. M., Zhou, P. & Chance, M. R. Conformation transition kinetics of regenerated Bombyx mori silk fibroin membrane monitored by time-resolved FTIR spectroscopy. *Biophys. Chem.* **89,** 25–34 (2001).

254. David J. Belton, Robyn Plowright, David L. Kaplan, and C. C. P. A Robust Spectroscopic Method for the Determination of Protein Conformational Composition-Application to the Annealing of Silk. *Acta Biomater.* **73,** 355–364 (2018).

255. Kim, H. H., Song, D. W., Kim, M. J., Ryu, S. J., Um, I. C., Ki, C. S. & Park, Y. H. Effect of silk fibroin molecular weight on physical property of silk hydrogel. *Polymer (Guildf).* **90,** 26–33 (2016).

256. Pepelanova, I., Kruppa, K., Scheper, T. & Lavrentieva, A. Gelatin-methacryloyl (GelMA) hydrogels with defined degree of functionalization as a versatile toolkit for 3D cell culture and extrusion bioprinting. *Bioengineering* **5,** (2018).

257. Silva, S. S., Popa, E. G., Gomes, M. E., Oliveira, M. B., Nayak, S., Subia, B., Mano, J. F., Kundu, S. C. & Reis, R. L. Silk hydrogels from non-mulberry and mulberry silkworm cocoons processed with ionic liquids. *Acta Biomater.* **9,** 8972–8982 (2013).

258. Pepelanova, I., Kruppa, K., Scheper, T. & Lavrentieva, A. Gelatin-Methacryloyl (GelMA) Hydrogels with Defined Degree of Functionalization as a Versatile Toolkit for 3D Cell Culture and Extrusion Bioprinting. *Bioengineering* **5,** 55 (2018).

259. Liang, H., Russell, S. J., Wood, D. J. & Tronci, G. A hydroxamic acid-methacrylated collagen conjugate for the modulation of inflammation-related MMP upregulation. *J. Mater. Chem. B* **6,** 3703–3715 (2018).

260. Pitarresi, G., Pierro, P., Palumbo, F. S., Tripodo, G. & Giammona, G. Photo-cross-linked hydrogels with polysaccharide-poly(amino acid) structure: New biomaterials for pharmaceutical applications. *Biomacromolecules* **7,** 1302–1310 (2006).

261. Aznar-Cervantes, S. D., Lozano-Perez, A. A., Garcia Montalbon, M., Villora, G., Vicente-Cervantes, D. & Cenis, J. L. Importance of refrigeration time in the electrospinning of silk fibroin aqueous solutions. *J. Mater. Sci.* **50,** 4879–4887 (2015).

262. Cui, X., Soliman, B. G., Alcala-Orozco, C. R., Li, J., Vis, M. A. M., Santos, M., Wise, S. G., Levato, R., Malda, J., Woodfield, T. B. F., Rnjak-Kovacina, J. & Lim, K. S. Rapid Photocrosslinking of Silk Hydrogels with High Cell Density and Enhanced Shape Fidelity. *Adv. Healthc. Mater.* **9,** (2020).

263. Kelly A. Burke, Dane C. Roberts, D. L. K. Silk Fibroin Aqueous-Based Adhesives Inspired by Mussel Adhesive Proteins Kelly. *Biomacromolecules* **17,** 237–245 (2016).

264. Fischer, D., Li, Y., Ahlemeyer, B., Krieglstein, J. & Kissel, T. In vitro cytotoxicity testing of polycations: influence of polymer structure on cell viability andhemolysis. **24,** 1121–1131 (2003).

265. Mazzoccoli, J. P., Feke, D. L., Baskaran, H. & Pintauro, P. N. Mechanical and Cell Viability Properties of Crosslinked Low and High MW PEGDA blends. *J. Biomed. Mater. Res. A* **93,** 558–566 (2010).

266. Chan, N. J., Gu, D., Tan, S., Fu, Q., Pattison, T. G., Connor, A. J. O. & Qiao, G. G. Spider-silk inspired polymeric networks by harnessing the mechanical potential of β-sheets through. *Nat. Commun.* **11,** (2020).

267. Kim, H., Park, M. N., Kim, J., Jang, J., Kim, H. K. & Cho, D. W. Characterization of cornea-specific bioink: high transparency, improved in vivo safety. *J. Tissue Eng.* **10,** (2019).

268. Zhang, B., Xue, Q., Li, J., Ma, L., Yao, Y., Ye, H., Cui, Z. & Yang, H. 3D bioprinting for artificial cornea: Challenges and perspectives. *Med. Eng. Phys.* **71,** 68–78 (2019).

269. Chen, F., Le, P., Fernandes-Cunha, G. M., Heilshorn, S. C. & Myung, D. Bio-orthogonally crosslinked hyaluronate-collagen hydrogel for suture-free corneal defect repair. *Biomaterials* **255,** 120176 (2020).

270. Fernandes-Cunha, G. M., Chen, K. M., Chen, F., Le, P., Han, J. H., Mahajan, L. A., Lee, H. J., Na, K. S. & Myung, D. In situ-forming collagen hydrogel crosslinked via multi-functional PEG as a matrix therapy for corneal defects. *Sci. Rep.* **10,** 1–13 (2020).

271. Cortina, M. & de la Cruz, J. *Keratoprostheses and Artificial Corneas*. (Springer-Verlag Berlin Heidelberg, 2015).

272. Fagerholm, P., Lagali, N. S., Merrett, K., Jackson, W. B., Munger, R., Liu, Y., Polarek, J. W., Söderqvist, M. & Griffith, M. A biosynthetic alternative to human donor tissue for inducing corneal regeneration: 24-Month follow-up of a phase 1 clinical study. *Sci. Transl. Med.* **2,** (2010).

273. Ferracci, G., Zhu, M., Ibrahim, M. S., Ma, G., Fan, T. F., Lee, B. H. & Cho, N. J. Photocurable Albumin Methacryloyl Hydrogels as a Versatile Platform for Tissue Engineering. *ACS Appl. Bio Mater.* (2020).

274. Lee, H. J., Fernandes-Cunha, G. M. & Myung, D. In situ-forming hyaluronic acid hydrogel through visible light-induced thiol-ene reaction. *React. Funct. Polym.* **131,** 29–35 (2018).

275. Koivusalo, L., Kauppila, M., Samanta, S., Parihar, V. S., Ilmarinen, T., Miettinen, S., Oommen, O. P. & Skottman, H. Tissue adhesive hyaluronic acid hydrogels for sutureless stem cell delivery and regeneration of corneal epithelium and stroma. *Biomaterials* **225,** 119516 (2019).

276. Isaacson, A., Swioklo, S. & Connon, C. J. 3D bioprinting of a corneal stroma equivalent. *Exp. Eye Res.* **173,** 188–193 (2018).
277. Tonsomboon, K. & Oyen, M. L. Composite electrospun gelatin fiber-alginate gel scaffolds for mechanically robust tissue engineered cornea. *J. Mech. Behav. Biomed. Mater.* **21,** 185–194 (2013).
278. Sani, E. S., Lassaletta, A. D., Wang, X., Assmann, A., Zhang, Y.-N., Weiss, A. S., Annabi, N., Cheng, G., Vegh, A., Khademhosseini, A., Gangadharan, S., Ruiz-Esparza, G. U. & Dehghani, B. Engineering a highly elastic human protein–based sealant for surgical applications. *Sci. Transl. Med.* **9,** (2017).
279. Mahdavi, S. S., Abdekhodaie, M. J., Kumar, H., Mashayekhan, S., Baradaran-Rafii, A. & Kim, K. Stereolithography 3D Bioprinting Method for Fabrication of Human Corneal Stroma Equivalent. *Ann. Biomed. Eng.* **48,** 1955–1970 (2020).
280. Kilic Bektas, C. & Hasirci, V. Cell loaded 3D bioprinted GelMA hydrogels for corneal stroma engineering. *Biomater. Sci.* **8,** 438–449 (2020).
281. Holland, C., Numata, K., Rnjak-Kovacina, J. & Seib, F. P. The Biomedical Use of Silk: Past, Present, Future. *Adv. Healthc. Mater.* **8,** (2019).
282. Chirila, T., Barnard, Z., Zainuddin, Harkin, D. G., Schwab, I. R. & Hirst, L. Bombyx mori silk fibroin membranes as potential substrata for epithelial constructs used in the management of ocular surface disorders. *Tissue Eng. A* **14,** 1203 (2008).
283. Higa, K., Takeshima, N., Moro, F., Kawakita, T., Kawashima, M., Demura, M., Shimazaki, J., Asakura, T., Tsubota, K. & Shimmura, S. Porous silk fibroin film as a transparent carrier for cultivated corneal epithelial sheets. *J. Biomater. Sci. Polym. Ed.* **22,** 2261–2276 (2011).
284. Barroso, I. A., Man, K., Villapun, V. M., Cox, S. S. & Ghag, A. K. Methacrylated Silk Fibroin Hydrogels: pH as a Tool to Control Functionality. *ACS Biomater. Sci. Eng.* (2021).
285. Ghobril, C. & Grinstaff, M. W. The chemistry and engineering of polymeric hydrogel adhesives for wound closure: A tutorial. *Chem. Soc. Rev.* **44,** 1820–1835 (2015).
286. Mohammed, S., Chouhan, G., Anuforom, O., Cooke, M., Walsh, A., Morgan-Warren, P., Jenkins, M. & de Cogan, F. Thermosensitive hydrogel as an in situ gelling antimicrobial ocular dressing. *Mater. Sci. Eng. C* **78,** 203–209 (2017).
287. Ana Salomé Veiga and Joel P. Schneider. Antimicrobial hydrogels for the treatment of infection. *Biopolymers* **100,** 637–644 (2013).

288. Andrews, J. M. Determination of minimum inhibitory concentrations. *J. Antimicrob. Chemother.* **48,** 5–16 (2001).

289. Hammer, A., Richoz, O., Mosquera, S. A., Tabibian, D., Hoogewoud, F. & Hafezi, F. Corneal biomechanical properties at different corneal cross-linking (CXL) irradiances. *Investig. Ophthalmol. Vis. Sci.* **55,** 2881–2884 (2014).

290. Freegard, T. J. The physical basis of transparency of the normal cornea. *Eye (Lond).* **11,** 465–471 (1997).

291. Taylor, Z. D., Garritano, J., Sung, S., Bajwa, N., Bennett, D. B., Nowroozi, B., Tewari, P., Sayre, J. W., Hubschman, J.-P., Deng, S. X., Brown, E. R. & Grundfest, W. S. THz and mm-Wave Sensing of Corneal Tissue Water Content: In Vivo Sensing and Imaging Results. *IEEE Trans. terahertz Sci. Technol.* **5,** 184–196 (2015).

292. Kim, S. H. & Chu, C. C. Synthesis and characterization of dextran-methacrylate hydrogels and structural study by SEM. *J. Biomed. Mater. Res.* **49,** 517–527 (2000).

293. Hoch, E., Hirth, T., Tovar, G. E. M. & Borchers, K. Chemical tailoring of gelatin to adjust its chemical and physical properties for functional bioprinting. *J. Mater. Chem. B* **1,** 5675–5685 (2013).

294. Hoch, E., Schuh, C., Hirth, T., Tovar, G. E. M. & Borchers, K. Stiff gelatin hydrogels can be photo-chemically synthesized from low viscous gelatin solutions using molecularly functionalized gelatin with a high degree of methacrylation. *J. Mater. Sci. Mater. Med.* **23,** 2607–2617 (2012).

295. Bryant J., S. & Anseth S., K. Hydrogel properties influence ECM production by chondrocytes photoencapsulated in poly(ethylene glycol) hydrogels. *J. Biomed. Mater. Res.* **59,** 63–72 (2002).

296. Hatami-Marbini, H. & Etebu, E. Rate dependent biomechanical properties of corneal stroma in unconfined compression. *Biorheology* **50,** 133–147 (2013).

297. Qin, X., Tian, L., Zhang, H., Chen, X. & Li, L. Evaluation of corneal elastic modulus based on Corneal Visualization Scheimpflug Technology. *Biomed. Eng. Online* **18,** 1–16 (2019).

298. Ahearne, M. & Coyle, A. Application of UVA-riboflavin crosslinking to enhance the mechanical properties of extracellular matrix derived hydrogels. *J. Mech. Behav. Biomed. Mater.* **54,** 259–267 (2016).

299. Engler, A. J., Sen, S., Sweeney, H. L. & Discher, D. E. Matrix Elasticity Directs Stem Cell Lineage Specification. *Cell* **126,** 677–689 (2006).

300. Wang, Z., Kumar, H., Tian, Z., Jin, X., Holzman, J. F., Menard, F. & Kim, K. Visible Light Photoinitiation of Cell-Adhesive Gelatin Methacryloyl Hydrogels for Stereolithography 3D Bioprinting. *ACS Appl. Mater. Interfaces* **10,** 26859–26869 (2018).

301. Murphy, C. M., Haugh, M. G. & O'Brien, F. J. The effect of mean pore size on cell attachment, proliferation and migration in collagen-glycosaminoglycan scaffolds for bone tissue engineering. *Biomaterials* **31,** 461–466 (2010).

302. Murphy, C. M. & O'Brien, F. J. Understanding the effect of mean pore size on cell activity in collagen-glycosaminoglycan scaffolds. *Cell Adhes. Migr.* **4,** 377–381 (2010).

303. Fleischer, S., Shapira, A., Regev, O., Nseir, N., Zussman, E. & Dvir, T. Albumin fiber scaffolds for engineering functional cardiac tissues. *Biotechnol. Bioeng.* **111,** 1246–1257 (2014).

304. Sariri, R. & Ghafoori, H. Tear proteins in health, disease, and contact lens wear. *Biochem.* **73,** 381–392 (2008).

305. Qin, X. H., Ovsianikov, A., Stampfl, J. & Liska, R. Additive manufacturing of photosensitive Hydrogels for tissue engineering applications. *BioNanoMaterials* **15,** 49–70 (2014).

306. Mahdavi, S. S., Abdekhodaie, M. J., Mashayekhan, S., Baradaran-Rafii, A. & Kim, K. Development and in vitro evaluation of photocurable GelMA/PEGDA hybrid hydrogel for corneal stromal cells delivery. *Mater. Today Commun.* **27,** 102459 (2021).

307. Applegate, M. B., Partlow, B. P., Coburn, J., Marelli, B., Pirie, C., Pineda, R., Kaplan, D. L. & Omenetto, F. G. Photocrosslinking of Silk Fibroin Using Riboflavin for Ocular Prostheses. *Adv. Mater.* **28,** 2417–2420 (2016).

308. Liu, J., Lawrence, B. D., Liu, A., Schwab, I. R., Oliveira, L. A. & Rosenblatt, M. I. Silk fibroin as a biomaterial substrate for corneal epithelial cell sheet generation. *Investig. Ophthalmol. Vis. Sci.* **53,** 4130–4138 (2012).

309. Klotz, B. J., Gawlitta, D., Rosenberg, A. J. W. P., Malda, J. & Melchels, F. P. W. Gelatin-Methacryloyl Hydrogels: Towards Biofabrication-Based Tissue Repair. *Trends Biotechnol.* **34,** 394–407 (2016).

310. Hu, W., Wang, Z., Xiao, Y., Zhang, S. & Wang, J. Advances in crosslinking strategies of biomedical hydrogels. *Biomater. Sci.* **7,** 843–855 (2019).

311. Narayanan, A., Xu, Y., Dhinojwala, A. & Joy, A. Advances in Photoreactive Tissue Adhesives Derived from Natural Polymers. *ChemEngineering* **4,** 32 (2020).

312. Agostinacchio, F., Mu, X., Dirè, S., Motta, A. & Kaplan, D. L. In Situ 3D Printing: Opportunities with Silk Inks. *Trends Biotechnol.* **39,** 719–730 (2021).
313. Nguyen, T.-M., Zorgani, A., Lescanne, M., Boccara, C., Fink, M. & Catheline, S. Diffuse shear wave imaging: toward passive elastography using low-frame rate spectral-domain optical coherence tomography. *J. Biomed. Opt.* **21,** 126013 (2016).
314. Mason, J. H., Luo, L., Reinwald, Y., Hallas-potts, A., Herrington, C. S. & Lin, C. Remote spatially variant debiased profiling of cell and tissue mechanical properties. 1–21 (2021).
315. Zhu, M., Wang, Y., Ferracci, G., Zheng, J., Cho, N. J. & Lee, B. H. Gelatin methacryloyl and its hydrogels with an exceptional degree of controllability and batch-to-batch consistency. *Sci. Rep.* **9,** 1–13 (2019).
316. Lee, B. H., Lum, N., Seow, L. Y., Lim, P. Q. & Tan, L. P. Synthesis and characterization of types A and B gelatin methacryloyl for bioink applications. *Materials (Basel).* **9,** 1–13 (2016).
317. Farris, S., Song, J. & Huang, Q. Alternative reaction mechanism for the cross-linking of gelatin with glutaraldehyde. *J. Agric. Food Chem.* **58,** 998–1003 (2010).
318. Teramoto, N., Hayashi, A., Yamanaka, K., Sakiyama, A., Nakano, A. & Shibata, M. Preparation and mechanical properties of photo-crosslinked fish gelatin/imogolite nanofiber composite hydrogel. *Materials (Basel).* **5,** 2573–2585 (2012).
319. Youssef, P. N., Sheibani, N. & Albert, D. M. Retinal light toxicity. *Eye* **25,** 1–14 (2011).
320. Partlow, B. P., Applegate, M. B., Omenetto, F. G. & Kaplan, D. L. Dityrosine Cross-Linking in Designing Biomaterials. *ACS Biomater. Sci. Eng.* **2,** 2108–2121 (2016).
321. Ma, S. Gelatin-based microfluidics device with the feature sizes smaller than 100 μm for production of oil-in-water emulsions. *Microfluid. Nanofluidics* **23,** 1–5 (2019).
322. Goto, R., Nishida, E., Kobayashi, S., Aino, M., Ohno, T. & Iwamura, Y. Gelatin Methacryloyl – Riboflavin (GelMA – RF) Hydrogels for Bone Regeneration. (2021).
323. Islam, M. M., Buznyk, O., Reddy, J. C., Pasyechnikova, N., Alarcon, E. I., Hayes, S., Lewis, P., Fagerholm, P., He, C., Iakymenko, S., Liu, W., Meek, K. M., Sangwan, V. S. & Griffith, M. Biomaterials-enabled cornea regeneration in patients at high risk for rejection of donor tissue transplantation. *npj Regen. Med.* **3,** (2018).
324. Grinstaff, M. W. Designing hydrogel adhesives for corneal wound repair. **28,** 5205–5214 (2007).
325. Bhatia, S. K., Arthur, S. D., Chenault, H. K., Figuly, G. D. & Kodokian, G. K. Polysaccharide-based tissue adhesives for sealing corneal incisions. *Curr. Eye Res.* **32,**

1045–1050 (2007).

326. Shahbazi, J., Marçal, H., Watson, S., Wakefield, D., Sarris, M. & Foster, L. J. R. Sutureless sealing of penetrating corneal wounds using a laser-activated thin film adhesive. *Lasers Surg. Med.* **43,** 490–498 (2011).

327. Samarawickrama, C., Samanta, A., Liszka, A., Fagerholm, P., Buznyk, O., Griffith, M. & Allan, B. Collagen-Based Fillers as Alternatives to Cyanoacrylate Glue for the Sealing of Large Corneal Perforations. *Cornea* **0,** 1 (2017).

328. Liang, Y., Li, Z., Huang, Y., Yu, R. & Guo, B. Dual-Dynamic-Bond Cross-Linked Antibacterial Adhesive Hydrogel Sealants with On-Demand Removability for Post-Wound-Closure and Infected Wound Healing. *ACS Nano* **15,** 7078–7093 (2021).

329. Hasani-Sadrabadi, M. M., Sarrion, P., Pouraghaei, S., Chau, Y., Ansari, S., Li, S., Aghaloo, T. & Moshaverinia, A. An engineered cell-laden adhesive hydrogel promotes craniofacial bone tissue regeneration in rats. *Sci. Transl. Med.* **12,** (2020).

330. Zhou, L., Dai, C., Fan, L., Jiang, Y., Liu, C., Zhou, Z., Guan, P., Tian, Y., Xing, J., Li, X., Luo, Y., Yu, P., Ning, C. & Tan, G. Injectable Self-Healing Natural Biopolymer-Based Hydrogel Adhesive with Thermoresponsive Reversible Adhesion for Minimally Invasive Surgery. *Adv. Funct. Mater.* **31,** 1–13 (2021).

331. Han, W., Zhou, B., Yang, K., Xiong, X., Luan, S., Wang, Y., Xu, Z., Lei, P., Luo, Z., Gao, J., Zhan, Y., Chen, G., Liang, L., Wang, R., Li, S. & Xu, H. Biofilm-inspired adhesive and antibacterial hydrogel with tough tissue integration performance for sealing hemostasis and wound healing. *Bioact. Mater.* **5,** 768–778 (2020).

332. Balakrishnan, B., Payanam, U., Laurent, A., Wassef, M. & Jayakrishnan, A. Efficacy evaluation of an in situ forming tissue adhesive hydrogel as sealant for lung and vascular injury. *Biomed. Mater.* **16,** (2021).

333. Hong, Y., Zhou, F., Hua, Y., Zhang, X., Ni, C., Pan, D., Jiang, D., Yang, L., Lin, Q., Zou, Y., Yu, D., Arnot, D. E., Zou, X., Zhu, L. & Zhang, S. A strongly adhesive haemostatic hydrogel for the repair of arterial and heart bleeds. *Nat. Commun.* 1–11 (2019).

334. Anthis, A. H. C., Hu, X., Matter, M. T., Neuer, A. L., Wei, K., Schlegel, A. A., Starsich, F. H. L. & Herrmann, I. K. Chemically Stable, Strongly Adhesive Sealant Patch for Intestinal Anastomotic Leakage Prevention. *Adv. Funct. Mater.* **31,** (2021).

335. Bayat, N., Zhang, Y., Falabella, P., Menefee, R., Whalen, J. J., Humayun, M. S. & Thompson, M. E. A reversible thermoresponsive sealant for temporary closure of ocular

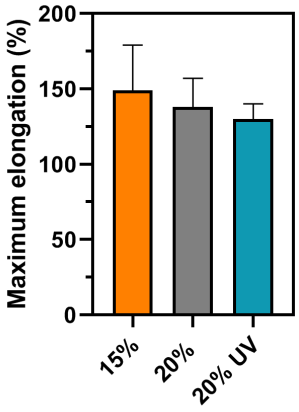
trauma. *Sci. Transl. Med.* **9,** (2017).

336. Xiang, L. & Cui, W. Biomedical application of photo-crosslinked gelatin hydrogels. *J. Leather Sci. Eng.* **3,** (2021).
337. Hutson, C. B., Nichol, J. W., Aubin, H., Bae, H., Yamanlar, S., Al-Haque, S., Koshy, S. T. & Khademhosseini, A. Synthesis and Characterization of Tunable Poly(Ethylene Glycol): Gelatin Methacrylate Composite Hydrogels. *Tissue Eng. Part A* **17,** 1713–1723 (2011).
338. Guimarães, C. F., Gasperini, L., Marques, A. P. & Reis, R. L. The stiffness of living tissues and its implications for tissue engineering. *Nat. Rev. Mater.* (2020). doi:10.1038/s41578-019-0169-1
339. Good, G. W. Light and Eye Damage. *Am. Optom. Assoc.* 1–13 (2014).
340. Fancy, D. A. & Kodadek, T. Chemistry for the analysis of protein-protein interactions: Rapid and efficient cross-linking triggered by long wavelength light. *Proc. Natl. Acad. Sci. U. S. A.* **96,** 6020–6024 (1999).
341. Gorth, D. & Webster, T. J. Matrices for tissue engineering and regenerative medicine. *Biomater. Artif. Organs* 270–286 (2010). doi:10.1533/9780857090843.2.270
342. Dell, S. J., Hovanesian, J. A., Raizman, M. B., Crandall, A. S., Doane, J., Snyder, M., Masket, S., Lane, S. & Fram, N. Randomized comparison of postoperative use of hydrogel ocular bandage and collagen corneal shield for wound protection and patient tolerability after cataract surgery. *J. Cataract Refract. Surg.* **37,** 113–121 (2011).
343. Mah, F. S. Effect on gel formation time of adding topical ophthalmic medications to resure sealant, an in situ hydrogel. *J. Ocul. Pharmacol. Ther.* **32,** 396–399 (2016).
344. Liang, Y., Liu, W., Han, B., Yang, C., Ma, Q., Zhao, W., Rong, M. & Li, H. Fabrication and characters of a corneal endothelial cells scaffold based on chitosan. *J. Mater. Sci. Mater. Med.* **22,** 175–183 (2011).
345. Pircher, M., Götzinger, E., Leitgeb, R., Fercher, A. F. & Hitzenberger, C. K. Measurement and imaging of water concentration in human cornea with differential absorption optical coherence tomography. *Opt. Express* **11,** 2190 (2010).
346. Menduni, F., Davies, L. N., Madrid-Costa, D., Fratini, A. & Wolffsohn, J. S. Characterisation of the porcine eyeball as an in-vitro model for dry eye. *Contact Lens Anterior Eye* **41,** 13–17 (2018).
347. Martínez-García, M. C., Merayo-Llovés, J., Blanco-Mezquita, T. & Mar-Sardaña, S. Wound healing following refractive surgery in hens. *Exp. Eye Res.* **83,** 728–735 (2006).

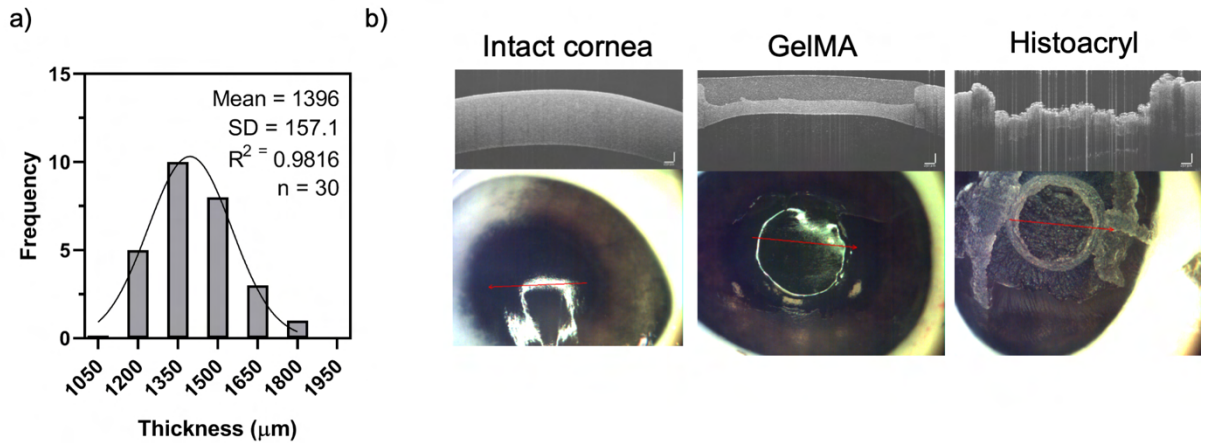
348. Formica, M. L., Awde Alfonso, H. G. & Palma, S. D. Biological drug therapy for ocular angiogenesis: Anti-VEGF agents and novel strategies based on nanotechnology. *Pharmacol. Res. Perspect.* **9,** 1–18 (2021).
349. Kim, L. A. & D'Amore, P. A. A brief history of anti-VEGF for the treatment of ocular angiogenesis. *Am. J. Pathol.* **181,** 376–379 (2012).
350. Sulaiman, R. S., Merrigan, S., Quigley, J., Qi, X., Lee, B., Boulton, M. E., Kennedy, B., Seo, S. Y. & Corson, T. W. A novel small molecule ameliorates ocular neovascularisation and synergises with anti-VEGF therapy. *Sci. Rep.* **6,** 1–11 (2016).
351. Chouhan, G., Moakes, R. J. A., Esmaeili, M., Hill, L. J., deCogan, F., Hardwicke, J., Rauz, S., Logan, A. & Grover, L. M. A self-healing hydrogel eye drop for the sustained delivery of decorin to prevent corneal scarring. *Biomaterials* **210,** 41–50 (2019).
352. Hill, L. J., Moakes, R. J. A., Vareechon, C., Butt, G., Ng, A., Brock, K., Chouhan, G., Vincent, R. C., Abbondante, S., Williams, R. L., Barnes, N. M., Pearlman, E., Wallace, G. R., Rauz, S., Logan, A. & Grover, L. M. Sustained release of decorin to the surface of the eye enables scarless corneal regeneration. *npj Regen. Med.* **3,** 1–12 (2018).
353. Bergman, M. B. Collagenase inhibitors: rationale for their use in treating corneal ulceration. Int Ophthalmol Clin.;15(4):49-66. (1975).
354. Hossain, P. The corneal melting point. *Eye* **26,** 1029–1030 (2012).
355. Mobaraki, M., Ghaffari, M., Yazdanpanah, A., Luo, Y. & Mills, D. K. Bioinks and bioprinting: A focused review. *Bioprinting* **18,** e00080 (2020).
356. Gordon, M. O. & Kass, M. A. What We Have Learned From the Ocular Hypertension Treatment Study. *Am. J. Ophthalmol.* **189,** xxiv–xxvii (2018).
357. Chae, J. J., Mulreany, D. G., Guo, Q., Lu, Q., Choi, J. S., Strehin, I., Espinoza, F. A., Schein, O., Trexler, M. M., Bower, K. S. & Elisseeff, J. H. Application of a collagen-based membrane and chondroitin sulfate-based hydrogel adhesive for the potential repair of severe ocular surface injuries. *Mil. Med.* **179,** 686–694 (2014).
358. Levental, I., Georges, P. C. & Janmey, P. A. Soft biological materials and their impact on cell function. *Soft Matter* **3,** 299–306 (2007).

APPENDIX A

CHAPTER SEVEN SUPPLEMENTARY MATERIAL

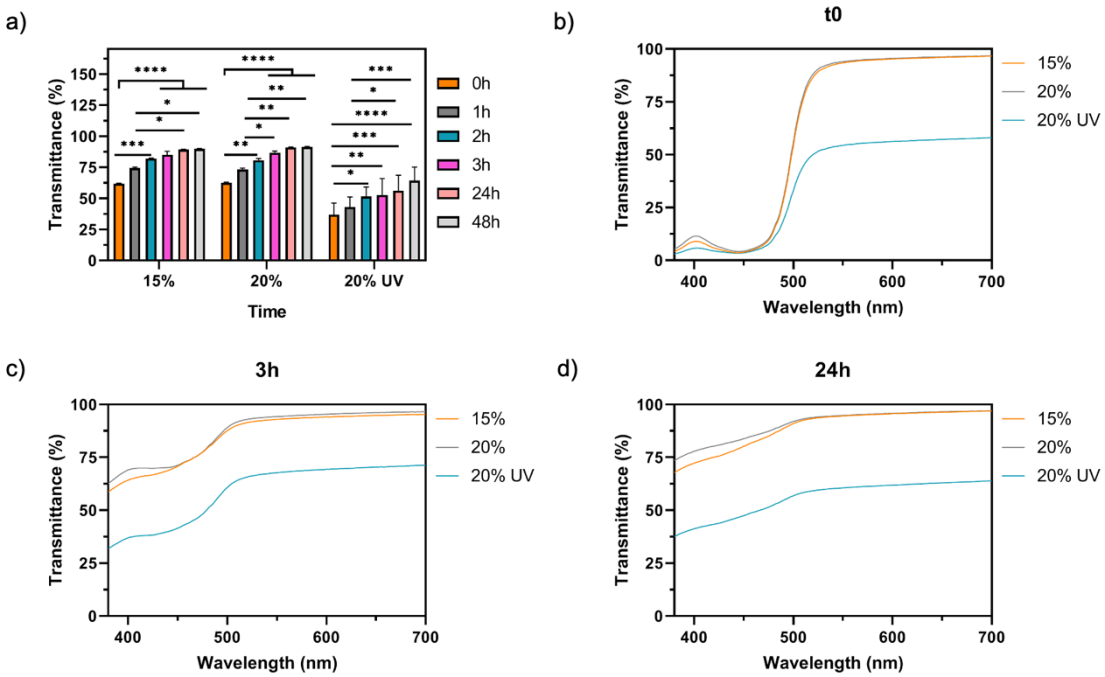


Supplementary Figure A.1 *– Tensile mechanical testing of GelMA hydrogels: elongation at the point of failure (%). Data presented as mean value ± SD.*



Supplementary Figure A.2 *– a) Central porcine corneal thickness distribution calculated from OCT images using ImageJ. b) Comparison between an intact cornea and an ocular injury filled with GelMA adhesive and*

Histoacryl. GelMA fills the injury by forming a smooth seal that restores the ocular curvature, while Histoacryl fails to fill the wound, creating a rough and opaque layer.



Supplementary Figure A.3 *– GelMA hydrogels transmittance in the visible range: a) average optical transmittance over time and optical transmittance profiles b) after curing (t0) and c) after 3 h and d) 24 h incubation in PBS at 32°C. Data presented as mean value ± SD (*p<0.05, **p<0.01, ***p< 0.001, ****p<0.0001).*

APPENDIX B

PUBLISHED PAPERS

ACS Biomaterials SCIENCE & ENGINEERING

pubs.acs.org/journal/abseba

Article

Methacrylated Silk Fibroin Hydrogels: pH as a Tool to Control Functionality

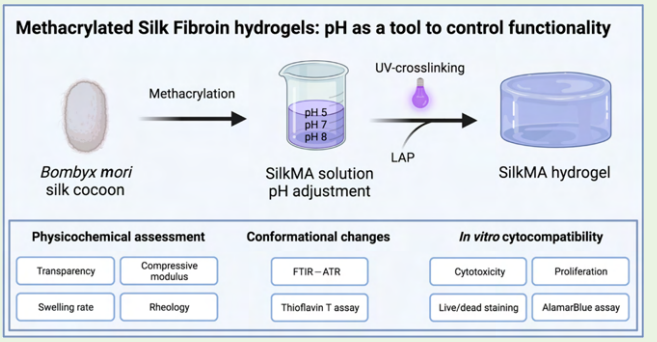
Inês A. Barroso, Kenny Man, Victor M. Villapun, Sophie C. Cox, and Anita K. Ghag*

Cite This: https://doi.org/10.1021/acsbiomaterials.1c00791

Read Online

ACCESS | Metrics & More | Article Recommendations

ABSTRACT: The last decade has witnessed significant progress in the development of photosensitive polymers for in situ polymerization and 3D printing applications. Light-mediated sol−gel transitions have immense potential for tissue engineering applications as cell-laden materials can be crosslinked within minutes under mild environmental conditions. Silk fibroin (SF) is extensively explored in regenerative medicine applications due to its ease of modification and exceptional mechanical properties along with cytocompatibility. To efficiently design SF materials, the in vivo assembly of SF proteins must be considered. During SF biosynthesis, changes in pH, water content, and metal ion concentrations throughout the silkworm gland divisions drive the transition from liquid silk to its fiber form. Herein, we study the effect of the glycidyl-methacrylate-modified SF (SilkMA) solution pH on the properties and secondary structure of SilkMA hydrogels by testing formulations prepared at pH 5, 7, and 8. Our results demonstrate an influence of the prepolymer solution pH on the hydrogel rheological properties, compressive modulus, optical transmittance, and network swellability. The hydrogel pH did not affect the in vitro viability and morphology of human dermal fibroblasts. This work demonstrates the utility of the solution pH to tailor the SilkMA conformational structure development toward utility and function and shows the need to strictly control the pH to reduce batch-to-batch variability and ensure reproducibility.



KEYWORDS: *silk, methacrylated silk, pH, hydrogel, β-sheet, regenerative medicine*

Downloaded via UNIV OF BIRMINGHAM on October 1, 2021 at 15:01:21 (UTC).
See https://pubs.acs.org/sharingguidelines for options on how to legitimately share published articles.

1. INTRODUCTION

Hydrogels have been extensively studied in the tissue engineering field due to their three-dimensional hydrophilic networks, biodegradability, and elasticity.[1,2] In particular, polypeptides (e.g., collagen, gelatin, and silk) are particularly attractive due to their resemblance with the native extracellular matrix environment.[3] Recently, there has been increasing interest in the development of photosensitive hydrogels for 3D printing and in situ polymerization applications. These materials can be combined with cells, growth factors, and bioactive factors and crosslinked within seconds using light. Despite these advantages, limited reproducibility and batch-to-batch variability remain the main preventive factors to the wide application of natural polymers in tissue engineering.

In the last decade, silk fibroin (SF) has proved itself to be one of the most versatile materials available for regenerative medicine applications. Its water-based processing and ease of modification along with exceptional mechanical properties, biocompatibility, and slow in vivo degradation make it an attractive material for regenerative medicine.[4,5] Silks are naturally derived fibrous proteins produced by spiders, silkworms, bees, moths, and scorpions.[6,7] The composition, structure, and properties of silk extracted from different species are variable. Silk obtained from the *Bombyx mori* (domesticated silkworm) has been most extensively studied and used in textile production for more than 4000 years.[8] *B. mori* silk is composed of two main proteins: sericin (20−30%) and SF (70−80%) with trace amounts of carbohydrates and waxes.[9] Since sericin generally yields an inflammatory response, this protein is typically removed through a process called degumming.[10]

To efficiently optimize SF materials and design synthetic polymers that mimic natural silk, the in vivo assembly of silk proteins must be understood.[11] In vivo, silk exhibits a water-soluble structure composed of random coil, α-helix, and hydrated β-strands. However, after spinning, SF assumes a remarkably stable and insoluble β-sheet crystalline structure

Received: June 15, 2021
Accepted: September 15, 2021

© XXXX American Chemical Society

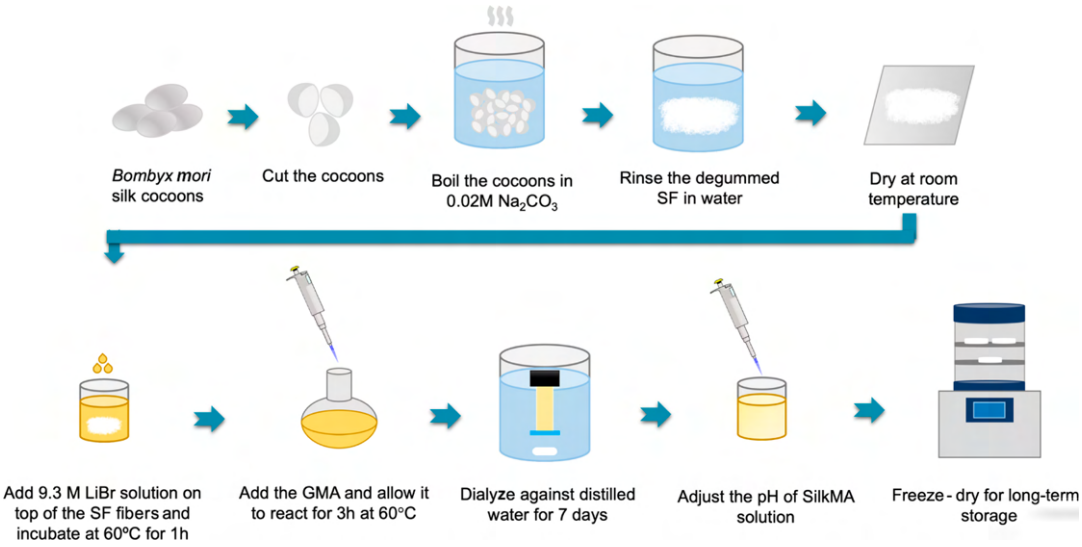


Figure 1. Workflow for SF extraction and SilkMA synthesis: degumming, dissolution in LiBr, methacrylation, dialysis, and freeze-drying.

stabilized by hydrogen bonds.[11] In the mulberry silkworm, *B. mori*, the silk glands consist of a posterior, middle, and anterior division, followed by the spinning duct.[11] As liquid SF flows through the secretory pathway, changes in pH, water content, and metal ion concentrations are thought to drive the transition from noncrystalline liquid silk to its fiber structure.[11] Foo et al. studied how variations in pH and salt concentrations throughout the silk glands affect the assembly of silk proteins during natural processing.[11] From the posterior to the anterior part of the secretory pathway, the pH decreases from 6.9 to 4.8. At near neutral pH, strong repulsive forces prevent protein−protein interactions due to the prevalence of negative charges.[12] As the acidity increases, the hydrophilic spacers (pI = 4.03), L-chain (pI = 5.06), and the N-termini (pI = 4.59) and C-termini (pI = 10.53) of the H-chain become less negatively charged. The charge suppression by acidification allows hydrophobic and hydrophilic interactions to occur and initiates changes in the protein secondary structure.[11,12] Simultaneously, the water content falls from 88 to 70%, and the cation concentration increases to neutralize the repulsion forces between the chains. This close packing is fundamental for the proper folding and formation of micellar structures, which will then aggregate and form globular structures before being converted into fibers due to the strain-induced β-sheet formation in the spinneret.[11]

The majority of studies published to date concerning the development of SF materials are based on protein self-assembly into β-sheet-rich networks, referred to as physical crosslinking. Many processes have been identified to induce β-sheet transition: decreased pH,[7,13,14] high temperatures,[15,16] addition of Ca^{2+} ions,[7] methanol/ethanol treatments,[17−21] and direct electric currents.[4,22,23] Strong shear forces mimicking the natural silkworm spinning process also induce gelation (e.g., sonication[24] and vortexing[25]). However, despite providing strength to the hydrogels through physical crosslinking, these β-sheet structures also result in brittle behavior as the crystals block long-range molecular displacements.[26] Therefore, despite their high stiffness, these hydrogels lack the adequate elastic properties needed for the repair of many tissues (e.g., skin and cartilage).[3] Furthermore, the protocols used to prepare physically crosslinked SF materials are incompatible with cell encapsulation due to long gelation times (from 30 min to several hours) and unsuitable environmental conditions, limiting the clinical application of these materials.[3]

Over the last decade, efforts to develop chemically crosslinked SF hydrogels have been made.[3,26] These materials have completely distinct properties when compared with the physically crosslinked hydrogels previously mentioned. Partlow et al. developed a highly elastic SF hydrogel using the horseradish peroxidase (HRP)-mediated crosslinking approach.[26] The gelation kinetics of these enzymatically crosslinked hydrogels can be tailored by changing the HRP and oxygen peroxidase (H_2O_2) content. Yan et al. prepared 16 wt % SF hydrogels with a storage modulus between several hundred Pa and 5 kPa within 5−21 min by changing the H_2O_2 concentration between 0.8 and 1.45‰.[3]

Recently, due to the increasing interest in 3D printing technologies, several polymers have been successfully chemically modified to allow photocrosslinking, such as collagen,[27] gelatin,[28−30] hyaluronan,[31,32] SF,[33] alginate,[31] dextran,[34] PVA,[28] or PEG.[35] Herein, we developed glycidyl-methacrylate-modified SF (SilkMA) hydrogels that can be prepared within minutes via free radical polymerization (chemical crosslinking). Notably, cells can be encapsulated within the hydrogels and the physical properties of the hydrogels can be easily tailored by changing the degree of methacrylation (DM %), polymer concentration, and the photoinitiator system.[33]

Due to the novelty of SilkMA hydrogels, little is known about the role of the prepolymer solution pH in the initial and long-term properties of the gels. Given the importance of pH changes during in vivo processing, we hypothesize that it will influence the overall properties of SilkMA gels and could be used to control the secondary structure toward functionality. The pH influence on the initial properties of SilkMA gels was studied in terms of physicochemical properties and cell behavior. Finally, the spontaneous conformation transitions under physiological conditions and the mechanically toughening impact of β-sheet crystallinity were also addressed. This work highlights the need to rigorously control the pH of silk prepolymer solutions to enhance the reproducible manufacturing process, thereby increasing the potential clinical adoption of silk-based materials for numerous therapeutic applications.

https://doi.org/10.1021/acsbiomaterials.1c00791
ACS Biomater. Sci. Eng. XXXX, XXX, XXX−XXX

2. METHODS

2.1. Preparation of Methacrylated SF (SilkMA). *2.1.1. SF Extraction.* *B. mori* cocoons were supplied by The Yarn Tree (Roanoke, USA). Each cocoon was sliced into four pieces, and the silkworms were discarded. To remove the sericin, 10 g of sliced cocoons was boiled in 4 L of 0.02 M Na_2SO_3 (Acros Organics, Belgium) for 30 min. Subsequently, the degummed SF was washed three times in 2 L of distilled water for 20 min and left in a fume hood overnight to dry at room temperature (Figure 1).

2.1.2. SilkMA Synthesis. Briefly, 25% (w/v) of degummed SF solution was prepared by pouring a 9.3 M lithium bromide solution, LiBr (Acros Organics, Belgium) on the tightly packed degummed SF fibers. The beaker was covered with an aluminum foil and transferred to an incubator at 60 °C. After 1 h, the fibers were completely dissolved and glycidyl methacrylate (GMA) (Sigma-Aldrich, USA) was added to the solution at a rate of 0.5 mL/min (10% v/v) and allowed to react for 3 h at 60 °C with a stirring speed of 300 rpm. The solution was then dialyzed against distilled water for 7 days at 4 °C using 12−14 kDa cutoff dialysis tubes (Thermo Scientific, USA). After dialysis, the SilkMA solution was diluted to 2% (w/v), and the pH was adjusted to 5, 7, or 8 using 1 mM sodium hydroxide solution (Sigma-Aldrich, USA). Last, SilkMA solutions were lyophilized for 2 days to generate a white porous foam, which was stored at −80 °C until further use.

2.2. Degree of Methacrylation. The degree of methacrylation (DM %) was quantified by proton nuclear magnetic resonance (^{1}H NMR). Briefly, 5 mg of SilkMA was dissolved in 600 μL of deuterium oxide (Sigma-Aldrich, USA). The ^{1}H NMR spectra of raw SF and SilkMA were recorded using a Bruker NEO NMR spectrometer fitted with a "smart"-BBFO probe (Bruker, Austria) operating at 400 MHz for 1 h. Spectra were recorded at 25 °C using 250 scans and a delay of 12 s between scans. Baseline and phase correction were applied before integrating the peaks of interest with Topspin software (Bruker, Austria). The signal from the aromatic amino acids (6.9−7.5 ppm) was used as the internal reference to normalize the amine signals (2.83−3.14 ppm).[33] As GMA is reported to react with SF through the primary amines on lysine residues, the extent of substitution was calculated by normalization to the number of free amino groups of the original SF.[33] The degree of methacrylation was calculated using the following equation

$$\text{DM}\ (\%) = \frac{\text{lysine integration signal of SilkMA}}{\text{lysine integration signal of SF}} \times 100 \quad (1)$$

2.3. Hydrogel Fabrication. SilkMA prepolymer solutions were prepared by dissolving an appropriate amount of SilkMA in distilled water at room temperature overnight. The resulting viscous solutions were filtrated using Miracloth (Merck Millipore, USA), and the final concentration was calculated. A fresh stock solution of 2% (w/v) lithium phenyl-2,4,6-trimethylbenzoylphosphinate (LAP) (Sigma-Aldrich, UK) in phosphate-buffered saline (PBS) with pH 7.4 (Sigma-Aldrich, UK) was prepared. The photoinitiator was added to the SilkMA solution to a final concentration of 0.5% (w/v), and the resulting solution was mixed at room temperature. The hydrogel precursor solutions were photocured through UV-light using an OmniCure S1500 (Lumen Dynamics, Ontario, Canada) with a 365 nm filter. Briefly, 200 μL of 15% (w/v) SilkMA prepolymer solution was pipetted onto a 12 mm cylindrical mould and then exposed to 3 mW/cm^2 UV-A for 5 min. In this study, three different SilkMA hydrogels were prepared: SilkMA pH 5 (SF5), SilkMA pH 7 (SF7), and SilkMA pH 8 (SF8).

2.4. Transparency. Light absorbance of hydrogels in the visible range (400−800 nm) was measured using a microplate reader (Spark Multimode, Tecan, Switzerland). The measurements were conducted in triplicate using SilkMA hydrogels (diameter = 12 mm, thickness = 1.2 mm) in PBS, with pure PBS serving as a blank control. Subsequently, the transmittance was calculated using the following equation

$$\text{transmittance}\ (\%) = 10^2 - \text{absorbance} \quad (2)$$

2.5. Swelling Properties. Since swelling characteristics are largely dependent on the polymer chain length, crosslinking density, and mesh size of the hydrogel, the same polymer batch was used to prepare all hydrogels, avoiding molecular weight and DM % variability.[36,37] SilkMA hydrogels with a diameter of 12 mm and a thickness of 1.2 mm were prepared (W_{t0}), and the samples were hydrated in PBS and placed in an incubator at 37 °C. After 24 h, the swollen weight (W_{swollen}) was measured. The swelling (SR) was calculated according to the following equation

$$\text{SR}\ (\%) = \frac{W_{\text{swollen}} - W_{t0}}{W_{t0}} \times 100 \quad (3)$$

The thickness of the fresh and swollen hydrogels was estimated using ImageJ software (NIH, version 2.0), and the expansion (%) in PBS after 24 h was calculated.

2.6. Rheology. The storage modulus (G') and loss modulus (G'') of freshly prepared SilkMA hydrogels were measured in the oscillatory mode at 37 °C using a plate−plate geometry and a 1.2 mm gap between plates (Kinexus Pro+, Malvern, UK). After running an amplitude sweep to determine the linear viscoelastic range (LVER), a frequency sweep was conducted between 0.01 and 10 Hz at 0.5% shear strain.

2.7. Mechanical Characterization. Cyclic testing was performed using an Instron 5542 mechanical tester (Instron, USA) with a 2 kN load cell. Cylindrical hydrogels (diameter = 8 mm, thickness = 2 mm) were prepared as previously described and incubated in PBS for 4 h prior to testing. The dimensions of the samples were determined using a digital caliper. Compressive tests were performed at a rate of 1 mm/min up to a maximum strain of 60% of the original height by performing eight cycles of loading and unloading. The compressive strain (mm) and load (N) were recorded using Bluehill 3 software. The compressive moduli were calculated from the slope of the linear region on the stress (kPa) versus strain (mm/mm) curves.

2.8. Fourier Transform Infrared Spectroscopy. Fourier transform infrared (FTIR) spectroscopy was used to assess conformational structural changes in SilkMA hydrogels prepared at pH 5, 7, or 8 after different incubation times (0, 7, 14, 21, and 28 days). Freeze-dried samples were analyzed using a Nicolet iS5 spectrometer equipped with an iD5 ATR accessory (Thermo Scientific, USA). For each spectrum, 64 scans were acquired in the spectral range of 4000−550 cm^{-1} with a resolution of 4 cm^{-1}. Fourier self-deconvolution (FSD) of the infrared spectra covering the Amide I region (1595−1705 cm^{-1}) was conducted using OMNIC software (Thermo Scientific, USA). Deconvolution was automatically performed using the Gaussian/Lorentzian line shape with a noise reduction factor of 0.3. The deconvoluted amide I spectra were area-normalized, and single band areas were used to calculate the percentage of secondary structures. The peak band assignment was based on the work of Hu et al.[38]

2.9. Thioflavin T Binding Assay. Thioflavin T (ThT) (Sigma-Aldrich, USA) was used to qualitatively study the β-sheet content overtime on hydrogels prepared at pH 5, 7, and 8. Briefly, the hydrogels were stained for 10 min in a freshly prepared 1% (w/v) ThT solution in PBS. Subsequently, the samples were rinsed with 70% (v/v) ethanol and washed three times with distilled water. A fluorescence intensity scan was performed using a microplate reader (Spark Multimode, Tecan, Switzerland) at 360 nm excitation, measuring the emission spectrum in the 400−700 nm range.

2.10. In Vitro Cell Studies. Human dermal fibroblasts (HDFs—ATCC Cat. PCS-201-012; Passage number 9) were cultured in Dulbecco's modified eagle medium (DMEM—Sigma-Aldrich, UK) and supplemented with 10% fetal bovine serum (Sigma-Aldrich, UK), 1% penicillin/streptomycin (Sigma-Aldrich, UK), and 2 mM L-glutamine (Sigma-Aldrich, UK). All cultures were maintained in tissue-culture-treated polystyrene flasks at 37 °C with 5% CO_2 in a humidified incubator and passaged at 80% confluency.

2.10.1. In Vitro Cytocompatibility of Uncured SilkMA Solutions. SilkMA prepolymer solutions were UV-sterilized for 20 min prior to use. Tissue-culture-treated 24-well plates (Corning, UK) were initially

https://doi.org/10.1021/acsbiomaterials.1c00791
ACS Biomater. Sci. Eng. XXXX, XXX, XXX−XXX

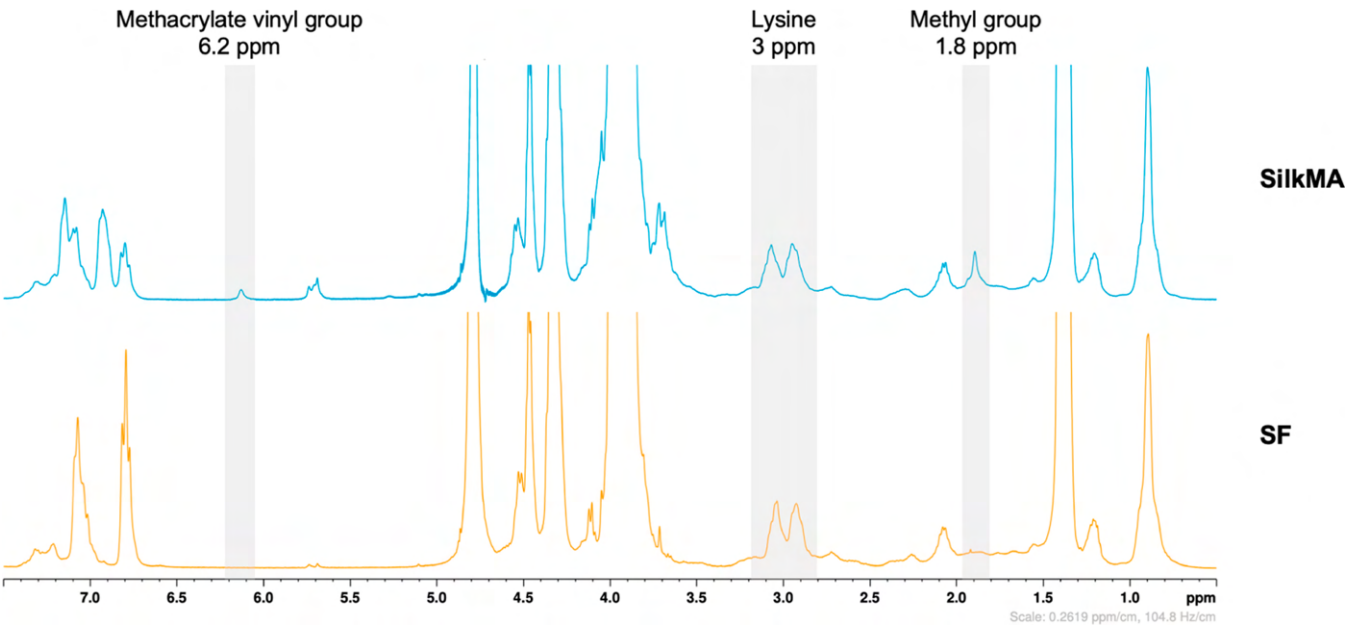


Figure 2. ^{1}H NMR spectra of SilkMA (top) and raw SF (bottom). The presence of the methacrylate vinyl group signal (δ = 6.2 ppm) and methyl group signal (δ = 1.8 ppm) after the removal of unreacted GMA by dialysis confirmed the covalent functionalization of SF with methacrylate groups.

seeded with HDFs (1×10^4 cells/well). After 24 h, DMEM was replaced with fresh supplemented DMEM containing 20% (v/v) prepolymer solution or 20% (v/v) PBS (control group). The monolayer cultures were incubated at 37 °C with 5% CO_2 in a humidified incubator, and cell viability, metabolic activity, and cell proliferation were assessed after 24 and 48 h.

2.10.2. In Vitro Cytocompatibility of SilkMA Hydrogels. SilkMA prepolymer solutions were prepared as previously described, and gelatin methacryloyl (GelMA—type A, bloom 300), a well-studied photosensitive polymer, was used for comparison purposes. Briefly, the 15% (w/v) GelMA prepolymer solution was prepared by dissolving an appropriate amount of polymer in PBS at 37 °C for 30 min. SilkMA and GelMA prepolymer solutions were sterilized by exposure to germicidal UV light for 20 min. Then, filter-sterile LAP was added to the SilkMA and GelMA prepolymer solutions to a final concentration of 0.5% (w/v), and the resulting solutions were mixed. The SilkMA and GelMA hydrogels were photocrosslinked using 3 mW/cm^2 UV-A for 5 min in 48-well suspension cell culture plates (Sarstedt, UK). After curing, the hydrogels were washed with sterile PBS (Sigma-Aldrich, UK) for 15 min and soaked in supplemented DMEM overnight. One hour before cell seeding, the hydrogel matrices were partially dried to potentiate cell penetration. Then, 60 μL of cell suspension was added dropwise onto each hydrogel (9×10^3 cells per scaffold), and samples were incubated for 1 h at 37 °C with 5% CO_2 to bolster cell adhesion. After 1 h, DMEM was carefully added to the wells without disturbing the cell-laden hydrogels.[39] The culture medium was changed every 2 days. Cell viability and metabolic activity were assessed after 2, 7, and 14 days.

2.10.2.1. Cell Viability. Cell viability was evaluated using a live/dead assay (Thermo Fisher, UK) following the manufacturer's protocol. Briefly, SYTO 10 green fluorescent nucleic acid stain (2 μL/mL) and ethidium homodimer-2 nucleic acid stain (2 μL/mL) were diluted in PBS to form the staining solution. At each time point, the cell medium was removed, and samples were incubated with the staining solution for 15 min in the dark at 37 °C. The staining solution was removed, and the samples were washed twice with PBS. The monolayer cultures and cell-seeded hydrogels were imaged with a fluorescence microscope (EVOS M5000, Thermo Fisher, UK) and a confocal scanning microscope (Zeiss LSM710, Carl Zeiss, Germany), respectively.

2.10.2.2. Metabolic Activity. AlamarBlue assay (Thermo Fisher, UK) was used to determine the relative metabolic activity according to the manufacturer's protocol. Briefly, the samples were incubated with 0.5 mL of 10% alamarBlue reagent in the culture medium for 4 h at 37 °C with 5% CO_2. Thereafter, 50 μL of the cell culture medium was transferred to a 96-well plate (Corning, UK), and the fluorescence intensity was measured using a microplate reader (Spark Multimode, Tecan, Switzerland) at an excitation wavelength of 540 nm and an emission wavelength of 590 nm. Acellular hydrogels were used as a negative control, and their fluorescence was subtracted from the same group seeded hydrogels to account for the background ($n \geq 4$).

2.10.2.3. Cell Proliferation. The DNA content was quantified using the Quant-iT PicoGreen DNA assay (Invitrogen, Life Technologies, UK). Briefly, cells were lysed in 0.1% Triton X-100 in PBS (Sigma-Aldrich, UK) and kept at −80 °C until further analysis. Cells were lysed following three freeze/thaw cycles between −80 and 37 °C with vortexing. After spinning down the samples at 300 g for 5 min to remove the nongenomic material, 10 μL of cell lysate was added to 90 μL of TE (10 mM Tris−HCl, 1 mM EDTA) buffer in a 96-well plate (Corning, UK). 100 μL of PicoGreen reagent was added to all samples and then incubated for 5 min. The fluorescence intensity was then measured with a microplate reader (Spark Multimode, Tecan, Switzerland) at excitation and emission wavelengths of 480 and 520 nm, respectively.

2.11. Statistical Analysis. For each experiment, at least three samples were tested. One- or two-way analysis of variance (ANOVA) and the Tukey test were used to determine statistically significant differences with GraphPad Prism 8.0 software. The level of significance was set at $p < 0.05$. Data are presented as mean value ± standard deviation (SD). Samples were tested in triplicate for each condition.

3. RESULTS

3.1. Physicochemical Characterization of SilkMA Gels. ^{1}H NMR spectroscopy was used to confirm the methacrylate functionalization of SF (Figure 2). The appearance of the characteristic resonances of the methacrylate vinyl group (olefinic hydrogen, δ = 6.2 ppm) and methyl group (methyl hydrogen, δ = 1.8 ppm) of GMA confirmed the

https://doi.org/10.1021/acsbiomaterials.1c00791
ACS Biomater. Sci. Eng. XXXX, XXX, XXX−XXX

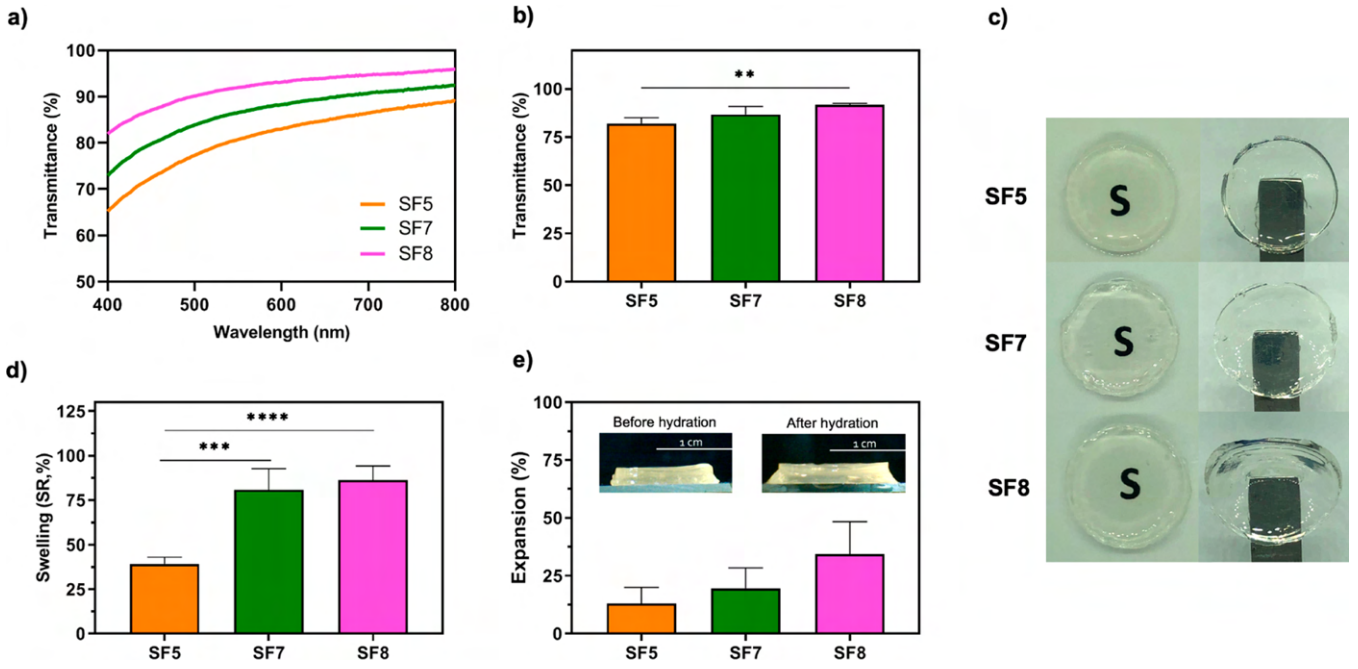


Figure 3. SilkMA hydrogel transmittance in the visible range: (a) transmittance profiles, (b) average optical transmittance, and (c) optical clarity and rigidity of SilkMA hydrogels (%). Swelling properties of SilkMA hydrogels in PBS at 37 °C: (d) swelling (%) and (e) hydrogel expansion (%). Hydrogel diameter = 12 mm. Data presented as mean value ± SD (*p < 0.05, **p < 0.01, ***p < 0.001, and ****p < 0.0001).

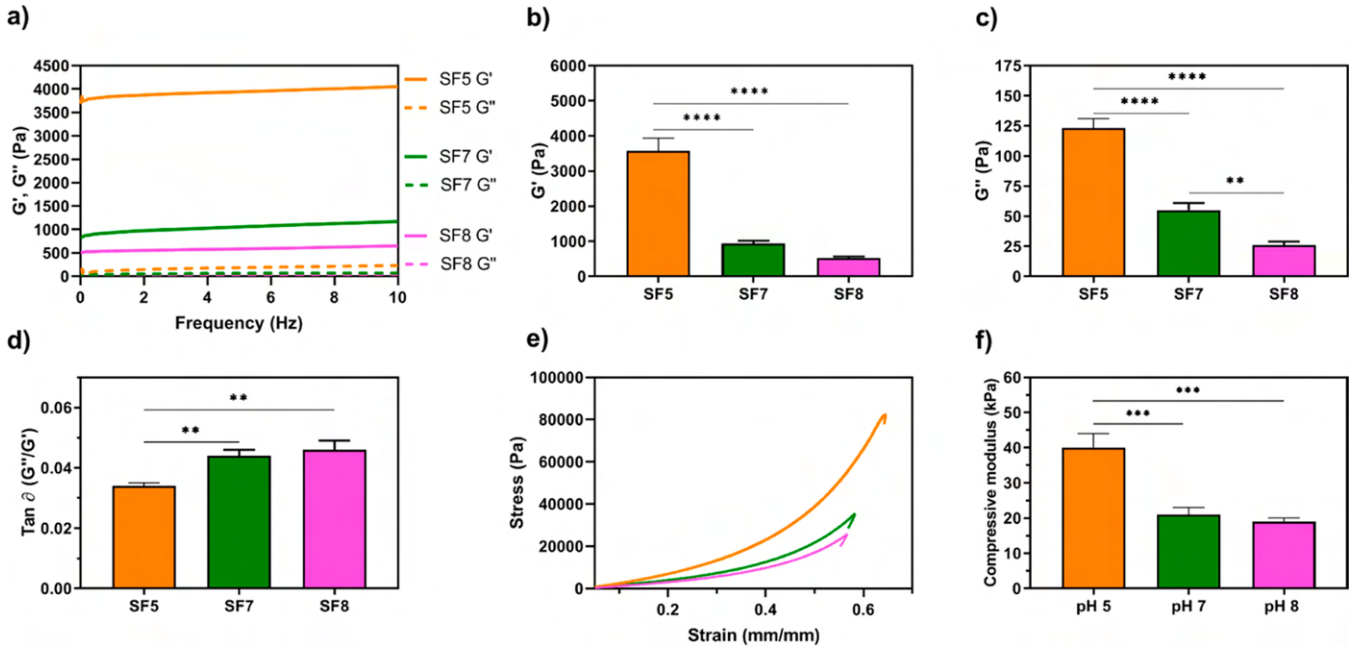


Figure 4. Rheological properties of SilkMA hydrogels: (a) representative frequency sweep, (b) storage modulus (G'), (c) loss modulus (G''), and (d) damping factor (tan δ). Cyclic compressive mechanical testing of SilkMA hydrogels: (e) representative compressive strain−stress curves and (f) compressive moduli. Data presented as mean value ± SD (*p < 0.05, **p < 0.01, ***p < 0.001, and ****p < 0.0001).

covalent functionalization of SF with methacrylate groups, while the absence of the epoxide ring group (aliphatic protons, δ = 2.82 and 2.67 ppm) indicates the complete removal of unreacted GMA through dialysis.[33,40] The decrease in the lysine methylene signal (δ = 3 ppm) indicated that the DM % was 35−40% after a 3 h reaction with 10% (v/v) GMA. In this work, three different hydrogel formulations were prepared: SF5, SF7, and SF8.

Transmittance profiles of 15% (w/v) SilkMA hydrogels in the visible light range are shown in Figure 3a. In general, all SilkMA hydrogels displayed high optical clarity, with transmittance values ranging from 82.1 ± 3.0 to 91.6 ± 0.9% (Figure 3b,c). The SilkMA hydrogels exhibited enhanced transparency in the visible range with increasing pH, with the SF8 hydrogel eliciting a statistically significant increase in transparency compared to the SF5 hydrogels (10.4 ± 2.3%, p < 0.01) (Figure 3b).

https://doi.org/10.1021/acsbiomaterials.1c00791
ACS Biomater. Sci. Eng. XXXX, XXX, XXX−XXX

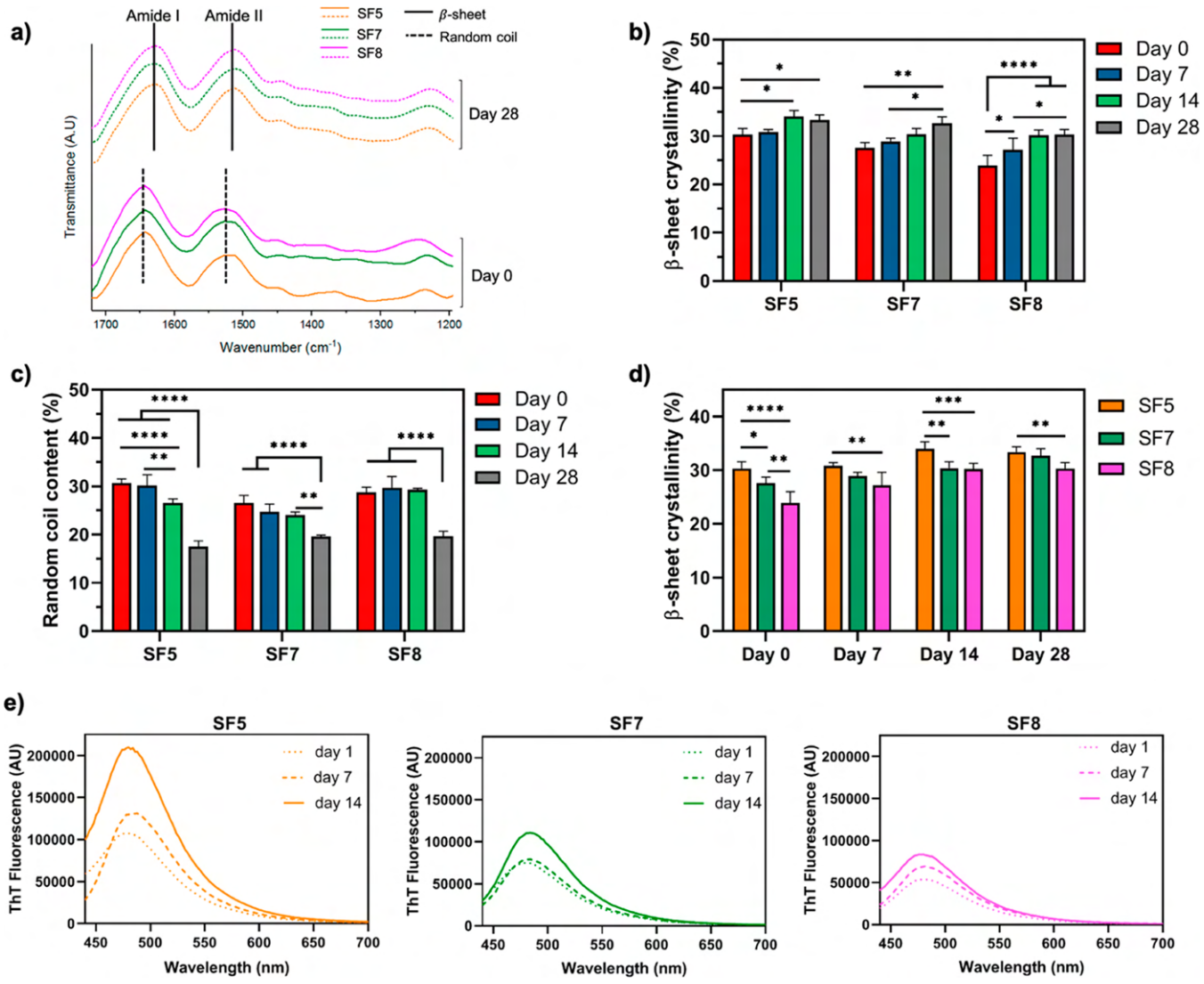


Figure 5. Study of conformational transitions on SilkMA hydrogels over time: (a) FTIR spectra of SilkMA hydrogels after crosslinking (day 0) and 28 days after incubation under physiological conditions, (b) β-sheet crystallinity content over time (days 0, 7, 14, and 28), (c) random coil content over time (days 0, 7, 14, and 28), and (d) comparison of the β-sheet content between groups at different time points (days 0, 7, 14, and 28). (e) ThT staining of SilkMA hydrogels at 1, 7, and 14 days. Emission spectrum in the 440−700 nm range under 360 nm excitation. Data presented as mean value ± SD (*p < 0.05, **p < 0.01, ***p < 0.001, and ****p < 0.0001).

To determine the swelling (SR), water uptake (q), and expansion, SF5, SF7, and SF8 hydrogels were incubated in PBS buffer at 37 °C for 24 h. The swelling characteristics were directly proportional to the hydrogel pH; the SR values of SF5, SF7, and SF8 were 39.3 ± 3.7, 80.9 ± 11.9, and 86.2 ± 7.9%, respectively, with SF7 (p < 0.001) and SF8 (p < 0.0001) exhibiting a 2-fold significant increase compared to SF5 (Figure 3d). As shown in Figure 3e, the expansion of SilkMA hydrogels in PBS is not statistically significant between groups, despite ranging from 13.0 ± 7.0 to 34.4 ± 13.9% for SF5 and SF8, respectively.

The viscoelastic properties of the SilkMA hydrogels were investigated via rheometry. The storage modulus (G') represents the instantaneous, elastic, and reversible response of a material to stretching and deformation of chemical bonds, while the loss modulus (G'') represents the time-dependent, viscous response, and irreversible rearrangement of the internal polymeric structure of the material.[41] First, the LVER was determined by varying the strain at a constant frequency. Up to 1% strain, all groups were structurally stable with constant values for G' and G'' (data not shown). Then, G' and G'' values of the hydrogels were recorded as a function of frequency (0.01−10 Hz, 0.5% strain) at 37 °C. As shown in Figure 4a, limited changes were observed in the storage modulus G' in the frequency range studied, confirming the high stability of the hydrogels. Moreover, G'' is an order of magnitude lower than G', which is a typical behavior of viscoelastic materials (Figure 4c). Importantly, our results indicate that decreasing the pH of the prepolymer solution resulted in significantly stiffer hydrogels; SF5 hydrogels had a storage modulus significantly greater than SF7 (p < 0.0001) and SF8 (p < 0.0001) hydrogels by 3- and 6-fold, respectively (Figure 4b). The differences in stiffness were noticeable when handling the hydrogels, with SF8 hydrogels being substantially more difficult to handle (Figure 3c). Finally, the damping factor ($\tan \delta = G''/G'$) was greater for SF7 and SF8 but lower than 0.08 for all groups, suggesting that all SilkMA hydrogels behaved as elastomeric materials (Figure 4d).[33,42]

https://doi.org/10.1021/acsbiomaterials.1c00791
ACS Biomater. Sci. Eng. XXXX, XXX, XXX−XXX

Table 1. Relative Content of Secondary Structures in SilkMA Hydrogels Incubated at 37 °C for 0, 7, 14, and 28 Days[a]

SilkMA sample	time (days)	side chains (%)	turns (%)	random coil (%)	α-helices (%)	β-sheet (%)
SF5	0	5 ± 0.4	23.6 ± 0.8	30.7 ± 0.8	10.5 ± 0.3	30.3 ± 1.3
	7	12.3 ± 3.3	16.2 ± 0.5	30.2 ± 2.2	10.5 ± 4.0	30.8 ± 0.6
	14	12.6 ± 0.8	18.8 ± 0.4	26.6 ± 0.8	8.0 ± 1.5	34.0 ± 1.3
	28	19.9 ± 2.1	22.5 ± 1.4	17.5 ± 1.2	6.8 ± 0.3	33.4 ± 1.0
SF7	0	14.6 ± 1.2	21.1 ± 0.4	26.6 ± 1.5	10.2 ± 0.4	27.6 ± 1.1
	7	16.0 ± 1.8	21.1 ± 0.9	24.7 ± 1.6	9.3 ± 0.4	28.9 ± 0.7
	14	15.6 ± 0.5	20.4 ± 1.9	24.0 ± 0.7	9.5 ± 0.5	30.4 ± 1.2
	28	24.5 ± 1.2	16.1 ± 0.6	19.6 ± 0.3	7.1 ± 0.6	32.7 ± 1.3
SF8	0	14.7 ± 1.4	22.5 ± 1.4	28.8 ± 1.0	10.1 ± 0.3	23.9 ± 2.1
	7	12.5 ± 4.2	19.1 ± 3.5	29.7 ± 2.3	11.5 ± 1.0	27.2 ± 2.4
	14	14.1 ± 0.4	15.6 ± 1.7	29.3 ± 0.3	10.8 ± 0.7	30.2 ± 1.1
	28	27.7 ± 1.7	15.4 ± 2.5	19.7 ± 1.0	7.0 ± 0.1	30.3 ± 1.1

[a]Data obtained from deconvolution of the infrared spectra covering the amide I region. Data presented as mean value ± SD (n = 4).

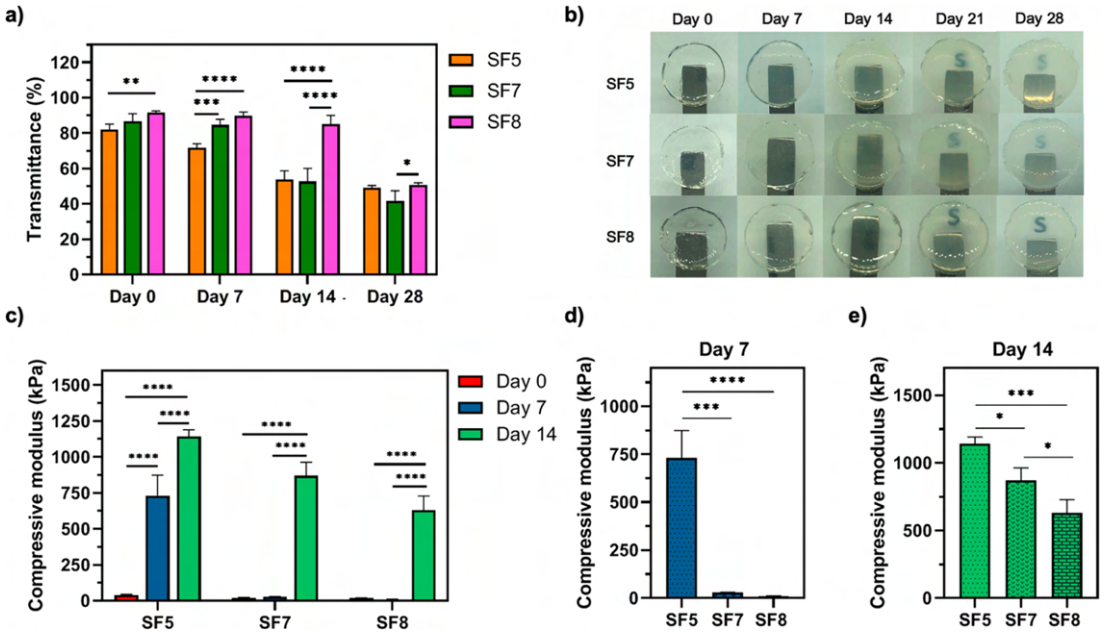


Figure 6. Study of the natural conformational changes in SilkMA hydrogels incubated in PBS at 37 °C. (a) Average optical transmittance in the visible range of SilkMA hydrogels at 0, 7, 14, and 28 days. (b) Appearance of SilkMA hydrogels after incubation for 0, 7, 14, 21, and 28 days (hydrogel diameter = 1 cm). (c) Mechanical toughening impact of the increasing β-sheet content on SilkMA hydrogels. (d) Compression moduli of SilkMA hydrogels after incubating for 7 days. (e) Compression moduli of SilkMA hydrogels after incubating for 14 days. Data presented as mean value ± standard deviation (*p < 0.05, **p < 0.01, ***p < 0.001, ****p < 0.0001).

The mechanical properties of SilkMA hydrogels were determined through compression testing. Our results revealed that all groups were mechanically stable for cyclic compressive mechanical testing (Figure 4e). In agreement with the rheology data, statistical analysis illustrated a significant pH effect on the compressive modulus of SilkMA hydrogels with SF5 hydrogels showcasing a significantly higher compressive modulus than SF7 and SF8 (p < 0.001). Specifically, the compressive modulus is 21 ± 2 kPa for SF7 and 40 ± 4 kPa for SF5, a 2-fold increase (Figure 4f).

3.2. Natural Conformational Changes in SilkMA Hydrogels over Time. SF materials are reported to suffer spontaneous conformational changes under physiological conditions.[3,5,43,44] To further understand the observed differences in the properties of SilkMA gels, the secondary structure of the hydrogels was studied using FTIR spectroscopy and a ThT binding assay (Figure 5). As shown in Figure 5a, the major bands of the protein infrared spectrum can be observed in SilkMA hydrogels: amide I (1700−1600 cm^{-1}), amide II (1600−1500 cm^{-1}), and amide III (1350−1200 cm^{-1}).[45] At day 0, the main absorption bands were observed at 1643 cm^{-1} (amide I) and 1525 cm^{-1} (amide II), which are characteristic of the random coil conformation. However, after incubating the hydrogels for 28 days under physiological conditions, these absorption bands shifted to 1629 cm^{-1} (amide I) and 1512 cm^{-1} (amide II), suggesting an increase in the β-sheet content.[45] Importantly, the amide I (1700−1600 cm^{-1}) region is very sensitive to the secondary structure and can be deconvoluted into discreet component bands, indicative of tyrosine side chains, random coil, turns, α-helixes, and β-sheet structures.[45,46] Deconvoluted amide I spectra were area-normalized, and the areas of the single bands were used to calculate the relative content of secondary structures, as shown in Table 1.

An increase in the β-sheet content was accompanied by a decrease in the random coil content upon aging for all groups

https://doi.org/10.1021/acsbiomaterials.1c00791
ACS Biomater. Sci. Eng. XXXX, XXX, XXX−XXX

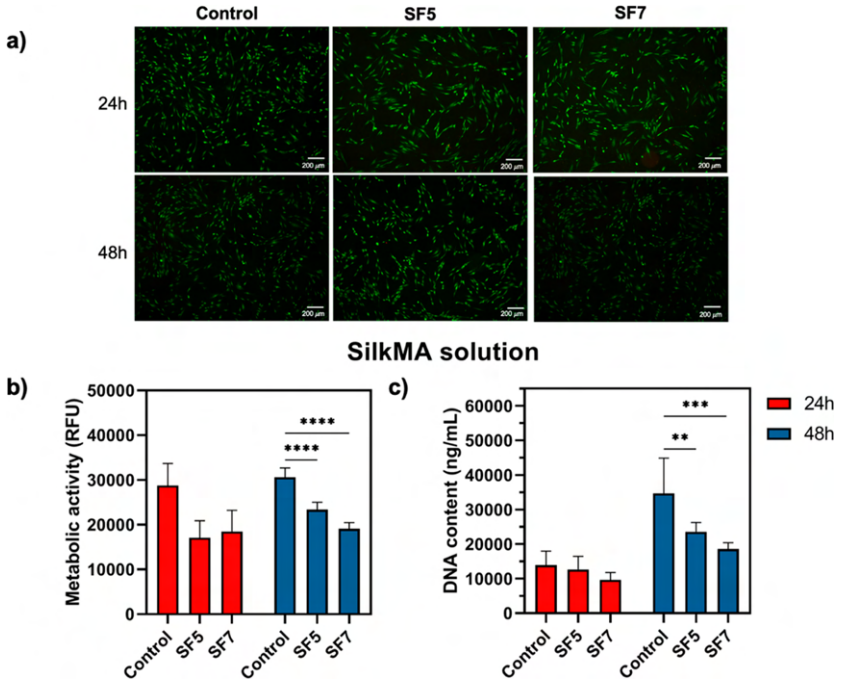


Figure 7. Cytotoxicity of uncrosslinked SilkMA prepolymer solutions. (a) Live/dead images of HDFs seeded on tissue culture well-plates with media (control) and media supplemented with SF5 and SF7 prepolymer solutions. Scale bar = 200 μm. (b) Quantification of the metabolic activity by the alamarBlue assay 24 and 48 h after cell seeding. (c) Quantification of cell proliferation by the PicoGreen DNA assay 24 and 48 h after cell seeding. Data presented as mean value ± SD (*p < 0.05, **p < 0.01, ***p < 0.001, and ****p < 0.0001).

studied (Figure 5b,c). Moreover, the β-sheet crystallinity was shown to be inversely proportional to the SilkMA hydrogel pH (Figure 5d). The β-sheet content was significantly different between the groups at day 0, corresponding to 30.3 ± 1.3, 27.6 ± 1.1, and 23.9 ± 2.1% for SF5, SF7, and SF8, respectively. In contrast, after 28 days of incubation and although the β-sheet crystallinity in SF5 is greater than those in SF7 and SF8, the difference is only statistically significant for the latter (p < 0.01).

ThT is a powerful fluorescent marker to identify β-aggregates, such as β-amyloid and β-sheet.[37,47] Herein, this staining approach was used to qualitatively confirm time-dependent conformational changes assessed by FTIR. Since the intensity is proportional to the sample mass, the hydrogels were prepared with the same volume of prepolymer solution. However, different degradation profiles might have interfered with the intensities obtained at days 7 and 14. The emission spectra of SilkMA hydrogels at days 1, 7, and 14 can be observed in Figure 5e. Our results show that the fluorescence intensity increased with time for all groups studied. Moreover, the fluorescence intensity is inversely proportional to the hydrogel pH, in agreement with the FTIR deconvolution data. When comparing the results at day 1, the maximum ThT fluorescence for SF5 (107000 AU) was higher than those for SF7 (75000 AU) and SF8 (54000 AU) hydrogels. Similarly, after 14 days, the SF5 maximum intensity (210000 AU) was 2- and 2.2-fold higher than SF7 (110000 AU) and SF8 (94000 AU).

To further analyze the effect of the spontaneous conformational transitions on the physical and mechanical properties of SilkMA hydrogels, the optical transmittance and compressive modulus were determined at different incubation time points (Figure 6). The obtained results show that the optical transparency of SilkMA hydrogels is directly proportional to the prepolymer solution pH and decreases over time, as the hydrogel crystallinity increases. As previously mentioned, the transmittance of SilkMA hydrogels at day 0 was between 82.1 ± 3.0 and 91.6 ± 0.9% for SF5 and SF8 hydrogels (p < 0.01), respectively (Figure 6a). Despite this 9.5% difference, all samples were initially transparent to the naked eye (Figure 6b). After 7 days, SF5 hydrogels had the highest decrease in transparency (12.1%) to 71.8 ± 2.3%, while SF8 hydrogels exhibited a reduction of 0.9% to 89.9 ± 1.4%, with the SF5 group displaying a significant reduction in transparency when compared to the SF7 (p < 0.001) and SF8 (p < 0.0001) gels. At day 14, the optical properties of SF5 and SF7 hydrogels were not statistically different; however, SF8 hydrogels had a transmittance of 85.1 ± 4.9%, which is higher than the transmittance of SF5 hydrogels at day 0 (83.9 ± 3.7%). After 28 days of incubation, the optical transmittance of all SilkMA groups decreased to values of approximately 50% (Figure 5a,b). Finally, the mechanical toughening impact of the increasing β-sheet content on the hydrogels was studied by cyclic compressive testing. The hydrogel stiffness consistently increased over time driven by the higher β-sheet crystallinity. The compressive modulus rose by 2 orders of magnitude for SF5 (from 40 kPa to 1.1 MPa) and 1 order of magnitude for SF7 (from 21 to 870 kPa) and SF8 (from 19 to 631 kPa) within 14 days (Figure 6c). The difference between day 0 and day 7 was not statistically significant for SF7 and SF8 samples; however, at day 7, SF5 showed a compressive modulus 25- and 81-fold superior to SF7 (p < 0.001) and SF8 (p < 0.0001), respectively (Figure 6d). After 14 days, the compressive modulus ranged from 631 kPa to 1.1 MPa, being statistically different between all groups (Figure 6e).

3.3. In Vitro Assessment of Cytocompatibility. The cytotoxicity of uncrosslinked SilkMA prepolymer solutions was studied by using HDF cells seeded on tissue culture well-plates

https://doi.org/10.1021/acsbiomaterials.1c00791
ACS Biomater. Sci. Eng. XXXX, XXX, XXX−XXX

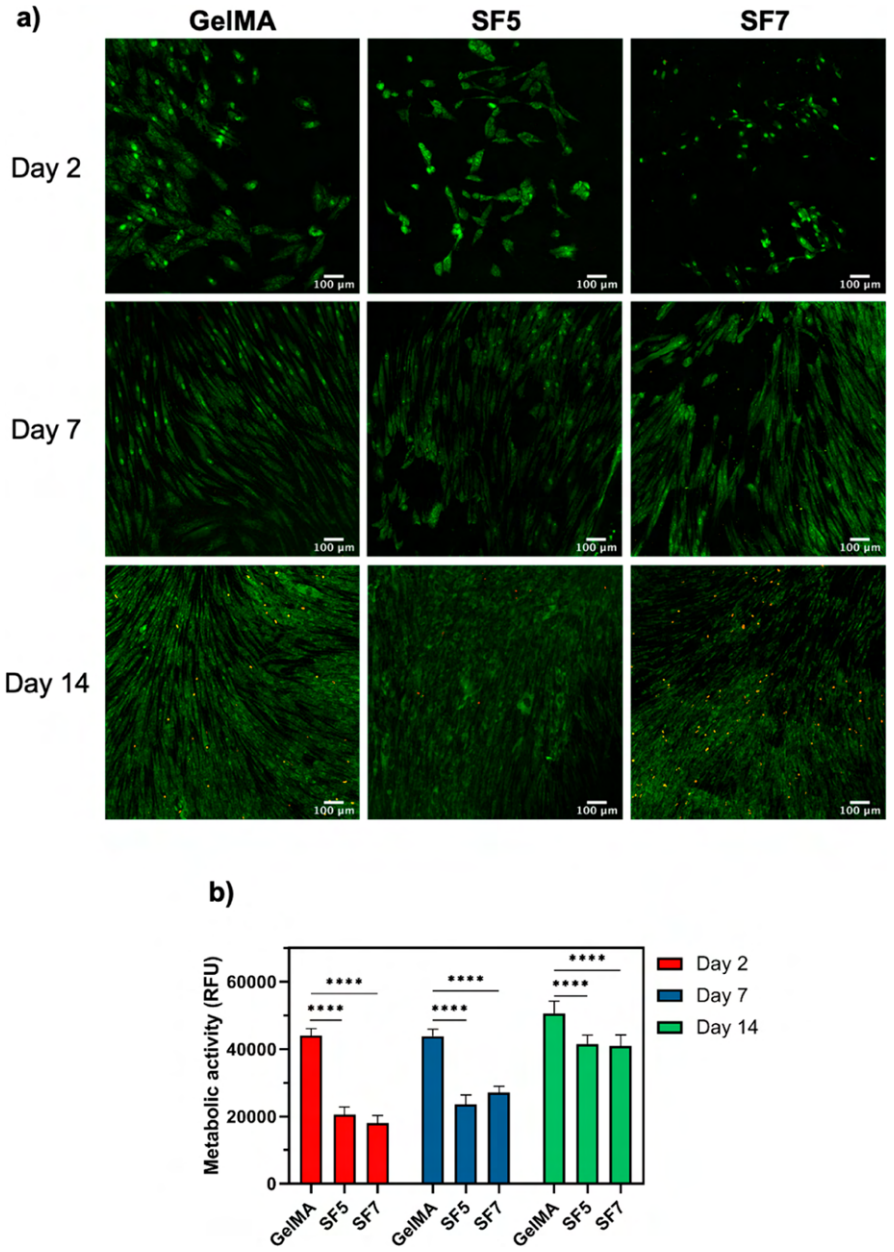


Figure 8. Cytotoxicity of SilkMA prepolymer hydrogels: (a) live/dead images of HDFs seeded on GelMA, SF5, and SF7 hydrogels. (b) Quantification of the metabolic activity by the alamarBlue assay 2, 7, and 14 days after cell seeding. Data presented as mean value ± SD (*$p < 0.05$, **$p < 0.01$, ***$p < 0.001$, and ****$p < 0.0001$).

and compared with cells cultured in complete media. Fluorescence staining (Figure 7a) indicates high cell viability (>90%) for all tested conditions, suggesting that SilkMA prepolymer solutions did not induce cytotoxicity. Variations in the cell metabolism and proliferation were not statistically different between SilkMA samples throughout the experiment, with a time-dependent increase observed in both groups. However, the controls showed a higher metabolic activity than SF5 ($p < 0.0001$) and SF7 ($p < 0.0001$) (Figure 7b). DNA content results were in agreement with the metabolic activity, with controls showing higher DNA concentration compared to SF5 ($p < 0.01$) and SF7 ($p < 0.001$) 48 h post seeding (Figure 7c).

The ability of SilkMA hydrogels to support cell attachment and proliferation was evaluated by the direct seeding of HDF cells on SF5 and SF7 hydrogels and compared with GelMA, an extensively studied hydrogel for 3D cell culture applications.[48] Cell viability, metabolic activity, and proliferation were assessed 2, 7, and 14 days post seeding. As shown in Figure 8a, live/dead staining showed that SilkMA hydrogels are capable of supporting cell attachment and proliferation for up to 14 days. Two days after seeding, most cells deposited on SilkMA hydrogels exhibited a rounded morphology with limited spreading, whereas cells on GelMA hydrogels actively spread, showing a spindle-shaped morphology characteristic of HDFs. This effect is in line with the available literature as previous reports indicate that SF from *B. mori* has limited initial cellular response as a result of limited adhesive amino acid sequences (e.g., RGD) on its composition.[42,49] However, 7 days post seeding, the cells exhibited a typical fibroblastic morphology and proliferated to reach confluence on the SilkMA gels, similar to that observed on GelMA hydrogels.

https://doi.org/10.1021/acsbiomaterials.1c00791
ACS Biomater. Sci. Eng. XXXX, XXX, XXX−XXX

After 14 days, some dead cells can be observed in all groups due to over confluency. This limited initial interaction for the SilkMA hydrogels is further observed in the metabolic activity measurements, which is likely to be influenced by cell adhesion. Cell metabolism was significantly ($p < 0.0001$) higher on GelMA hydrogels at each time point (Figure 8b). However, despite both SilkMA groups showing a significantly lower metabolic activity than GelMA at day 7, specifically 46% (SF5, $p < 0.0001$) and 39% (SF7, $p < 0.0001$), this difference decreases to approximately 19% for both groups ($p < 0.0001$) after 14 days (Figure 8b). The metabolic activity of cells seeded on SF5 and SF7 was not statistically different at each time point assessed, with a time-dependent increase in the metabolic activity observed in both groups.

4. DISCUSSION

Over the last decade, efforts to develop chemically crosslinked SF hydrogels have been made.[3,26] Herein, we developed a glycidyl-methacrylate-modified SF solution that can be chemically crosslinked within a few minutes using light. Cells can be encapsulated within the hydrogels by gentle mixing with the prepolymer solution before crosslinking. Several natural and synthetic polymers such as gelatin, collagen, or hyaluronic acid have been previously methacrylated.[50−52] Vinyl-containing monomers, such as GMA and methacrylic anhydride, are commonly used to methacrylate proteins. After dialysis, the purified methacrylated-protein solution has a pH between 4.5 and 5.5, in contrast with the neutral pH of pure silk solutions. Considering the role of pH in the molecular aggregation of SF proteins in vivo, we hypothesize that the pH of the prepolymer solution will play a determinant role in the short- and long-term properties of SilkMA hydrogels, being essential to control the function and ensure reproducible manufacturing.

To study the impact of the prepolymer solution pH on the properties of SilkMA gels, three different formulations were prepared: SF5, SF7, and SF8. In general, all SilkMA hydrogels presented high transparency and elasticity and were easy to handle (Figure 3c). Despite perceptible differences in rigidity, all SilkMA gels behaved as viscoelastic solids, as demonstrated by the higher G' for all groups studied (Figure 4a). When freshly prepared hydrogels were studied, we found that SF5 hydrogels exhibited a significantly greater storage and compressive modulus than SF7 and SF8 hydrogels (Figure 4b,f).

To further understand the observed differences in the properties of SilkMA gels, the secondary structure of the gels was investigated using FTIR. Since the amide I region of the spectra is very sensitive to the secondary structure, it can be deconvoluted using a FSD algorithm to determine the relative contribution of each structure fraction.[45,46] As shown in Table 1, our results show a time-dependent reduction in the random coil content, accompanied by a β-sheet content rise for all groups. The conformational changes assessed by FTIR were qualitatively confirmed using ThT staining, a fluorescent marker that binds β-sheet structures (Figure 5e). Time-dependent conformational transitions are expected in silk-based materials and have been previously reported by other authors.[3,5,44,53,54]

As described by Burke et al., the hydrogen bonding between adjacent β-sheets (physical crosslinking) is responsible for the aqueous insolubility and remarkable mechanical properties of SF.[55] In this work, the mechanical toughening impact of the β-sheet crystallinity was studied by compressive mechanical testing. As shown in Figure 6c, the hydrogel stiffness consistently increased over time for all studied groups, in agreement with the FTIR data. Remarkably, the compressive modulus of SF5 hydrogels increased by 2 orders of magnitude in 14 days, while SF7 and SF8 gels increased by an order of magnitude. Typically, one of the strategies used to enhance the mechanical strength of gels is by increasing the polymer concentration; however, it may negatively impact cell viability and proliferation within the scaffold as reported in the literature.[56,57] Herein, we demonstrated that by adjusting the pH of the prepolymer solution, SilkMA hydrogel stiffness can be tailored without changing the polymer concentration or the molecular weight. Despite improving the compressive modulus, which might be advantageous for certain applications, the increase in crystallinity has a negative impact on elasticity. As shown in Figure 3b,c, both the optical transparency and the swelling characteristics were shown to be significantly lower for SF5 gels.

Swelling properties are critical for tissue engineering applications since a material's water content influences the transport of oxygen, nutrients, and metabolites, as well as the viability and proliferation of cells.[58] As shown in Figure 3d, SF5 has enhanced structural stability against swelling, with a significantly lower SR than SF7 and SF8 ($p < 0.001$ and $p < 0.0001$, respectively). A decrease in the network swellability is expected with an increase in the hydrophobic β-sheet content.[59] On day 0, the β-sheet content was shown to be significantly different between samples, with SF5 having on average 6.4 and 2.7% higher crystallinity than SF7 and SF8, respectively (Table 1 and Figure 5d). Moreover, swelling can have an impact on the overall shape of a material, which must be retained in vivo.[33] These materials should have a minimal volume change, thereby reducing the risk of implant mismatch and imparting additional stress on the surrounding tissues.[60] Thus, the dimensional stability of in situ crosslinked hydrogels is of critical importance. All experimental groups retained their shape and were easily handled in the swollen state. Although hydrogel expansion was not statistically significant between experimental groups, the volume increase seems to be proportional to the hydrogel pH, in agreement with the swelling characteristics (Figure 3f).

One of the outstanding properties of SF hydrogels is the high optical transparency in the visible range. This property is of utmost importance for many applications in tissue engineering, such as corneal substitutes and ocular adhesives.[39,61,62] In this work, we have quantified hydrogel transparency over time for the different studied groups. As shown in Figure 6a, the transparency of SF hydrogels progressively decreased after curing. Remarkably, SF8 remained optically clear after 14 days of incubation (transmittance > 85%), while SF5 and SF7 gels became opaque, transmittance ≈ 53% (Figure 6b). It has been previously reported that SF-based hydrogels become increasingly opaque over time, as the main protein conformation changes from random coil to the β-sheet crystalline form.[3,37,44] It is important to note that crystallinity is not the only factor determining the transparency of hydrogels since amorphous materials can still be opaque.[37] Since all SilkMA hydrogels were prepared at the same concentration, the ratio of polymeric network/water phase is the same. However, as shown in Figure 3d, the swelling characteristics are statistically different between the samples. The higher water content in

https://doi.org/10.1021/acsbiomaterials.1c00791
ACS Biomater. Sci. Eng. XXXX, XXX, XXX−XXX

SF7 and SF8 hydrogels might also play a role in the increased optical clarity.

Due to the short photocrosslinking times and mild environmental conditions, SilkMA hydrogels can be used to deliver cells. However, SF is reported to lack cell binding sequences necessary for cellular adhesion and proliferation.[42,49] In this study, the cytocompatibility of uncrosslinked SilkMA prepolymer solutions and SilkMA hydrogels was assessed in vitro. As shown in Figure 7, SilkMA prepolymer solutions did not induce cytotoxicity despite the significantly lower metabolic activity and proliferation in comparison with the control. HDF adhesion to SF5 and SF7 hydrogels was compared with GelMA, a material which provides cells with an optimal biological environment such as adhesion sequences.[48] As shown in Figure 8a, SilkMA hydrogels exhibited low toxicity, although the hydrogels showed a delayed attachment and lower metabolic activity relative to the control. Despite the previously mentioned differences in stiffness and hydrophilicity, the metabolic activity of HDFs on SF5 and SF7 gels was not statistically significant. In summary, the pH of the gels did not affect cytocompatibility. Importantly, our findings showed that the seeded HDFs were able to spread and proliferate on the SilkMA hydrogels, similar to the observations on the GelMA control. The cytocompatibility of SilkMA hydrogels confirmed that SF is a promising material for tissue engineering. In the future, it would be interesting to evaluate the impact of pH-induced scaffold properties on the behavior of cells more sensitive to environmental stimuli (e.g., stem cells). This would provide a greater understanding of the effects of pH control on the mechanotransductive properties of the SilkMA hydrogels.

5. CONCLUSIONS

The present work studies the effect of the prepolymer solution pH on the initial and long-term properties of SilkMA hydrogels. We have demonstrated that (1) the pH of the prepolymer solution can be effectively used to control the SilkMA conformational structure development toward utility and function and (2) strict pH control is necessary to ensure reproducibility as physical crosslinking influences the hydrogel properties independently of the parameters controlling the chemical crosslinking reaction (e.g., DM %, polymer/photoinitiator concentration, and so forth.). Furthermore, we developed injectable, highly elastic, and transparent SilkMA hydrogels that can be photocrosslinked within minutes. These gels are suitable for cell encapsulation and displayed adequate physicochemical properties for tissue engineering applications. In the future, we believe SilkMA has the potential to be applied in the design of bioinks and bioresins.

6. DATA AVAILABILITY STATEMENT

The raw/processed data required to reproduce these findings cannot be shared at this time due to technical or time limitations.

AUTHOR INFORMATION

Corresponding Author

Anita K. Ghag − *School of Chemical Engineering, University of Birmingham, Edgbaston B15 2TT Birmingham, U.K.;* orcid.org/0000-0002-6650-3394; Email: A.K.Ghag@bham.ac.uk

Authors

Inês A. Barroso − *School of Chemical Engineering, University of Birmingham, Edgbaston B15 2TT Birmingham, U.K.*

Kenny Man − *School of Chemical Engineering, University of Birmingham, Edgbaston B15 2TT Birmingham, U.K.;* orcid.org/0000-0002-7946-9375

Victor M. Villapun − *School of Chemical Engineering, University of Birmingham, Edgbaston B15 2TT Birmingham, U.K.*

Sophie C. Cox − *School of Chemical Engineering, University of Birmingham, Edgbaston B15 2TT Birmingham, U.K.*

Complete contact information is available at: https://pubs.acs.org/10.1021/acsbiomaterials.1c00791

Funding

This research did not receive any specific grant from funding agencies in the public, commercial, or not-for-profit sectors.

Notes

The authors declare no competing financial interest.

ACKNOWLEDGMENTS

The authors would like to sincerely thank Dr. Salvador D. Aznar-Cervantes and Dr. José L. Cenis for their help with SF extraction processes and Dr. Cécile Le Duff for her assistance with ^{1}H NMR spectroscopy.

REFERENCES

(1) Piras, C. C.; Smith, D. K. Multicomponent polysaccharide alginate-based bioinks. *J. Mater. Chem. B* **2020**, *8*, 8171.

(2) Sun, M.; Sun, X.; Wang, Z.; Guo, S.; Yu, G.; Yang, H. Synthesis and properties of gelatin methacryloyl (GelMA) hydrogels and their recent applications in load-bearing tissue. *Polymers* **2018**, *10*, 1290.

(3) Yan, L.-P.; Silva-Correia, J.; Ribeiro, V. P.; Miranda-Gonçalves, V.; Correia, C.; Da Silva Morais, A.; Sousa, R. A.; Reis, R. M.; Oliveira, A. L.; Oliveira, J. M.; Reis, R. L. Tumor Growth Suppression Induced by Biomimetic Silk Fibroin Hydrogels. *Sci. Rep.* **2016**, *6*, 31037.

(4) Tabatabai, A. P.; Kaplan, D. L.; Blair, D. L. Rheology of reconstituted silk fibroin protein gels: The epitome of extreme mechanics. *Soft Matter* **2015**, *11*, 756−761.

(5) Costa, J. B.; Silva-Correia, J.; Oliveira, J. M.; Reis, R. L. Fast Setting Silk Fibroin Bioink for Bioprinting of Patient-Specific Memory-Shape Implants. *Adv. Healthcare Mater.* **2017**, *6*, 1701021.

(6) Qi, Y.; Wang, H.; Wei, K.; Yang, Y.; Zheng, R. Y.; Kim, I. S.; Zhang, K. Q. A review of structure construction of silk fibroin biomaterials from single structures to multi-level structures. *Int. J. Mol. Sci.* **2017**, *18*, 237.

(7) Kim, U.-J.; Park, J.; Li, C.; Jin, H.-J.; Valluzzi, R.; Kaplan, D. L. Structure and properties of silk hydrogels. *Biomacromolecules* **2004**, *5*, 786−792.

(8) Matsumoto, A.; Chen, J.; Collette, A. L.; Kim, U.-J.; Altman, G. H.; Cebe, P.; Kaplan, D. L. Mechanisms of Silk Fibroin Sol−Gel Transitions. *J. Phys. Chem. B* **2006**, *110*, 21630−21638.

(9) Wray, L. S.; Hu, X.; Gallego, J.; Georgakoudi, I.; Omenetto, F. G.; Schmidt, D.; Kaplan, D. L. Effect of processing on silk-based biomaterials: Reproducibility and biocompatibility. *J. Biomed. Mater. Res., Part B* **2011**, *99*, 89−101.

(10) Kundu, B.; Kurland, N. E.; Bano, S.; Patra, C.; Engel, F. B.; Yadavalli, V. K.; Kundu, S. C. Silk proteins for biomedical applications: Bioengineering perspectives. *Prog. Polym. Sci.* **2014**, *39*, 251−267.

(11) Foo, C. W. P.; Bini, E.; Hensman, J.; Knight, D. P.; Lewis, R. V.; Kaplan, D. L. Role of pH and charge on silk protein assembly in insects and spiders. *Appl. Phys. A: Mater. Sci. Process.* **2006**, *82*, 223−233.

(12) Terry, A. E.; Knight, D. P.; Porter, D.; Vollrath, F. pH induced changes in the rheology of silk fibroin solution from the middle division of Bombyx mori silkworm. *Biomacromolecules* **2004**, *5*, 768−772.
(13) Fini, M.; Motta, A.; Torricelli, P.; Giavaresi, G.; Nicoli Aldini, N.; Tschon, M.; Giardino, R.; Migliaresi, C. The healing of confined critical size cancellous defects in the presence of silk fibroin hydrogel. *Biomaterials* **2005**, *26*, 3527−3536.
(14) Nagarkar, S.; Nicolai, T.; Chassenieux, C.; Lele, A. Structure and gelation mechanism of silk hydrogels. *Phys. Chem. Chem. Phys.* **2010**, *12*, 3834.
(15) Luo, K.; Yang, Y.; Shao, Z. Physically Crosslinked Biocompatible Silk-Fibroin-Based Hydrogels with High Mechanical Performance. *Adv. Funct. Mater.* **2016**, *26*, 872−880.
(16) Dong, T.; Mi, R.; Wu, M.; Zhong, N.; Zhao, X.; Chen, X.; Shao, Z. The regenerated silk fibroin hydrogel with designed architecture bioprinted by its microhydrogel. *J. Mater. Chem. B* **2019**, *7*, 4328−4337.
(17) Hofmann, S.; Wong Po Foo, C. T.; Rossetti, F.; Textor, M.; Vunjak-Novakovic, G.; Kaplan, D. L.; Merkle, H. P.; Meinel, L. Silk fibroin as an organic polymer for controlled drug delivery. *J. Controlled Release* **2006**, *111*, 219−227.
(18) Gil, E. S.; Spontak, R. J.; Hudson, S. M. Effect of β-sheet crystals on the thermal and rheological behavior of protein-based hydrogels derived from gelatin and silk fibroin. *Macromol. Biosci.* **2005**, *5*, 702−709.
(19) Alessandrino, A.; Marelli, B.; Arosio, C.; Fare, S.; Tanzi, M. C.; Freddi, G. Electrospun silk fibroin mats for tissue engineering. *Eng. Life Sci.* **2008**, *8*, 219−225.
(20) Ghosh, S.; Parker, S. T.; Wang, X.; Kaplan, D. L.; Lewis, J. A. Direct-write assembly of microperiodic silk fibroin scaffolds for tissue engineering applications. *Adv. Funct. Mater.* **2008**, *18*, 1883−1889.
(21) Zhang, X.; Pan, Z. Microstructure transitions and dry-wet spinnability of Silk fibroin protein from Waste silk quilt. *Polymers* **2019**, *11*, 1622.
(22) Leisk, G. G.; Lo, T. J.; Yucel, T.; Lu, Q.; Kaplan, D. L. Electrogelation for protein adhesives. *Adv. Mater.* **2010**, *22*, 711−715.
(23) Wang, S.-D.; Zhang, K.-Q. Electrogelation and rapid prototyping of Bombyx mori silk fibroin. *Mater. Lett.* **2016**, *169*, 5−9.
(24) Wang, X.; Kluge, J. A.; Leisk, G. G.; Kaplan, D. L. Sonication-induced gelation of silk fibroin for cell encapsulation. *Biomaterials* **2008**, *29*, 1054−1064.
(25) Yucel, T.; Cebe, P.; Kaplan, D. L. Vortex-induced injectable silk fibroin hydrogels. *Biophys. J.* **2009**, *97*, 2044−2050.
(26) Partlow, B. P.; Hanna, C. W.; Rnjak-Kovacina, J.; Moreau, J. E.; Applegate, M. B.; Burke, K. A.; Marelli, B.; Mitropoulos, A. N.; Omenetto, F. G.; Kaplan, D. L. Highly tunable elastomeric silk biomaterials. *Adv. Funct. Mater.* **2014**, *24*, 4615−4624.
(27) Mazzocchi, A.; Devarasetty, M.; Huntwork, R.; Soker, S.; Skardal, A. Optimization of collagen type I-hyaluronan hybrid bioink for 3D bioprinted liver microenvironments. *Biofabrication* **2018**, *11*, 015003.
(28) Lim, K. S.; Levato, R.; Costa, P. F.; Castilho, M. D.; Alcala-Orozco, C. R.; Van Dorenmalen, K. M. A.; Melchels, F. P. W.; Gawlitta, D.; Hooper, G. J.; Malda, J.; Woodfield, T. B. F. Bio-resin for high resolution lithography-based biofabrication of complex cell-laden constructs. *Biofabrication* **2018**, *10*, 034101.
(29) Lim, K. S.; Abinzano, F.; Bernal, P. N.; Albillos Sanchez, A.; Atienza-Roca, P.; Otto, I. A.; Peiffer, Q. C.; Matsusaki, M.; Woodfield, T. B. F.; Malda, J.; Levato, R. One-Step Photoactivation of a Dual-Functionalized Bioink as Cell Carrier and Cartilage-Binding Glue for Chondral Regeneration. *Adv. Healthcare Mater.* **2020**, *9*, 1901792.
(30) Lim, K. S.; Klotz, B. J.; Lindberg, G. C. J.; Melchels, F. P. W.; Hooper, G. J.; Malda, J.; Gawlitta, D.; Woodfield, T. B. F. Visible Light Cross-Linking of Gelatin Hydrogels Offers an Enhanced Cell Microenvironment with Improved Light Penetration Depth. *Macromol. Biosci.* **2019**, *19*, 1900098.
(31) Smeds, K. A.; Pfister-Serres, A.; Miki, D.; Dastgheib, K.; Diane, L.; Hatchell, M. W. G. Photocrosslinkable polysaccharides for in situ hydrogel formation. *J. Biomed. Mater. Res.* **2000**, *54*, 115.
(32) Kesti, M.; Müller, M.; Becher, J.; Schnabelrauch, M.; D'Este, M.; Eglin, D.; Zenobi-Wong, M. A versatile bioink for three-dimensional printing of cellular scaffolds based on thermally and photo-triggered tandem gelation. *Acta Biomater.* **2015**, *11*, 162−172.
(33) Kim, S. H.; Yeon, Y. K.; Lee, J. M.; Chao, J. R.; Lee, Y. J.; Seo, Y. B.; Sultan, M. T.; Lee, O. J.; Lee, J. S.; Yoon, S. I.; Hong, I. S.; Khang, G.; Lee, S. J.; Yoo, J. J.; Park, C. H. Precisely printable and biocompatible silk fibroin bioink for digital light processing 3D printing. *Nat. Commun.* **2018**, *9*, 1620.
(34) Pescosolido, L.; Schuurman, W.; Malda, J.; Matricardi, P.; Alhaique, F.; Coviello, T.; Van Weeren, P. R.; Dhert, W. J. A.; Hennink, W. E.; Vermonden, T. Hyaluronic acid and dextran-based semi-IPN hydrogels as biomaterials for bioprinting. *Biomacromolecules* **2011**, *12*, 1831−1838.
(35) Dubbin, K.; Tabet, A.; Heilshorn, S. C. Quantitative criteria to benchmark new and existing bio-inks for cell compatibility. *Biofabrication* **2017**, *9*, 044102.
(36) Kamoun, E. A.; Omer, A. M.; Abu-Serie, M. M.; Khattab, S. N.; Ahmed, H. M.; Elbardan, A. A. Photopolymerized PVA-g-GMA Hydrogels for Biomedical Applications: Factors Affecting Hydrogel Formation and Bioevaluation Tests. *Arabian J. Sci. Eng.* **2018**, *43*, 3565−3575.
(37) Kim, H. H.; Song, D. W.; Kim, M. J.; Ryu, S. J.; Um, I. C.; Ki, C. S.; Park, Y. H. Effect of silk fibroin molecular weight on physical property of silk hydrogel. *Polymer* **2016**, *90*, 26−33.
(38) Hu, X.; Kaplan, D.; Cebe, P. Determining Beta-Sheet Crystallinity in Fibrous Proteins by Thermal Analysis and Infrared Spectroscopy. *Macromolecules* **2006**, *39*, 6161−6170.
(39) Bhattacharjee, P.; Fernández-Pérez, J.; Ahearne, M. Potential for combined delivery of riboflavin and all-trans retinoic acid, from silk fibroin for corneal bioengineering. *Mater. Sci. Eng., C* **2019**, *105*, 110093.
(40) Sharifi, S.; Islam, M. M.; Sharifi, H.; Islam, R.; Koza, D.; Reyes-Ortega, F.; Alba-Molina, D.; Nilsson, P. H.; Dohlman, C. H.; Mollnes, T. E.; Chodosh, J.; Gonzalez-Andrades, M. Tuning gelatin-based hydrogel towards bioadhesive ocular tissue engineering applications. *Bioact. Mater.* **2021**, *6*, 3947−3961.
(41) Guimarães, C. F.; Gasperini, L.; Marques, A. P.; Reis, R. L. The stiffness of living tissues and its implications for tissue engineering. *Nat. Rev. Mater.* **2020**, *5*, 351.
(42) Buitrago, J. O.; Patel, K. D.; El-Fiqi, A.; Lee, J.-H.; Kundu, B.; Lee, H.-H.; Kim, H.-W. Silk fibroin/collagen protein hybrid cell-encapsulating hydrogels with tunable gelation and improved physical and biological properties. *Acta Biomater.* **2018**, *69*, 218−233.
(43) Singh, Y. P.; Bandyopadhyay, A.; Mandal, B. B. 3D Bioprinting Using Cross-Linker-Free Silk-Gelatin Bioink for Cartilage Tissue Engineering. *ACS Appl. Mater. Interfaces* **2019**, *11*, 33684−33696.
(44) Ribeiro, V. P.; Silva-Correia, J.; Gonçalves, C.; Pina, S.; Radhouani, H.; Montonen, T.; Hyttinen, J.; Roy, A.; Oliveira, A. L.; Reis, R. L.; Oliveira, J. M. Rapidly responsive silk fibroin hydrogels as an artificial matrix for the programmed tumor cells death. *PLoS One* **2018**, *13*, No. e0194441.
(45) Wei, Q.-N.; Huang, A.-M.; Lin, M.; Huang, Z.; Huang, X.; Qiang, P.-P.; Zhu-Ping Gong, L. Z. Structure Regulation of Silk Fibroin Films for Controlled Drug Release. *J. Appl. Polym. Sci.* **2012**, *125*, No. E477.
(46) Chen, X.; Shao, Z.; Marinkovic, N. S.; Miller, L. M.; Zhou, P.; Chance, M. R. Conformation transition kinetics of regenerated Bombyx mori silk fibroin membrane monitored by time-resolved FTIR spectroscopy. *Biophys. Chem.* **2001**, *89*, 25−34.
(47) Belton, D. J.; Plowright, R.; Kaplan, D. L.; Perry, C. C. A robust spectroscopic method for the determination of protein conformational composition - Application to the annealing of silk. *Acta Biomater.* **2018**, *73*, 355−364.
(48) Pepelanova, I.; Kruppa, K.; Scheper, T.; Lavrentieva, A. Gelatin-methacryloyl (GelMA) hydrogels with defined degree of functional-

https://doi.org/10.1021/acsbiomaterials.1c00791
ACS Biomater. Sci. Eng. XXXX, XXX, XXX−XXX

ization as a versatile toolkit for 3D cell culture and extrusion bioprinting. *Bioengineering* **2018**, *5*, 55.
(49) Silva, S. S.; Popa, E. G.; Gomes, M. E.; Oliveira, M. B.; Nayak, S.; Subia, B.; Mano, J. F.; Kundu, S. C.; Reis, R. L. Silk hydrogels from non-mulberry and mulberry silkworm cocoons processed with ionic liquids. *Acta Biomater.* **2013**, *9*, 8972−8982.
(50) Pepelanova, I.; Kruppa, K.; Scheper, T.; Lavrentieva, A. Gelatin-Methacryloyl (GelMA) Hydrogels with Defined Degree of Functionalization as a Versatile Toolkit for 3D Cell Culture and Extrusion Bioprinting. *Bioengineering* **2018**, *5*, 55.
(51) Liang, H.; Russell, S. J.; Wood, D. J.; Tronci, G. A hydroxamic acid-methacrylated collagen conjugate for the modulation of inflammation-related MMP upregulation. *J. Mater. Chem. B* **2018**, *6*, 3703−3715.
(52) Pitarresi, G.; Pierro, P.; Palumbo, F. S.; Tripodo, G.; Giammona, G. Photo-cross-linked hydrogels with polysaccharide-poly(amino acid) structure: New biomaterials for pharmaceutical applications. *Biomacromolecules* **2006**, *7*, 1302−1310.
(53) Aznar-Cervantes, S. D.; Lozano-Pérez, A. A.; García Montalbán, M.; Víllora, G.; Vicente-Cervantes, D.; Cenis, J. L. Importance of refrigeration time in the electrospinning of silk fibroin aqueous solutions. *J. Mater. Sci.* **2015**, *50*, 4879−4887.
(54) Cui, X.; Soliman, B. G.; Alcala-Orozco, C. R.; Li, J.; Vis, M. A. M.; Santos, M.; Wise, S. G.; Levato, R.; Malda, J.; Woodfield, T. B. F.; Rnjak-Kovacina, J.; Lim, K. S. Rapid Photocrosslinking of Silk Hydrogels with High Cell Density and Enhanced Shape Fidelity. *Adv. Healthcare Mater.* **2020**, *9*, 1901667.
(55) Burke, K. A.; Roberts, D. C.; Kaplan, D. L. Silk Fibroin Aqueous-Based Adhesives Inspired by Mussel Adhesive Proteins Kelly. *Biomacromolecules* **2016**, *17*, 237−245.
(56) Fischer, D.; Li, Y.; Ahlemeyer, B.; Krieglstein, J.; Kissel, T. In vitro cytotoxicity testing of polycations: influence of polymer structure on cell viability and hemolysis. *Biomaterials* **2003**, *24*, 1121−1131.
(57) Mazzoccoli, J. P.; Feke, D. L.; Baskaran, H.; Pintauro, P. N. Mechanical and Cell Viability Properties of Crosslinked Low and High MW PEGDA blends. *J. Biomed. Mater. Res., Part A* **2010**, *93*, 558−566.
(58) Li, L.; Lu, C.; Wang, L.; Chen, M.; White, J.; Hao, X.; McLean, K. M.; Chen, H.; Hughes, T. C. Gelatin-Based Photocurable Hydrogels for Corneal Wound Repair. *ACS Appl. Mater. Interfaces* **2018**, *10*, 13283−13292.
(59) Chan, N. J.-A.; Gu, D.; Tan, S.; Fu, Q.; Pattison, T. G.; O'Connor, A. J.; Qiao, G. G. Spider-silk inspired polymeric networks by harnessing the mechanical potential of β-sheets through network guided assembly. *Nat. Commun.* **2020**, *11*, 1630.
(60) Assmann, A.; Vegh, A.; Ghasemi-Rad, M.; Bagherifard, S.; Cheng, G.; Sani, E. S.; Ruiz-Esparza, G. U.; Noshadi, I.; Lassaletta, A. D.; Gangadharan, S.; Tamayol, A.; Khademhosseini, A.; Annabi, N. A highly adhesive and naturally derived sealant. *Biomaterials* **2017**, *140*, 115−127.
(61) Kim, H.; Park, M. N.; Kim, J.; Jang, J.; Kim, H. K.; Cho, D. W. Characterization of cornea-specific bioink: high transparency, improved in vivo safety. *J. Tissue Eng.* **2019**, *10*, 2041731418823382.
(62) Zhang, B.; Xue, Q.; Li, J.; Ma, L.; Yao, Y.; Ye, H.; Cui, Z.; Yang, H. 3D bioprinting for artificial cornea: Challenges and perspectives. *Med. Eng. Phys.* **2019**, *71*, 68−78.

https://doi.org/10.1021/acsbiomaterials.1c00791
ACS Biomater. Sci. Eng. XXXX, XXX, XXX−XXX

Check for updates

Received: 26 October 2021 | Revised: 6 January 2022 | Accepted: 1 March 2022

DOI: 10.1002/jbm.a.37381

RESEARCH ARTICLE

Society For Biomaterials | WILEY

Photocurable antimicrobial silk-based hydrogels for corneal repair

Inês A. Barroso | Kenny Man | Thomas J. Hall | Thomas E. Robinson | Sophie E. T. Louth | Sophie C. Cox | Anita K. Ghag

School of Chemical Engineering, University of Birmingham, Birmingham, UK

Correspondence
Anita K. Ghag, School of Chemical Engineering, University of Birmingham, Edgbaston B15 2TT, Birmingham, UK.
Email: a.k.ghag@bham.ac.uk

Abstract

Corneal transplantation is the current gold standard treatment to restore visual acuity to patients with severe corneal diseases and injuries. Due to severe donor tissue shortage, efforts to develop a corneal equivalent have been made but the challenge remains unmet. Another issue of concern in ocular surgery is the difficult instillation and fast drainage of antibiotic ocular eye drops as bacterial infections can jeopardize implant success by delaying or impairing tissue healing. In this study, we developed antimicrobial silk-based hydrogels that have the potential to be photoactivated in situ, fully adapting to the corneal injury shape. Gentamicin-loaded methacrylated-silk (SilkMA) hydrogels were prepared within minutes using low UV intensity (3 mW/cm^2). SilkMA gels provided a Young's modulus between 21 and 79 kPa together with a light transmittance spectrum and water content (83%–90%) similar to the human cornea. Polymer concentration (15%–25%) was found to offer a tool for tailoring the physical properties of the hydrogels. We confirmed that the methacrylation did not affect the material's in vitro degradation and biocompatibility by observing fibroblast adhesion and proliferation. Importantly, agar diffusion tests showed that the synthesized hydrogels were able to inhibit *Staphylococcus aureus* and *Pseudomonas aeruginosa* growth for 72 h. These characteristics along with their injectability and viscoelasticity demonstrate the potential of SilkMA hydrogels to be applied in several soft tissue engineering fields. As such, for the first time we demonstrate the potential of photocurable antimicrobial SilkMA hydrogels as a novel biomaterial to facilitate corneal regeneration.

KEYWORDS
antimicrobial, cornea, regenerative medicine, silk fibroin

1 | INTRODUCTION

The cornea is a transparent avascular tissue located on the outermost surface of the eye. It is responsible for the protection of the inner ocular structures against trauma and infections, while playing a pivotal role in light transmission and focusing (80% of the eye refractive power).[1–3] Corneal diseases and injuries can lead to corneal thinning and opacification, eventually leading to blindness. Currently, corneal blindness is estimated to affect 23 million people worldwide, with less than 1.5% of patients benefiting from a corneal transplant due to severe tissue shortage.[2,4] Although imposing risks of donor driven

[Corrections updated on 17th Mar 2022; after first online publication. The word "methacrylic anhydride side groups" has been changed to "methacrylate side groups".]

This is an open access article under the terms of the Creative Commons Attribution-NonCommercial License, which permits use, distribution and reproduction in any medium, provided the original work is properly cited and is not used for commercial purposes.
© 2022 The Authors. *Journal of Biomedical Materials Research Part A* published by Wiley Periodicals LLC.

infection and rejection, corneal transplantation is still the gold standard treatment to restore visual acuity to patients .[2,5,6] Fully synthetic prostheses KPro (keratoprosthese) are currently the only non-allogenic treatment approved for human use.[7] Although innovations in prosthesis design and postoperative management has improved treatment outcomes,[8] this procedure is associated with serious complications, such as glaucoma, retinal detachment and infections, while also requiring a high level of skill from the practitioner.[9] Due to the limitations of current clinical strategies, there has been extensive research focused on the use of polymeric biomaterials to replace damaged corneal tissue.[2,4] The use of injectable polymeric biomaterials such as hydrogels are favorable as they can either be administered directly to the corneal injury and crosslinked in situ using different methods[2,4,10–13] or 3D printed into complex and anatomically relevant geometries.[5,6,14,15] Upon implantation the artificial corneal substitute should act as a functional cornea nurturing tissue ingrowth and regeneration with low inflammatory host response. The engineered material should also be fully biodegradable, eliminating the need for further surgeries.[16] Challenges associated with bioengineered corneal substitutes include high optical transparency, sufficient cohesive strength to withstand the intraocular pressure (IOP) and eye movements, permeability to metabolites, and ability to prevent infections while sustaining epithelial and stromal cell-ingrowth.

Recently, efforts to develop stromal fillers and corneal substitutes have been made.[2,4,12,17] Fernandes-Cunha et al. developed collagen hydrogels cross-linked via multi-arm-PEG-N-hydroxysuccinimide (NHS). The gels were cross-linked within 5–10 min without the use of catalysts and its physical properties were modulated as function of the PEG concentration and number of arms. In vivo studies demonstrated that the hydrogels could be formed in situ without the use of sutures and were proven to support multi-layered re-epithelization.[4] Chen et al. used strain-promoted azide-alkyne cycloaddition to crosslink hyaluronate-collagen hydrogels under ambient conditions without the need for external initiators. The material showed a transmittance over 95% in the visible range. Hydrogels were crosslinked in situ without the need of sutures and remained clear on the rabbit corneal defect for 7 days supporting re-epithelization.[2] However, although these strategies do not require any external triggers or catalysts, they might not be suitable for applications that require fast cross-linking (30–120 s) or cell-encapsulation given the chemistry used.

Light-mediated hydrogel gelation has immense potential for regenerative medicine as cell-laden hydrogels can be cross-linked within minutes in mild environmental conditions. Importantly, photocurable hydrogels provide the clinician with increased flexibility in controlling in situ gelation when compared with other methods.[2,4] These photosensitive polymers have the potential to be applied as stromal fillers (in situ cross-linking)[1,3,11,12,18] or used to develop a patient-specific artificial cornea using 3D printing technologies such as lithography and extrusion-based bioprinting.[5,15,19–21] Sani et al. developed a highly biocompatible and transparent GelMA-based filler for corneal reconstruction. The hydrogels were photocured within minutes using visible light (100 mW/cm^2) and a photoinitiator solution composed of Eosin Y (photoinitiator), TEA (co-initiator), and VC (co-monomer). In vivo studies performed using a rabbit stromal defect model demonstrated the sealing efficacy of the material while allowing re-epithelization and stromal regeneration.[18]

Silk fibroin (SF)-based biomaterials have been extensively studied for numerous tissue engineering applications due to their amenability to modification, outstanding transparency, mechanical strength, and biodegradability, making it an attractive material for corneal regenerative applications.[22,23] In particular, SF membranes have been widely explored for corneal and retinal reconstruction due to their permeability and high transparency (90.6%).[24–26] However, most studies concerning SF hydrogels are based on the protein self-assembly into β-sheet-rich networks.[27] Despite providing strength to the hydrogels through physical crosslinking, these β-sheet structures decrease the optical clarity and elasticity of the gels since the crystals block long-range molecular displacements. Furthermore, the clinical application of these materials is limited due to the long gelation times and harsh environmental conditions used to induce β-sheet formation (e.g., low pH, vortexing, or methanol treatments).[27] Thus, chemically modifying SF via the addition of methacrylate side groups allows for the covalent crosslinking of SF hydrogels via photocrosslinking. This provides increased mechanical strength but also allows for greater control of the in situ cross-linking kinetics. Finally, SilkMA prepolymer solutions are injectable and liquid at room temperature which makes solution handling easier than gelatin or GelMA. Thus, there is tremendous potential of harnessing photocurable SF-based hydrogels for corneal regeneration.

Bacterial infections can cause corneal scarring and prolong or impair the wound healing process.[28,29] Therefore, the application of antibiotic eye drops and ointments is standard procedure post-surgery. However, its efficacy is limited due to fast ocular drainage and difficulties in instillation.[30] The hydrophilic nature of SF provides a solubilizing environment for antibiotics, anti-inflammatory agents, and growth factors, ultimately increasing the functionality of the medical device.[31]

In this study, we investigated the development of a photocurable antimicrobial SF hydrogel for corneal regeneration. SF was modified by methacrylation to yield a photosensitive solution that can be chemically cross-linked within minutes using UV light. As shown in Figure 1, the physical, mechanical, and biological properties of methacrylated-silk (SilkMA) hydrogels, including water content, rheology, porosity, compressive modulus, degradation, and in vitro biocompatibility were studied. Finally, the drug release profile and antimicrobial properties of gentamicin-loaded SilkMA were assessed. The development of a semi-synthetic silk-based hydrogel has potential to be applied in ocular surface reconstruction due to its viscoelasticity, cytocompatibility, and antimicrobial properties.

2 | METHODS

2.1 | Silk fibroin extraction

Bombyx Mori cocoons were supplied by The Yarn Tree (Roanoke). Each cocoon was sliced into four pieces and the silkworms were

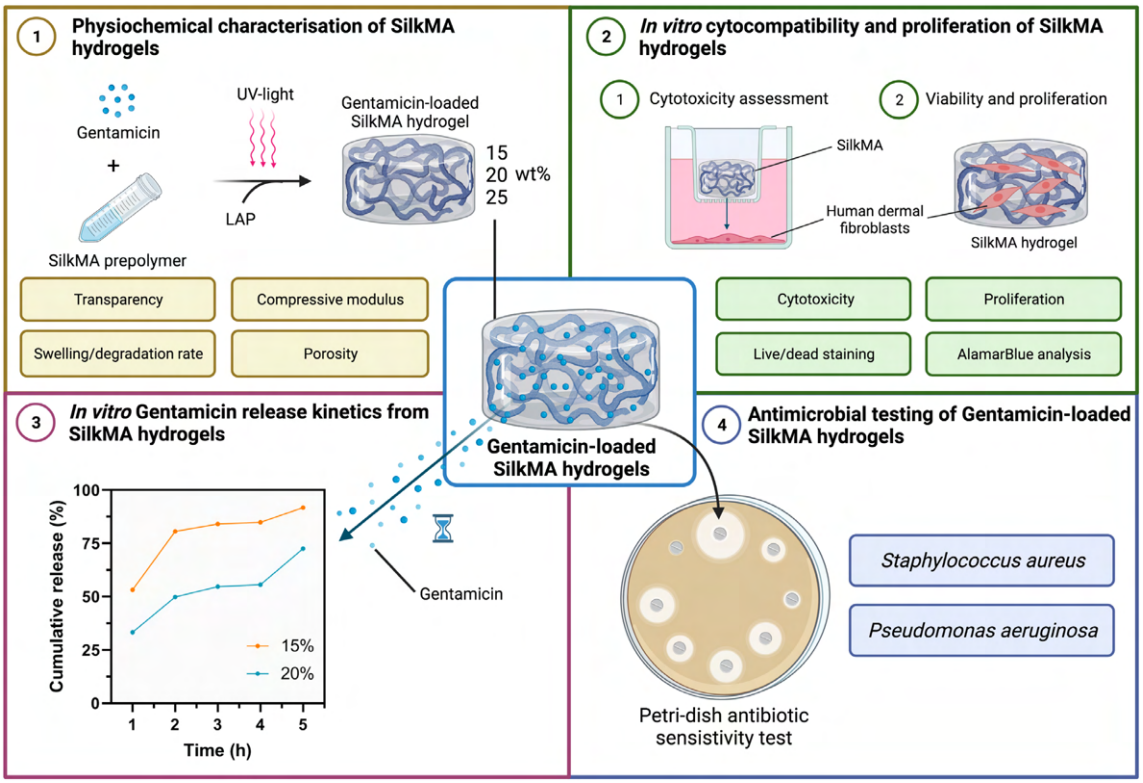


FIGURE 1 Experimental outline investigating the properties of gentamicin-loaded SilkMA hydrogels. (1) Photocrosslinking of 15%, 20%, and 25% gentamicin-loaded SilkMA hydrogels. The transparency in the visible range, swelling, in vitro degradation, porosity/pore size, compressive Young's modulus, and rheological properties of the SilkMA hydrogels were studied. (2) In vitro cytocompatibility of gentamicin-loaded SilkMA hydrogels. Firstly, the cytocompatibility of SF and SilkMA prepolymer solutions and SilkMA hydrogels was assessed. Then, the ability of human dermal fibroblast (HDF) cells to attach and proliferate on SilkMA hydrogels was studied and compared with GelMA hydrogels. (3) In vitro gentamicin drug release from SilkMA hydrogels. The cumulative drug release of gentamicin from SilkMA hydrogels and gentamicin concentration in the media were calculated. (4) Antimicrobial testing of gentamicin-SilkMA hydrogels. The antimicrobial activity of SilkMA hydrogels against two of the most common causes of ocular infections, *Staphylococcus aureus* and *Pseudomonas aeruginosa* was assessed in vitro

discarded. To remove the sericin, 10 g of sliced cocoons were boiled in 4 L of 0.02 M Na_2SO_3 (Acros Organics, Belgium) for 30 min. Subsequently, the degummed silk fibroin (SF) was washed three times in 2 L of distilled water for 20 min and left in a fume hood overnight to dry at room temperature.

2.2 | SilkMA synthesis

Briefly, 25% (wt/vol) of degummed SF solution was prepared by pouring a 9.3 M lithium bromide (LiBr) solution (Acros Organics, Belgium) on the tightly packed degummed silk fibroin fibers. After incubation at 60°C for 1 h, the fibers were completely dissolved and glycidyl methacrylate (GMA) (Sigma-Aldrich) was added to the solution (10% vol/vol) and allowed to react for 3 h at 60°C with a stirring speed of 300 rpm. The solution was then dialyzed against distilled water for 7 days at 4°C using 12–14 kDa cut-off dialysis tubes (Thermo Scientific). After dialysis, the SilkMA solution was diluted to 2% (wt/vol), and the pH adjusted to 7.4 using 1 mM sodium hydroxide solution (Sigma-Aldrich). Lastly, SilkMA solutions were lyophilized for 2 days to generate a white porous foam, which was stored at −80°C until further use.

2.3 | Degree of methacrylation

The degree of methacrylation (DM%) was quantified by proton nuclear magnetic resonance (^{1}H-NMR). Briefly, 5 mg of SilkMA were dissolved in 600 μl deuterium oxide (Sigma-Aldrich). The ^{1}H-NMR spectra of raw SF and SilkMA were recorded using a Bruker NEO NMR spectrometer fitted with a "smart"-BBFO probe (Bruker, Austria) operating at 400 MHz for 1 h. Spectra were recorded at 25°C using 250 scans and a delay of 12 s between scans. Baseline and phase correction were applied before integrating the peaks of interest with Topspin software (Bruker, Austria). The signal from the aromatic amino acids (6.9–7.5 ppm) was used as the internal reference to normalize the amine signals (2.83–3.14 ppm).[19] As GMA reacts with SF through the primary amines on lysine residues, the extent of substitution was calculated by normalization to the number of free amino groups of original SF. The degree of methacrylation was calculated using the following equation:

$$\text{DM}\,(\%) = \frac{\text{lysine integration signal of SilkMA}}{\text{lysine integration signal of SF}} \times 100 \quad (1)$$

2.4 | Preparation of gentamicin-loaded SilkMA gels

In this work, three different formulations were tested: 15%, 20%, and 25% (wt/vol) SilkMA gels loaded with 0.2% (wt/vol) gentamicin sulphate (G-Biosciences). Briefly, 15%, 20%, and 25% SilkMA solutions were prepared by dissolving an appropriate amount of SilkMA in phosphate-buffered saline (PBS, pH 7.4) (Sigma-Aldrich, UK) at room temperature overnight. The resulting viscous solutions were filtrated using Miracloth (Merck Millipore). A fresh stock solution of 2% (wt/vol) lithium phenyl-2,4,6-trimethylbenzoylphospinate (LAP) (Sigma-Aldrich, UK) in PBS was prepared. The photoinitiator was added to the SilkMA solution to a final concentration of 0.5% (wt/vol) and the resulting solution was mixed at room temperature. The hydrogel precursor solutions were photocured through UV-light using an OmniCure S1500 (Lumen Dynamics, Ontario, Canada) with a 365 nm filter. Briefly, 200 μl of SilkMA prepolymer solution was pipetted onto a 12 mm cylindrical mold and then exposed to 3 mW/cm^2 of UV-A for 5 min.

2.5 | Transparency

Light absorbance of hydrogels in the visible range (400–800 nm) was measured using a microplate reader (Spark Multimode, Tecan, Switzerland). The measurements were carried out in triplicate using SilkMA hydrogels (radius = 6 mm, thickness = 1.2 mm) in PBS with pure PBS serving as a blank control. Subsequently, the transmittance was calculated using Equation (2).

$$\text{Transmittance}\,(\%) = 10^{2-\text{Absorbance}} \quad (2)$$

2.6 | Swelling properties

SilkMA hydrogels with a radius of 6 mm and a thickness of 1.2 mm were prepared. Immediately after calculating the initial hydrogel weight (m_{t0}), three samples from each condition were immediately freeze-dried ($m_{t0,dry}$) and three samples were hydrated in PBS and placed in an incubator at 32°C. After 24 h, samples were blotted dry using filter paper and the swollen weight ($m_{swollen}$) was measured. Finally, the swollen hydrogels were lyophilized and weighed to determine the dry sample weight ($m_{swollen,dry}$). The sol fraction is a measurement of the macromers not crosslinked in the hydrogel network and was defined as the mass loss after 24 h.[32,33] The mass swelling ratio (q), water content (WC), and mass loss were calculated according to the following equations:

$$\text{Mass swelling ratio}\,(q) = \frac{m_{swollen}}{m_{t0,dry}} \quad (3)$$

$$\text{Water content}\,(\%) = \frac{m_{swollen} - m_{t0,dry}}{m_{swollen}} \times 100 \quad (4)$$

$$\text{Mass loss}\,(\%) = \frac{m_{t0,dry} - m_{swollen,dry}}{m_{t0,dry}} \times 100 \quad (5)$$

The thickness of the fresh and swollen hydrogels was estimated using ImageJ software (version 2.0) and the expansion (%) in PBS after 24 h calculated. Tests were performed in triplicate.

2.7 | Rheological characterization

The storage modulus (G′) and loss modulus (G″) of freshly prepared hydrogels were measured in oscillatory mode. A frequency sweep was conducted between 0.01 and 10 Hz at 0.5% shear strain at 32°C using a plate-plate geometry (Kinexus Pro+, Malvern, UK). The experiments were conducted in triplicate. The damping factor (tan δ) was calculated using the following equation:

$$\tan\delta = \frac{G''}{G'} \quad (6)$$

2.8 | Enzymatic degradation

Disc-shaped hydrogels (radius = 3 mm, thickness = 2 mm) were prepared as previously described. After photocrosslinking, five samples of each group were immediately freeze-dried to calculate the initial weight. To determine the in vitro degradation, five samples of each group were placed in 1.5 ml tubes with 1 ml of 1 U/ml collagenase II in PBS (Fisher Scientific, UK) or in 1 ml PBS (control group) and incubated at 32°C for 2, 5, and 7 days. At the end of the incubation period the hydrogels were lyophilized. The degradation was calculated using the following equation:

$$\text{Degradation}\,(\%) = \frac{m_{t0,dry} - m_{dry}}{m_{dry}} \times 100 \quad (7)$$

Where $m_{t0,dry}$ is the initial dry weight of the hydrogels and m_{dry} is the final dry weight of the sample after degradation ($n = 5$).

2.9 | Micro-computed tomography

Freeze-dried hydrogels were scanned using the Skyscan 1172 (Bruker, Germany) with 80 kV beam voltage and 100 μA current, 140 ms exposure per projection, 12.99 μm pixel size, rotation step 0.6° and 4 frame averaging. The same parameters were used for all scans. 2D projections were reconstructed and visualized using

NRecon (Version 1.6.10, Bruker) and CTVox (Version 3.0, Bruker), respectively. Further numerical analysis was performed in CTAn (Bruker).

2.10 | Scanning electron microscopy

Scanning electron microscopy (SEM) was used to assess the morphology and pore size of freeze-dried hydrogels. All samples (diameter = 6 mm, thickness = 2 mm) were mounted onto aluminum stubs using carbon tape and gold sputter coated. Images were captured using a TM3030Plus benchtop SEM (Hitachi High Technologies, Schaumburg) at an electron acceleration voltage of 15 kV.

2.11 | Mechanical characterization

Cyclic testing was performed using an Instron 5542 mechanical tester (Instron) with a 2 kN load cell. Cylindrical hydrogels (radius = 4 mm, thickness = 2 mm) were prepared as previously described and incubated in PBS for 4 h prior to testing. The dimensions of the samples were determined using a digital caliper. Compressive tests were performed at a rate of 1 mm/min up to a maximum strain of 60% of the original height by performing 8 cycles of loading and unloading. The compressive strain (mm) and load (N) was recorded using Bluehill 3 software. The Young's modulus was calculated from the slope of the linear region on the stress (kPa) versus strain (mm/mm) curves. Samples were tested in triplicate for each condition.

2.12 | In vitro cytocompatibility of SilkMA hydrogels

Human Dermal Fibroblasts (HDFs—ATCC Cat. PCS-201-012; Passage number 9) were cultured in Dulbecco's modified eagle medium (DMEM—Sigma-Aldrich, UK) and supplemented with 10% fetal bovine serum (Sigma-Aldrich, UK), 1% penicillin/streptomycin (Sigma-Aldrich, UK) and 2 mM L-glutamine (Sigma-Aldrich, UK). All cultures were maintained in tissue culture treated polystyrene flasks at 37°C with 5% CO_2 in a humidified incubator and passaged at 80% confluency.

2.12.1 | Cell viability

Fifteen percent SF and SilkMA pre-polymer solutions and SilkMA hydrogels were UV-sterilized for 20 min prior to use. Tissue culture treated 24-well plates (Corning, UK) were initially seeded with HDFs (1×10^4 cells/well). After 24 h, 100 μl of each sample was added to 24 well ThinCert cell culture inserts (Greiner Bio-One, UK) with 0.4 μm pore size. The monolayer cultures were incubated at 37°C with 5% CO_2 in a humidified incubator. Cell viability was evaluated using a Live/Dead assay (Thermo Fisher, UK) according to the manufacturer's instructions. Briefly, SYTO 10 green fluorescent nucleic acid stain (2 μl/ml) and ethidium homodimer-2 nucleic acid stain (2 μl/ml) were diluted in PBS to form the staining solution. At each time point, cell medium was removed, and samples were incubated with the staining solution for 15 min in the dark at 37°C. The staining solution was removed, and the samples were washed twice with PBS. The monolayer cultures were imaged with a fluorescent microscope (EVOS M5000, Thermo Fisher, UK) at days 1 and 3.

2.12.2 | 2D cell seeding on SilkMA gels

Fifteen percent SilkMA pre-polymer solutions were prepared as previously described and gelatin methacryloyl (GelMA - type A, bloom 300) was used as the control. Briefly, 15% (wt/vol) GelMA pre-polymer solution was prepared by dissolving an appropriate amount of polymer in PBS at 37°C for 30 min. Then, LAP was added to the GelMA solution to a final concentration of 0.5% (wt/vol) and the resulting solution was mixed at 37°C. SilkMA and GelMA pre-polymer solutions were UV-sterilized and photocrosslinked as described above in 48-well suspension cell culture plates (Sarstedt, UK). After curing, the hydrogels were washed with sterile PBS (Sigma-Aldrich, UK) for 15 min and soaked in supplemented DMEM overnight. One hour before cell seeding, the hydrogel matrices were partially dried to potentiate cell penetration. Then, 60 μl of cell suspension was added drop-wise onto each hydrogel (9×10^3 cells per scaffold) and samples were incubated for 1 h at 37°C with 5% CO_2 to bolster cell adhesion. After 1 h, DMEM was carefully added to the wells without disturbing the cell-laden hydrogels.[34] Culture medium was changed every 2 days.

2.12.3 | 2D cell metabolic activity

AlamarBlue™ assay (Thermo Fisher, UK) was used to determinate the relative metabolic activity according to the manufacturer's protocol. Briefly, the samples were incubated with 0.5 ml of 10% alamarBlue™ reagent in culture medium for 4 h at 37°C with 5% CO_2. Thereafter, 50 μl of cell culture medium were transferred to a 96-well plate (Corning, UK) and the fluorescence intensity was measured with a microplate reader (Spark Multimode, Tecan, Switzerland) using an excitation wavelength of 540 nm and an emission wavelength of 590 nm. Acellular hydrogels were used as a negative control and their fluorescence was subtracted from the same group seeded hydrogels to account for the background ($n \geq 4$).

2.13 | In vitro release of gentamicin from SilkMA gels

To study the in vitro drug release profile of gentamicin from SilkMA hydrogels, samples were incubated in 0.5 ml PBS in 48-well tissue-culture plates at 32°C. As prepared SilkMA hydrogels were used as blank. At each

time point, 33 μl of media was withdrawn from the well and immediately mixed with 33 μl of phthaldialdhehyde reagent (OPA, Sigma-Aldrich, UK) and 33 μl isopropanol (Sigma-Aldrich, UK) in a 96-well UV-transparent microplate (Greiner Bio-One, UK). The withdrawn samples were replaced with equal volumes of fresh PBS. Gentamicin release was measured with a microplate reader (Spark Multimode, Tecan, Switzerland) in fluorescence using an excitation wavelength of 340 nm and an emission wavelength of 430 nm. The concentration of gentamicin was extrapolated from a previously validated calibration curve and divided by the total amount of gentamicin encapsulated in the hydrogel to obtain the percentage released ($n = 5$).

2.14 | In vitro antimicrobial efficacy testing

2.14.1 | Preparation of bacterial inocula

Luria Bertani broth (Sigma-Aldrich, UK) and Luria Bertani broth with agar (Sigma-Aldrich, UK) were prepared using distilled water and at concentrations of 20 and 35 g/L, respectively. Both broth and broth with agar were then sterilized via autoclaving for 20 min at 121°C under 100 KPa of pressure (Astell, UK). Overnight cultures of *Staphylococcus aureus* (ATCC 29213) and *Pseudomonas aeruginosa* (NCTC 13437) were prepared whereby one bacterial colony was inoculated in 5 ml of LB broth. Using a Jenway 6300 UV–VIS spectrophotometer (Cole Parmer, UK) optical density measurements were taken at 600 nm for each overnight culture. Cultures were then diluted to an optical density of 0.06. Luria Bertani broth with agar was poured to form agar plates. These were then inoculated with the bacterial cultures using a hockey stick spreader.

2.14.2 | Zones of inhibition

Fifteen percent and 20% gentamicin loaded SilkMA gels prepared as previously described, were placed onto the inoculated plates and incubated at 37°C for 24 h. The zones of inhibition (ZOI) formed from inhibited bacterial growth were then measured and recorded. SilkMA gels were then transferred from the 24 h plates onto freshly inoculated agar plates, incubated for a further 24 h and with measurements taken at 48 h. This process was repeated to obtain inhibitory results after 72 h. Each SilkMA formulation and bacterial strain were run in triplicate.

2.15 | Statistical analysis

For each experiment, at least three samples were tested. One or two-way analysis of variance (ANOVA) and the Tukey test were used to determine statistically significant differences with GraphPad Prism 8.0 software. The level of significance was set at $p < .05$. Data are presented as mean value ± *SD*.

3 | RESULTS

3.1 | Physicochemical characterization of SilkMA Gels

H^1-NMR spectroscopy showed that 35%–40% of SF lysine groups were functionalized with methacrylate groups (Figure S1). Three different SilkMA hydrogel concentrations (wt/vol %) were prepared: 15%, 20%, and 25%. The optical transmittance measurements of SilkMA hydrogels in the visible range (400–800 nm) are shown in Figure 2A,B. The transparency of 15% and 20% SilkMA hydrogels was 83 ± 3% and 80 ± 1%, respectively, with both hydrogels showing high optical clarity (Figure 2C).[35] However, a negative correlation between hydrogel concentration and transmittance was observed, with 25% hydrogels having a statistically significant lower transparency (63 ± 2%) compared with 15% and 20% ($p < .001$). To determine the mass swelling ratio (q), water content and the expansion, hydrogels were incubated in PBS at the ocular temperature (32°C) for 24 h. The swelling characteristics were inversely proportional to the polymer concentration; the q of the 15, 20 and 25% gel was 9.8 ± 0.2, 8.6 ± 0.2, and 5.8 ± 0.1 respectively, with 15% and 20% ($p < .0001$) showing a significantly higher q values compared with 25% (Figure 2D). The water content results followed a similar trend, with 15% (89.8 ± 0.3%) and 20% (88.3 ± 0.4%) exhibiting significantly higher values ($p < .0001$) compared with 25% (82.7 ± 0.3%) (Figure 2E). As shown in Figure 2F, 15% SilkMA hydrogels (28.5 ± 7.1) exhibited a twofold significant higher expansion in PBS compared with 20% (14.4 ± 4.7) and 25% (14.3 ± 4.1) gels ($p < .05$).

Storage modulus (G′) and loss modulus (G″) represent the elastic and reversible response of the materials and the viscous and irreversible rearrangement of the polymeric structure of the hydrogel, respectively.[36] As shown in Figure 3A, G′ is one order of magnitude higher than G″ regardless of the SilkMA concentration, which is a typical behavior of elastomeric materials.[19] Moreover, a positive correlation between the rheological properties and polymer concentration was observed (Figure 3B,C); 25% (10.4 ± 0.2 kPa) hydrogels had a significantly higher G′ than 20% (3.0 ± 0.4 kPa, $p < .0001$) and 15% (1.1 ± 0.3 kPa, $p < .0001$) hydrogels by 3 and ninefold, respectively, while 20% hydrogels shown a threefold higher G′ than 15% gels ($p < .001$). Despite observing a nonsignificant difference in G″ between 15% and 20% SilkMA gels, G″ was proportional to the polymer concentration, ranging from 45 to 568 Pa for 15% and 25% hydrogels, respectively; 25% SilkMA hydrogels presented greater G″ than 15% ($p < .001$) and 20% (164 Pa, $p < .001$) gels by a 4 and 12-fold factor. Finally, the damping factor was lower than 0.06 for all the groups studied, suggesting a solid-like behavior (Figure 3D).[37]

The in vitro susceptibility of SilkMA gels to enzymatic degradation was studied by incubating the hydrogels in 1 U/ml collagenase II for up to 7 days. Our results show that there was a time-dependent increase in degradation, with higher polymer concentrations exhibiting lower mass loss over time. As shown in Figure 4A, no significant differences were observed between the groups after 2 and 5 days of incubation. However, at day 7, 15% SilkMA gels were completely

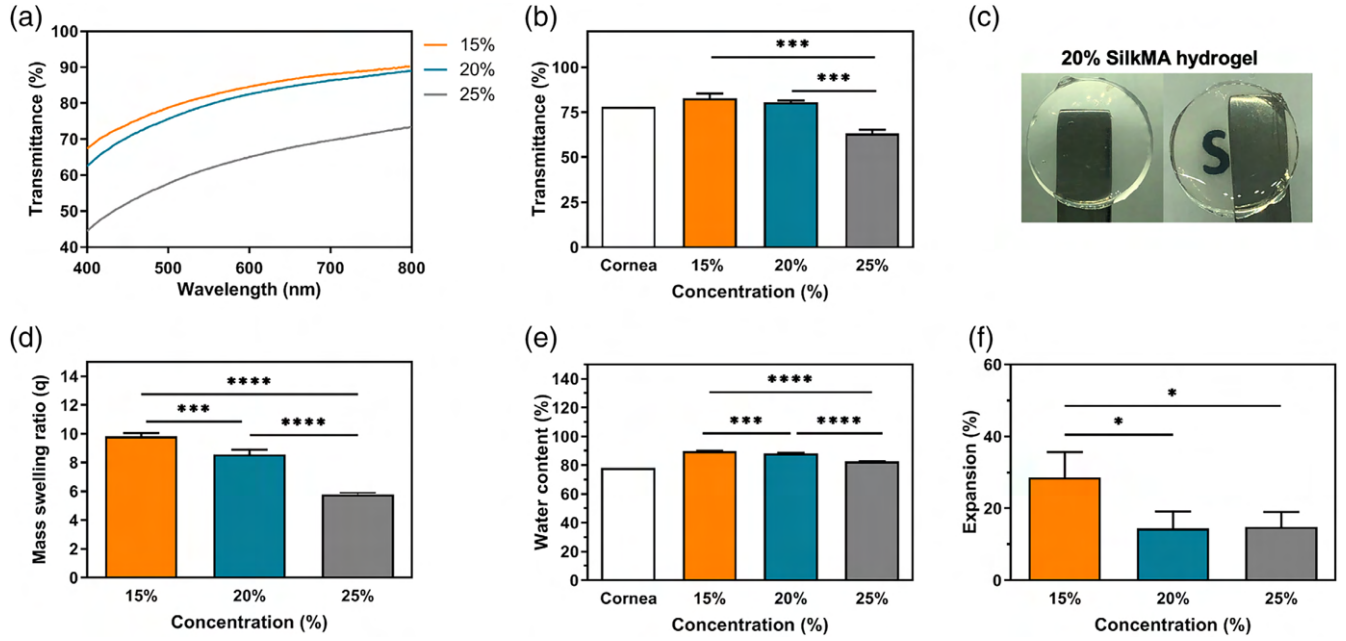


FIGURE 2 SilkMA hydrogels transparency ($n = 3$): (A) transmittance profiles, (B) average optical transmittance in the visible range, and (C) optical clarity. Hydrogel diameter = 10 mm. Swelling characteristics of SilkMA hydrogels in PBS at 32°C ($n = 3$): (D) swelling ratio (q), (E) water content (%), and (F) expansion (%). Data presented as mean value ± *SD* (*p<.0001)

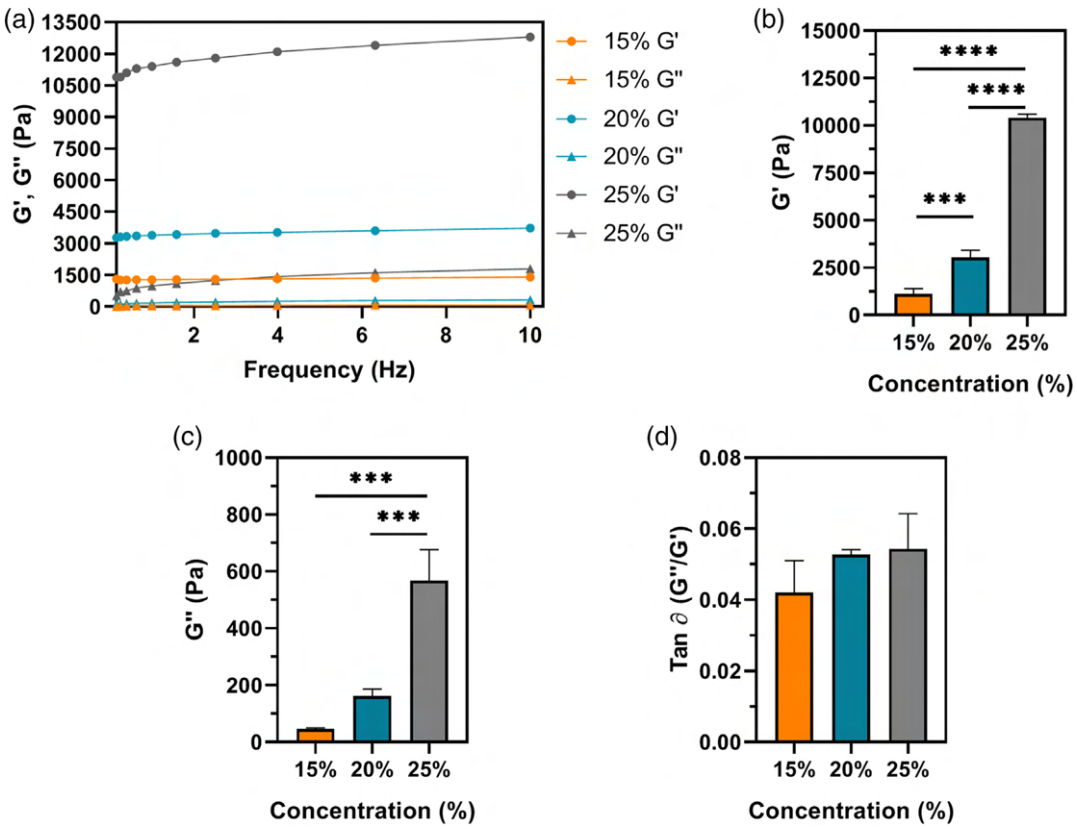


FIGURE 3 Rheological properties of SilkMA hydrogels ($n = 3$): (A) representative frequency sweep, (B) storage modulus (G′), (C) loss modulus (G″) and (D) damping factor (tan ∂). Data presented as mean value ± *SD* (*p<.05, **p<.01, ***p<.001, ****p<.0001)

degraded, while 20% and 25% SilkMA showed a degradation of 88 ± 2% and 69 ± 12% (p <.01), respectively. Due to the importance of the optical and swelling properties in the design of materials for corneal engineering, only SilkMA 15% and 20%, formulations with similar

characteristics to the human cornea, were chosen for further characterization.[38] The crosslinking efficiency was measured by mass loss, which is defined by the amount of uncrosslinked polymer after photocuring.[39] Regardless of the polymer concentration, there was no significant difference in mass loss (≃5%, Figure 4B), suggesting that the increase in concentration and viscosity did not impact the mixing between the polymer and the photoinitiator/gentamicin solution or the free radical diffusion within the material during crosslinking. Finally, the mechanical performance of the SilkMA hydrogels was assessed by compressive mechanical testing (Figure 4C). In agreement with the rheology data, 20% hydrogels showed a significantly higher Young's modulus than 15% gels (p <.0001). Specifically, the Young's modulus was 21 ± 2 kPa for 15% and 79 ± 2 kPa for 20%, a fourfold increase (Figure 4D).

The microstructure and morphology of SilkMA hydrogels were investigated using micro-CT and SEM analysis. Micro-CT scanning was used to determine the porosity, pore size and pore wall thickness within the 15% and 20% SilkMA hydrogels (Figure 5A). As shown in Figure 5B, the total porosity was 79 ± 2% and 72 ± 2% for 15 and 20% SilkMA (p <.05), respectively. However, despite the differences in porosity, the scaffolds exhibited similar pore thickness (≃26 μm, Figure 5C) and pore size distributions (Figure 5D,E), with a mean pore size of 56 ± 4 μm and 56 ± 3 μm for 15% and 20% SilkMA scaffolds, respectively (Figure 5F). SEM images revealed a uniform and interconnected pore structure for both groups (Figure 5G,H).

3.2 | In vitro assessment of cytocompatibility

The cytocompatibiliy of SF and SilkMA prepolymer solutions and SilkMA hydrogels was studied using HDF cells seeded on tissue culture well-plates. Fluorescence staining (Figure 6A) indicates high cell viability (> 90%) for all tested conditions, suggesting that SF and SilkMA materials did not induce toxicity. After 72 h, cells reached confluency for all groups studied. Furthermore, the ability of SilkMA gels to support cell attachment and proliferation was studied by direct seeding of HDF cells on SilkMA hydrogels and compared with GelMA, another semisynthetic-polymer and broadly used material for 3D cell culture applications.[40] As shown in Figure 6B, the metabolic activity progressively increased over the course of 14 days for both groups studied. The difference between the metabolic activity of HDF cells seeded on GelMA and SilkMA is only statistically significant at day 1 (p <.0001), with cells seeded on SilkMA hydrogels exhibiting a 47% lower metabolic activity. On days 2, 7, and 14, there was a 10% difference in cell metabolic activity between GelMA and SilkMA samples, however, it is not statistically significant (Figure 6B).

3.3 | In vitro drug release studies

The release kinetics of gentamicin from 15% and 20% SilkMA hydrogels was studied. As shown in Figure 7A, 15 and 20% hydrogels

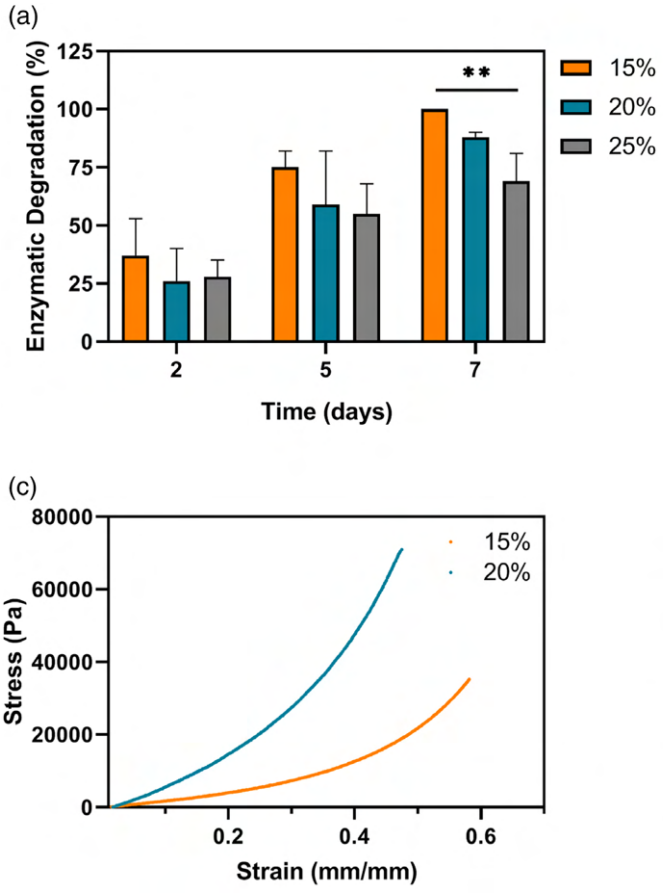


FIGURE 4 (A) In vitro degradation of SilkMA hydrogels incubated in 1 U/ml collagenase II at 32°C for 2, 5, and 7 days ($n = 5$). (B) Measurement of the macromers not crosslinked in the hydrogel network after photocrosslinking (mass loss, %) ($n = 3$). Cyclic compressive mechanical testing of SilkMA hydrogels ($n = 3$): (C) representative compressive strain-stress curves and (D) Young's moduli. Data presented as mean value ± *SD* (*p<.05, **p<.01, ***p<.001, ****p<.0001)

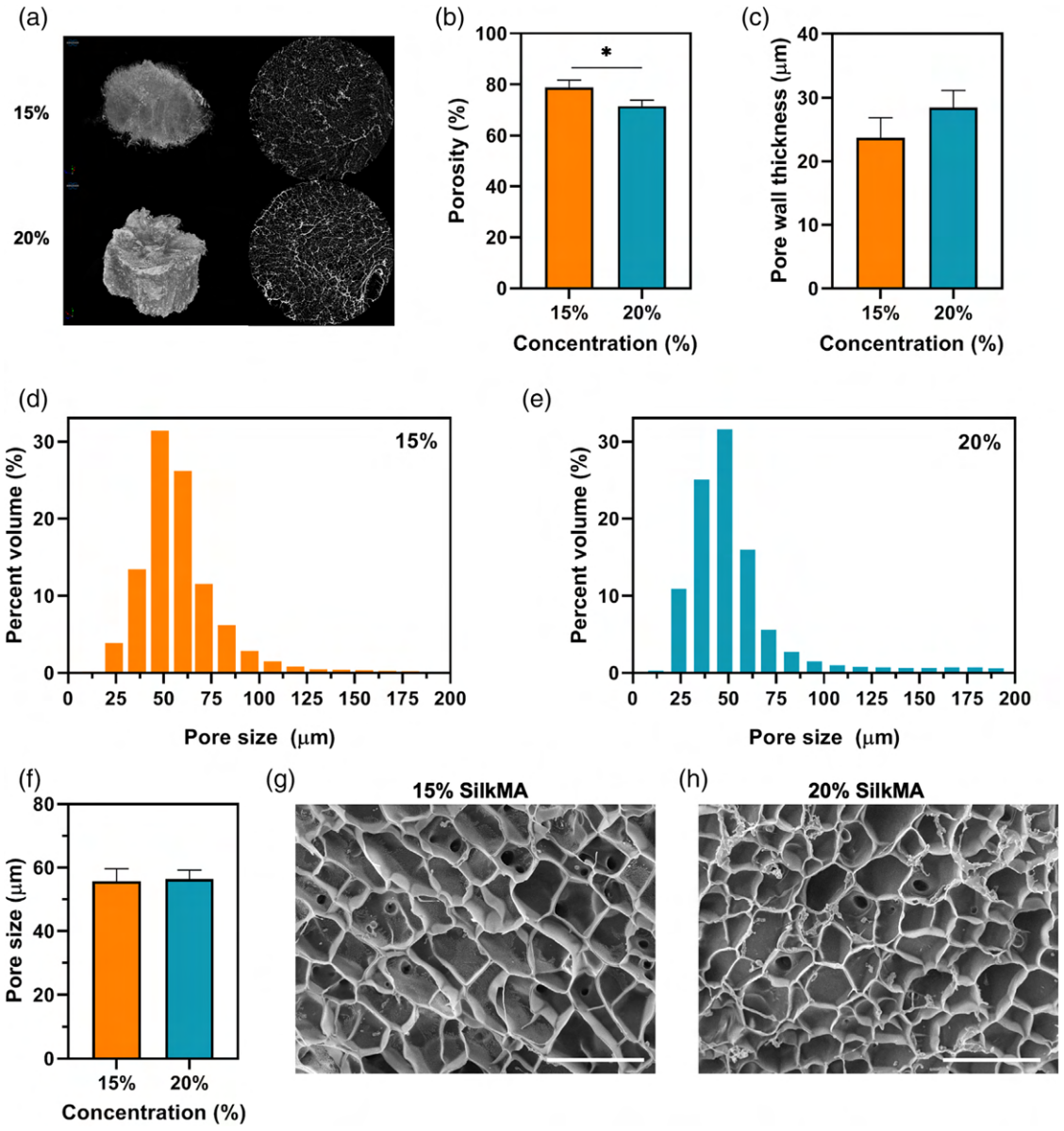


FIGURE 5 Morphology and microstructure analysis of SilkMA hydrogels after freeze drying ($n = 3$): (A) 3D micro-CT reconstruction and 2D images (slices) of SilkMA scaffolds. Diameter = 7 mm. Quantitative analysis of porosity by micro-CT: (B) total porosity, (C) mean pore thickness, (D,E) pore size distribution in the hydrogels, and (F) mean pore size. Representative SEM images of freeze-dried SilkMA scaffolds: (G) 15% SilkMA, and (H) 20% SilkMA. Scale bar: 150 μm. Data presented as mean value ± *SD* (**p*<.05, ***p*<.01, ****p*<.001, *****p*<.0001)

released 53 ± 4% and 33 ± 8% (p <.02) of the total content of gentamicin within 1 h. After 2 and 5 h, 15% SilkMA gels released 84 ± 4% and 92 ± 4% (p >0.05), respectively, of the total gentamicin encapsulated, while 20% SilkMA hydrogels delivered 55 ± 4% and 72 ± 13% (p <.02), respectively. The concentration of gentamicin in the media after 24 and 48 h was determined and compared with the minimum inhibitory concentration (MIC) of gentamicin for *S.aureus* and *P. aeruginosa*. Fifteen percent and 20% SilkMA hydrogel delivered concentrations above the MIC for *S.aureus* (8 μg/ml) and *P.aeuruginosa* (2 μg/ml) after 24 and 48 h incubation.[41] As shown in Figure 7B, the concentration of gentamicin in the media was ~85 ± 6 μg/ml and 15 ± 2 μg/ml after 24 and 48 h, respectively, for both groups.

3.4 | Antimicrobial efficacy testing

Agar diffusion tests were performed to study the antimicrobial efficacy of gentamicin-loaded SilkMA gels against *S.aureus* and *P. aeruginosa*. Briefly, 15% and 20% SilkMA gels were prepared and placed on culture dishes uniformly covered with *S.aureus* or *P. aeruginosa*. After incubation at 37°C for 24 h, the zones of inhibition (ZOI) were recorded, and the same hydrogel was transferred to a freshly inoculated plate. This process was repeated until a ZOI was present. As shown in Figure 7D,E, both 15 and 20% SilkMA hydrogels inhibited the growth of *S.aureus* and *P.aeruginosa* for 72 h. However, no statistical difference was observed between the ZOI of 15 and

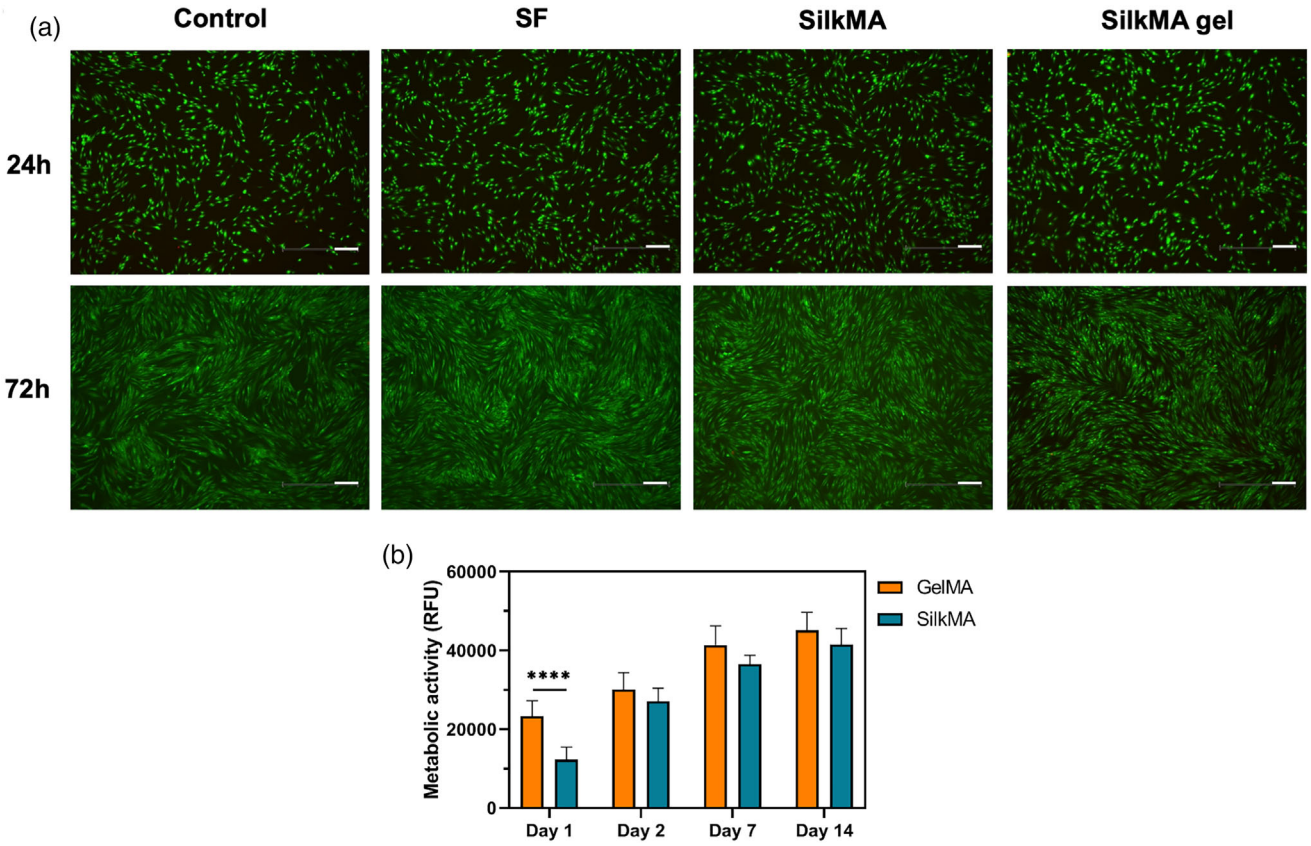


FIGURE 6 Cytocompatibility study: (A) Live/Dead images of HDFs seeded on tissue culture well-plates with media (control) and SF/SilkMA solutions and SilkMA gels in inserts ($n = 3$). Scale bar = 200 μm. (B) Quantification of the metabolic activity of HDFs seeded on SilkMA and GelMA hydrogels by AlamarBlue assay 1, 2, 7, and 14 days after cell seeding ($n = 5$). Data presented as mean value ± *SD* (*****p<.0001)

20% SilkMA hydrogels throughout the experiment (Figure 7C). ZOI varied from 2.6 ± 0.2 cm and 3.0 ± 0.3 cm after 24 h to 1.4 ± 0.1 cm and 1.5 ± 0.1 cm after 72 h for *S.aureus* and *P.aeruginosa*, respectively (Figure 7C). Finally, gentamicin-free SilkMA gels did not inhibit bacterial growth (data not shown).

4 | DISCUSSION

In most cases, vision lost due to corneal-related injuries can be reversed with a corneal transplant. However, currently there is a severe mismatch between supply and demand of cadaveric donor corneal tissue (less than 1:70).[15,16] Despite recent efforts to develop corneal stroma equivalents, the clinical need remains unmet with no products available for routine use.[5,14,15] In this study, we developed an injectable and light-polymerizable SilkMA solution by modifying silk's lysine amino acids with methacrylate groups.

The photosensitive SilkMA solutions have potential to be crosslinked in situ using low UV-A intensities. In 2016, the US Food and Drug Administration (FDA) approved a therapy called corneal crosslinking (CXL) to treat patients with post LASIK/PRK ectasia and progressive corneal thinning (keratoconus). CXL uses UV-A light and riboflavin to stiffen the cornea by inducing covalent bonds between corneal collagen molecules.[42,43] During the treatment, riboflavin is added to the cornea and photoactivated with UV-A light at 365 nm with irradiance of 3 mW/cm^2 for 30 min.[44] In this study, the wavelength and intensity were chosen in agreement with CXL procedure, however instead of irradiating the eye for 30 minutes, the gels set within 5 min with minimal heat production. The impact of polymer concentration on the physical and mechanical properties of the hydrogels was studied. Our results indicate that SilkMA concentration influenced the transparency, swelling characteristics, rheology and mechanical properties of the hydrogels.

The optical functions of the cornea include 80% of the total ocular refractive power, UV light filtering (< 400 nm), and visible light transmission.[38,45] Thus, a successful corneal substitute needs to have similar light transmittance to the native human cornea to replicate its visual acuity. The transmittance results obtained for 15% and 20% SilkMA hydrogels in the visible range match the values reported in the literature for a healthy human cornea (78%–80%).[35,46] Also, the light transmittance spectrum of the human cornea published by Freegard is very similar to the spectra obtained for 15% and 20% SilkMA, with 62% and 90% light transmittance at 400 and 780 nm, respectively.[46]

Another important factor influencing the overall transparency of a hydrogel is the water content. The high hydrophilic character of hydrogels makes them attractive materials for tissue engineering

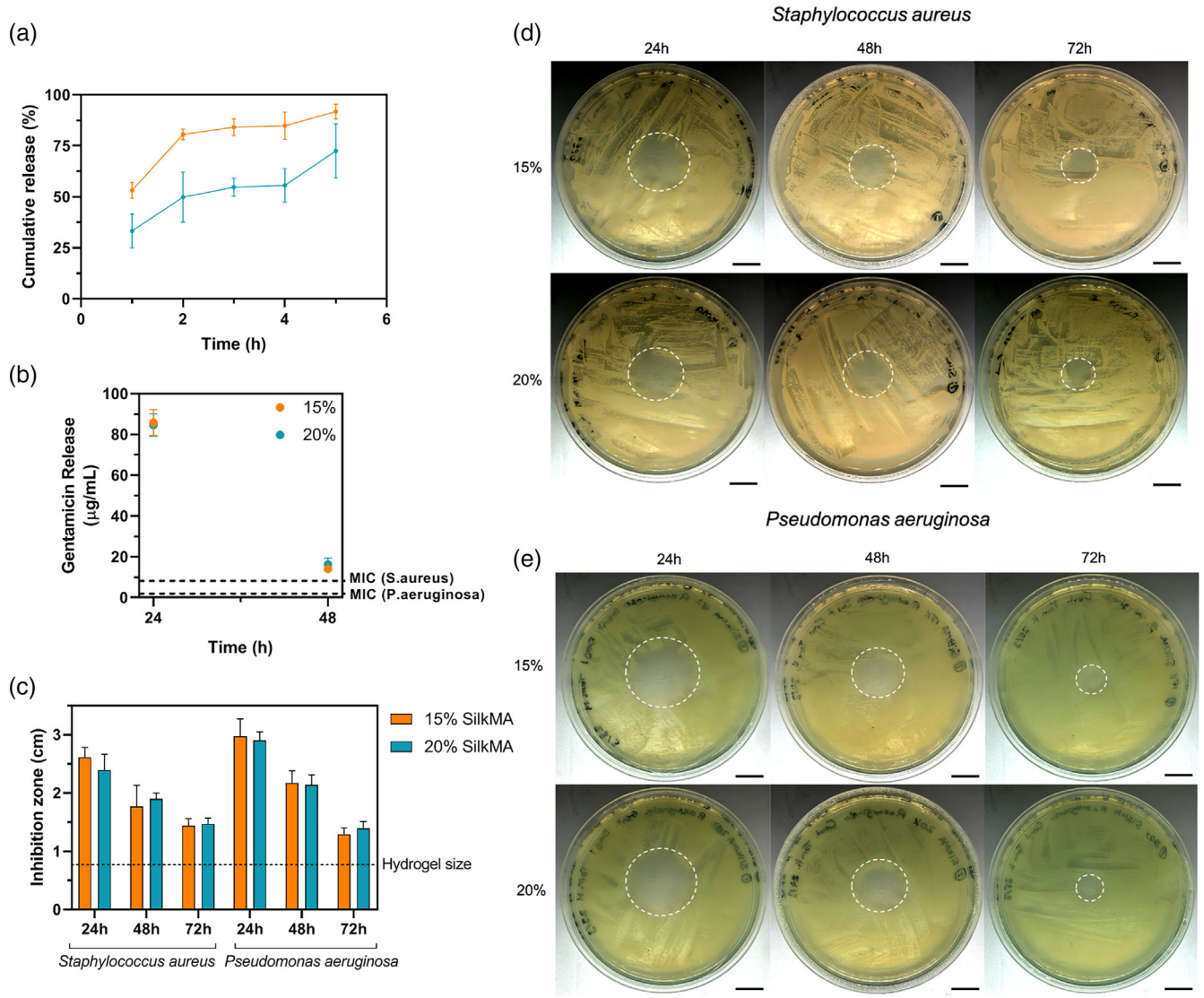


FIGURE 7 In vitro properties of gentamicin-loaded SilkMA hydrogels ($n = 5$): (A) Cumulative gentamicin drug release from SilkMA scaffolds after 1, 2, 3, 4, and 5 h. (B) Gentamicin concentration in the media after 24 and 48 h. Zone of inhibition study ($n = 3$): (C) Average zone of inhibition of SilkMA hydrogels after 24, 48, and 72 h. (D) Staphylococcus aureus, and (E) Pseudomonas aeruginosa. Scale bar = 1.5 cm

applications since the swelling characteristics affect the diffusion and distribution of nutrients, oxygen, and the functionality of encapsulated cells.[1] In vivo variations in water content cause a decrease in corneal transparency due to the changes in the collagen fibrillar spacing and are correlated with several pathologies and diseases (e.g., corneal graft rejection, keratoconus, and Fuchs' dystrophy).[47,48] In this study, all groups showed water content values similar to the human cornea (75%–85%).[45,48] However, as previously reported in the literature, the mass swelling of SilkMA hydrogels decreased with higher polymer concentrations.[10,49–51] An increase in the concentration of photocrosslinkable groups results in a higher crosslinking density, which ultimately creates a tighter hydrogel network and a lower mass swelling ratio. The storage and compressive Young's modulus were directly proportional to the polymer concentration, also indicating a greater crosslinking density. Bryant et al. studied the critical effect of the mass swelling ratio in the formation of a functional ECM.[52] The primary components of cartilage, glycosaminoglycan (GAG) and collagen, were evaluated histologically when varying q from 4.2 to 9.3. Results showed that q has a great effect on cell function. Despite having a similar GAG content in all hydrogels, its distribution depends on the gel properties. In systems with a q of 9.3 (low crosslinking density), GAG molecules were homogenously distributed throughout the gel. On the other hand, in highly crosslinked gels with q values lower than 5.2, GAGs were retained in pericellular regions.[52] In this work, all groups studied presented a q >5.2, with values ranging between 9.8 ± 0.2 and 5.8 ± 0.1 for 15% and 25% SilkMA gels, respectively.[53] Moreover, swelling properties can also affect the overall shape of the material. A successful corneal substitute should have minimal volume change thereby reducing the risk of implant mismatch and imparting stress on the surrounding tissues.[53] All experimental

groups handled well and retained their shape in the swollen state. However, 15% SilkMA hydrogels showed a twofold higher expansion percent than 20% and 25% SilkMA (p <.05).

The success of a corneal substitute is dependent on its ability to sustain epithelial and stromal regeneration. Controlling the degradation rate is paramount since the hydrogel's in vivo degradation should match that of corneal regeneration. Herein, we demonstrate that SilkMA hydrogels can be enzymatically degraded in vitro. A negative correlation between the polymer concentration and the polymer reactivity to enzymatic degradation was observed. At higher cross-linking densities, the enzyme accessibility to the cleavage sites of SF is restricted, decreasing the reactivity of hydrogels to enzymatic degradation.[10] However, the in vitro degradation rate reported in this study is not representative of the ocular in vivo microenvironment. The corneal environment is not as dilute as the conditions used in the swelling and degradation study. In vivo, the surface of the cornea is wetted by the tear film while the overall corneal hydration is controlled by a pumping mechanism in the endothelium.[13] Also, the concentration of collagenase II used in this experiment is not likely to be comparable to the concentrations found in the eye. Nevertheless, our results demonstrate that the chemical modifications on the SF structure did not affect the biodegradability of the polymer. In the future, the actual swelling characteristics, expansion percentage and the rate of in vitro degradation should be studied in an environment more representative of the ocular conditions (e.g., porcine eye model).

Indeed, 25% SilkMA gels exhibited a significantly lower transparency (p <.001) and swelling ratio (p <.0001) than 15% and 20% SilkMA gels. Given the importance of transparency and nutrient transport in the success of a corneal substitute, we chose to move forward with 15 and 20% SilkMA formulations due to their superior transparency and swelling characteristics.

Comprising ~90% of the corneal thickness, the stroma provides the cornea with its mechanical and optical properties due to the lamellar interweaving of collagen fibrils embedded in a hydrated matrix.[54,55] The cornea shows an increase in stiffness associated with age that could be related with a decrease in interfibrillar spacing and an increase in cross-linking between collagen molecules.[56] Despite being essential for the diagnosis of corneal diseases and corneal function maintenance, the rheological and mechanical properties of the cornea are not completely understood and the values reported in the literature span over a large range.[57,58] Hatami-Marbini et al. studied the dynamic shear properties of the corneal stroma using oscillatory experiments. The average G′ and G″ varied from 2 to 8 kPa and 0.3 to 1.2 kPa, respectively. However, hydrogels derived from biopolymers or corneal ECM are reported to have poor mechanical properties compared with the native tissue.[59] In this work, only 20% SilkMA hydrogels exhibited a storage modulus within the above-mentioned range (3.0 ± 0.4 kPa). Despite the lower G″ of SilkMA hydrogels (0.04–0.6 kPa), the overall rheological properties of SilkMA hydrogels are higher than previously investigated light-free collagen-based hydrogels.[2,4] Ferraci et al. synthesized 10%, 15%, and 20% photocurable bovine serum albumin (BSA-MA) with different degrees of substitution (DM = 73%–100%) using UV light (150 mW/cm^2, 6 min). The compressive modulus of 15 and 20% BSA-MA hydrogels with 92 DM% was ~18 and 30 kPa, respectively.[10] In this work, despite using a considerably lower DM% (40%) and intensity (3 mW/cm^2), the compressive modulus of 15% and 20% SilkMA hydrogels was 21 and 79 kPa, respectively. This demonstrates the potential of SilkMA-LAP system for tissue engineering applications, using a relatively low light intensity, hydrogels with excellent mechanical properties can be prepared due to the outstanding mechanical properties of silk proteins.

Moreover, substrate stiffness is reported to influence stem cell differentiation and proliferation.[60,61] Similarly, the hydrogel microstructure also plays an important role in cytocompatibility since porosity and pore size have previously been reported to influence cellular attachment, migration, and tissue ingrowth.[62,63] Although having low porosity (< 80%), which is required for structural properties, both 15 and 20% SilkMA hydrogels showed interconnected and uniform sized pores with an average pore size higher than 50 μm. Murphy et al. investigated the relationship between scaffold pore size and cell activity in bone tissue engineering. Scaffolds with small pores and increased surface area may show higher levels of initial cell attachment, however, the improved cell infiltration provided by scaffolds with larger pore sizes ultimately outweighs this effect.[62,63] In this study, we firstly verified the cytocompatibility of the SF/SilkMA prepolymer solutions and SilkMA hydrogels. Live/dead results showed that the modified and unmodified polymers, photoinitiator, and degradation products did not induce cytotoxicity after 72 h. Then, the hydrogel's ability to support cell attachment was studied. It has been previously reported that silk does not possess cell-adhesion sequences (e.g., RGD) present in other proteins, such as collagen, gelatin, or laminin.[37,64] However, SilkMA hydrogels were shown to support adhesion and proliferation of HDFs for the entire duration of the experiment and the differences between the metabolic activity in SilkMA and GelMA cell-laden hydrogels was only statistically significant at day 1 (p <.0001). The attachment of HDF cells to the SilkMA hydrogels possibly resulted from the hydrophilic nature of the hydrogels and their ability to immobilize adhesive proteins from the serum (e.g., vitronectin and fibrinogen).[10,65] In the future, the viability of cells encapsulated within SilkMA gels should be studied to confirm the suitability of SilkMA as biomaterial and study the impact of photocrosslinking. Importantly, the pore size obtained in this study should not compromise cell viability. Wang et al. encapsulated NIH-3T3 fibroblasts in EY-GelMA hydrogels with similar pore sizes to the SilkMA hydrogels studied here (> 50 μm). The cell viability of 15% and 20% EY-GelMA hydrogels 24 h post cell-seeding was 85.9% and 91.5% (p <.01), respectively. The improved biocompatibility of 20% EY-GelMA gels was attributed to its higher stiffness.[61] In one of the first studies published using SilkMA, Kim et al. demonstrated the suitability of SilkMA bioinks for cell encapsulation. NIH/3T3 fibroblasts were suspended in 10%–30% SilkMA or 10% GelMA (control) and printed using DLP. The authors concluded that cells remained viable regardless of the concentration, with 30% SilkMA gels having a cell proliferation as high as 10% GelMA despite the smaller pore size (≃ 40 μm).[19]

The antibacterial efficiency of gentamicin-loaded SilkMA hydrogels was assessed against *S.aureus* and *P.aeruginosa*, two of the most common causes of ocular infections.[30] Agar diffusion experiments were performed to test the antibacterial properties of 15% and 20% SilkMA hydrogels. Both groups inhibited bacterial growth for 72 h and the ZOIs were not statistically significant between groups throughout the experiment. The fact that the ZOIs for *P.aeruginosa* are higher than *S.aureus* is expected since the MIC for the latter is four times higher.[41] Following the confirmation that the gentamicin-loaded SilkMA hydrogels successfully inhibited bacterial growth, the drug release kinetics and gentamicin concentration in the media were studied. We observed a rapid drug release for both groups with 15% and 20% SilkMA hydrogels releasing 92 ± 4% and 72 ± 13% within 5 h, respectively. In this study, the gentamicin was solely entrapped in the polymer network. Consequently, a quick initial release and a negative correlation between the polymer concentration and the gentamicin drug release rate were expected since loose polymer networks are less able to retain the drug, yielding a quicker release. Importantly, both groups delivered antibiotic concentrations higher than the MIC in the first 48 h which is critical for the successful eradication of a bacterial strain. We believe this discrepancy between the results regarding the antimicrobial testing (agar diffusion test) and the in vitro drug release experiment are due to the different nature of the experiments. When solid agar was used, the drug release profile was slower since only one surface of the gel was in contact with the agar and less liquid volume was available for elution, delaying the drug diffusion. Then, the drug-loaded in the hydrogels was enough to inhibit bacterial growth for 72 h. However, for drug release studies, the hydrogels were soaked in PBS. Since the contact area between the gel and the media was higher, gentamicin was released within a few hours (burst release). However, neither of these conditions is representative of the ocular in vivo microenvironment. In the future, the hydrogels should be tested in an ocular model that considers the presence of the tear film, blinking, and ocular movements. Together, we have demonstrated the photocurable SilkMA hydrogels are able to successfully deliver antimicrobial agents and control their release kinetics to effectively inhibit bacterial growth, ultimately enhancing the potential clinical efficacy of this corneal substitute.

In the present study, we have demonstrated the development of SilkMA hydrogels that replicate the corneal physical properties, in addition to being biodegradable and cytocompatible. The hydrogel biodegradability was tested with collagenase II, an enzyme that can be naturally found in tears.[66] Ideally the material degradation should match de novo tissue formation as cells would secrete enzymes as they migrate. Therefore, we expect the degradation properties of the hydrogels to be linked to cellular integration and tissue formation. Also, gentamicin-loaded SilkMA hydrogels were proven effective against *S.aureus* and *P.aeruginosa*, two of the most common causes of ocular infections, which could improve the overall graft acceptance of this material when compared to the conventional therapies.[30] To our knowledge, this is the first study to assess the utility of SilkMA hydrogels for corneal applications.

The focus of the biological studies carried out in this study was the assessment of SilkMA's cytocompatibility given that the semi-synthetic polymer and the photoinitiator could be a source of cytotoxicity. In the future, the in vitro adhesion, differentiation, and tissue formation of corneal cells within these constructs needs to be investigated. Moreover, due to the difficulty in replicating the complex corneal physiological environment in vitro, such as the ocular movement, blinking, or tear film, in vivo experiments will be required to further understand the therapeutic potential of this material in the repair of corneal injuries. More specifically, the ability of SilkMA hydrogels to fill the corneal defects, support corneal re-epithelization, deliver the optimum release kinetics following surgery and degrade in situ will be addressed.

5 | CONCLUSION

In conclusion, these findings demonstrate the development of an injectable and photocurable SilkMA hydrogel system for corneal regeneration. The material can be either crosslinked in situ within minutes at neutral pH and without heat production using a low-intensity UV light or printed using lithography-based biofabrication techniques. We demonstrated that gentamicin-loaded SilkMA hydrogels are biodegradable, biocompatible, and antimicrobial along with exhibiting optical and mechanical properties similar to the native human cornea. Taken together, these findings demonstrate the considerable potential that SilkMA hydrogels possess as a corneal substitute. To our knowledge, this is the first study to report the utility of photocurable SilkMA hydrogels to promote cornea regeneration.

DATA AVAILABILITY STATEMENT

The data that support the findings of this study are available from the corresponding author upon reasonable request.

ORCID

Kenny Man https://orcid.org/0000-0002-7946-9375
Sophie E. T. Louth https://orcid.org/0000-0003-3065-8201
Sophie C. Cox https://orcid.org/0000-0003-4746-0322
Anita K. Ghag https://orcid.org/0000-0002-6650-3394

REFERENCES

1. Li L, Lu C, Wang L, et al. Gelatin-based photocurable hydrogels for corneal wound repair. *ACS Appl Mater Interfaces*. 2018;10:13283-13292.
2. Chen F, Le P, Fernandes-Cunha GM, Heilshorn SC, Myung D. Bio-orthogonally crosslinked hyaluronate-collagen hydrogel for suture-free corneal defect repair. *Biomaterials*. 2020;255:120176.
3. Kilic Bektas C, Burcu A, Gedikoglu G, Telek HH, Ornek F, Hasirci V. Methacrylated gelatin hydrogels as corneal stroma substitutes: in vivo study. *J Biomater Sci Polym Ed*. 2019;30:1803-1821.
4. Fernandes-Cunha GM, Chen KM, Chen F, et al. In situ-forming collagen hydrogel crosslinked via multi-functional PEG as a matrix therapy for corneal defects. *Sci Rep*. 2020;10:1-13.
5. Duarte Campos DF, Rohde M, Ross M, et al. Corneal bioprinting utilizing collagen-based bioinks and primary human keratocytes. *J Biomed Mater Res - Part A*. 2019;107:1945-1953.

6. Kim H, Park MN, Kim J, Jang J, Kim HK, Cho DW. Characterization of cornea-specific bioink: high transparency, improved in vivo safety. *J Tissue Eng*. 2019;10:204173141882338.
7. Khosravimelal S, Mobaraki M, Eftekhari S, Ahearne M, Seifalian AM, Gholipourmalekabadi M. Hydrogels as emerging materials for cornea wound healing. *Small*. 2021;17:2006335.
8. Cortina M, de la Cruz J. *Keratoprostheses and Artificial Corneas*. Springer-Verlag; 2015.
9. Fagerholm P, Lagali NS, Merrett K, et al. A biosynthetic alternative to human donor tissue for inducing corneal regeneration: 24-month follow-up of a phase 1 clinical study. *Sci Transl Med*. 2010;2:46ra61.
10. Ferracci G, Zhu M, Ibrahim MS, et al. Photocurable albumin methacryloyl hydrogels as a versatile platform for tissue engineering. *ACS Appl Bio Mater*. 2020;3:920-934.
11. Lee HJ, Fernandes-Cunha GM, Myung D. In situ-forming hyaluronic acid hydrogel through visible light-induced thiol-ene reaction. *React Funct Polym*. 2018;131:29-35.
12. Sharifi S, Islam MM, Sharifi H, et al. Tuning gelatin-based hydrogel towards bioadhesive ocular tissue engineering applications. *Bioact Mater*. 2021;6:3947-3961.
13. Koivusalo L, Kauppila M, Samanta S, et al. Tissue adhesive hyaluronic acid hydrogels for sutureless stem cell delivery and regeneration of corneal epithelium and stroma. *Biomaterials*. 2019;225:119516.
14. Isaacson A, Swioklo S, Connon CJ. 3D bioprinting of a corneal stroma equivalent. *Exp Eye Res*. 2018;173:188-193.
15. Zhang B, Xue Q, Li J, et al. 3D bioprinting for artificial cornea: challenges and perspectives. *Med Eng Phys*. 2019;71:68-78.
16. Tonsomboon K, Oyen ML. Composite electrospun gelatin fiber-alginate gel scaffolds for mechanically robust tissue engineered cornea. *J Mech Behav Biomed Mater*. 2013;21:185-194.
17. Sani ES, Lassaletta AD, Wang X, et al. Engineering a highly elastic human protein–based sealant for surgical applications. *Sci Transl Med*. 2017;9(410):eaai7466.
18. Shirzaei Sani E, Kheirkhah A, Rana D, et al. Sutureless repair of corneal injuries using naturally derived bioadhesive hydrogels. *Sci Adv*. 2019;5:eaav1281.
19. Kim SH, Yeon YK, Lee JM, et al. Precisely printable and biocompatible silk fibroin bioink for digital light processing 3D printing. *Nat Commun*. 2018;9:1-14.
20. Mahdavi SS, Abdekhodaie MJ, Kumar H, Mashayekhan S, Baradaran-Rafii A, Kim K. Stereolithography 3D bioprinting method for fabrication of human corneal stroma equivalent. *Ann Biomed Eng*. 2020;48:1955-1970.
21. Kilic Bektas C, Hasirci V. Cell loaded 3D bioprinted GelMA hydrogels for corneal stroma engineering. *Biomater Sci*. 2020;8:438-449.
22. Tabatabai AP, Kaplan DL, Blair DL. Rheology of reconstituted silk fibroin protein gels: the epitome of extreme mechanics. *Soft Matter*. 2015;11:756-761.
23. Costa JB, Silva-Correia J, Oliveira JM, Reis RL. Fast setting silk fibroin bioink for bioprinting of patient-specific memory-shape implants. *Adv Healthc Mater*. 2017;6:1-8.
24. Holland C, Numata K, Rnjak-Kovacina J, Seib FP. The biomedical use of silk: past, present, future. *Adv Healthc Mater*. 2019;8:1800465.
25. Chirila T, Barnard Z, Zainuddin, Harkin DG, Schwab IR, Hirst LW. Bombyx mori silk fibroin membranes as potential substrata for epithelial constructs used in the management of ocular surface disorders. *Tissue Eng A*. 2008;14:1203-1211.
26. Higa K, Takeshima N, Moro F, et al. Porous silk fibroin film as a transparent carrier for cultivated corneal epithelial sheets. *J Biomater Sci Polym Ed*. 2011;22:2261-2276.
27. Barroso IA, Man K, Villapun VM, Cox SS, Ghag AK. Methacrylated silk fibroin hydrogels: pH as a tool to control functionality. *ACS Biomater Sci Eng*. 2021;7(10):4779-4791.
28. Ghobril C, Grinstaff MW. The chemistry and engineering of polymeric hydrogel adhesives for wound closure: a tutorial. *Chem Soc Rev*. 2015;44:1820-1835.
29. Mohammed S, Chouhan G, Anuforom O, et al. Thermosensitive hydrogel as an in situ gelling antimicrobial ocular dressing. *Mater Sci Eng C*. 2017;78:203-209.
30. Khalil IA, Saleh B, Ibrahim DM, et al. Ciprofloxacin-loaded bioadhesive hydrogels for ocular applications. *Biomater Sci*. 2020;8:5196-5209.
31. Veiga AS, Schneider JP. Antimicrobial hydrogels for the treatment of infection. *Biopolymers*. 2013;100:637-644.
32. Cui X, Soliman BG, Alcala-Orozco CR, et al. Rapid Photocrosslinking of silk hydrogels with high cell density and enhanced shape Fidelity. *Adv Healthc Mater*. 2020;9:1-15.
33. Lim KS, Levato R, Costa PF, et al. Bio-resin for high resolution lithography-based biofabrication of complex cell-laden constructs. *Biofabrication*. 2018;10:034101.
34. Bhattacharjee P, Fernández-Pérez J, Ahearne M. Potential for combined delivery of riboflavin and all-trans retinoic acid, from silk fibroin for corneal bioengineering. *Mater Sci Eng C*. 2019;105:110093.
35. Rafat M, Li F, Fagerholm P, et al. PEG-stabilized carbodiimide crosslinked collagen-chitosan hydrogels for corneal tissue engineering. *Biomaterials*. 2008;29:3960-3972.
36. Guimarães CF, Gasperini L, Marques AP, Reis RL. The stiffness of living tissues and its implications for tissue engineering. *Nat Rev Mater*. 2020;5:351-370.
37. Buitrago JO, Patel KD, El-Fiqi A, et al. Silk fibroin/collagen protein hybrid cell-encapsulating hydrogels with tunable gelation and improved physical and biological properties. *Acta Biomater*. 2018;69:218-233.
38. Ahearne M, Fernández-Pérez J, Masterton S, Madden PW, Bhattacharjee P. Designing Scaffolds for Corneal Regeneration. *Adv Funct Mater*. 2020;30:1908996.
39. Lim KS, Schon BS, Mekhileri NV, et al. New visible-light Photoinitiating system for improved print Fidelity in gelatin-based bioinks. *ACS Biomater Sci Eng*. 2016;2:1752-1762.
40. Pepelanova I, Kruppa K, Scheper T, Lavrentieva A. Gelatin-methacryloyl (GelMA) hydrogels with defined degree of functionalization as a versatile toolkit for 3D cell culture and extrusion bioprinting. *Bioengineering*. 2018;5:55.
41. Andrews JM. Determination of minimum inhibitory concentrations. *J Antimicrob Chemother*. 2001;48:5-16.
42. Randleman JB, Khandelwal SS, Hafezi F. Corneal cross-linking. *Surv Ophthalmol*. 2015;60:509-523.
43. Jeng BH. *Advances in Medical and Surgical Cornea*. Springer-Verlag; 2014. doi:10.1007/978-3-662-44888-5
44. Hammer A, Richoz O, Mosquera SA, Tabibian D, Hoogewoud F, Hafezi F. Corneal biomechanical properties at different corneal cross-linking (CXL) irradiances. *Investig Ophthalmol Vis Sci*. 2014;55:2881-2884.
45. Mobaraki M, Abbasi R, Vandchali SO, Ghaffari M, Moztarzadeh F, Mozafari M. Corneal repair and regeneration: current concepts and future directions. *Front Bioeng Biotechnol*. 2019;7:1-20.
46. Freegard TJ. The physical basis of transparency of the normal cornea. *Eye (Lond)*. 1997;11(Pt 4):465-471.
47. Kotecha A. What biomechanical properties of the cornea are relevant for the clinician? *Surv Ophthalmol*. 2007;52:109-114.
48. Taylor ZD, Garritano J, Sung S, et al. THz and mm-wave sensing of corneal tissue water content: in vivo sensing and imaging results. *IEEE Trans Terahertz Sci Technol*. 2015;5:184-196.
49. Kim SH, Chu CC. Synthesis and characterization of dextran-methacrylate hydrogels and structural study by SEM. *J Biomed Mater Res*. 2000;49:517-527.
50. Hoch E, Hirth T, Tovar GEM, Borchers K. Chemical tailoring of gelatin to adjust its chemical and physical properties for functional bioprinting. *J Mater Chem B*. 2013;1:5675-5685.

51. Hoch E, Schuh C, Hirth T, Tovar GEM, Borchers K. Stiff gelatin hydrogels can be photo-chemically synthesized from low viscous gelatin solutions using molecularly functionalized gelatin with a high degree of methacrylation. *J Mater Sci Mater Med*. 2012;23:2607-2617.
52. Bryant JS, Anseth SK. Hydrogel properties influence ECM production by chondrocytes photoencapsulated in poly(ethylene glycol) hydrogels. *J Biomed Mater Res*. 2002;59:63-72.
53. Assmann A, Vegh A, Ghasemi-Rad M, et al. A highly adhesive and naturally derived sealant. *Biomaterials*. 2017;140:115-127.
54. Frederick S, Brightbill MD, McDonnell PJ, McGhee CNJ, Farjo AA. *Corneal Surgery: Theory Technique and Tissue*. Mosby; 2009.
55. Brunette I, Roberts CJ, Vidal F, et al. Alternatives to eye bank native tissue for corneal stromal replacement. *Prog Retin Eye Res*. 2017;59:97-130.
56. Elsheikh A, Wang D, Brown M, Rama P, Campanelli M, Pye D. Assessment of corneal biomechanical properties and their variation with age. *Curr Eye Res*. 2007;32:11-19.
57. Hatami-Marbini H, Etebu E. Rate dependent biomechanical properties of corneal stroma in unconfined compression. *Biorheology*. 2013;50:133-147.
58. Qin X, Tian L, Zhang H, Chen X, Li L. Evaluation of corneal elastic modulus based on corneal visualization Scheimpflug technology. *Biomed Eng Online*. 2019;18:1-16.
59. Ahearne M, Coyle A. Application of UVA-riboflavin crosslinking to enhance the mechanical properties of extracellular matrix derived hydrogels. *J Mech Behav Biomed Mater*. 2016;54:259-267.
60. Engler AJ, Sen S, Sweeney HL, Discher DE. Matrix elasticity directs stem cell lineage specification. *Cell*. 2006;126:677-689.
61. Wang Z, Kumar H, Tian Z, et al. Visible light Photoinitiation of cell-adhesive gelatin Methacryloyl hydrogels for Stereolithography 3D bioprinting. *ACS Appl Mater Interfaces*. 2018;10:26859-26869.
62. Murphy CM, Haugh MG, O'Brien FJ. The effect of mean pore size on cell attachment, proliferation and migration in collagen-glycosaminoglycan scaffolds for bone tissue engineering. *Biomaterials*. 2010;31:461-466.
63. Murphy CM, O'Brien FJ. Understanding the effect of mean pore size on cell activity in collagen-glycosaminoglycan scaffolds. *Cell Adhes Migr*. 2010;4:377-381.
64. Silva SS, Popa EG, Gomes ME, et al. Silk hydrogels from non-mulberry and mulberry silkworm cocoons processed with ionic liquids. *Acta Biomater*. 2013;9:8972-8982.
65. Fleischer S, Shapira A, Regev O, Nseir N, Zussman E, Dvir T. Albumin fiber scaffolds for engineering functional cardiac tissues. *Biotechnol Bioeng*. 2014;111:1246-1257.
66. Sariri R, Ghafoori H. Tear proteins in health, disease, and contact lens wear. *Biochemistry*. 2008;73:381-392.

SUPPORTING INFORMATION

Additional supporting information may be found in the online version of the article at the publisher's website.

How to cite this article: Barroso IA, Man K, Hall TJ, et al. Photocurable antimicrobial silk-based hydrogels for corneal repair. *J Biomed Mater Res*. 2022;110(7):1401-1415. doi:10.1002/jbm.a.37381

bioengineering

MDPI

Article

Photocurable GelMA Adhesives for Corneal Perforations

Inês A. Barroso, Kenny Man, Thomas E. Robinson, Sophie C. Cox and Anita K. Ghag *

School of Chemical Engineering, University of Birmingham, Birmingham B15 2TT, UK; IXP799@student.bham.ac.uk (I.A.B.); k.l.man@bham.ac.uk (K.M.); TER281@student.bham.ac.uk (T.E.R.); S.C.Cox@bham.ac.uk (S.C.C.)

* Correspondence: a.k.ghag@bham.ac.uk

Abstract: The current treatments for the management of corneal and scleral perforations include sutures and adhesives. While sutures are invasive, induce astigmatism and carry a risk of infection, cyanoacrylate glues are toxic, proinflammatory and form an opaque and rough surface that precludes vision. Consequently, the clinical need for a fast curing and strong tissue adhesive with minimised cytotoxicity and host inflammation remains unmet. In this paper, we engineer a gelatine methacryloyl (GelMA) adhesive that can be crosslinked in situ within 2 min using UV or visible light and a riboflavin (RF)/sodium persulfate (SPS) system. Optical coherence tomography (OCT) images demonstrated that the flowable GelMA adhesive could completely fill corneal wounds and restore the ocular curvature by forming a smooth contour on the ocular surface. Further, ex vivo studies in porcine eyes showed that GelMA bioadhesives exhibited burst pressures that were comparable to cyanoacrylates (49 $\pm$ 9 kPa), with the hydrogels exhibiting a transmittance (90%), water content (85%) and storage modulus (5 kPa) similar to the human cornea. Finally, using human dermal fibroblasts, we showed that our GelMA adhesive was non-toxic and could effectively support cell adhesion and proliferation. Taken together, the adhesive's performance, injectability and ease of administration, together with gelatin's availability and cost-effectiveness, make it a potential stromal filler or sealant for corneal and conjunctival applications.

Keywords: adhesives; cornea; gelatin

check for updates

Citation: Barroso, I.A.; Man, K.; Robinson, T.E.; Cox, S.C.; Ghag, A.K. Photocurable GelMA Adhesives for Corneal Perforations. *Bioengineering* **2022**, *9*, 53. https://doi.org/10.3390/bioengineering9020053

Academic Editor: Dimitrios Karamichos

Received: 29 November 2021
Accepted: 19 January 2022
Published: 28 January 2022

Publisher's Note: MDPI stays neutral with regard to jurisdictional claims in published maps and institutional affiliations.

Copyright: © 2022 by the authors. Licensee MDPI, Basel, Switzerland. This article is an open access article distributed under the terms and conditions of the Creative Commons Attribution (CC BY) license (https://creativecommons.org/licenses/by/4.0/).

1. Introduction

Globally, corneal blindness is estimated to affect approximately 23 million people, with an estimated 1.5 million new cases per year [1,2]. Corneal wounds and perforations can arise from infections, traumatic injuries, surgical procedures (e.g., cataract surgery), autoimmune diseases (e.g., ulcerative keratitis) or degenerative disorders [3,4]. Full-thickness corneal injuries can leak and allow the ingress of pathogens into the eye. Therefore, given the risk of ocular morbidity and vision loss, corneal perforations are considered surgical emergencies [5]. Currently, the sealing of corneal wounds remains challenging for surgeons and sutures are still the gold standard treatment for the closure of ocular wounds due to their high tensile strength [5,6]. However, sutures are time consuming to position, inflict additional trauma to the tissues, can act as a nidus for infection, induce astigmatism and often require secondary removal procedures [2,7,8].

In contrast, tissue adhesives are an appealing alterative to the use of sutures. Tissue adhesives exhibit lower infection rates, can be delivered through smaller applicators and form a continuous seal, adapting to the wound morphology and distributing the load, thereby decreasing scarring [9,10]. The development of an effective and safe tissue adhesive could reduce surgical and hospitalisation time, lower the incidence of complications and reduce leakage from wounds [2]. Specifically, the ideal material to repair corneal perforations must be optically clear to allow vision, exhibit strong adhesive properties to the naturally moist ocular surface, provide healing enhancement without scarring or vascularisation and have a rapid in situ crosslinking after application [2,10–14]. Nowadays, ocular adhesives

can be divided into two main groups: naturally derived (e.g., fibrin-based) and synthetic adhesives (e.g., cyanoacrylate and PEG-based) [4].

In ocular surgery, fibrin sealants have been used to seal corneal perforations (with and without an amniotic membrane), lens capsule lacerations and to repair leaking blebs [4,15]. Fibrin glues are biodegradable, easy to apply and show minimal toxicity together with improved comfort. The main drawbacks of these bioinspired glues are the potential risk of disease transmission and fast degradation in vivo (within days to weeks), which limits its use and/or requires re-application. Currently, fibrin-based adhesives are mainly used for amniotic membrane fixation [4,15,16]. Although cyanoacrylate-based adhesives (CAs) are not FDA approved for ophthalmic use, these adhesives have been used off-label in the eye for several decades [17,18]. In ocular surgery, CAs are reported to be toxic, proinflammatory and are associated with many postoperative complications, such as keratitis [19,20], unintentional entry into the anterior chamber [21,22], corneal neovascularization and scar formation [4,16,23]. Nonetheless, CAs remain a useful tool in the treatment of ocular surgical emergencies due to their quick preparation, easy application and effective and secure performance. Another class of synthetic tissue adhesives are based on the FDA-approved polymer poly(ethylene glycol) (PEG). PEG-based adhesives are safe, well tolerated, elastic and biodegradable, work independently of the clotting cascade, do not carry risks of disease transmission and some formulations remain in situ longer than fibrin sealants [24,25]. ReSure (Ocular Therapeutix, Bedford, MA, USA) and OcuSeal (BD Medical, Le Pont de Claix, France) are approved for sealing corneal incisions. However, despite being useful to reinforce suture sealing and close corneal incisions, these adhesives are not appropriate to function as stromal fillers due to poor mechanical properties, high swelling rates and short in vivo retention [24,26,27].

Over the last decade, several polymers have been studied in an effort to develop novel tissue adhesives, such as alginate [28,29], chondroitin sulphate [30], chitosan [28,31,32], tropoelastin [33], gelatine [11,13,34–37], poly(acrylamide-methyl acrylate-acrylic acid) [38] and N-iso-propylacrylamide copolymerized with butylacrylate [39]. However, currently the clinical needs are still unmet with no materials specifically approved for the filling and repair of corneal defects [40].

Gelatine is a promising biomaterial for the repair of corneal defects given its availability, cost-effectiveness, water solubility and presence of both cell-binding sites (e.g., RGD peptide sequence) and matrix metalloproteinase (MMPs) motifs that promote cellular adhesion and allow enzymatic degradation, respectively [41,42]. However, it requires modification to enable mechanical tailoring via chemical crosslinking. Once methacrylic/methacryloyl groups (GelMA) are introduced, these bioadhesives can be photocrosslinked under physiological conditions within seconds. The final adhesive properties can be tailored by changing the initial gel strength of raw gelatine (Bloom factor), the degree of methacryloyl functionalisation (DF%), polymer concentration, light characteristics and time. Recently, GelMA-based adhesives photocrosslinked using type I photoinitiators, such as LAP (Lithium phenyl-2,4,6 trimethylbenzoylphosphinate) [36] and Irgacure-2959 [11,13,35,43], or type II photoinitiators, such as ruthenium/SPS [34], RF/TEA (triethanolamine) [44] and Eosin Y/VC(N-vinylcaprolactam)/TEA [37,45–48], have been investigated for different applications. In ocular surgery, there have been studies on the development of GelMA adhesives/hydrogels to be photocrosslinked in situ [13,37,45,48] or implanted after curing [35].

In this paper, we develop an optically clear and injectable gelatine-based adhesive that can seal corneal defects. In this work, we use RF as a photoinitiator since it is already being used in corneal crosslinking (CXL), an FDA-approved procedure to treat patients with post laser in situ keratomileusis (LASIK) ectasia and progressive corneal thinning (keratoconus) [49,50]. Furthermore, RF is a naturally occurring photosensitive molecule (vitamin B2) and absorbs light in both the UV (365 nm) and visible range [51]. In this study, GelMA bioadhesives of different polymer concentrations are crosslinked using UV or visible light and a photoinitiator system composed by RF and SPS: 15 (w/v)% and

20 (*w*/*v*)% GelMA crosslinked with visible light (referred as 15% and 20%, respectively) and 20 (*w*/*v*)% GelMA crosslinked with UV light (20% UV).

To our knowledge, this is the first work investigating GelMA hydrogel formation via riboflavin/SPS mediated photocrosslinking. As shown in Figure 1, the physicochemical, adhesive, and biological properties of GelMA bioadhesives are characterised. Briefly, we conclude that GelMA bioadhesives can be injected in situ and rapidly seal full-thickness corneal perforations (≤2 min). The adhesives restored the corneal curvature by forming a smooth and transparent seal, while withstanding intraocular pressures comparable to Histoacryl (33–50 kPa). The versatility of the semi-synthetic bioadhesives developed in this study to function on dry, semi-dry and wet substrates make them suitable to be applied not only for sealing corneal and conjunctival lacerations, but also in different physiological conditions (e.g., skin).

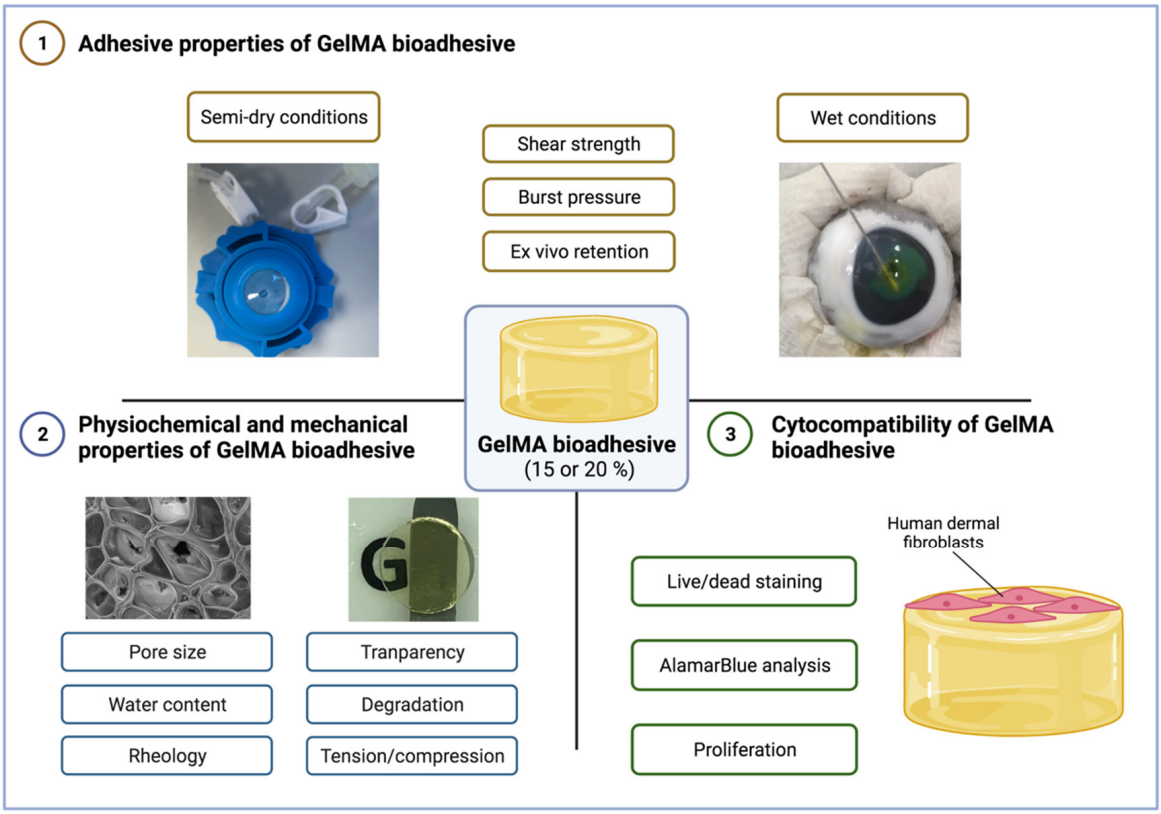


Figure 1. Schematic outline investigating the properties of GelMA bioadhesives. Figure created with BioRender.com (last accessed 8 November 2021).

2. Materials and Methods

2.1. GelMA Synthesis

Briefly, a 10% (*w*/*v*) gelatine type A solution (porcine skin, 300 bloom strength, Sigma-Aldrich, Gillingham, UK) was dissolved in phosphate-buffered saline (PBS, Sigma-Aldrich, Gillingham, UK) at 60 °C for 30 min. Methacrylic anhydride (MA, Sigma-Aldrich, Gillingham, UK) was added to the gelatine solution to a final concentration of 6% (*v*/*v*) and left to react for 2 h at 50 °C under vigorous stirring. After the reaction period, the solution was transferred to 50 mL tubes and the unreacted MA was partially removed by centrifugation at 3500 rpm for 5 min at room temperature. The solution was then dialysed against distilled water for 7 days at 37 °C using 12–14 kDa cut-off dialysis tubes (Thermo Scientific, Paisley, UK). After dialysis, the GelMA solution was diluted to 2% (*w*/*v*) and the pH adjusted to 7.4 using 1 mM sodium hydroxide solution (Sigma-Aldrich, Gillingham, UK). Lastly, GelMA solutions were lyophilised for 2 days to generate a white porous foam, which was stored at −80 °C until further use.

2.2. Degree of Functionalisation

The degree of functionalisation (DF%) was quantified by proton nuclear magnetic resonance (^{1}H-NMR). Briefly, 5 mg of GelMA was dissolved in 600 µL deuterium oxide (Sigma-Aldrich, Gillingham, UK). The ^{1}H-NMR spectra of raw gelatine and GelMA were recorded using a 400 MHz spectrometer (Brucker, Billerica, MA, USA). Baseline and phase correction were applied before integrating the peaks of interest with Topspin software (Brucker, Billerica, MA, USA). The phenylalanine signal (7.2–7.5 ppm) was used as the internal reference to normalise the amine signals (3.13–3.22 ppm) of lysine [52]. As MA reacts with gelatine through the primary amines on lysine residues, the extent of substitution was calculated by normalisation to the number of free amino groups of raw gelatine. The degree of functionalisation was calculated using the following equation:

$$\mathrm{DF}(\%) = \frac{\text{lysine integration signal of GelMA}}{\text{lysine integration signal of Gelatin}} \times 100 \quad (1)$$

2.3. Preparation of GelMA Bioadhesives

GelMA prepolymer solutions were prepared by dissolving an appropriate amount of polymer in PBS at 60 °C for 30 min. Fresh stock solutions of 40 mM phosphated riboflavin (RF, Sigma-Aldrich, Gillingham, UK) and 456 mM sodium persulfate (SPS, Sigma-Aldrich, Gillingham, UK) in PBS were prepared. The photoinitiator system RF/SPS was added to the GelMA solution to a final concentration of 2/20 mM and the resulting solution was vigorously mixed at 60 °C. The hydrogel precursor solutions were photocured using 30 mW/cm^2 UV light with an OmniCure S1500 (Excelitas Technologies, Ontario, Canada) with a 365 nm filter or using 100 mW/cm^2 visible light (Knightsbridge FLF Floodlight, RS, Corby, UK). Briefly, 200 µL of GelMA prepolymer solution was pipetted onto a 12 mm cylindrical mould and then exposed to light for 2 min. In this work, three different formulations were tested: 15 (*w*/*v*)% and 20 (*w*/*v*)% GelMA crosslinked with visible light (referred as 15% and 20%, respectively) and 20 (*w*/*v*)% GelMA crosslinked with UV light (20% UV).

2.4. Adhesive Properties

2.4.1. Ex Vivo Burst Pressure

The ability of engineered adhesives to seal corneal perforations was assessed on wet and dry conditions. Porcine eyes were chosen as an ex vivo model due to their availability, which allowed freshly enucleated eyes to be obtained from a local butcher on a daily basis. To study adhesion on wet conditions, a full-thickness incision was created on the porcine eyeball using a 2 mm biopsy punch and 20 µL of GelMA adhesive or Histoacryl (control group, B. Braun Surgical S.A., Barcelona, Spain) was added to the perforation and cured in situ. Then, the sealed eyes were connected to a pressure testing system (Figure 2b) through the insertion of a 27-gauge needle into the anterior chamber of a porcine eyeball. Finally, a syringe pump (SINO SN-50F66, SINO MDT, Shenzhen, China) injected PBS mixed with fluorescein (Sigma-Aldrich, Gillingham, UK) into the anterior chamber at a rate of 20 mL/h, while a wireless pressure sensor (PASCO, Roseville, CA, USA) recorded the intraocular pressure. The test was stopped at adhesive failure or when the pressure reached 50 kPa (n = 8). The burst pressure on dry conditions was studied by mounting a porcine cornea with a 2 mm full-thickness perforation on a Barron artificial anterior chamber (AAC, Katena, Parsippany, New Jersey, USA) (Figure 2b). The burst pressure was measured as previously described (n = 8).

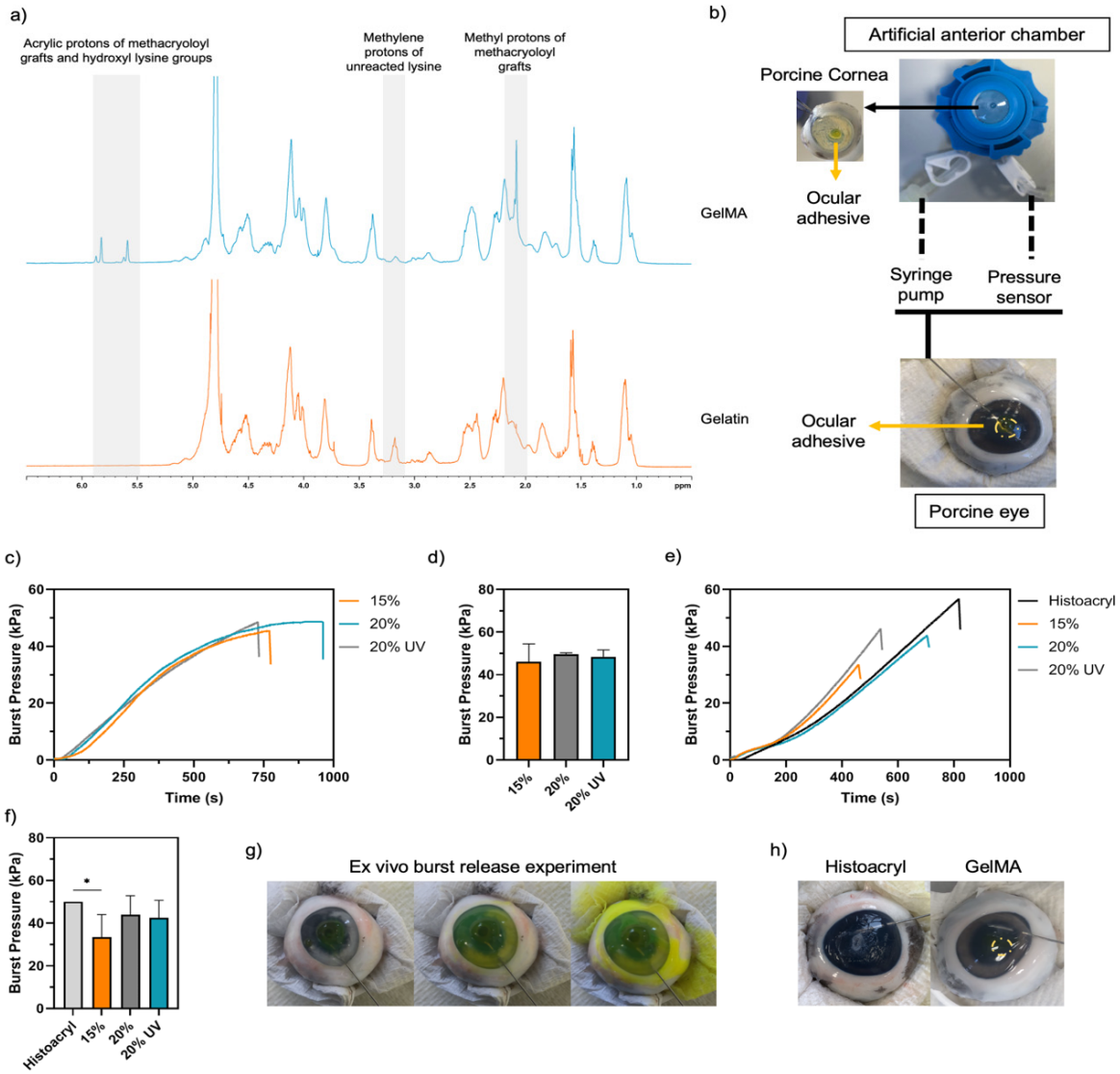


Figure 2. (**a**) ^{1}H-NMR spectra of GelMA (top) and unfunctionalized gelatine (bottom). Ex vivo burst pressure of GelMA adhesives. (**b**) Schematic of the ex vivo burst pressure measurement set-up. A Barron artificial anterior chamber was used to assess the GelMA adhesion in semi-dry conditions. A porcine cornea with a 2 mm full-thickness injury was mounted on the chamber. To simulate the in vivo conditions, a full-thickness injury in a porcine eyeball was sealed with GelMA adhesive. In both systems, a fluorescein solution was injected using a syringe pump until bursting. (**c**) Representative pressure curves of the studied groups when the cornea was mounted in the artificial anterior chamber. (**d**) Mean burst pressure of GelMA adhesives in the artificial anterior chamber (n = 8). (**e**) Representative pressure curves of the studied groups and Histoacryl glue in the porcine eyeball. (**f**) Mean burst pressure of GelMA adhesives and Histoacryl glue in the porcine eyeball (n = 8). (**g**) Porcine eyeball before, during and after the burst pressure experiment. (**h**) Appearance of full-thickness corneal injuries sealed with Histoacryl and GelMA. Data presented as mean value ± SD (* $p < 0.05$).

2.4.2. Lap Shear Strength

The shear strength of GelMA adhesives and Histoacryl (control group, B. Braun Surgical S.A., Barcelona, Spain) was tested according to the modified ASTM F2255-05 standard for tissue adhesives using an Instron 5542 mechanical tester (Instron, Norwood, MA, USA) with a 2 kN load cell. As substrate, two pieces of glass slides (50 × 10 mm) were coated with 20% (w/v) gelatine solution (porcine, 300 bloom, Sigma-Aldrich, Gillingham, UK) at 60 °C

and left to dry at room temperature overnight. Then, 20 µL of prepolymer solution was crosslinked between two gelatine-coated glass slides (total area = 100 mm^2). The two glass slides were placed between two pieces of double-sided tape, fastened to the instrument's tension grips and extended with a strain rate of 2 mm/min (Figure 3a). The shear strength of the adhesives was calculated at the detachment point on dry and wet substrates (n = 7).

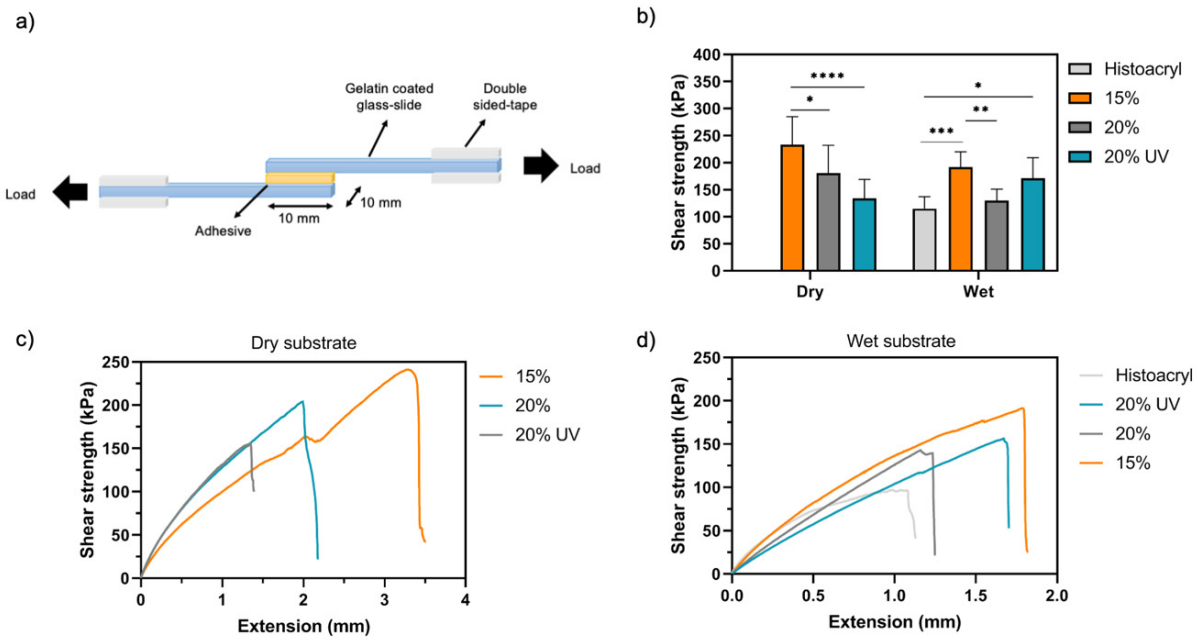


Figure 3. In vitro shear strength of GelMA adhesives: (**a**) Schematic of the lap shear strength test and (**b**) mean shear strength of GelMA bioadhesives and Histoacryl in wet and dry conditions. (**c**,**d**) Representative stress–strain curves of GelMA hydrogels and Histoacryl in dry and wet substrates, respectively. Data presented as mean value ± SD (* $p < 0.05$, ** $p < 0.01$, *** $p < 0.001$, **** $p < 0.0001$).

2.5. Transparency

Light absorbance of hydrogels in the visible range was measured using a microplate reader (Spark Multimode, Tecan, Männedorf, Switzerland). The measurements were carried out in triplicate using GelMA hydrogels in PBS (diameter = 12 mm, thickness = 1.2 mm), with pure PBS serving as a blank control. Subsequently, the transmittance was calculated using the following equation:

$$\text{Transmittance } (\%) = 10^{2-\text{Absorbance}} \quad (2)$$

2.6. Swelling Properties

Immediately after preparation, three samples (diameter = 12 mm, thickness = 1.2 mm) from each condition were freeze dried ($m_{t0,dry}$) and three samples were hydrated in PBS and placed in an incubator at 32 °C. After 24 h, the samples were blotted dry using a filter paper and the swollen weight ($m_{swollen}$) was measured. Finally, the swollen hydrogels were lyophilised and weighed to determine the dry sample weight ($m_{swollen,dry}$). The mass loss is a measurement of the macromers not crosslinked in the hydrogel network [53]. The water content and mass loss were calculated according to the following equations:

$$\text{Water content } (\%) = \frac{m_{swollen} - m_{t0,dry}}{m_{swollen}} \times 100 \quad (3)$$

$$\text{Mass loss} = \frac{m_{t0,dry} - m_{swollen,dry}}{m_{t0,dry}} \times 100 \quad (4)$$

2.7. Enzymatic Degradation

Disc-shaped hydrogels (diameter = 6 mm, thickness = 2 mm) were prepared as previously described. After photocrosslinking, five samples of each group were immediately freeze dried to calculate the initial weight. To determine the in vitro degradation, 5 samples of each group were placed in 1.5 mL tubes with 1 mL of 1 U/mL collagenase II in PBS (Thermo Fisher Scientific, Waltham, MA, USA) or in 1 mL PBS (control group) and incubated at 37 °C for 1, 3 and 7 days. At the end of the incubation period the hydrogels were lyophilised. The degradation was calculated using the following equation:

$$\text{Degradation } (\%) = \frac{m_{t0,dry} - m_{dry}}{m_{dry}} \times 100 \quad (5)$$

2.8. Micro Computed Tomography

Freeze-dried hydrogels were scanned using a Skyscan 1172 (Bruker, Billerica, MA, USA) with 80 kV beam voltage and 100 µA current, 140 ms exposure per projection, 12.99 µm pixel size, rotation step 0.6° and 4 frame averaging. The same parameters were used for all scans. The XY projections were reconstructed into a 3D model using NRecon (Bruker). A cylindrical volume of interest was taken in the centre of each sample, excluding any outside space. A binary threshold was then applied to this volume of interest to separate polymer material and air in the pores of the sample. The pore size distribution was then calculated using the 3D analysis software in CTAn (Bruker). Sample reconstructions were visualized in 3D using CTVox (Bruker). The experiments were conducted in triplicate.

2.9. Scanning Electron Microscopy

Scanning electron microscopy (SEM) was used to assess the morphology of the surface of the freeze-dried hydrogels. All samples (diameter = 6 mm, thickness = 2 mm) were mounted onto aluminium stubs using carbon tape and gold sputter coated. Images were captured using a TM3030Plus benchtop SEM (Hitachi High Technologies, Schaumburg, IL, USA) at an electron acceleration voltage of 15 kV.

2.10. Rheological Characterisation

The viscoelastic properties of the hydrogels were investigated via rheometry. The storage modulus and loss modulus of freshly prepared hydrogels were measured in oscillatory mode at 32 °C using a plate–plate geometry and a 1.2 mm gap between plates (Kinexus Pro+, Malvern Instruments, Malvern, UK). A frequency sweep was conducted between 0.01–10 Hz at 0.5% shear strain. The experiments were conducted in triplicate. The damping factor (tan δ) was calculated using the following equation:

$$\tan\ \delta = \frac{G''}{G'} \quad (6)$$

2.11. Mechanical Characterisation

2.11.1. Compressive Modulus

Cyclic testing was performed using an Instron 5542 mechanical tester (Instron, Norwood, MA, USA) with a 2 kN load cell. Cylindrical hydrogels were prepared as previously described and incubated in PBS for 4 h prior to testing. The dimensions of the samples were determined using a digital calliper. Compressive tests were performed at a rate of 1 mm/min up to a maximum strain of 60% of the original height by performing 8 cycles of loading and unloading. The compressive strain (mm) and load (N) was recorded using Bluehill 3 software (Instron, Norwood, MA, USA). The compressive moduli were calculated from the slope of the linear region on the stress (kPa) versus strain (mm/mm) curves. Samples were tested in triplicate for each condition.

2.11.2. Tensile Modulus

Uniaxial tensile testing was performed using an Instron 5542 mechanical tester (Instron, Norwood, MA, USA) with a 100 N load cell. Hydrogels were prepared as previously described in dog-bone shaped moulds (width = 4 mm, gauge length = 10 mm) and incubated in PBS for 4 h prior to testing. After measuring the swollen sample dimensions using a digital calliper, hydrogels were placed between two pieces of double-sided tape, fastened to the instrument's tension grips and extended at a rate of 2 mm/min until failure. The load (N) and tensile strain (mm) were measured using Bluehill 3 software and the tensile modulus was calculated from the slope of the stress–strain curves. The tensile strength and maximum elongation were obtained at point of failure. At least five samples were tested for each condition.

2.12. Ex Vivo Retention Time

Freshly enucleated porcine eyes were obtained from a local butcher. After the creation of a 5 mm corneal defect with a biopsy punch (50% deep), 10 µL of prepolymer solution were applied to the defect site and photocrosslinked. OCT imaging was used to assess the ability of the engineered adhesives to fill the corneal defect and adhere to the corneal stroma immediately after photocrosslinking (t_0) and to study the dimensional stability and retention time of the hydrogels after incubation. Samples were imaged with a Telesto II SD-OCT System (Thorlabs, Lübeck, Germany) at t_0 and after 1, 3 and 7 days of incubation in 20 mL of PBS with 5% penicillin/streptomycin (Sigma-Aldrich, Gillingham, UK) at 4 °C.

2.13. In Vitro Cytocompatibility of GelMA Hydrogels

Human dermal fibroblasts (HDFs, ATCC, USA Passage number 9) were cultured in Dulbecco's modified eagle medium (DMEM, Sigma-Aldrich, Gillingham, UK) and supplemented with 10% foetal bovine serum (Sigma-Aldrich, Gillingham, UK), 1% penicillin/streptomycin (Sigma-Aldrich, Gillingham, UK) and 2 mM L-glutamine (Sigma-Aldrich, Gillingham, UK). All cultures were maintained in tissue culture treated polystyrene flasks at 37 °C with 5% CO_2 in a humidified incubator and passaged at 80% confluency.

2.13.1. 2D Cell Seeding on GelMA Gels

GelMA pre-polymer solutions were prepared, UV sterilised and photocrosslinked as previously described in 48-well suspension cell culture plates (Sarstedt, Nümbrecht, Germany). After curing, 100 µL of DMEM was added to the hydrogels to prevent dehydration. One hour before cell seeding, the hydrogel matrices were partially dried to potentiate cell penetration. Then, 60 µL of cell suspension was added dropwise onto each hydrogel (9×10^3 cells per scaffold) and samples were incubated for 1 h at 37 °C with 5% CO_2 to bolster cell adhesion. After 1 h, DMEM was carefully added to the wells without disturbing the cell-laden hydrogels [54]. The culture medium was changed every two days.

2.13.2. Cell Viability

Cell viability was evaluated using a live/dead assay (Thermo Fisher Scientific, Waltham, MA, USA) following the manufacturer's protocol. Briefly, SYTO 10 green fluorescent nucleic acid stain (2 µL/mL) and ethidium homodimer-2 nucleic acid stain (2 µL/mL) were diluted in PBS to form the staining solution. At each time point, the samples were incubated with the staining solution for 15 min in the dark at 37 °C. The staining solution was removed, and the samples were washed twice with PBS. The cell-seeded hydrogels were imaged with a confocal scanning microscope (Zeiss LSM710, Carl Zeiss, Jena, Germany).

2.13.3. Metabolic Activity

Alamar Blue assay (Thermo Fisher Scientific, Waltham, MA, USA) was used to determinate the relative metabolic activity according to the manufacturer's directions. In short, the samples were incubated with 0.5 mL of 10% Alamar Blue reagent in culture medium for 4 h at 37 °C with 5% CO_2. Thereafter, 50 µL of cell culture medium were

transferred to a 96-well plate (Corning, Corning, NY, USA) and the fluorescence intensity was measured with a microplate reader (Spark Multimode, Tecan, Männedorf, Switzerland) using an excitation wavelength of 540 nm and an emission wavelength of 590 nm. Acellular hydrogels were used as a negative control and their fluorescence was subtracted from the same group seeded hydrogels to account for the background ($n \geq 4$).

2.13.4. Cell Proliferation

DNA content was quantified using the Quant-iT PicoGreen DNA assay (Life Technologies, Paisley, UK). Briefly, cell-laden hydrogels were lysed in 0.1% TritonTM X-100 in PBS (Sigma-Aldrich, Gillingham, UK) via performing freeze–thaw cycles between 37 °C and –80 °C. After spinning down the samples at 300 g for 5 min to remove non-genomic material, 10 µL of cell lysate was added to 90 µL of TE (10 mM Tris-HCl, 1 mM EDTA) buffer in a 96-well plate (Corning, Corning, NY, USA). A total of 100 µL of PicoGreen was added to all samples and then incubated for 5 min. The fluorescence intensity was then measured with a microplate reader (Spark Multimode, Tecan, Männedorf, Switzerland) at an excitation and emission wavelength of 480 and 520 nm, respectively.

2.14. Statistical Analysis

For each experiment, at least three samples were tested. One or two-way analysis of variance (ANOVA) and Tukey's test were used to determine statistically significant differences with GraphPad Prism 8.0 software (GraphPad Software, San Diego, CA, USA). The level of significance was set at $p < 0.05$. Data are presented as mean value ± standard deviation (SD).

3. Results

3.1. Synthesis of GelMA Bioadhesives

^{1}H-NMR spectroscopy was used to confirm the methacryloyl functionalisation of GelMA (Figure 2a). The ^{1}H-NMR of GelMA displays peaks in the 5–6 ppm range and at ~1.8 ppm, corresponding to the acrylic protons of methacryloyl of lysine and hydroxyl lysine groups and the methyl proton of methacryloyl grafts, respectively [55–57]. These groups are absent in the spectra of unmodified gelatine, indicating the covalent functionalisation of gelatine with the methacryloyl groups. The marked decrease in the free lysine signal at 3.1–3.2 ppm indicated that the DF% was 60% after 2 h reaction with 6% (*v*/*v*) MA.

3.2. Adhesive Properties of GelMA Bioadhesives

The success of a bioadhesive depends on its adhesion and retention at the wound site [29]. In this study, burst pressure and lap shear tests were performed to characterise the GelMA bioadhesive properties in semi-dry and wet conditions. A cyanoacrylate-based adhesive (Histoacryl, B. Braun Surgical S.A., Barcelona, Spain) was used as a positive control due to its off-label application in surgical emergencies involving corneal perforations. To quantitively assess the mechanical adhesion of GelMA bioadhesives to the corneal tissue under liquid pressure, GelMA formulations were tested using two different set-ups: an artificial anterior chamber (AAC) and a porcine eye (Figure 2b,g). In the first method, after making a 2 mm full-thickness central injury, the cornea is removed with a scalpel and mounted on the AAC. As only the cornea is mounted on the AAC, this method tests the corneal adhesive performance in a semi-dry environment. However, since liquids at the wound–adhesive interface are a barrier to strong surface bonding and, in case of a corneal perforation, the eye leaks aqueous humour, the performance of GelMA bioadhesives was also studied in the porcine eyeball with a full-thickness perforation. This experimental setup is closer to the real situation and represents the worst-case scenario. In both systems, a fluorescein solution was progressively injected until bursting or reaching the pump's maximum pressure of 50 kPa. The average burst pressure of GelMA bioadhesives on the AAC was between 46 ± 8 and 50 ± 1 kPa. The difference was not statistically significant between the groups ($p > 0.05$) (Figure 2c,d). As expected, the burst pressures obtained

when sealing corneal injuries on the porcine eyeball were lower than in the AAC, with 15%, 20% and 20% UV GelMA bioadhesives exhibiting burst pressures of 33 ± 11, 49 ± 9 and 48 ± 8 kPa, respectively, while Histoacryl had a burst pressure superior to 50 kPa (Figure 2e,f). However, only 15% GelMA and the control were statistically significant ($p < 0.05$). Despite showing high adhesive strength on wet substrates, Histoacryl showed no adhesion onto semi-dry corneal tissue. Furthermore, when this glue was used an opaque and rough patch formed, while GelMA formed a smooth and transparent seal that could restore the curvature of the cornea (Figure 2h). Finally, we observed that the bioadhesive failure position was generally on the interface between the hydrogel and the cornea, suggesting that the adhesion force is lower than the adhesive strength.

Next, lap shear tests were used to investigate the adhesion strength of GelMA bioadhesives to wet and dry substrates (Figure 3a). In line with the results obtained in the burst pressure experiment, when a liquid layer is present on the interface between the substrate and the adhesive, lower shear strengths were obtained for all the groups tested (Figure 3b). However, the minimum strength at break was around 130 kPa for both conditions tested. More specifically, the highest shear strength on dry conditions was obtained for 15% (233 ± 52 kPa), which was significantly higher than 20% (181 ± 51 kPa, $p < 0.05$) and 20% UV (134 ± 35 kPa, $p < 0.0001$). Histoacryl failed to glue the dry gelatine-coated glass slides (Figure 3b,c). On a wet substrate, Histoacryl exhibited a shear strength of 115 ± 22 kPa, which was significantly lower than the results obtained for 15% (192 ± 28 kPa, $p < 0.001$) and 20% UV (171 ± 38 kPa, $p < 0.05$) (Figure 3b,d). Finally, the GelMA bioadhesive failure was caused by hydrogel detachment from the gelatine coating as residual GelMA could be found on one side of the gelatine-coated glass slide after the test (delamination).

3.3. Physicochemical Characterisation of GelMA Bioadhesives

The optical transparency of GelMA bioadhesives over time is shown in Figure 4a. After photocrosslinking, 15 and 20% GelMA adhesives were macroscopically clear and lightly yellow, with an optical transmittance of ~62 ± 0.5% (Figure 4b). As riboflavin leaches out from the matrices, the transmittance of GelMA adhesives progressively increased and, after 3 and 24 h, it was approximately 86 ± 0.5% and 91 ± 0.5%, respectively, for both 15 and 20% GelMA adhesives. However, 20% UV samples were not optically clear, showing a maximum transparency of 64.2 ± 11% (Figure 4a,b). The optical transmittance of 20% UV was significantly lower than 15 and 20% at all time points ($p < 0.0001$).

To determine the water content, mass loss and the percentage of expansion, 15, 20 and 20% UV GelMA bioadhesives were incubated in PBS at the ocular temperature for 24 h. The water content was shown to be higher than 84% throughout all groups studied; however, 20% UV (84.1 ± 0.3%) displayed a significantly lower water content than 15% (85.1 ± 0.5%, $p < 0.01$) and 20% (85.5 ± 0.3%, $p < 0.001$) samples (Figure 4c). Moreover, regardless of polymer concentration or light source used, no significant differences were observed in the percentage of uncrosslinked monomers within the hydrogel network (mass loss = 3–5%) (Figure 4d). This result, together with the fact that the material was easily handled in the swollen state (Figure 4b) and no residual uncured solution could be observed in the mould after curing, suggest complete crosslinking [53]. The expansion of GelMA bioadhesives in PBS was not statistically different between groups, despite ranging from 7.3 ± 0.6% to 10.0 ± 0.9% for 15 and 20% GelMA bioadhesives, respectively ($p > 0.05$) (Figure 4e). Finally, as shown in Figure 4f, GelMA bioadhesives displayed minimal volume changes and high dimensional stability in the swollen state.

The susceptibility of GelMA bioadhesives to enzymatic degradation was studied in vitro by incubating the hydrogels in 1 U/mL collagenase II for up to 7 days. As shown in Figure 4g, our results show that there was a time-dependent increase in degradation. After 1 and 2 days, the GelMA bioadhesive degradation was around 39% and 55%, respectively. Although no significant differences were observed between the studied groups, after 7 days, 15% bioadhesives (78 ± 9%) showed a degradation that was around ~10% higher than 20% (66 ± 5%) and 20% UV (68 ± 7%) samples.

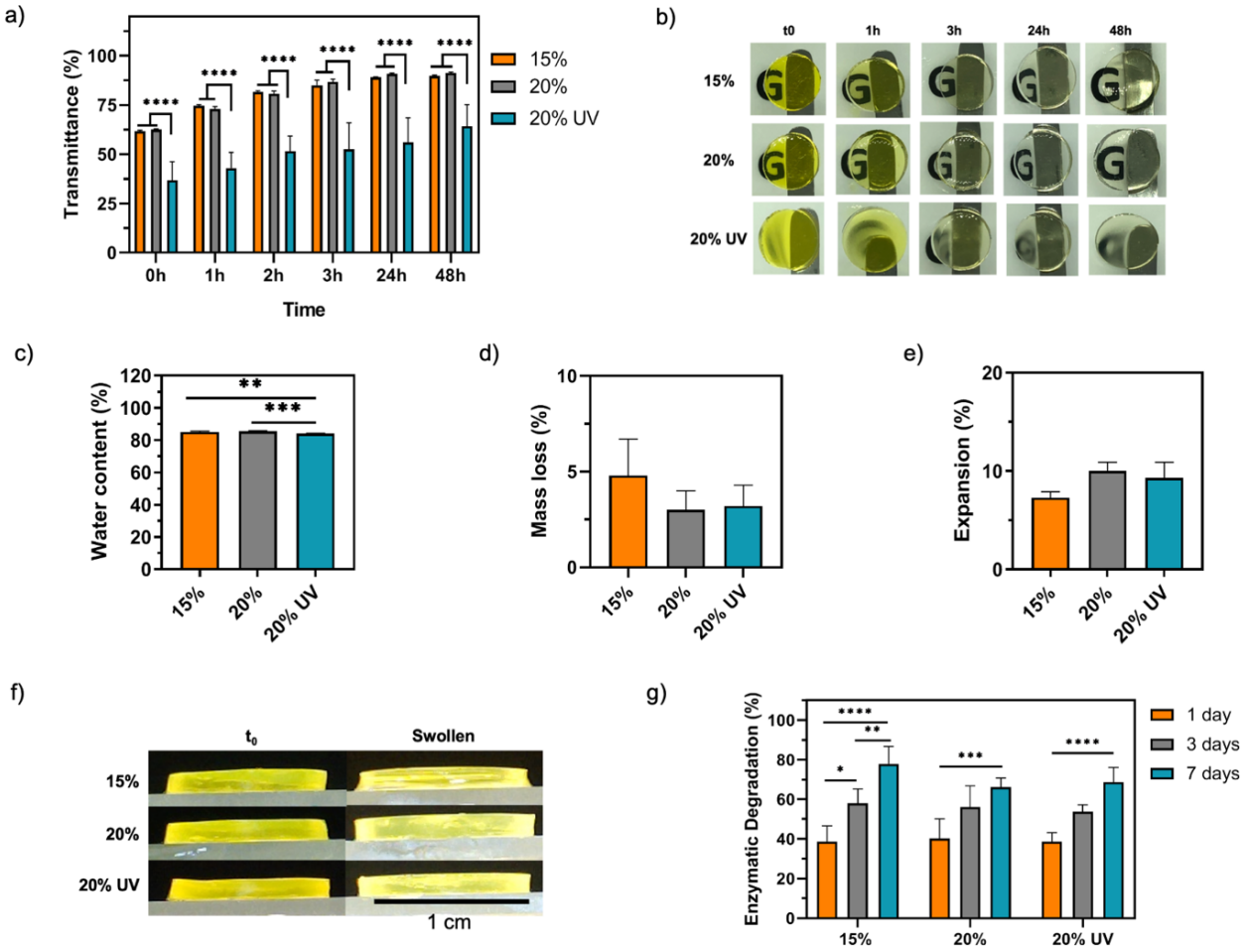


Figure 4. In vitro characterisation of GelMA bioadhesives. GelMA hydrogels transmittance in the visible range: (**a**) average optical transmittance and (**b**) optical transparency of the hydrogels overtime. Hydrogel diameter = 1 cm. Swelling properties of GelMA hydrogels in PBS at 32 °C: (**c**) equilibrium water content (%), (**d**) mass loss (%), (**e**) expansion (%) in PBS and (**f**) lateral image of the hydrogels after photocrosslinking (t_0) and after 24 h incubation in PBS (swollen). (**g**) In vitro degradation of GelMA hydrogels incubated in 1 U/mL collagenase II at 32 °C for 1, 3 and 7 days. Data are presented as mean value ± SD (* $p < 0.05$, ** $p < 0.01$, *** $p < 0.001$, **** $p < 0.0001$).

The microstructure of GelMA bioadhesives was investigated using SEM and micro-CT analysis. SEM images of the adhesive's surface revealed a uniform and interconnected pore structure for all studied groups (Figure 5a). Since SEM images suggest that 20% UV bioadhesives have a smaller pore size than 15 and 20% samples, micro-CT was subsequently used to investigate the internal structure of the bioadhesives. As shown in Figure 5b–d, the pore size distribution was different between the studied groups. The narrower size distribution observed for 20% bioadhesives suggests a negative correlation between polymer concentration and size distribution. Likewise, the light wavelength and intensity used also seem to affect size distribution as 20% UV bioadhesives showed a narrower size distribution compared to 20%. We observed that, for 20% samples, 19 ± 5% and 20 ± 2% of the pores had 50 and 100 µm, respectively, while the prevalence of 50 and 100 µm pores in 20% UV adhesives was 35 ± 5% and 16 ± 3%, respectively (Figure 5c,d). As shown in Figure 5e, the total porosity of 15, 20 and 20% UV bioadhesives was 67 ± 4, 59 ± 6 and 25 ± 3%, respectively. The porosity of 20% UV samples was significantly lower than 15% ($p < 0.0001$) and 20% ($p < 0.001$). Likewise, the structure thickness of 20% UV samples (142 ± 10 µm) was significantly higher than 15% (79 ± 16 µm, $p < 0.01$) and 20% (91 ± 8 µm, $p < 0.01$) bioadhesives (Figure 5f). Finally, the average pore size of 15, 20 and 20% UV samples

was significantly different and equal to 167 ± 24, 118 ± 11 and 74 ± 6 µm, respectively (Figure 5g).

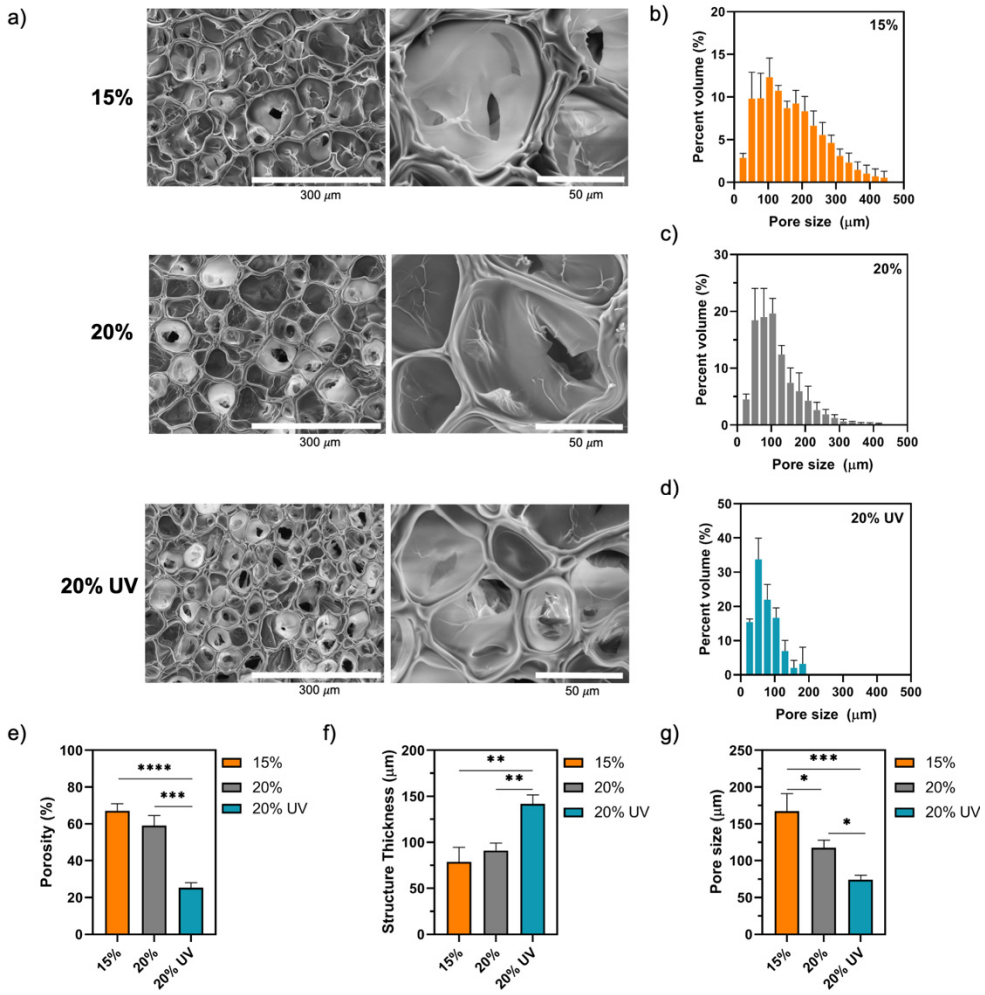


Figure 5. GelMA bioadhesives morphology and microstructure analysis after freeze drying. (**a**) Representative SEM images of GelMA scaffolds at different magnifications. Quantitative analysis of porosity by micro-CT: (**b**–**d**) pore size distribution in the hydrogels, (**e**) total porosity, (**f**) mean pore wall thickness and (**g**) mean pore size. Data are presented as mean value ± SD (* $p < 0.05$, ** $p < 0.01$, *** $p < 0.001$ and **** $p < 0.0001$).

The viscoelastic properties of GelMA bioadhesives were studied via oscillatory rheometry. Storage (G′) and loss (G″) modulus represent the elastic and reversible response of the material and the viscous and irreversible rearrangement of its polymeric structure, respectively [58,59]. As shown in Figure 6a,b, a positive correlation between G′ and the polymer concentration was observed. A total of 15% bioadhesives (3.4 ± 0.1 kPa) had a 55% lower G′ than 20% (5.5 ± 0.9 kPa, $p < 0.05$) and 20% UV (5.2 ± 1.1 kPa, $p < 0.05$). The G″ values were not statistically different between groups, ranging from 107 and 163 kPa (Figure 6c). Moreover, the damping factor (G″/G′) was lower than 0.03 for all the samples (Figure 6d). Then, the mechanical performance of GelMA bioadhesives was assessed by compressive and tensile mechanical testing (Figure 6e,g). In agreement with the rheology data, statistical analysis showed a significant effect of polymer concentration on the compressive and tensile moduli (Figure 6f,h). The compressive modulus of 15% bioadhesives (84 ± 4 kPa) was significantly lower than 20% (207 ± 9 kPa, $p < 0.0001$) and 20% UV (255 ± 25 kPa, $p < 0.0001$) samples, a difference of approximately 3-fold (Figure 6f). Despite this difference, all groups resisted 8 cycles of 60% strain without apparent damage, demonstrating the

mechanical stability of GelMA bioadhesives. Additionally, our results showed that 15% samples (34 ± 9 kPa) exhibited lower tensile modulus than 20% (51 ± 6 kPa, $p < 0.01$) and 20% UV (60 ± 7 kPa, $p < 0.001$) adhesives (Figure 6h). Higher compressive and tensile moduli were observed for 20% UV samples when compared to 20%; however, only the difference in the compressive moduli was significant ($p < 0.01$). Finally, the ultimate tensile strength of 15, 20 and 20% UV bioadhesives was 36 ± 5, 50 ± 10 and 47 ± 10 kPa, respectively ($p > 0.05$, Figure 6i), and the maximum elongation was between 130–150% ($p > 0.05$, Supplementary Figure S1).

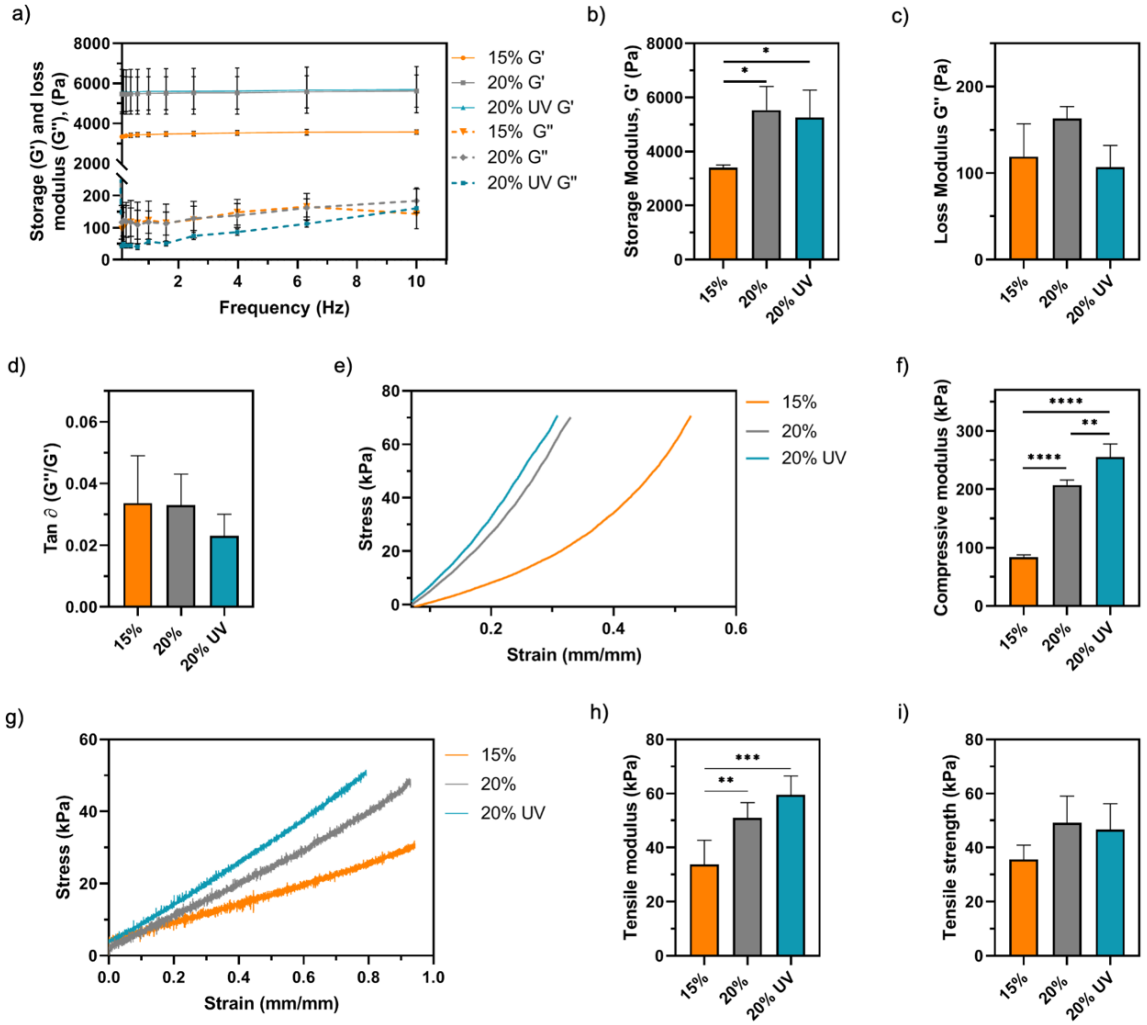


Figure 6. Rheological properties of GelMA bioadhesives: (**a**) frequency sweep, (**b**) storage modulus (G′), (**c**) loss modulus (G″) and (**d**) damping factor (tan δ). Cyclic compressive mechanical testing of GelMA hydrogels: (**e**) representative compressive stress–strain curves and (**f**) compressive moduli. Tensile mechanical testing of GelMA hydrogels: (**g**) representative tensile stress–strain curves, (**h**) tensile moduli and (**i**) maximum tensile strength. Data are presented as mean value ± SD (* $p < 0.05$, ** $p < 0.01$, *** $p < 0.001$, **** $p < 0.0001$).

3.4. Ex Vivo Retention of GelMA Bioadhesives

Next, ex vivo analysis was carried out to assess if the GelMA bioadhesive could fill a partial-thickness corneal injury and restore the corneal curvature. We observed that GelMA could be administered to the wound bed as a flowable liquid, fill the injury and adapt to the wound shape prior to physical crosslinking. As shown in Figure 7, GelMA bioadhesives formed a smooth contour on the corneal surface. The hydrogel remained optically clear after placement and exhibited excellent adhesion to the corneal tissue. After 24 h, stromal

swelling could be observed due to absorption of water by the ex vivo cornea. Despite the increasing stromal pressure, all studied groups were retained in situ, without any signs of detachment, degradation, or shape loss at day 7.

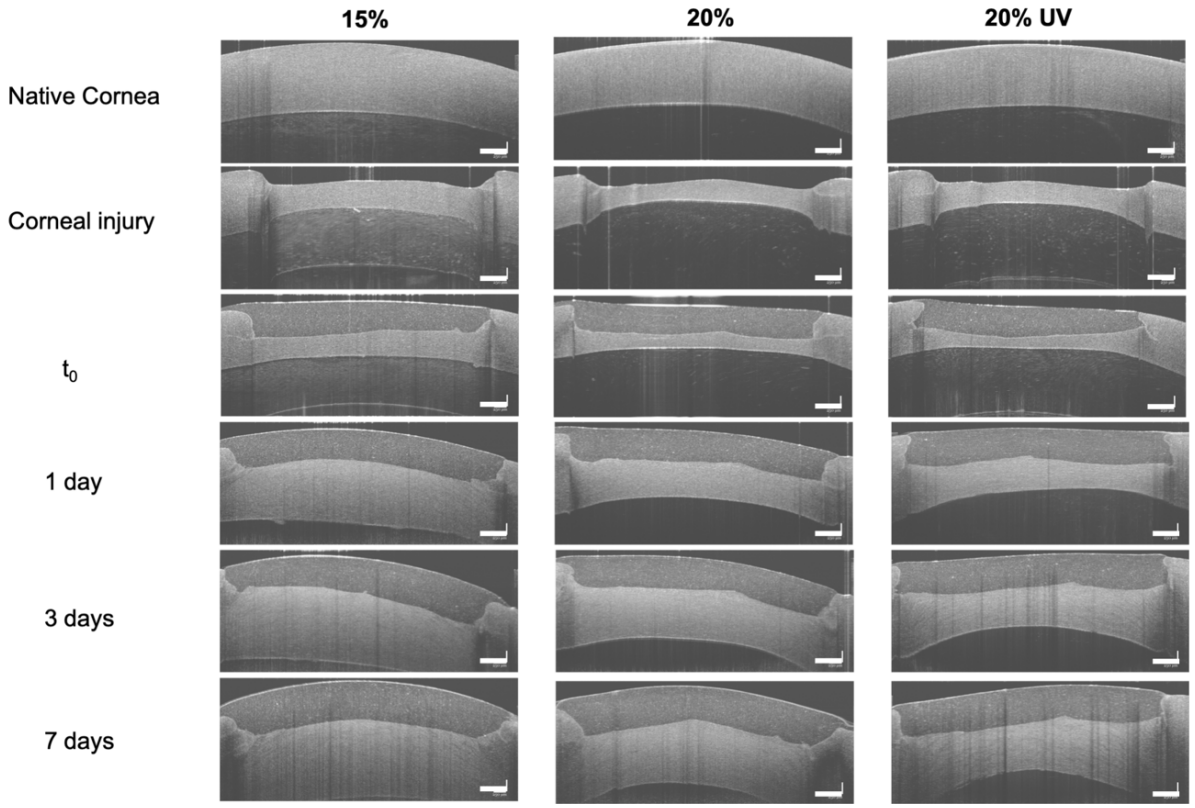


Figure 7. Ex vivo optical coherence tomography images of the native porcine cornea, partial-thickness corneal injury (≃50% deep) and GelMA bioadhesives immediately after photocrosslinking (t_0) and after 1, 3 and 7 days. Scale bar = 500 μm.

3.5. In Vitro Assessment of Cytocompatibility

The viability, metabolic activity and proliferation of HDFs seeded on GelMA bioadhesives were evaluated. As shown in Figure 8a, live/dead images indicate high-cell viability for all tested conditions, with cells exhibiting a fibroblast-like morphology suggesting that GelMA bioadhesives did not induce toxicity. All groups were capable of supporting cell attachment and proliferation, with cell confluency being reached within 7 days. Since no dead cells were observed in the live/dead images, the proliferation of cells on the hydrogels was subsequently quantified. The DNA-normalised metabolic activity of HDFs cells seeded on 20% and 20% UV GelMA bioadhesives was slightly higher than 15% samples throughout the experiment (Figure 8b). However, the difference was only significant between 15 and 20% GelMA bioadhesives at day 7 ($p < 0.05$).

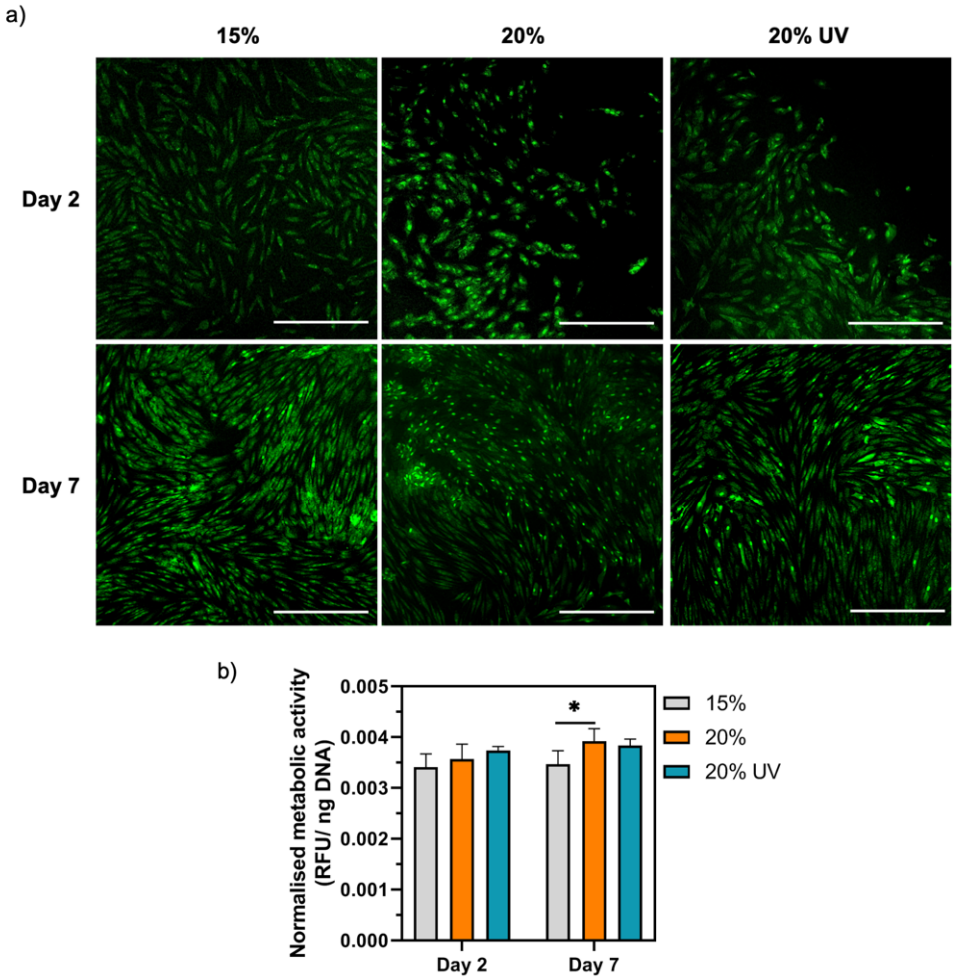


Figure 8. Cytotoxicity of GelMA hydrogels. (**a**) Live/Dead images of HDFs seeded on GelMA adhesives. Scale bar = 45 µm. (**b**) Normalized metabolic activity 2 and 7 days after cell seeding. Data are presented as mean value ± SD (* $p < 0.05$).

4. Discussion

Currently, there is a clinical need to develop strong and leak-free tissue adhesives that preserve corneal tissue function, decreasing postoperative morbidity and improving patient comfort [2]. While CA glues are toxic and associated with a range of complications, biocompatible fibrin and PEG-based adhesives are weak and degrade quickly making them ineffective to be applied as stromal fillers and for long-term treatments. This study aims to engineer a biocompatible and optically clear GelMA-based stromal filler with the adequate mechanical and adhesive properties to seal full-thickness corneal perforations.

Ease of use and rapid gelation times are essential characteristics for the clinical suitability, acceptance and success of an adhesive. To achieve fast gelation ($\leq$2 min), the photosensitive GelMA prepolymer solution was mixed with RF and SPS. As shown in Supplementary Figure S2, RF is a naturally occurring photosensitive molecule with a distinct absorption peak in the UV ($\lambda = 375$ nm) and visible ($\lambda = 450$ nm) range, which have high molar extinction coefficients (Supplementary Table S1). Photoinitiators with lower extinction coefficients would require longer irradiation times or higher photoinitiators/accelerators concentrations that are incompatible with the desired application given the increased photocrosslinking time and possible cytotoxic effects. In addition, the fact that both visible and UV can trigger the free-radical crosslinking reaction allows the photocrosslinking capability testing of both wavelengths. Since light is a form of electromagnetic energy, depending on its intensity, both UV, visible and infrared light can cause ocular damage [60]. Nevertheless, several ocular structures absorb or scatter some of the

light entering the eye, protecting the retina from damage. In this study, the UV wavelength (365 nm) and riboflavin (2.66 mM) concentration were chosen in agreement with CXL therapy [54]. Li et al. used UV radiation (365 nm, 35 mW/cm^2, 2 min) to crosslink a thiol-acrylate hydrogel on a rabbit's cornea. Post-implantation histological examination did not find any signs of inflammation or tissue damage on the corneal epithelium, stroma or endothelium [13]. Importantly, the photocrosslinking parameters used by Li et al. were very similar to the conditions used in this study to cure 20% UV GelMA (365 nm, 30 mW/cm^2, 2 min). In this study, the photocrosslinking capability of visible light (lower energy) was also assessed through the preparation of 15 and 20% GelMA bioadhesives. Lastly, RF's slow gelation kinetics would be incompatible with the desired application [61]. To overcome this issue, we utilised SPS, an electron acceptor that is reported to enable the fast and safe photocrosslinking of polymers [61,62]. The 15, 20% and 20% UV GelMA bioadhesives were crosslinked under physiological conditions since all components are water soluble and the system RF/SPS is not susceptible to oxygen inhibition. Taken together, we showed the importance of employing the appropriate photoinitiator/curing system on the utility of the corneal adhesive in the clinical setting.

The burst pressure is the most relevant parameter to assess the efficacy of GelMA bioadhesives in sealing full-thickness corneal perforations under liquid pressure. Thus, the mechanical adhesion of GelMA formulations was assessed in porcine eyes and compared with Histoacryl (CA). CA adhesives are proinflammatory, induce corneal vascularization and scarring, and inhibit corneal tissue regeneration [23]. Still, given its strong adhesion strength, fast polymerisation and ease of use, these adhesives are currently used 'off-label' by ophthalmologists to seal ocular wounds [18]. In this work, no significant differences in the burst pressure were observed between 20 and 20% UV GelMA samples and the control, even though 15% bioadhesives showed a significantly lower burst pressure than Histoacryl. GelMA bioadhesives could withstand on average an IOP between 33 and 49 kPa without leakages, values that are at least 17-fold higher than the human physiological IOP range (2 $\pm$ 0.4 kPa, Figure 2f) [63]. Recently, several different photoinitiator systems have been combined with GelMA, drastically affecting the final properties of the hydrogels [11,13,34–37,43,45–48]. As shown in Supplementary Figure S3, the ocular burst pressure obtained using LAP (~11 kPa) was around 4-times lower than RF/SPS (~48 kPa, $p < 0.0001$), highlighting the advantages of using this system when crosslinking GelMA hydrogels.

After surgery and during the healing process the adhesives will be subjected to shear forces due to eyelid and eyeball movements. This will likely cause patient discomfort and potentially result in implant failure. Therefore, we evaluated the physical robustness of our GelMA bioadhesive in satisfying these critical parameters. We employed the in vitro lap shear tests to investigate the adhesive's performance on wet and dry substrates. The average shear strength of GelMA bioadhesives was higher than Histoacryl, which was only not significantly lower than 20% GelMA (Figure 3b). Moreover, GelMA achieved strong adhesion in dry (gelatine-coated glass slides), semi-wet (porcine cornea mounted on ACC) and wet (full-thickness injury in eye) substrates, while Histoacryl was only effective to glue wet substrates. This highlights the versatility of GelMA bioadhesives and supports their suitability to be applied in dynamic in vivo conditions.

CAs are reported to fail in adhering to wet surfaces due to their solidification immediately upon exposure to water [36]. The moisture on the ocular surface needs to be carefully controlled and the adhesive rapidly applied, as it might polymerize before entering in contact with the wound bed. Due to this fast (10–60 s) but uncontrolled polymerization, together with a very low viscosity, the successful application of CA glues remains a challenge and specialised training is required [18]. Nonetheless, fast sealing is of utmost importance as it avoids glue dilution due to continuous fluid egress from the wound. In this study, once the GelMA bioadhesive is heated to 37 °C, the flowable polymer can be added to the ocular injury. After filling the wound bed, the solution will physically crosslink upon

cooling since the ocular temperature is around 32 °C, forming an adhesive plug within seconds. Then, this reversible seal can be chemically crosslinked with light.

As shown in Supplementary Figure S4b, in addition to fail as a stromal filler, Histoacryl also creates a rough and opaque seal that precludes vision and makes the visualisation of infectious infiltrates and wound healing assessment challenging (Figure 2h) [4]. Usually, a bandage contact lens is often needed to improve patient comfort [18]. In contrast, GelMA adhesives formed a smooth contour and restored the ocular curvature (Figure 7). The 15 and 20% GelMA adhesives were macroscopically clear with a light-yellow colour after curing and exhibited a transmittance of ~63% (Figure 4a,b). This lower transmittance value was due to the RF being trapped within the gel absorbing light in the 400–500 nm range (Supplementary Figure S5). Since RF does not participate in the crosslinking reaction, the optical transmittance increases to ~85% after 2–3 h as RF diffuses out of the hydrogel. This value is higher than the reported human corneal transmittance (78–80%) [64,65]. Although the filler will suffer degradation and remodelling in vivo, the bioadhesive needs to have similar transmittance to the human cornea to replicate visual acuity. However, 20% UV bioadhesives were opaque with an average transmittance of ~64% (Figure 4a,b). We observed a 2-fold decrease in the porosity and a significant pore size decrease (~37%) when UV light was used to crosslink 20% GelMA, which are thought to cause light scattering, affecting transparency. Together, our findings indicate the 15 and 20% GelMA bioadhesives show suitable optical properties for corneal engineering applications. Further, as previously reported by Gorth et al., we observed a negative correlation between the porosity and pore size and the tensile and compressive moduli of the adhesive (Figure 6f,h) [66]. However, the pore structure did not influence the adhesive's burst pressure (Figure 2d,f).

Lastly, CA adhesives form a water-tight, but inflexible, bond to tissue, which makes its application inadequate for tissues with physiological movement. In the management of ocular perforations, CA glue patching is reported to be successful only when the perforation is smaller than 1 mm and, in 30 to 50% of the cases, the glue needs to be reapplied due to leaks [18,23]. Consequently, an ideal adhesive for corneal perforations needs to be tough, but pliable. Hatami-Marbini studied the dynamic shear properties of corneal stroma using oscillatory experiments, showing that corneal G′ and G″ varied from 2 to 8 kPa and 0.3 to 1.2 kPa, respectively [67]. In this work, all formulations exhibited a G′ within the mentioned range (3.4 to 5.5 kPa); however, the G″ of our hydrogels was out of range (~0.1 kPa). Importantly, the hydrogels showed a G″ that was an order of magnitude lower than G′, confirming the viscoelastic behaviour of GelMA bioadhesives (Figure 6b,c) [68].

Whilst commercially available fibrin and CA-based adhesives are not approved for ocular use, some PEG-based sealants were granted approval for corneal incision sealing [69,70]. However, it is important to note that these adhesives have not been designed for long-term integration in the cornea. Despite being useful in reinforcing suture sealing, these materials are inappropriate to function as stromal fillers due to poor adhesion, high swelling rates and short retention times (few hours to a couple days). ReSure is the only FDA-approved sealant for intraoperative management of corneal incisions, while OcuSeal is the only option approved in Europe [69,71,72]. Since these sealants are composed by 89% of water, they form a smooth and lubricious surface, avoiding the use of a bandage contact lens for improved comfort [73]. However, they are reported to be sloughed off in tears within 1–4 days due to eyelid movement and PEG hydrolysis/enzymatic degradation [18,69,71,74–76]. Additionally, despite exhibiting lower swelling than other PEG-adhesives, the weight increase in ReSure is approximately 35% [72]. Hydrophilic hydrogels are 3D water-swellable networks. High swelling ratios weaken the mechanical properties, potentiate degradation and impact the overall shape of the adhesives, which might influence sealing and induce pressure on the surrounding tissues. GelMA adhesives showed high dimensional stability with an expansion between 7 and 10%, thereby reducing the risk of implant mismatch (Figure 4e,f). Additionally, all studied formulations exhibited water content values similar to the human cornea (72–85%) [77–79].

Strong adhesion to the host tissue and in situ retention are paramount for the success of a bioadhesive [28]. The ex vivo retention of GelMA bioadhesives was studied by making a 50% deep corneal injury in porcine corneas. The average thickness the porcine cornea is approximately 1400 µm, whilst the human cornea is on average 500–700 µm thick (Supplementary Figure S4a) [80]. OCT images show negligible bioadhesive degradation in PBS over the course of the experiment (Figure 7). Corneal swelling and loss of corneal transparency was observed after 24 h due to ex vivo absorption of large amounts of water by the stromal proteoglycans [81,82]. Importantly, 15 and 20% GelMA bioadhesives remained optically clear throughout the experiment. Despite the increased stromal swelling pressure, GelMA bioadhesives remained attached to the cornea demonstrating a strong tissue bond.

The GelMA adhesive strength depends on its cohesion (crosslinking density) and interfacial adhesiveness to the wound bed [28]. Such strong adhesion to the tissue is expected to arise from a synergistic effect between physical interaction (mechanical interlocking to the ECM), covalent bonding, hydrogen bonding and electrostatic and hydrophobic interactions [33,37,38]. As previously reported, the methacrylic/methacryloyl groups on GelMA can react with the thiol and amine groups on the tissue, imparting tissue adhesion due to the formation of chemical bonds between the two surfaces [46]. Furthermore, functional groups on GelMA backbone (e.g., –OH, $–NH_2$) can also form hydrogen bonds with the corresponding component on the tissue interface [30]. Taken together, our results show that GelMA adhesives are dimensionally stable and restore the corneal curvature, while showing a strong adhesion and retained transparency in vitro.

As with CAs, the rapid and uncontrollable polymerisation of ReSure and OcuSeal works both in favour and against them. Since these sealants polymerise within 10–20 s after mixing, a late application might result in polymer hardening within the applicator [33]. Conversely, if the adhesive is applied too early, the wound will not be properly sealed due to the low viscosity of the material [73,75]. Before exposure to light, GelMA forms a plug within the wound, but the adhesive is soft and can still be easily removed. The use of light to crosslink GelMA bioadhesives hardens the polymer and allows tuning over the polymerization rate depending on the desired mechanical properties (chemical crosslinking).

The synergy between the mechanical and biological adhesive characteristics is of utmost importance in the adhesive's success by preventing corneal scarring and vascularisation. Consequently, the absence of cell adhesion moieties in CAs and PEG-based adhesives halts its application as stromal fillers since cell adhesion is an essential step for successful tissue regeneration [37,72]. In this work, a protein-based polymer was chosen due to its biocompatibility, biodegradability and presence of cell adhesion sites (e.g., RGD sequences). Albeit having a negligible degradation in PBS, a time-dependent degradation in the presence of collagenase II was observed, demonstrating the biodegradability of the GelMA adhesives (Figure 4g). The fact that the bioadhesive can be enzymatically degraded, allowing cells to remodel their environment, is essential for wound repair. According to our results, the engineered hydrogels were not toxic and could support the adhesion and proliferation of HDFs over 7 days, confirming the cytocompatibility of the adhesive (Figure 8). These results also confirm that the reagents used in the photocrosslinking reaction (RF/SPS) were not cytotoxic at the concentrations used in this study. Previous studies using similar concentrations of SPS reported that this molecule is rapidly consumed during the photocrosslinking reaction to levels that are not cytotoxic to cells (<20 µm) [34,61].

Recently, some authors have used the Eosin Y/TEA/VC system to photocrosslink GelMA (GelCORE) [45,48] and glycidyl methacrylate-modified gelatine (GELGYM) bioadhesive hydrogels [37]. Both adhesives supported cell adhesion and proliferation. GelCORE effectively sealed corneal defects and induced stromal regeneration and re-epithelization in a rabbit stromal defect model [45]. Sani et al. compared the burst pressures of ReSure and GelCORE (20% GelMA, Eosin Y, TEA, VC, 100 mW/cm^2, visible light, 4 min) on 2 mm full-thickness injuries on rabbit eyes. The authors obtained a burst pressure of 30 ± 4 and 15 ± 6 kPa for GelCORE and ReSure, respectively [45]. In this study, the average burst pressure GelMA (visible light, 2 min) on a 2 mm full-thickness injury on a porcine cornea

was 49 ± 9 kPa (Figure 2d). Shorter gelling times improve the clinical usability of these adhesives given the importance of rapid polymerisation on the performance and overall acceptance of tissue adhesives [45,48].

To our knowledge, this is the first study to investigate GelMA hydrogel formation via RF/SPS mediated photocrosslinking. We demonstrated that GelMA bioadhesives are effective on both wet and dry substrates, highlighting its versatility and potential to be applied in different physiological conditions. Considering that our optimised formulation (20% GelMA) showed an averaged burst pressure of 49 ± 9 kPa and knowing that the normal physiological and hypertensive blood pressures are approximately 8–19 and 40 kPa, respectively, we hypothesise that GelMA bioadhesives could meet the criteria for vascular sealants [36]. Moreover, GelMA adhesives could also be assessed as corneal stromal substitutes replacing the need for donor corneas in keratoplasty. Finally, the main limitation of GelMA bioadhesives is related with the usability, as both the polymer and RF/SPS need to be reconstituted in PBS and heated to 37 °C and an external light source is required to crosslink the bioadhesive. Due to the difficulty in replicating in vitro the ocular complex physiological environment, long-term experiments in an ex vivo ocular model or in vivo will be required to further evaluate the intrinsically linked physical and biological attributes of these photocurable bioadhesives, such as light effect in retinal toxicity, cytotoxicity, host response and the adhesive performance and degradation in the eye (ocular movements, blinking and tear film). The delivery of antibiotics, growth factors or anti-inflammatory agents from GelMA bioadhesives should be considered in the future since the biopolymer hydrophilic nature provides a solubilizing environment for the incorporation of many bioactive molecules.

5. Conclusions

This work describes the synthesis and characterisation of a novel protein-based bioadhesive for the treatment of corneal perforations. The injectable bioadhesive, composed by GelMA and a riboflavin/sodium persulfate photoinitiator system, can be photocrosslinked in situ within 2 min using either UV or visible light. Ex vivo experiments in porcine eyes demonstrated complete sealing of full-thickness corneal perforations in the absence of sutures. The engineered adhesive has high translational potential due to its superior adhesion to both wet and dry substrates, outstanding physical properties, viscoelasticity and cytocompatibility in comparison to the commercially available options (e.g., fibrin glue, ReSure and cyanoacrylates).

Supplementary Materials: The following are available online at https://www.mdpi.com/article/10.3390/bioengineering9020053/s1. Table S1: Comparison between different biocompatible photoinitiators: toxicity, water solubility and molar extinction coefficient at different wavelengths (365, 405, 450, 500 and 500 nm); Figure S1: Tensile mechanical testing of GelMA bioadhesives: elongation at the point of failure; Figure S2: Normalised absorption spectrum of riboflavin aqueous solution; Figure S3: Mean burst pressure of GelMA adhesives photocrosslinked with LAP and RF-SPS photoinitiator system; Figure S4: Central porcine corneal thickness distribution and comparison between an intact cornea and an ocular injury filled with GelMA adhesive and Histoacryl; Figure S5: GelMA hydrogels transmittance in the visible range.

Author Contributions: I.A.B.: conceptualization, methodology, validation, formal analysis, investigation, and writing—original draft preparation; K.M.: methodology, investigation, and writing—review and editing, T.E.R.: methodology, investigation; S.C.C.: supervision, and Writing—Review and editing; A.K.G.: project administration, supervision, and Writing—Review and editing. All authors have read and agreed to the published version of the manuscript.

Funding: This research received no external funding.

Institutional Review Board Statement: Not applicable.

Informed Consent Statement: Not applicable.

Data Availability Statement: The data presented in this study are available on request from the corresponding author.

Acknowledgments: The authors would like to thank Cécile Le Duff for her assistance with ^{1}H-NMR spectroscopy.

Conflicts of Interest: The authors declare no conflict of interest.

References

1. Islam, M.M.; Buznyk, O.; Reddy, J.C.; Pasyechnikova, N.; Alarcon, E.I.; Hayes, S.; Lewis, P.; Fagerholm, P.; He, C.; Iakymenko, S.; et al. Biomaterials-enabled cornea regeneration in patients at high risk for rejection of donor tissue transplantation. *Npj Regen. Med.* **2018**, *3*, 2. [CrossRef] [PubMed]
2. Bhatia, S.K. *Biomaterials for Clinical Applications*; Springer: New York, NY, USA, 2010; ISBN 9788578110796.
3. Grinstaff, M.W. Designing hydrogel adhesives for corneal wound repair. *Biomaterials* **2007**, *28*, 5205–5214. [CrossRef] [PubMed]
4. Bhatia, S.S. Ocular surface sealants and adhesives. *Ocul. Surf.* **2006**, *4*, 146–154. [CrossRef]
5. Tan, J.; Foster, L.J.R.; Watson, S.L. Corneal Sealants in Clinical Use: A Systematic Review. *Curr. Eye Res.* **2020**, *45*, 1025–1030. [CrossRef] [PubMed]
6. Bhatia, S.K.; Arthur, S.D.; Chenault, H.K.; Figuly, G.D.; Kodokian, G.K. Polysaccharide-based tissue adhesives for sealing corneal incisions. *Curr. Eye Res.* **2007**, *32*, 1045–1050. [CrossRef]
7. Hashemi, H.; Dadgostar, A. Automated lamellar therapeutic keratoplasty with fibrin adhesive in the treatment of anterior corneal opacities. *Cornea* **2011**, *30*, 655–659. [CrossRef]
8. Kaufman, H.E.; Insler, M.S.; Ibrahim-Elzembely, H.A.; Kaufman, S.C. Human Fibrin Tissue Adhesive for Sutureless Lamellar Keratoplasty and Scleral Patch Adhesion: A Pilot Study. *Ophthalmology* **2003**, *110*, 2168–2172. [CrossRef]
9. Annabi, N.; Yue, K.; Tamayol, A.; Khademhosseini, A. Elastic sealants for surgical applications. *Eur. J. Pharm. Biopharm.* **2015**, *95*, 27–39. [CrossRef]
10. Petrie, E.M. Cyanoacrylate adhesives in surgical applications: A critical review. *Rev. Adhes. Adhes.* **2014**, *2*, 253–310. [CrossRef]
11. Assmann, A.; Vegh, A.; Ghasemi-Rad, M.; Bagherifard, S.; Cheng, G.; Sani, E.S.; Ruiz-Esparza, G.U.; Noshadi, I.; Lassaletta, A.D.; Gangadharan, S.; et al. A highly adhesive and naturally derived sealant. *Biomaterials* **2017**, *140*, 115–127. [CrossRef]
12. Shahbazi, J.; Marçal, H.; Watson, S.; Wakefield, D.; Sarris, M.; Foster, L.J.R. Sutureless sealing of penetrating corneal wounds using a laser-activated thin film adhesive. *Lasers Surg. Med.* **2011**, *43*, 490–498. [CrossRef] [PubMed]
13. Li, L.; Lu, C.; Wang, L.; Chen, M.; White, J.; Hao, X.; McLean, K.M.; Chen, H.; Hughes, T.C. Gelatin-Based Photocurable Hydrogels for Corneal Wound Repair. *ACS Appl. Mater. Interfaces* **2018**, *10*, 13283–13292. [CrossRef] [PubMed]
14. Mehdizadeh, M.; Yang, J. Design Strategies and Applications of Tissue Bioadhesives. *Macromol. Biosci.* **2013**, *13*, 271–288. [CrossRef] [PubMed]
15. Panda, A.; Kumar, S.; Kumar, A.; Bansal, R.; Bhartiya, S. Fibrin glue in ophthalmology. *Indian J. Ophthalmol.* **2009**, *57*, 371. [CrossRef]
16. Jhanji, V.; Young, A.L.; Mehta, J.S.; Sharma, N.; Agarwal, T.; Vajpayee, R.B. Management of Corneal Perforation. *Surv. Ophthalmol.* **2011**, *56*, 522–538. [CrossRef]
17. Oelker, A.M.; Grinstaff, M.W. Ophthalmic adhesives: A materials chemistry perspective. *J. Mater. Chem.* **2008**, *18*, 2521–2536. [CrossRef]
18. Trujillo-de Santiago, G.; Sharifi, R.; Yue, K.; Sani, E.S.; Kashaf, S.S.; Alvarez, M.M.; Leijten, J.; Khademhosseini, A.; Dana, R.; Annabi, N. Ocular adhesives: Design, chemistry, crosslinking mechanisms, and applications. *Biomaterials* **2019**, *197*, 345–367. [CrossRef]
19. Cavanaugh, T.B.; Gottsch, J.D. Infectious keratitis and cyanoacrylate adhesive. *Am. J. Ophthalmol.* **1991**, *111*, 466–472. [CrossRef]
20. Ferry, A.P.; Barnert, A.H. Granulomatous Keratitis Resulting From use of Cyanoacrylate Adhesive for Closure of Perforated Corneal Ulcer. *Am. J. Ophthalmol.* **1971**, *72*, 538–541. [CrossRef]
21. Markowitz, G.D.; Orlin, S.E.; Frayer, W.C.; Andrews, A.P.; Prince, R.B. Corneal Endothelial Polymerization of Histoacryl Adhesive: A Report of a New Intraocular Complication. *Ophthalmic Surg. Lasers Imaging Retin.* **1995**, *26*, 256–258. [CrossRef]
22. Siegal, J.E.; Zaidman, G.W. Surgical removal of cyanoacrylate adhesive after accidental instillation in the anterior chamber. *Ophthalmic Surg.* **1989**, *20*, 179–181. [CrossRef]
23. Samarawickrama, C.; Samanta, A.; Liszka, A.; Fagerholm, P.; Buznyk, O.; Griffith, M.; Allan, B. Collagen-Based Fillers as Alternatives to Cyanoacrylate Glue for the Sealing of Large Corneal Perforations. *Cornea* **2018**, *37*, 609–616. [CrossRef] [PubMed]
24. Bouten, P.J.M.; Zonjee, M.; Bender, J.; Yauw, S.T.K.; Van Goor, H.; Van Hest, J.C.M.; Hoogenboom, R. The chemistry of tissue adhesive materials. *Prog. Polym. Sci.* **2014**, *39*, 1375–1405. [CrossRef]
25. Natour, E.; Suedkamp, M.; Dapunt, O.E. Assessment of the effect on blood loss and transfusion requirements when adding a polyethylene glycol sealant to the anastomotic closure of aortic procedures: A case-control analysis of 102 patients undergoing Bentall procedures. *J. Cardiothorac. Surg.* **2012**, *7*, 1. [CrossRef]
26. Covidien. *DuraSeal Package Insert*; Covidien: Mansfield, MA, USA, 2005.
27. *CoSeal Package Insert*; Baxter: Hong Kong, China, 2006.

28. Liang, Y.; Li, Z.; Huang, Y.; Yu, R.; Guo, B. Dual-Dynamic-Bond Cross-Linked Antibacterial Adhesive Hydrogel Sealants with On-Demand Removability for Post-Wound-Closure and Infected Wound Healing. *ACS Nano* **2021**, *15*, 7078–7093. [CrossRef]
29. Hasani-Sadrabadi, M.M.; Sarrion, P.; Pouraghaei, S.; Chau, Y.; Ansari, S.; Li, S.; Aghaloo, T.; Moshaverinia, A. An engineered cell-laden adhesive hydrogel promotes craniofacial bone tissue regeneration in rats. *Sci. Transl. Med.* **2020**, *12*. [CrossRef]
30. Zhou, L.; Dai, C.; Fan, L.; Jiang, Y.; Liu, C.; Zhou, Z.; Guan, P.; Tian, Y.; Xing, J.; Li, X.; et al. Injectable Self-Healing Natural Biopolymer-Based Hydrogel Adhesive with Thermoresponsive Reversible Adhesion for Minimally Invasive Surgery. *Adv. Funct. Mater.* **2021**, *31*, 2007457. [CrossRef]
31. Han, W.; Zhou, B.; Yang, K.; Xiong, X.; Luan, S.; Wang, Y.; Xu, Z.; Lei, P.; Luo, Z.; Gao, J.; et al. Biofilm-inspired adhesive and antibacterial hydrogel with tough tissue integration performance for sealing hemostasis and wound healing. *Bioact. Mater.* **2020**, *5*, 768–778. [CrossRef]
32. Balakrishnan, B.; Payanam, U.; Laurent, A.; Wassef, M.; Jayakrishnan, A. Efficacy evaluation of an in situ forming tissue adhesive hydrogel as sealant for lung and vascular injury. *Biomed. Mater.* **2021**, *16*, 044106. [CrossRef]
33. Sani, E.S.; Lassaletta, A.D.; Wang, X.; Assmann, A.; Zhang, Y.-N.; Weiss, A.S.; Annabi, N.; Cheng, G.; Vegh, A.; Khademhosseini, A.; et al. Engineering a highly elastic human protein–based sealant for surgical applications. *Sci. Transl. Med.* **2017**, *9*, eaai7466.
34. Elvin, C.M.; Vuocolo, T.; Brownlee, A.G.; Sando, L.; Huson, M.G.; Liyou, N.E.; Stockwell, P.R.; Lyons, R.E.; Kim, M.; Edwards, G.A.; et al. A highly elastic tissue sealant based on photopolymerised gelatin. *Biomaterials* **2010**, *31*, 8323–8331. [CrossRef]
35. Kilic Bektas, C.; Burcu, A.; Gedikoglu, G.; Telek, H.H.; Ornek, F.; Hasirci, V. Methacrylated gelatin hydrogels as corneal stroma substitutes: In vivo study. *J. Biomater. Sci. Polym. Ed.* **2019**, *30*, 1803–1821. [CrossRef]
36. Hong, Y.; Zhou, F.; Hua, Y.; Zhang, X.; Ni, C.; Pan, D.; Jiang, D.; Yang, L.; Lin, Q.; Zou, Y.; et al. A strongly adhesive haemostatic hydrogel for the repair of arterial and heart bleeds. *Nat. Commun.* **2019**, *10*, 2060. [CrossRef]
37. Sharifi, S.; Islam, M.M.; Sharifi, H.; Islam, R.; Koza, D.; Reyes-Ortega, F.; Alba-Molina, D.; Nilsson, P.H.; Dohlman, C.H.; Mollnes, T.E.; et al. Tuning gelatin-based hydrogel towards bioadhesive ocular tissue engineering applications. *Bioact. Mater.* **2021**, *6*, 3947–3961. [CrossRef]
38. Anthis, A.H.C.; Hu, X.; Matter, M.T.; Neuer, A.L.; Wei, K.; Schlegel, A.A.; Starsich, F.H.L.; Herrmann, I.K. Chemically Stable, Strongly Adhesive Sealant Patch for Intestinal Anastomotic Leakage Prevention. *Adv. Funct. Mater.* **2021**, *31*, 2007099. [CrossRef]
39. Bayat, N.; Zhang, Y.; Falabella, P.; Menefee, R.; Whalen, J.J.; Humayun, M.S.; Thompson, M.E. A reversible thermoresponsive sealant for temporary closure of ocular trauma. *Sci. Transl. Med.* **2017**, *9*. [CrossRef]
40. Fernandes-Cunha, G.M.; Chen, K.M.; Chen, F.; Le, P.; Han, J.H.; Mahajan, L.A.; Lee, H.J.; Na, K.S.; Myung, D. In situ-forming collagen hydrogel crosslinked via multi-functional PEG as a matrix therapy for corneal defects. *Sci. Rep.* **2020**, *10*, 16671. [CrossRef]
41. Xiang, L.; Cui, W. Biomedical application of photo-crosslinked gelatin hydrogels. *J. Leather Sci. Eng.* **2021**, *3*, 3. [CrossRef]
42. Klotz, B.J.; Gawlitta, D.; Rosenberg, A.J.W.P.; Malda, J.; Melchels, F.P.W. Gelatin-Methacryloyl Hydrogels: Towards Biofabrication-Based Tissue Repair. *Trends Biotechnol.* **2016**, *34*, 394–407. [CrossRef]
43. Hutson, C.B.; Nichol, J.W.; Aubin, H.; Bae, H.; Yamanlar, S.; Al-Haque, S.; Koshy, S.T.; Khademhosseini, A. Synthesis and Characterization of Tunable Poly(Ethylene Glycol): Gelatin Methacrylate Composite Hydrogels. *Tissue Eng. Part A* **2011**, *17*, 1713–1723. [CrossRef]
44. Goto, R.; Nishida, E.; Kobayashi, S.; Aino, M.; Ohno, T.; Iwamura, Y. Gelatin Methacryloyl—Riboflavin (GelMA—RF) Hydrogels for Bone Regeneration. *Int. J. Mol. Sci.* **2021**, *22*, 1635. [CrossRef] [PubMed]
45. Sani, E.S.; Kheirkhah, A.; Rana, D.; Sun, Z.; Foulsham, W.; Sheikhi, A.; Khademhosseini, A.; Dana, R.; Annabi, N. Sutureless repair of corneal injuries using naturally derived bioadhesive hydrogels. *Sci. Adv.* **2019**, *5*, eaav1281. [CrossRef] [PubMed]
46. Tavafoghi, M.; Sheikhi, A.; Tutar, R.; Jahangiry, J.; Baidya, A.; Haghniaz, R.; Khademhosseini, A. Engineering Tough, Injectable, Naturally Derived, Bioadhesive Composite Hydrogels. *Adv. Healthc. Mater.* **2020**, *9*, 1901722. [CrossRef] [PubMed]
47. Annabi, N.; Rana, D.; Shirzaei Sani, E.; Portillo-Lara, R.; Gifford, J.L.; Fares, M.M.; Mithieux, S.M.; Weiss, A.S. Engineering a sprayable and elastic hydrogel adhesive with antimicrobial properties for wound healing. *Biomaterials* **2017**, *139*, 229–243. [CrossRef] [PubMed]
48. Khalil, I.A.; Saleh, B.; Ibrahim, D.M.; Jumelle, C.; Yung, A.; Dana, R.; Annabi, N. Ciprofloxacin-loaded Bioadhesive Hydrogels for Ocular Applications. *Biomater. Sci.* **2020**, *8*, 5196–5209. [CrossRef] [PubMed]
49. Randleman, J.B.; Khandelwal, S.S.; Hafezi, F. Corneal cross-linking. *Surv. Ophthalmol.* **2015**, *60*, 509–523. [CrossRef]
50. Jeng, B.H. *Advances in Medical and Surgical Cornea*; Springer: Berlin/Heidelberg, Germany, 2014; ISBN 9783662448878.
51. Lee, H.J.; Fernandes-Cunha, G.M.; Myung, D. In situ-forming hyaluronic acid hydrogel through visible light-induced thiol-ene reaction. *React. Funct. Polym.* **2018**, *131*, 29–35. [CrossRef]
52. Wang, Z.; Tian, Z.; Menard, F.; Kim, K. Comparative study of gelatin methacrylate hydrogels from different sources for biofabrication applications. *Biofabrication* **2017**, *9*, 044101. [CrossRef]
53. Cui, X.; Soliman, B.G.; Alcala-Orozco, C.R.; Li, J.; Vis, M.A.M.; Santos, M.; Wise, S.G.; Levato, R.; Malda, J.; Woodfield, T.B.F.; et al. Rapid Photocrosslinking of Silk Hydrogels with High Cell Density and Enhanced Shape Fidelity. *Adv. Healthc. Mater.* **2020**, *9*, 1901667. [CrossRef]
54. Bhattacharjee, P.; Fernández-Pérez, J.; Ahearne, M. Potential for combined delivery of riboflavin and all-trans retinoic acid, from silk fibroin for corneal bioengineering. *Mater. Sci. Eng. C* **2019**, *105*, 110093. [CrossRef]

55. Zhu, M.; Wang, Y.; Ferracci, G.; Zheng, J.; Cho, N.J.; Lee, B.H. Gelatin methacryloyl and its hydrogels with an exceptional degree of controllability and batch-to-batch consistency. *Sci. Rep.* **2019**, *9*, 6863. [CrossRef] [PubMed]
56. Lee, B.H.; Lum, N.; Seow, L.Y.; Lim, P.Q.; Tan, L.P. Synthesis and characterization of types A and B gelatin methacryloyl for bioink applications. *Materials* **2016**, *9*, 797. [CrossRef] [PubMed]
57. Pahoff, S.; Meinert, C.; Bas, O.; Nguyen, L.; Klein, T.J.; Hutmacher, D.W. Effect of gelatin source and photoinitiator type on chondrocyte redifferentiation in gelatin methacryloyl-based tissue-engineered cartilage constructs. *J. Mater. Chem. B* **2019**, *7*, 1761–1772. [CrossRef] [PubMed]
58. Barroso, I.A.; Man, K.; Villapun, V.M.; Cox, S.S.; Ghag, A.K. Methacrylated Silk Fibroin Hydrogels: pH as a Tool to Control Functionality. *ACS Biomater. Sci. Eng.* **2021**, *7*, 4779–4791. [CrossRef]
59. Guimarães, C.F.; Gasperini, L.; Marques, A.P.; Reis, R.L. The stiffness of living tissues and its implications for tissue engineering. *Nat. Rev. Mater.* **2020**, *5*, 351–370. [CrossRef]
60. Good, G.W. Light and Eye Damage. *Am. Optom. Assoc.* **2014**, 1–13.
61. Piluso, S.; Flores Gomez, D.; Dokter, I.; Moreira Texeira, L.; Li, Y.; Leijten, J.; Van Weeren, R.; Vermonden, T.; Karperien, M.; Malda, J. Rapid and cytocompatible cell-laden silk hydrogel formation: Via riboflavin-mediated crosslinking. *J. Mater. Chem. B* **2020**, *8*, 9566–9575. [CrossRef]
62. Fancy, D.A.; Kodadek, T. Chemistry for the analysis of protein-protein interactions: Rapid and efficient cross-linking triggered by long wavelength light. *Proc. Natl. Acad. Sci. USA* **1999**, *96*, 6020–6024. [CrossRef]
63. Wang, Y.X.; Xu, L.; Wei, W.B.; Jonas, J.B. Intraocular pressure and its normal range adjusted for ocular and systemic parameters. The Beijing eye study 2011. *PLoS ONE* **2018**, *13*, e0196926. [CrossRef]
64. Rafat, M.; Li, F.; Fagerholm, P.; Lagali, N.S.; Watsky, M.A.; Munger, R.; Matsuura, T.; Griffith, M. PEG-stabilized carbodiimide crosslinked collagen-chitosan hydrogels for corneal tissue engineering. *Biomaterials* **2008**, *29*, 3960–3972. [CrossRef]
65. Freegard, T.J. The physical basis of transparency of the normal cornea. *Eye* **1997**, *11 Pt 4*, 465–471. [CrossRef] [PubMed]
66. Gorth, D.; Webster, T.J. Matrices for tissue engineering and regenerative medicine. In *Biomaterials for Artificial Organs*; Woodhead Publishing: Sawston, UK, 2010; pp. 270–286. [CrossRef]
67. Hatami-Marbini, H. Viscoelastic shear properties of the corneal stroma. *J. Biomech.* **2014**, *47*, 723–728. [CrossRef] [PubMed]
68. Kim, S.H.; Yeon, Y.K.; Lee, J.M.; Chao, J.R.; Lee, Y.J.; Seo, Y.B.; Sultan, M.T.; Lee, O.J.; Lee, J.S.; Yoon, S.I.; et al. Precisely printable and biocompatible silk fibroin bioink for digital light processing 3D printing. *Nat. Commun.* **2018**, *9*, 1620. [CrossRef] [PubMed]
69. BD. *BD Ocuseal Liquid Bandage Leaflet*; BD: Le Pont de Claix, France, 2009.
70. Ocular Therapeutix, Inc. ReSure Sealant Instructions for Use. Ocular Therapeutix: Bedford, MA, USA, 2014.
71. Dell, S.J.; Hovanesian, J.A.; Raizman, M.B.; Crandall, A.S.; Doane, J.; Snyder, M.; Masket, S.; Lane, S.; Fram, N. Randomized comparison of postoperative use of hydrogel ocular bandage and collagen corneal shield for wound protection and patient tolerability after cataract surgery. *J. Cataract Refract. Surg.* **2011**, *37*, 113–121. [CrossRef]
72. FDA. *ReSure Summary of Safety and Effectiveness Data*; FDA: Bedford, MA, USA, 2014.
73. Potvin, R.; Makari, S. Cataract surgery and methods of wound closure: A review. *Clin. Ophthalmol.* **2015**, *9*, 921–928. [CrossRef]
74. Mah, F.S. Effect on gel formation time of adding topical ophthalmic medications to resure sealant, an in situ hydrogel. *J. Ocul. Pharmacol. Ther.* **2016**, *32*, 396–399. [CrossRef]
75. Uy, H.S.; Kenyon, K.R. Surgical outcomes after application of a liquid adhesive ocular bandage to clear corneal incisions during cataract surgery. *J. Cataract Refract. Surg.* **2013**, *39*, 1668–1674. [CrossRef]
76. Lerit, S.J.T.; Abano, J.M.R. Comparison of Tensile Strength of Fibrin Glue, 2-Octyl Cyanoacrylate, Liquid Ocular Bandage, and Conventional Nylon 10-0 Sutures in Corneal Laceration Repair in an Animal Model. *Philipp. Acad. Opthamlmol.* **2012**, *37*, 52–58.
77. Liang, Y.; Liu, W.; Han, B.; Yang, C.; Ma, Q.; Zhao, W.; Rong, M.; Li, H. Fabrication and characters of a corneal endothelial cells scaffold based on chitosan. *J. Mater. Sci. Mater. Med.* **2011**, *22*, 175–183. [CrossRef]
78. Taylor, Z.D.; Garritano, J.; Sung, S.; Bajwa, N.; Bennett, D.B.; Nowroozi, B.; Tewari, P.; Sayre, J.W.; Hubschman, J.-P.; Deng, S.X.; et al. THz and mm-Wave Sensing of Corneal Tissue Water Content: Electromagnetic Modeling and Analysis. *Physiol. Behav.* **2016**, *176*, 139–148. [CrossRef]
79. Pircher, M.; Götzinger, E.; Leitgeb, R.; Fercher, A.F.; Hitzenberger, C.K. Measurement and imaging of water concentration in human cornea with differential absorption optical coherence tomography. *Opt. Express* **2010**, *11*, 2190. [CrossRef] [PubMed]
80. Brightbill, F.S.; McDonnell, P.J.; McGhee, C.N.; Farjo, A.A.; Serdarevic, O. *Corneal Surgery: Theory Technique and Tissue*; Elsevier Health Sciences: Amsterdam, The Netherlands, 2009; ISBN 9780323048835.
81. Oie, Y.; Nishida, K. Corneal regenerative medicine. *Regen. Ther.* **2016**, *5*, 40–45. [CrossRef] [PubMed]
82. Huang, Y.X. Corneal tissue engineering. *Biointegr. Med. Implant Mater. Sci. Des.* **2010**, 86–115.